UNIVERSITY OF CALIFORNIA

Los Angeles

Design of Concrete Composites for Advanced Functionality and Sustainability

A dissertation submitted in partial satisfaction of the

requirements for the degree Doctor of Philosophy

in Materials Science and Engineering

by

Gabriel David Falzone

2019

ABSTRACT OF THE DISSERTATION

Design of Concrete Composites for Advanced Functionality and Sustainability

by

Gabriel David Falzone

Doctor of Philosophy in Materials Science and Engineering

University of California, Los Angeles, 2019

Professor Gaurav Sant, Chair

Concrete presents a significant challenge to the environmental sustainability of the construction sector, being responsible for nearly 9 % of annual global carbon dioxide (CO_2) emissions that contribute to climate change. CO_2 emissions related to concrete construction may be reduced by: (a) improving the thermal performance of building envelopes to minimize heating/air conditioning energy inputs, (b) extending the service lifetime of concrete infrastructure, or (c) replacing ordinary portland cement (OPC) by alternative binders that emit less CO_2 in their production. Three pathways towards these ends are highlighted:

a. Using concretes that contain functional **inclusions** (e.g., phase change materials – PCMs) is one method *to improve the thermal performance of building envelopes*. While the energy benefits of these concretes have been well-established, the potential for soft PCM inclusions to degrade the mechanical performance of concrete composites may limit their use.

b. Reducing the tendency of steel **reinforcement** within concrete to corrode is a critical step towards *extending infrastructural service lifetimes.* Typical corrosion mitigation strategies do not directly reduce the abundance of deleterious chloride ions (e.g., from de-icing salts or seawater) and are therefore difficult to implement successfully.

c. To directly reduce the embodied CO_2 emissions of concrete, it is necessary to *develop low-carbon cementitious **binders***, i.e., carbonate binders that gain strength by converting gaseous CO_2 into stable solid minerals. Development of material formulations and processing routes for scalable production of concrete components via carbonation has remained a critical challenge.

This dissertation provokes and addresses research questions pertinent to each of these pathways. First, the mechanical behavior of cementitious composites containing PCMs is studied to aid in the development of improved predictive models and PCM dosage guidelines. Second, a novel cementitious formulation featuring unprecedented chloride-scavenging potential is designed and predicted to significantly delay the onset of reinforcing steel corrosion via finite element modeling. Finally, the CO_2 mineralization reactions and strength development of carbonate binders containing portlandite ($Ca(OH)_2$) are investigated, towards the production of low-carbon concrete by CO_2 capture/utilization from flue gases. These advancements stimulate pathways for the design of sustainable concrete composites that reduce CO_2 emissions from the construction sector.

The dissertation of Gabriel David Falzone is approved.

Dwight Christopher Streit

George M. DeShazo

Richard B. Kaner

John Wright Wallace

Gaurav Sant, Committee Chair

University of California, Los Angeles

2019

Table of Contents

List of Figures

List of Tables

Preface

First, I must thank my graduate advisor, Professor Gaurav Sant for his mentorship and support throughout my Ph.D. studies. Second, I express my deep appreciation to my committee for their time and guidance. I would like to thank my research collaborators for their efforts and inspiration, including: Professor Laurent Pilon, Professor Mathieu Bauchy, Magdalena Balonis, Aditya Kumar, Dale Bentz, Isabella Pignatelli, Bu Wang, and Erika Callagon La Plante, all members of the LC^2 and PARISlab and other collaborators. Finally, I would like to express my utmost gratitude to my girlfriend, family, friends, for their unwavering patience, encouragement, and love that helped raise me up throughout my Ph.D. journey.

This dissertation contains modified versions of manuscripts that have been published in journal articles, have been submitted to journals, or are currently in preparation for publication. All research was conducted in the Laboratory for the Chemistry of Construction Materials (LC^2) and the core-facility Molecular Instrumentation Center (MIC) at the University of California, Los Angeles (UCLA). As such, the authors acknowledge the support that has made these laboratories and their operations possible. The contents of each paper reflect the views and opinions of the authors, who are responsible for the accuracy of the datasets presented therein, and do not reflect the views and/or policies of the funding agencies, nor do the contents constitute a specification, standard or regulation.

Chapter two is a version of [Falzone, G.; Falla, G. P.; Wei, Z.; Zhao, M.; Kumar, A.; Bauchy, M.; Neithalath, N.; Pilon, L.; Sant, G. The Influences of Soft and Stiff Inclusions on the Mechanical

Properties of Cementitious Composites. *Cem. Concr. Comp.* **2016**, *71*, 153–165, dx.doi.org/10.1016/j.cemconcomp.2016.05.008]. G. Falzone oversaw the experimental program, analyzed the experimental data with respect to the effective medium approximations, and prepared the manuscript. G. Puerta-Falla, Z. Wei., and M. Zhao prepared specimens and performed measurements of compressive strength and modulus of elasticity. A. Kumar assessed interparticle spacing via a microstructural packing algorithm. M. Bauchy, N. Neithalath, L. Pilon, and G. Sant provided insightful analysis of the results and added to the discussion. G. Sant was the PI overseeing all research activities. All authors assisted in revising and proofreading the manuscript. The authors acknowledge financial support for this research provisioned by the California Energy Commission (Contract: PIR: 12-032), the University of California, Los Angeles (UCLA) and National Science Foundation (CMMI: 1130028). The last author acknowledges discretionary support provided by the Edward K. and Linda L. Rice Endowed Chair in Materials Science.

Chapter three is a version of [Falzone, G.; Balonis, M.; Sant, G. X-AFm Stabilization as a Mechanism of Bypassing Conversion Phenomena in Calcium Aluminate Cements. *Cem. Concr. Res.* **2015**, *72*, 54–68, dx.doi.org/10.1016/j.cemconres.2015.02.022]. G. Falzone performed all experiments, analyzed experimental data, and wrote the manuscript. M. Balonis performed the thermodynamic modeling and analyzed data. G. Sant conceived of and oversaw the research as PI, in addition to assisting in data analysis. All authors assisted in revising the manuscript. The authors acknowledge financial support for this research provisioned by the University of California, Los Angeles (UCLA), Yara Industrial Nitrates and National Science Foundation (CMMI: 1066583 and 1401533). The authors would like to acknowledge provision of materials by Kerneos Aluminate Technologies and Yara International. The last author would also like to acknowledge discretionary

support for this research provided by the Edward K. and Linda L. Rice Endowed Chair in Materials Science.

Chapter four is a version of [Falzone, G.; Balonis, M.; Bentz, D.; Jones, S.; Sant, G. Anion Capture and Exchange by Functional Coatings: New Routes to Mitigate Steel Corrosion in Concrete Infrastructure. *Cem. Concr. Res.* **2017**, *101*, 82–92, dx.doi.org/10.1016/j.cemconres. 2017.08.021]. G. Falzone performed all experiments and modeling and wrote the manuscript. S. Jones and D. Bentz assisted in formulating the finite element model. M. Balonis performed thermodynamic modeling to provide modeling inputs. G. Sant was the PI supervising the research and assisted in data analysis. All authors participated in revising and strengthening the manuscript. The authors acknowledge financial support for this research provided by: The National Science Foundation (CMMI: 1401533 and CAREER: 1253269), University of California, Los Angeles (UCLA) and Yara Industrial Nitrates. The authors acknowledge the support that has made possible the Engineering Laboratory at the National Institute of Standards and Technology (NIST) (in which the study was performed) and its operations. The authors thank Prof. Bruce Dunn/Jonathan Lau for access to electrochemical characterization tools. MB and GNS acknowledge Professor Fredrik P. Glasser (University of Aberdeen, Scotland) for his insights and stimulating discussions regarding ion exchange processes.

Chapter five is a version of a manuscript in preparation for publication [Falzone, G.; Mehdipour, I.; Callagon La Plante, E.; Sant, G. Understanding CO_2 Mineralization Kinetics and Conversion Limits of Alkaline Solid Particulates and Composites. *RSC Green Chem.* **2019**, *In Preparation for Publication*.]. G. Falzone performed the experiments, analyzed the data, and wrote the manuscript.

All authors contributed to data analysis and manuscript revisions. G. Sant was the PI. The authors acknowledge financial support for this research from the Department of Energy: Office of Fossil Energy via the National Energy Technology Laboratory (NETL; DE-FE0029825 and DE-FE0031718), The Anthony and Jeanne Pritzker Family Foundation and the National Science Foundation (CAREER Award: 1253269).

Chapter six is a version of a manuscript that has been submitted for publication [Mehdipour, I.; Falzone, G.; Callagon La Plante, E.; Pilon, L.; Simonetti, D.; Neithalath, N.; Sant, G. How Microstructure and Pore Moisture Affect Strength Gain in Portlandite-Enriched Composites that Mineralize CO_2. *ACS Sustain. Chem. Eng.* **2019**, *Submitted*.]. I. Mehdipour and G. Falzone contributed equally to this work. I. Mehdipour performed the experiments. I. Mehdipour and G. Falzone analyzed the data and wrote the manuscript. All authors contributed to revising the manuscript and data interpretation. G. Sant was the PI. The authors acknowledge financial support for this research from the Department of Energy: Office of Fossil Energy via the National Energy Technology Laboratory (NETL; DE-FE0029825 and DE-FE0031718), The Anthony and Jeanne Pritzker Family Foundation and the National Science Foundation (CAREER Award: 1253269). The authors acknowledge Alex Hall (Suffolk Construction), James McDermott (Rusheen Capital Management / U.S. Renewables Group) and Edward Muller (Transocean / AeroVironment) for many stimulating discussions and for their insights over the course of this research.

Biographical Sketch

2014 B.S., Materials Engineering
University of California, Los Angeles
Los Angeles, CA, USA

2014-2019 Graduate Student Researcher/Teaching Assistant
University of California, Los Angeles
Los Angeles, CA, USA

Selected journal publications (out of 24 total):

Falzone, G.; Balonis, M.; Sant, G. X-AFm Stabilization as a Mechanism of Bypassing Conversion Phenomena in Calcium Aluminate Cements. *Cem. Concr. Res.* **2015**, *72*, 54–68.

Vance, K.; **Falzone, G.**; Pignatelli, I.; Bauchy, M.; Balonis, M.; Sant, G. Direct Carbonation of Ca(OH)2 Using Liquid and Supercritical CO2: Implications for Carbon-Neutral Cementation. *Ind. Eng. Chem. Res.* **2015**, *54* (36), 8908–8918.

Falzone, G.; Falla, G. P.; Wei, Z.; Zhao, M.; Kumar, A.; Bauchy, M.; Neithalath, N.; Pilon, L.; Sant, G. The Influences of Soft and Stiff Inclusions on the Mechanical Properties of Cementitious Composites. *Cem. Concr. Comp.* **2016**, *71*, 153–165.

Oey, T.; Kumar, A.; **Falzone, G.**; Huang, J.; Kennison, S.; Bauchy, M.; Neithalath, N.; Bullard, J. W.; Sant, G. The Influence of Water Activity on the Hydration Rate of Tricalcium Silicate. *J. Am. Ceram. Soc.* **2016**, *99* (7), 2481–2492.

Thiele, A. M.; Wei, Z.; **Falzone, G.**; Young, B. A.; Neithalath, N.; Sant, G.; Pilon, L. Figure of Merit for the Thermal Performance of Cementitious Composites Containing Phase Change Materials. *Cem. Concr. Comp.* **2016**, *65*, 214–226.

Krishnan, N. A.; Wang, B.; **Falzone, G.**; Le Pape, Y.; Neithalath, N.; Pilon, L.; Bauchy, M.; Sant, G. Confined Water in Layered Silicates: The Origin of Anomalous Thermal Expansion Behavior in Calcium-Silicate-Hydrates. *ACS Appl. Mater. Inter.* **2016**, *8* (51), 35621–35627.

Falzone, G.; Balonis, M.; Bentz, D.; Jones, S.; Sant, G. Anion Capture and Exchange by Functional Coatings: New Routes to Mitigate Steel Corrosion in Concrete Infrastructure. *Cem. Concr. Res.* **2017**, *101*, 82–92.

Puerta-Falla, G.; Balonis, M.; **Falzone, G.**; Bauchy, M.; Neithalath, N.; Sant, G. Monovalent Ion Exchange Kinetics of Hydrated Calcium-Alumino Layered Double Hydroxides. *Ind. Eng. Chem. Res.* **2017**, *56* (1), 63–74.

Wei, Z.; **Falzone, G.**; Das, S.; Saklani, N.; Le Pape, Y.; Pilon, L.; Neithalath, N.; Sant, G. Restrained Shrinkage Cracking of Cementitious Composites Containing Soft PCM Inclusions: A Paste (Matrix) Controlled Response. *Mater. Design* **2017**, *132*, 367–374.

Wei, Z.; **Falzone, G.**; Wang, B.; Thiele, A.; Puerta-Falla, G.; Pilon, L.; Neithalath, N.; Sant, G. The Durability of Cementitious Composites Containing Microencapsulated Phase Change Materials. *Cem. Concr. Comp.* **2017**, *81*, 66–76.

Young, B. A.; **Falzone, G.**; She, Z.; Thiele, A. M.; Wei, Z.; Neithalath, N.; Sant, G.; Pilon, L. Early-Age Temperature Evolutions in Concrete Pavements Containing Microencapsulated Phase Change Materials. *Constr. Build. Mater.* **2017**, *147*, 466–477.

Okoronkwo, M. U.; **Falzone, G.**; Wada, A.; Franke, W.; Neithalath, N.; Sant, G. Rheology-Based Protocol to Establish Admixture Compatibility in Dense Cementitious Suspensions. *J. Mater. Civ. Eng.* **2018**, *30* (7), 04018122.

Wei, Z.; Wang, B.; **Falzone, G.**; La Plante, E. C.; Okoronkwo, M. U.; She, Z.; Oey, T.; Balonis, M.; Neithalath, N.; Pilon, L.; Sant, G. Clinkering-Free Cementation by Fly Ash Carbonation. *J. CO2 Util.* **2018**, *23*, 117–127.

Young, B. A.; **Falzone, G.**; Wei, Z.; Sant, G.; Pilon, L. Reduced-Scale Experiments to Evaluate Performance of Composite Building Envelopes Containing Phase Change Materials. *Constr. Build. Mater.* **2018**, *162*, 584–595.

Ketel, S.; **Falzone, G.**; Wang, B.; Washburn, N.; Sant, G. A Printability Index for Linking Slurry Rheology to the Geometrical Attributes of 3D-Printed Components. *Cem. Concr. Comp.* **2018**.

Timmons, J.; **Falzone, G.**; Balonis, M.; Bauchy, M.; Sant, G. Anomalous Variations in the Viscous Activation Energy of Suspensions Induced by Fractal Structuring. *J. Colloid Interf. Sci.***2018**, *530*, 603–609.

Mehdipour, I.; **Falzone, G.**; Callagon La Plante, E.; Pilon, L.; Simonetti, D.; Neithalath, N.; Sant, G. How Microstructure and Pore Moisture Affect Strength Gain in Portlandite-Enriched Composites that Mineralize CO_2. *ACS Sustain. Chem. Eng.* **2019**, *Submitted*.

Falzone, G.; Mehdipour, I.; Callagon La Plante, E.; Sant, G. Understanding CO_2 Mineralization Kinetics and Conversion Limits of Alkaline Solid Particulates and Composites. *RSC Green Chem.* **2019**, *In Preparation for Publication*.

Selected conference presentations (out of 4 total):

"Direct carbonation of $Ca(OH)_2$ using liquid and supercritical CO_2: A potential route towards CO2-neutral cementation," **Falzone, G.**; Vance, K.; Pignatelli, I.; Wang, B,: Bauchy, M.; Balonis, M.; Sant, G.; 1st International Conference on Grand Challenges in Construction Materials (IGCMAT), Los Angeles, CA, 2016.

"Anion Capture and Exchange by Functional Coatings: New Routes to Mitigate Steel Corrosion in Concrete Infrastructure," **Falzone, G.**; Balonis, M.; Bentz, D.; Jones, S.; Sant, G.; ACI Fall Convention 2017, Anaheim, CA, 2017.

Chapter 1. Introduction and background

Concrete, a mixture of ordinary portland cement (OPC), water, fine aggregates, and coarse aggregates,[1] is the foundation of modern infrastructure. OPC, the binding agent in concrete, consists primarily of anhydrous calcium silicates, which react with water to form calcium silicate hydrate (C-S-H), an amorphous gel featuring variable ratios of calcium-to-silicon.[2] This reaction (hydration) provides strength in concrete, binding aggregates together and causing the transition from fluid to solid states, i.e., setting, and continued development of strength and engineering properties.[3] The setting transition enables concrete mixtures to be easily formed into desired geometries by casting them into formwork. This is significant, as the passive setting and hardening engendered by cement hydration reactions allow geometries to be formed on the construction site (or in off-site facilities), at ambient temperatures and with minimal intervention. This ability is one of the major benefits of concrete compared to other structural materials (e.g., steel, wood). Concrete is also attractive for its durability with respect to contact with soil and water, which may contain various aggressive chemical species relative to other materials, and in that the raw ingredients that make up cement (siliceous clays, sand, limestone, iron ore, gypsum)[4] and concrete are highly abundant and may be found (with local variations) across the world. It is because of these reasons that concrete is one of the world's most highly used materials, featuring a global production of ≈ 30 billion tons per year.[5]

Due to the massive scale of its production, concrete presents a significant challenge improving the environmental sustainability of the construction industry, especially as it pertains to reducing construction-associated greenhouse gas (GHG) emissions. The dominant source of CO_2

emissions embodied within concrete production is the manufacturing of OPC. As a reference, global concrete production incorporates ≈ 4.5 billion tons of ordinary portland cement (OPC) yearly, the manufacture of which contributes nearly 9 % of global CO_2 emissions (see Figure 1.1a).[5,6] Approximately 0.9 tons of CO_2 is emitted per ton of OPC produced.[7] This carbon footprint results from the decarbonation (calcination) reaction of quarried, crushed limestone ($CaCO_3$) – which directly emits CO_2[5,7] – and from the combustion necessary to heat cement kilns to drive clinkering reactions. Limestone calcination is performed at temperatures around 800 °C in order to provide lime (CaO) during the cement manufacturing process. Clinkering reactions, however, require further heating to temperatures of ≈ 1450 °C, for the silicates present in the raw meal to react with lime, forming the anhydrous calcium silicates (Ca_3SiO_5 and Ca_2SiO_4) that make up OPC. Additional CO_2 emissions are embodied in the energy required for grinding the quenched nodules of cement clinker into a fine powder, and in transportation of raw materials and the finished cement. Although concrete is a rather carbon-efficient material on a mass basis relative to other structural materials (e.g., structural steel), concrete-associated carbon emissions constitute a significant challenge to the greening of the construction industry due to the scale of the concrete market. This is further exacerbated by the lack of suitable replacements for concrete in applications such as streets, highways, bridges, and building foundations.

To impactfully advance the sustainability of the built environment, the GHG emissions embodied in the production of cementing systems must be transformatively addressed. Despite high industrial inertia, making fundamental changes to the production of cement has become increasingly pressing. This need is spurred by the growing consensus regarding the need to manage anthropogenic GHG emissions, as indicated by the implementation of carbon cap-and-trade

systems and penalties around the world.[8,9] The cement/concrete industry (and the broader construction sector) is especially vulnerable to cost penalties associated with CO_2 emissions, due to its high resource intensity, traditionally low profit margins, and lack of actionable alternative routes. The need to reduce the carbon impact of the construction sector, in both emissions embodied in materials and in operational energy expenditures, has become clear, as signaled by industry trends and regulations. Sustainable and low-carbon construction codes (e.g., CALgreen, ZERO Code™)[10,11] and certifications (e.g., LEED, Living Building Challenge)[12,13] have become increasingly important mechanisms by which buildings are designed, constructed, and marketed. Although such standards have been somewhat adopted (see Figure 1.1b), the fraction of construction projects that achieve such certifications remains in the minority. Further, even when LEED certifications are achieved, the use of dominantly prescriptive specifications for sustainability has proven an imperfect strategy. For example, some studies have indicated that LEED-certified buildings have provided negligible operational energy savings compared to comparable non-certified buildings.[14,15] Such findings motivate the increasing use of performance-based criteria to describe operational building energy consumption. Approximately 42 % of all U.S. is consumed by building operations (Figure 1.1c).[16] Although energy inputs associated with materials and construction initially dominate building-related emissions, this is reversed over the service lifetime of a building. For example, in a typical residential dwelling, operational energy expenditures make up ≈ 75 % of the energy consumption of a building (with ≈ 25 % attributed to materials/products) within 50 years after construction.[16] Zero net energy (ZNE) construction seeks to address this problem by reducing energy demands to an extent that on-site renewable energy sources (e.g., photovoltaic panels) are sufficient.[17,18] While such designs are possible, these

systems are only feasible when on-site energy demand may be first minimized via passive means, due to budget and sizing limitations of PVs, and considerations of project aesthetics.

The first focus in addressing the environmental impacts associated with the production of construction materials (including concrete), has been the rigorous quantification of embodied CO_2 emissions, etc., via environmental product declarations (EPDs). These EPDs are developed by manufacturers or environmental consultants, following a product-tailored methodology outlined in a product category rule (PCR) and verified by third party operator. The value of such EPDs has been made clear in both LEED standards, in which providing EPDs yields LEED credits, but also under legislation, such as the Buy Clean California Act (California AB-262).[19] The Buy Clean Act seeks to reduce the carbon intensity of construction in California by mandating that state-funded construction projects utilize materials that fall within a maximum global warming potential (GWP). All eligible materials mandated by the law (carbon steel rebar, structural steel, flat glass, and mineral wool insulation board) must demonstrate compliance to the outlined GWP limit via EPDs, prior to installation. The law currently does not directly impact concrete, but rather acts indirectly through regulating steel rebar. However, this regulation points to the rising importance of EPDs as a mechanism for the quantification, and ultimately reduction of GWP associated with the production of construction materials. Indeed, such legislation is being examined more broadly, to close "carbon loopholes" in trade that may exist in regions with strict regulations on carbon emissions related to manufacturing and/or energy. Similarly, the most recent rendition of LEED (v4) provides credits for reducing embodied CO_2 emissions, and the Living Building Challenge mandates that all emissions associated with construction/materials be offset by the one-time purchase of carbon offsets from an approved provider.

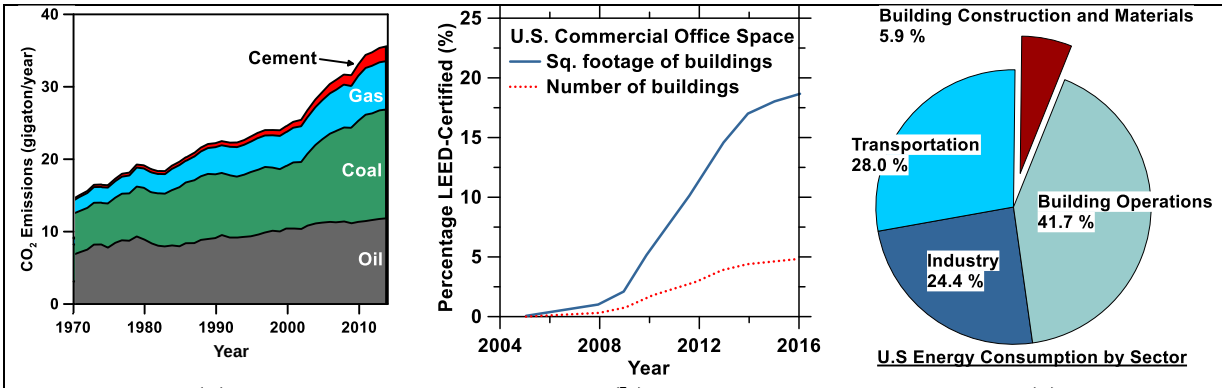

(a) **(b)** **(c)**

Figure 1.1: (a) Trends in global carbon emissions over time, indicating the scale of cement-related emissions relative to energy-related emissions.[20] **(b)** The percentage of LEED-certified commercial office buildings (by number and square footage) within the United States.[21] **(c)** Energy consumption in the United States divided by sector, indicating the significant impacts of building operations, construction, and materials (a combined 47.6 % of consumption).[16]

In addition to reducing the embodied CO_2 emissions of the materials, efforts to enhance the sustainability of the built environment may also act by extending the service lifetime of the structure, which reduces the frequency of demolition/rebuilding (which are highly energy and resource intensive). Yielding significant enhancements in service life of concrete construction requires expanding the specification criteria of concrete mixture designs beyond the simple basis of compressive strength, towards durability performance-based designs. For example, such a strategy has led to the development of concretes designed to feature low permeability to aqueous species (i.e., chloride) which may initiation corrosion of steel rebar. However, these solutions are still imperfect, as they often utilize prescriptive measures, rather than considerations of practical performance. The magnitude of the problem is indicated by the United States' consistently poor infrastructure ratings (N.B. ASCE's 2017 Infrastructure Report Card assigned the U.S. a D+, with bridges receiving a C+).[22] Furthermore, ≈ 40 % of the 614,387 bridges, in the United States are 50 years or older, and the average age of bridges has consistently increasing, with many bridges approaching their design life. Therefore, significant advances in extending the service lifetime and

quality of construction are in order, and the development of concrete formulations that enable improved durability is expected to feature a key role.

Altogether, the discussion above highlights: (a) that achieving quantifiable improvements in environmental sustainability has become increasingly important in the construction industry, a trend that will continue in time, and (b) that material solutions relating to concrete comprise a significant (but not complete) portion of the solution to these challenges. Guided by this motivation, the research described herein is focused on redesigning concrete composites at the component level, i.e., aggregate/inclusions, steel reinforcement, and the cementitious binder. Each thrust focuses on redefining the functionality of one of these components, as to target application-specific improvements in sustainability. Chapter 2 describes the mechanical behavior of cementitious composites containing functional inclusions (phase change materials – PCMs) which are designed to enhance the thermal performance of concrete building envelopes. The study aims to develop improved predictive models of mechanical behavior (specifically the modulus of elasticity) of such composites, and to inform PCM dosage guidelines that negate their detrimental influences on modulus of elasticity. Chapters 3 and 4 describe the development of an alternative cementitious binder formulation featuring unprecedented chloride-scavenging potential and which bypasses commonly deleterious degradation mechanisms. The ability of this formulation to mitigate steel reinforcement corrosion, i.e., demonstrating improved durability performance when employed as cover layers on concrete infrastructure, is benchmarked via finite element modeling. Chapters 5 and 6 discuss the development of low-carbon cementitious binders that gain strength by converting gaseous CO_2 into stable solid minerals. The kinetics and conversion limits of CO_2 mineralization reactions of alkaline solid reactants such as portlandite ($Ca(OH)_2$) are investigated. The strength development that results from CO_2 mineralization is also evaluated in detail, with

focus on elucidating the effects of component microstructure and pore water saturation. Chapter 7 offers an overall summary and conclusions, and stimulates directions for future research, primarily with respect to CO_2 mineralization. The research described herein stimulates pathways for the design of sustainable concrete composites that reduce the environmental impact of the construction sector.

Chapter 2. The influences of soft and stiff inclusions on the mechanical properties of cementitious composites

2.1. Introduction

Cementitious composites consist of hard mineral inclusions embedded in an inorganic polymeric matrix.[2] The matrix is dominantly composed of a calcium silicate hydrate phase which forms upon the reaction of cement with water.[2] Inclusions are embedded in cementing composites to reduce cost, since mineral aggregate inclusions (i.e., stone and sand) are far less expensive than cement, or to alter performance, such as to improve their stiffness.[23] There is interest in embedding microencapsulated phase change materials (PCM) to concrete to improve its thermal inertia, e.g., for building envelope applications. Indeed, based on their ability to store and release heat, PCMs increase the thermal inertia of building materials, and can thus improve the energy efficiency of buildings.[24–29] More recently, Fernandes et al.[30] also demonstrated the ability of PCM inclusions to reduce thermal cracking in cementitious systems. In such cases, it has been noted that while the addition of PCM improves thermal performance, it degrades the mechanical properties (i.e., both elastic modulus and compressive strength).[30]

Several studies have noted that the compressive strength of cementitious materials decreases with increasing PCM content.[30–32] However, data on the influence of PCMs on the stiffness of cementitious composites are far less available. Any reductions in the mechanical properties are problematic, as for reasons of structural capacity, even in building envelope applications, it is necessary that cement-based composites demonstrate sufficient strength and stiffness. Since PCMs

are soft inclusions, i.e., substantially weaker than the inorganic cementing matrix, parallels can be drawn to the additions of other soft inclusions to cementitious systems, e.g., of rubber inclusions, EPS (expanded polystyrene) inclusions etc., which may be added to reduce the density of concrete.[33–41] While these studies indicate similar trends as in the case of PCM additions, i.e., the mechanical properties degrade with increasing inclusion content, they seldom present complete experimental data of elastic moduli (*E*, *K* or *G*), and less often utilize EMAs to describe composite properties in relation to inclusion characteristics. Thus, this study has three main aims:

- To quantify experimentally the reduction in stiffness (modulus of elasticity, *E*) that is caused by the addition of microencapsulated PCMs to cementitious mortars and to assess the success of the countermeasure of adding stiff (i.e., quartz) inclusions,
- To critically assess the ability of EMAs to predict the stiffness (i.e., modulus of elasticity) of cementitious materials containing both soft and stiff inclusions. While such studies have often been carried out for the case of inclusions stiffer than the matrix, far fewer studies have considered the case of both stiff and soft inclusions embedded simultaneously, and,
- To develop design rules which permit the formulation of composites with a modulus of elasticity that is equivalent to the paste matrix, even when soft inclusions are added, with due consideration of the properties/volume fractions of matrix and inclusion components.

2.2 Background

2.2.1 Experimental studies of the mechanical properties of cementitious composites

Experimental studies of cementitious composites containing "weak" inclusions have frequently relied on measurements of compressive strength as an indication of mechanical properties. Eldin and Senouci[34] measured the compressive strength of concretes containing tire rubber added by replacement of mineral aggregate. Their experimental data fit the empirical model of Popovics,[42] which predicts an exponential decay in the compressive strength with increasing inclusion volume fraction. Le Roy et al.[43] presented compressive strength data of concrete containing EPS beads. The data were fit to a hyperbolic function that accounted for the maximum packing fraction of EPS, which was modified by an empirical "fitting factor". Hunger et al.[31] measured the compressive strength of concretes containing PCMs and observed a 13% decrease in strength for each 1 % increase in PCM dosage (by mass of concrete). Cui et al.[44] noted a 1 % decrease in compressive strength for each 1 % increase in PCM mass percentage in a cement paste matrix.

The influence of soft inclusions on the effective modulus of elasticity of cementitious composites has been far less frequently evaluated. Ghaly and Gill[45] measured the modulus of elasticity of concrete containing plastic chips at various water-to-cement ratios (w/c, by mass). The reduction in the modulus of elasticity due to plastic inclusions was presented as a function of the percent area of plastic inclusions measured in 2D slices. Their data was fit to an exponential relation, but the scatter in experimental data was large. Ganjian et al.[46] measured the modulus of elasticity of concretes containing scrap tire rubber. They observed a decrease in the modulus as a function of

rubber volume fraction, but no attempt was made to describe these trends by fitting models or by the use of effective medium approximations. Xu et al.[47] noted an approximately linear decrease in the measured modulus of elasticity of EPS-containing concretes, and fit the data to an empirical polynomial relation. While these studies present valuable experimental data of the influence of soft inclusions on effective moduli, the mixture designs considered are not conducive to assessing the simultaneous effect of the addition of stiff inclusions. This is because they utilized the mortar (cement paste + stiff inclusions) as the matrix. In summary, while all of these studies clearly highlight the negative effects of soft inclusions on the mechanical response of concretes, the relations developed do not offer quantitative guidelines for predicting composite properties based on the mixture proportions and component properties, as they require fitting to empirical data, and are often mixture specific.

2.2.2 Effective medium approximations and their application to cementitious composites

Concrete comprises inclusions embedded in a cement paste matrix. Due to "*wall effects"* which hamper particle packing near flat surfaces, and/or the formation of a water-rich zone around non-reactive inclusions, a surrounding layer of porous, and therefore weaker hydration products known as the interfacial transition zone (ITZ), develops around the aggregates.[48] This effect is independent of inclusion stiffness, but depends on particle size, i.e., a thicker ITZ forms around larger aggregates.[49,50] This results in cementitious microstructures consisting at a minimum of three material components, i.e., (i) the cement paste matrix, (ii) the aggregate inclusions, and (iii) the ITZ. While pores are present in the matrix (including in the ITZ) and aggregates, they are not considered as a discrete component, but rather their influence is lumped into the elastic response of the paste matrix and aggregates, respectively.[51] The addition of PCMs further complicates the

organization of cementitious microstructures due to another component being added. To better evaluate these aspects, this section provides an overview of effective medium approximations (EMAs) for the mechanical properties of composite media and highlights how formulation details, e.g., the volume fractions of components, their spatial distribution, and the properties of inclusions, the matrix and interfacial regions may influence the property predictions.[23] In general, all the EMAs discussed assume that the individual material components are: (i) homogeneous, (ii) isotropic, and (iii) are (essentially) linear elastic.

The parallel (isostrain) and series (isostress) formulations developed by Voigt[52] and Reuss,[53] respectively, can be applied to estimate the lower and upper bounds on the elastic moduli of two-component composites. Hansen[54] noted that the isostrain assumption is better when the stiffness of the matrix is greater than that of the inclusion, and the opposite for the isostress case. Hill[55] highlighted that the arithmetic mean of the Reuss and Voigt EMAs can be used as an approximation within these bounds, often referred to as the Reuss-Voigt-Hill (RVH) average.

Hashin and Shtrikman (H-S)[56] developed bounds for the elastic moduli of multi-component composites, which were proved to be the tightest bounds possible without any consideration of microstructural geometry.[57] Walpole's formulation of these bounds, which is readily extended to "N" component composites, is expressed as[57]

$$\left[\sum_{r=1}^{N}\phi_r\left(K_l^{'}+K_r\right)^{-1}\right]^{-1}-K_l^{'}\le K_{eff}\le\left[\sum_{r=1}^{N}\phi_r\left(K_g^{'}+K_r\right)^{-1}\right]^{-1}-K_g^{'} \qquad \textbf{(2.1a)}$$

$$\left[\sum_{r=1}^{N}\phi_r\left(G_l^{'}+G_r\right)^{-1}\right]^{-1}-G_l^{'}\le G_{eff}\le\left[\sum_{r=1}^{N}\phi_r\left(G_g^{'}+G_r\right)^{-1}\right]^{-1}-G_g^{'} \quad \textbf{(2.1b)}$$

where: $K_l^{'}=\frac{4}{3}G_l$, $K_g^{'}=\frac{4}{3}G_g$, $G_l^{'}=\frac{3}{2}\left(\frac{1}{G_l}+\frac{10}{9K_l+8G_l}\right)^{-1}$, and $G_g^{'}=\frac{3}{2}\left(\frac{1}{G_g}+\frac{10}{9K_l+8G_l}\right)^{-1}$. In this equation, K_l and G_l are the least bulk and shear moduli of the components, while K_g and G_g are the greatest. The subscript "r" refers to the r^{th} component in the composite. Nilsen and Monteiro[58] observed that experimental elastic moduli of cementitious composites often lie below the H-S lower bound. They attributed this mismatch to the presence of the weaker ITZ and concluded that three-component EMAs must be used in such cases. While such aspects are relevant to the case of PCM-containing concretes, as highlighted below, the H-S bounds are known to be very wide when the ratio of the stiffnesses of the individual components is greater than 10.[59] Le Roy et al.[43] found that the Hashin-Shtrikman upper bound provided a reasonable fit to experimental modulus of elasticity data EPS-containing concrete.

Hobbs[60] derived EMAs for the Young's modulus for two cases: (a) when the Poisson's ratios of the components are identical, and (b) when there is considerable mismatch in Poisson's ratios and the inclusions are assumed to be voids (such that $E_i \approx 0$). The two resulting equations for the effective composite modulus of elasticity based on these assumptions are, respectively

$$E_{eff}=E_m\left[1+\frac{2\phi_i\left(E_i-E_m\right)}{\left(E_i+E_m\right)-\phi_i\left(E_i-E_m\right)}\right] \quad \textbf{(2.2a)}$$

and $$E_{eff} = E_m \left[\frac{\left(1 - 2\nu_{eff}\right)\left(1 - \phi_i\right)}{\left(1 - 2\nu_m\right)\left(1 + \phi_i\right)} \right] \quad \textbf{(2.2b)}$$

where E_{eff} is the effective composite modulus of elasticity, E_i and E_m are the moduli of elasticity of the inclusions and matrix. The volume fractions ϕ_i and ϕ_m of the inclusions and the matrix, respectively are such that $\phi_i + \phi_m = 1$. The effective Poisson's ratio of the composite is $\nu_{eff,}$ while ν_i and ν_m are the Poisson's ratios of the inclusion and matrix. In Equation 2b, it is unclear what value to assume for the effective Poisson's ratio of the composite. The Poisson's ratio is often calculated from the effective RVH-averaged bulk (K) and shear (G) moduli. However, the present study applies the RVH-averaged Poisson's ratio, given by

$$\nu_{eff} = \left[\left(\nu_i \phi_i + \nu_m \phi_m\right) + \left(\frac{\nu_i \nu_m}{\nu_i \phi_m + \nu_m \phi_i} \right) \right] / 2 \quad \textbf{(2.2c)}$$

This relation was selected as it yielded a more gradual transition in the Poisson's ratio with PCM addition thereby offering better agreement with measured modulus of elasticity data (see also supplementary information, Section 2.7 for further discussion).

Rigorous EMAs of composite properties require consideration of the geometrical features of inclusion dispersion in the composite to render accurate predictions. This is more so when the inclusions are softer than the matrix, and hence inclusion shape may be influential.[61] The generalized self-consistent method (GSCM) popularized by Christensen and Lo[62] is one such EMA

for predicting elastic moduli. The effective shear modulus of the composite via the GSCM is obtained from the non-negative root of the equation[63]

$$\alpha\left[\left(G_{eff}/G_m\right)-1\right]^2+\beta\left[\left(G_{eff}/G_m\right)-1\right]+\gamma=0 \tag{2.3}$$

where the parameters α, β, and γ are dependent upon the Poisson's ratios of the inclusion and matrix, as well as the inclusion volume fraction.[62] Christensen[64] also detailed a formulation of the bulk modulus of the composite which is identical to the result of the composite sphere assemblage of Hashin.[65] Huang et al.[66] demonstrated a simple approximation for the GSCM for application to N-component composites.

Mori and Tanaka[67] developed a method for calculating the elastic moduli of a composite based on the concept of eigenstrains and 'average stress' in the matrix. For a composite of randomly distributed spherical inclusions at relatively large concentrations, the relevant Mori-Tanaka (M-T) equations for bulk and shear modulus are expressed as[67]

$$K_{eff}=K_m+\frac{\phi_i\left(K_i-K_m\right)}{1+\left(1-\phi_i\right)\frac{K_i-K_m}{K_m+\frac{4}{3}G_m}} \tag{2.4a}$$

$$G_{eff}=G_m+\frac{\phi_i\left(G_i-G_m\right)}{1+\left(1-\phi_i\right)\frac{G_i-G_m}{G_m+F_m}} \tag{2.4b}$$

where, for spherical inclusions, $F_m = \left(\frac{G_m}{6}\right)\frac{9K_m + 8G_m}{K_m + 2G_m}$. These equations can also be written for multi-component composites.[68] Weng[69] showed that the Mori-Tanaka formulation is equivalent to the Hashin-Shtrikman upper or lower bounds of a composite containing spherical inclusions of either hard or soft homogeneous and isotropic particles, respectively. For multi-component composites, however, Norris[70] demonstrated that the bulk modulus predicted by the Mori-Tanaka scheme can exceed the Hashin-Shtrikman bounds for certain combinations of mechanical properties of the different constituents, e.g., in a three-component composite where the inclusion bulk moduli are two to three times greater than that of the matrix.

Kuster and Toksöz (K-T)[71] used a wave-scattering analogy to develop an EMA for the elastic moduli of composites composed of a continuous matrix containing randomly embedded, polydisperse, spherical homogeneous inclusions. Berryman and Berge[72] found that this EMA and that of Mori and Tanaka are accurate only when the inclusion volume fraction is less than 0.30. The multi-component Kuster-Toksöz equations for bulk and shear modulus as written by Berryman and Berge[72] are given by

$$\left(K_{eff} - K_m\right)\frac{K_m + \frac{4}{3}G_m}{K_{eff} + \frac{4}{3}G_m} = \sum_{i=1}^{N}\phi_i\left(K_i - K_m\right)P^{m,i} \qquad \textbf{(2.5a)}$$

$$\left(G_{eff} - G_m\right)\frac{G_m + \frac{4}{3}F_m}{G_{eff} + \frac{4}{3}F_m} = \sum_{i=1}^{N}\phi_i\left(G_i - G_m\right)Q^{m,i} \qquad \textbf{(2.5b)}$$

where, for spherical inclusions, $P^{m,i} = \frac{K_m + \frac{4}{3}G_m}{K_i + \frac{4}{3}G_m}$, $Q^{m,i} = \frac{G_m + F_m}{G_i + F_m}$, and the subscript "i=1" corresponds to the matrix. F_m is the same as given in the Mori-Tanaka EMA (see Equation 2.4).

The differential effective medium theory (D-EMT) replaces an incremental volume fraction of the matrix with inclusion, such that the inclusion volume fraction can be approximated as dilute. The particle and matrix are homogenized, and the incremental replacement is repeated, such that large inclusion volume fractions can be incorporated into the effective matrix. This approach prevents phase inversion, which is necessary when the ratio of moduli between the components is large, e.g., in the case of air voids or soft inclusions. Scalar D-EMT equations for the bulk and shear moduli of a composite of isotropic spheres oriented in an isotropic matrix are given by[73]

$$\frac{\mathrm{d}K_{eff}}{\mathrm{d}\phi_i} = \left[\frac{K_i - K_{eff}}{1-\phi_i}\right]\left[\frac{K_{eff} + K'}{K_i + K'}\right] \qquad \textbf{(2.6a)}$$

$$\frac{\mathrm{d}G_{eff}}{\mathrm{d}\phi_i} = \left[\frac{G_i - G_{eff}}{1-\phi_i}\right]\left[\frac{G_{eff} + G'}{G_i + G'}\right] \qquad \textbf{(2.6b)}$$

where, $K' = \frac{4}{3}G_{eff}$, $G' = \left(\frac{G_{eff}}{6}\right)\frac{9K_{eff} + 8G_{eff}}{K_{eff} + 2G_{eff}}$; and $K_{eff} = K_m$ and $G_{eff} = G_m$ at $\phi_i = 0$. These equations form a set of coupled non-linear ordinary differential equations, solutions to which render the elastic moduli of the two-component composite. These equations can be solved by a 4th order Runge-Kutta scheme.[74] Miled et al.[75] found that the differential scheme best predicted the

effective modulus of elasticity of EPS-mortar specimens concretes over a large range of EPS volume fractions in composites where the matric has a Poisson's ratio of 0.20. However, their experiments were not designed to describe the combined influences of soft and stiff inclusions in cementitious composites, as the matrix constituted the combination of the stiff aggregates and cement paste.

Due to the existence of the ITZ in cementitious composites, it is necessary to consider a shell of ITZ around the inclusions as part of an "effective particle." Garboczi and Berryman (G-B)[76] utilized the GSCM to homogenize an effective particle of aggregate and its ITZ, which was then homogenized into the cement-paste matrix via D-EMT. The use of D-EMT is well-suited to the microstructure of cementitious composites, as their aggregates are always discrete particles in a continuous matrix. However, D-EMT exhibits a dependency on the order in which inclusions are embedded into the matrix when the inclusions may have differing properties, i.e., the results may change whether the stiff or soft inclusion is first homogenized into the matrix component, when multiple aggregate components are present.[77] Therefore, GSCM is utilized, considering 3D spherical particles (inclusions), to simplify the concrete microstructure into two components (i.e., effective particle including the aggregate + ITZ, and cement paste). GSCM considers concentric spheres (e.g., core + shell), and is therefore ideal for homogenization of effective inclusion-shell particles. This method has been shown to agree very well with both experimental data and results obtained via the finite element method (FEM)[76] for cementitious composites.

2.2.3 Comments on the elastic properties of the interfacial transition zone (ITZ)

Consideration of the ITZ component in EMAs requires knowledge of its elastic properties and volume fraction in concrete. Accounts from the literature typically assign the ITZ a modulus of elasticity ranging between 50 % and 80 % that of the bulk cement paste matrix.[78] Here, the ITZ was assigned a modulus of elasticity 50 % that of the matrix, i.e., $E_{ITZ} = 0.5 \cdot E_m$, for all inclusion-containing composites.[79] The Poisson's ratio of the ITZ was assumed equivalent to that of the paste matrix.[78,80,81] Although the ITZ "in reality" demonstrates a gradient of properties as a function of distance from the surface of an encompassed aggregate particle, it is often modeled as a homogeneous section with a constant thickness.[76,82,83] Therefore, the ITZ thickness around quartz particles is assumed independent of the particle diameter and taken as $t_{ITZ,q} = 10$ μm, which represents the lower bound of experimental observations of ITZ thickness (around 10-50 μm).[82,84–86] The quartz particles were assumed to be spherical with a size equal to their median diameter ($d_{50,q}$, Figure 2.1). This assumption is justified due to the relatively small elastic mismatch between the elastic moduli of the quartz inclusion and the cement paste matrix ($0.13 \leq E_m / E_q \leq 0.23$), as a function of matrix age). Indeed, this tends to minimize the influence of inclusion shape.[87–89] These properties produce a relation for the ITZ volume fraction, $\phi_{ITZ,q} = ((t_{ITZ,q} + d_{50,q}/2)^3/(d_{50,q}/2)^3\text{-}1) \cdot \phi_q$ for a given quartz volume fraction ϕ_q. For example, this equation yields an ITZ volume fraction $\phi_{ITZ,q} = 0.025$ for a quartz inclusion volume fraction $\phi_q = 0.30$ and median diameter $d_{50,q} = 365$ μm.

Few, if any studies have discussed the existence and properties of ITZs around particles as small as the PCM microcapsules used in the present study.[90,91] As the PCM microcapsules were only slightly larger than the cement grains ($d_{50,p} \approx 20$ μm), they were expected to exhibit a reduced wall effect in comparison to quartz inclusions.[92,93] A simple assumption to account for this is that the

ITZ thickness scales linearly with microcapsule size, so that the ITZ surrounding PCM inclusions was modelled as $t_{ITZ,p} = C \cdot r_p$, where $C = 0.25$ and r_p is the PCM microcapsule radius (μm). The value of C was selected such that the ITZ thickness at the maximum PCM microcapsule size matched that of the quartz particles. As a result of this assumption of the ITZ thickness, the volume fraction of PCM-related ITZ in the composite followed a radius-independent relation given by $\phi_{ITZ,p} = (C^3+3C^2+3C)\cdot\phi_p$. As such, for a PCM volume fraction $\phi_p = 0.30$, the associated ITZ volume fraction within the composite was predicted as $\phi_{ITZ,p} = 0.29$ when $C = 0.25$. This implies that the cement paste matrix which accounted for 0.70 of the composite volume, included 0.29 ITZ, as a volume fraction, with the residual 0.41 volume fraction being a bulk matrix phase, free of ITZ induced inhomogeneities. These assumptions were used throughout the study.

2.3 Materials and Experimental Methods

An ASTM C150[94] compliant Type I/II ordinary portland cement (OPC) was used. The OPC had a nominal mineralogical composition of: 56.5 % Ca_3SiO_5, 18.0 % Ca_2SiO_4, 11.4 % $Ca_4Al_2Fe_2O_{10}$, 6.3 % $Ca_3Al_2O_6$, 4.6 % $CaCO_3$, and 1.1 % $CaSO_4 \cdot 2H_2O$. A microencapsulated PCM, MPCM24D produced by Microtek Laboratories Inc. was used as a *soft inclusion*. The PCM consisted of a paraffin core encapsulated within a melamine-formaldehyde (MF) shell. Graded quartz sand, compliant with ASTM C778[95] was used as a stiff inclusion. A Beckman Coulter Static Light Scattering (SLS) Particle Analyzer (LS13-320) was used to determine the particle size distributions (PSDs) of the OPC, the PCM microcapsules, and the quartz sand after ultrasonication in isopropanol to ensure dispersion of inclusions to primary particles (Figure 2.1). The complex refractive indices of these materials at a wavelength of 750 nm were taken as 1.70 + 0.10*i*,[96] 1.53 + 0.00*i*, [97] and 1.54 + 0.00*i*, [98] respectively. The maximum uncertainty in the PSDs was ≈ 6 % based on 6 replicates.

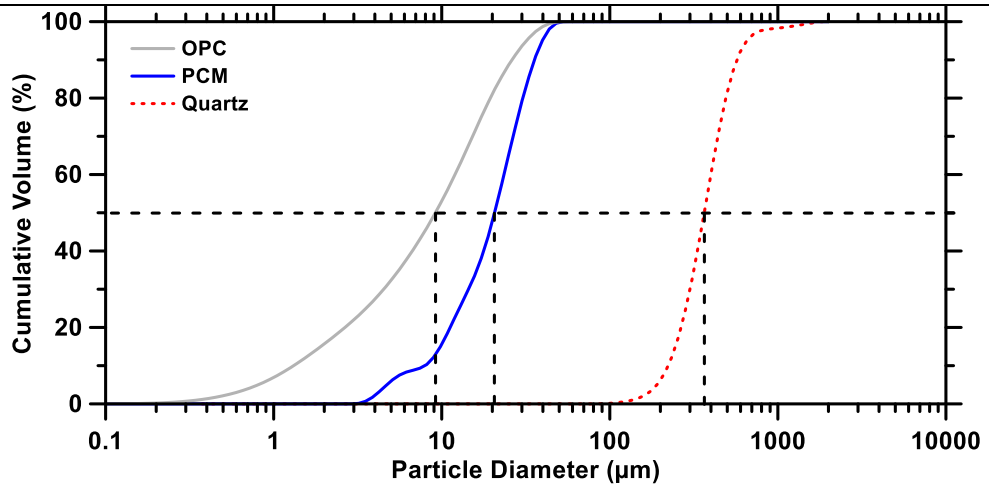

Figure 2.1: The particle size distributions of the OPC, PCM, and quartz inclusions used in the cementitious composites. The OPC, microencapsulated PCM, and quartz inclusions have median diameters $d_{50,c} \approx 9$ µm, $d_{50,p} \approx 20$ µm, and $d_{50,q} \approx 365$ µm, respectively.

Model cementitious composites were prepared as per ASTM C305[99] in the form of cement pastes (OPC + water mixture), PCM mortars (PCM + cement paste), quartz mortars (quartz + cement paste) and mixed mortars (PCM + quartz + cement paste). All mixtures were prepared at a fixed water-to-cement ratio w/c = 0.45 on a per mass basis. Inclusions were added at volume fractions of 0.05, 0.10, 0.20, and 0.30 for PCM mortars and at 0.10, 0.20, 0.30, and 0.55 for quartz mortars. Two series of mixed mortars, i.e., those containing both PCM and quartz inclusions, were also evaluated for total inclusion volume fractions of 0.30 (0.10, 0.15, 0.20 PCM; remainder quartz) and 0.55 (0.10, 0.20 PCM; remainder quartz), respectively. Glenium 7500®, a high range water-reducing admixture manufactured by BASF Corporation was used to enhance the fluidity of the mixtures. The dosage of water-reducer used corresponds to a maximum level of 2 % by mass of cement.

The modulus of elasticity was measured for all mixtures as described in ASTM C469[100] – a standard procedure for measuring such properties using cylindrical specimens (*diameter x height*, 10.16 cm x 20.32 cm). Measurements were carried out after 1, 3, 7, and 28 days for specimens cured at 25.0 ± 0.1 °C in saturated limewater (i.e., under immersion). Modulus of elasticity was measured using a MTS 311.31 closed-loop servo-hydraulic instrument provisioned with digital data acquisition and recording facilities. Quick-setting gypsum plaster "Hydrostone" was used for capping the cylindrical specimens. This ensured that the specimen was aligned with the loading axis and that the ends were in proper contact with the compression platens. The experimental chord modulus of elasticity E_{eff} (i.e., equivalent to E_m in the case of plain cement paste) of the composite specimens was calculated according to ASTM C469[100]

$$E_{eff} = \frac{\sigma_2 - \sigma_1}{\varepsilon_2 - \varepsilon_1} \quad \textbf{(2.7)}$$

where σ_2 is the stress developed at 40 % of the peak load, σ_1 is the stress developed at strain ε_1 = 50 με, and ε_2 is the strain produced by stress σ_2. These parameters are illustrated in Figure 2.2. The data reported represent the average of three replicate samples, with a coefficient of variation of ≈ 7 %. It should be noted that the selection of 40 % of peak load is made to ensure compliance to ASTM C469, as this stress level often corresponds to service stress levels in concrete. This stress very slightly influences the modulus of elasticity in the range 10 % ≤ σ_2 ≤ 40 % - suggesting modest, damage accumulation in this stress range, as desirable to ensure a nearly linear elastic response.[101] While the modulus of elasticity begins to increase for stress levels lower than 10 %, this is expected, as the measured chord modulus of elasticity begins to approach a value corresponding to the dynamic elastic modulus of the composite.[23,102]

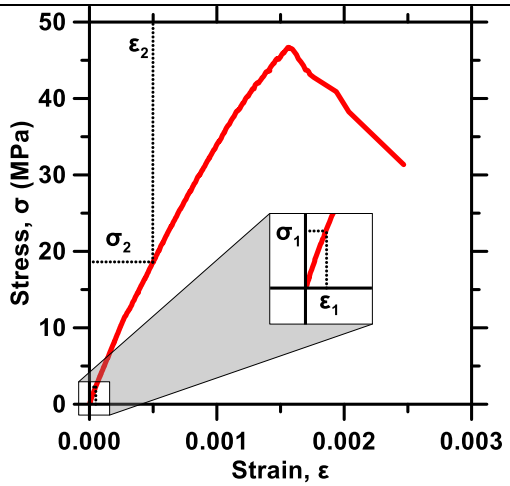

Figure 2.2: A representative stress-strain curve for a cementitious mortar from which the chord elastic modulus is determined as per ASTM C469.[100] σ_2 is 40 % of the peak stress, and ε_2 is the corresponding strain at stress σ_2. σ_1 is the stress at ε_1 = 0.00005 (i.e., 50 με).

Measurements of compressive strength of the composites were carried out as per ASTM C109[103] using cubic specimens (5 cm x 5 cm x 5 cm) after curing for 1, 3, 7, and 28 days at 25 ± 0.1 °C in saturated limewater. The strength reported is the average of three replicates, with a coefficient of variation (i.e., the standard deviation/mean) of ≈ 5 %.

The modulus of elasticity and Poisson's ratios of the microencapsulated PCM (subscript "p") and quartz (subscript "q") inclusions were taken from the literature as: E_p = 0.0557 GPa, ν_p = 0.499,[104] and E_q = 72 GPa, ν_q = 0.22.[105] The measured modulus of elasticity of the plain paste was used as the age-dependent modulus of the matrix, which at 28 days was E_m (t = 28) = 16.75 ± 1.09 GPa The Poisson's ratio of the cement paste matrix was selected as ν_m = 0.22.[23] Unless stated otherwise, the results presented represent the modulus of elasticity and compressive strength of the composite specimens at an age of 28 days. This is because, structural design codes (e.g., ACI 318)[106] often consider material properties at 28 days as an input in structural design.

2.4 Results and Discussion

2.4.1 Experimental data

Figure 2.3 shows the modulus of elasticity and compressive strength measured on a series of model composites containing microencapsulated PCM inclusions (i.e., PCM mortars), quartz inclusions (i.e., quartz mortars) and PCM + quartz inclusions (i.e., mixed mortars). As expected, increasing volume fractions of inclusions less stiff than the cement paste matrix decreased the composite stiffness,[41] while increasing stiffer inclusion volumes fractions increased composite stiffness.[54,58,61,107] More interestingly, the reduction in modulus of elasticity due to the addition of soft inclusions was somewhat mitigated by the simultaneous addition of stiff inclusions. This is significant as it demonstrates a method for reducing the stiffness reduction noted in cementitious composites due to microencapsulated PCMs or other soft inclusion additions. Thus, for particular combinations of inclusion volume fractions, the composite stiffness can be greater than that of the paste matrix. This assures the existence of a critical ratio of stiff-to-soft inclusions such that composite stiffness is equivalent to that of the paste.

The compressive strength of single inclusions mixtures showed an upper limit that was enforced by the strength of the paste matrix in the case of quartz mortars, and a lower limit that scaled in proportion to the PCM inclusion volume fraction. This is expected as the paste is the weakest-link in the quartz mortar, but when present, PCM microcapsules become the critical strength controlling defects whose influence increases with their content in the system. It should be noted that the introduction of PCM microcapsules has no appreciable effect on the hydration of cement paste

(see Fernandes et al.).[30] Therefore, the cement paste matrix is expected to demonstrate equivalent properties, regardless of PCM additions, or not.

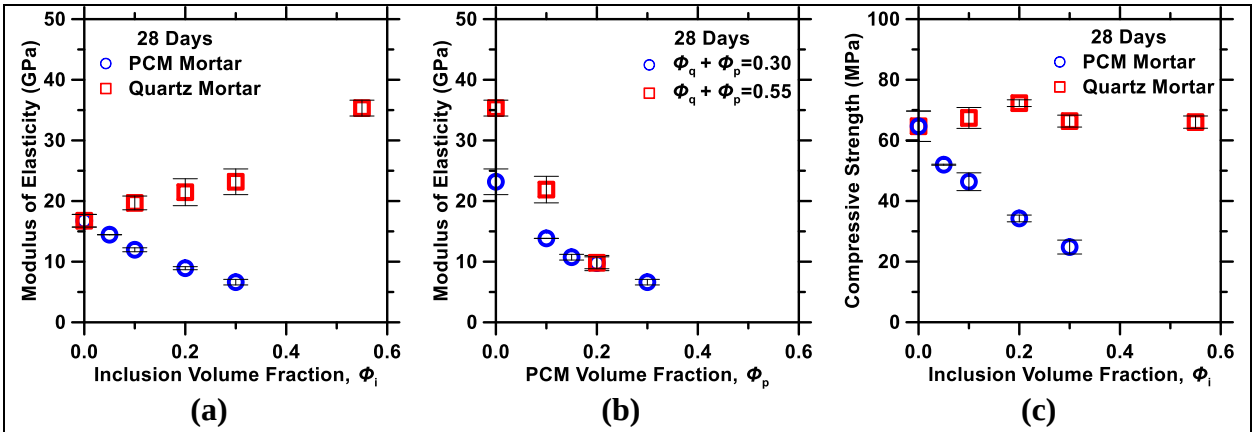

Figure 2.3: The experimentally measured modulus of elasticity for: **(a)** single inclusion mortars, and **(b)** mixed mortars; and **(c)** the compressive strength of all composite specimens.

2.4.2 Correlating measured data to microstructural descriptors

The elastic properties of ceramic-type solids are known to depend on both the volume fraction of the weakest component (typically porosity) and its character (i.e., size distribution, shape).[108] As the elastic properties depend on stress transfer through the solids, the minimum solid area between pores (MSA) has been suggested as a parameter that describes the effects of the spatial distribution of porosity on mechanical properties.[108–110] To better link the measured data to microstructural features of this nature, a stochastic packing algorithm with periodic boundary conditions was implemented.[111,112] This algorithm used the measured particle size distributions and volume fractions of materials as inputs (i.e., of cement, PCM microcapsules, quartz particles, and water, in the form of void space) to pack spherical particles in a 3D-REV (representative elementary volume) with dimensions of 5 x 5 x 5 mm^3. Microstructural generation and packing was permitted

such that the minimum centroidal distance (i.e., C_D, μm, for polydisperse particles) between two proximal particles was always greater than the sum of their radii ($C_D > r_1 + r_2$). This method was described in detail by Kumar et al.[113]

The measured modulus of elasticity and the compressive strength of each class of composite was investigated as a function of the mean spacing between inclusion surfaces, which approximates the thickness of the paste matrix (i.e., including pores and the ITZ) between inclusions.[114] This parameter is qualitatively, in 1-D, similar to the MSA, as they both describe the "load-bearing skeleton" of the composite. Figures 2.4(a) and 2.4(b) plot these mechanical properties as a function of mean spacing between inclusion surfaces for PCM mortars and quartz mortars, respectively. Note that the results presented do not consider the effects of inclusion agglomeration, and thus are more qualitative than exact. The modulus of elasticity of PCM mortars increased as inter-PCM microcapsule distance increased due to the increasing thickness of the solid paste. The opposite trend was observed in quartz mortars, which are in essence an inverted system (stiff inclusions separated by a somewhat more compliant matrix). These mean distances were correlated to the volume fraction of inclusions in each composite. As an example, an increase in inclusion volume fraction from 0.10 to 0.30 reduced inter-PCM microcapsule spacing from 16.4 μm to 5.6 μm, and reduced inter-quartz particle spacing from 320.2 μm to 108.5 μm. This was a reflection of the small size of PCM inclusions relative to quartz inclusions, as many more PCM microcapsules than quartz particles were required to achieve a given volume fraction. Figure 2.4(c) illustrates the influence of the spacing between all inclusion particles (both stiff and soft) on modulus of elasticity in mixed mortars. Note that this interparticle distance was approximately equivalent to the inter-PCM microcapsule distance as the PCM microcapsules controlled the paste film thickness (and thus the

material's failure response) due to their small size and weak character. The mixed mortars showed an increase in modulus of elasticity with spacing, demonstrating that the thickness of the solid (cement paste + quartz) between PCM inclusions acted as the critical stiffness-controlling parameter as suggested above.

The compressive strength of the composites followed trends similar to the modulus of elasticity when PCM inclusions were present (Figures 2.4a and 2.4c). As expected, the strength of PCM mortars decreased significantly with decreasing PCM spacing (increasing PCM volume fraction). In quartz mortars (Figure 2.4b), compressive strength was approximately independent of inclusion spacing and quartz content. Thus, quartz inclusions were unable to influence the compressive strength of the composite, as the weaker cement paste acted as the critical (failure inducing) link. As a result, in contrast to the modulus of elasticity, the compressive strength reduction due to PCM microcapsules addition in mixed mortars could not be offset by supplemental (stiff) inclusion additions. Thus, in mixed mortars, the PCM microcapsule volume fraction controlled compressive strength regardless of quartz inclusions, as the PCMs acted as the *critical defect* in the system.

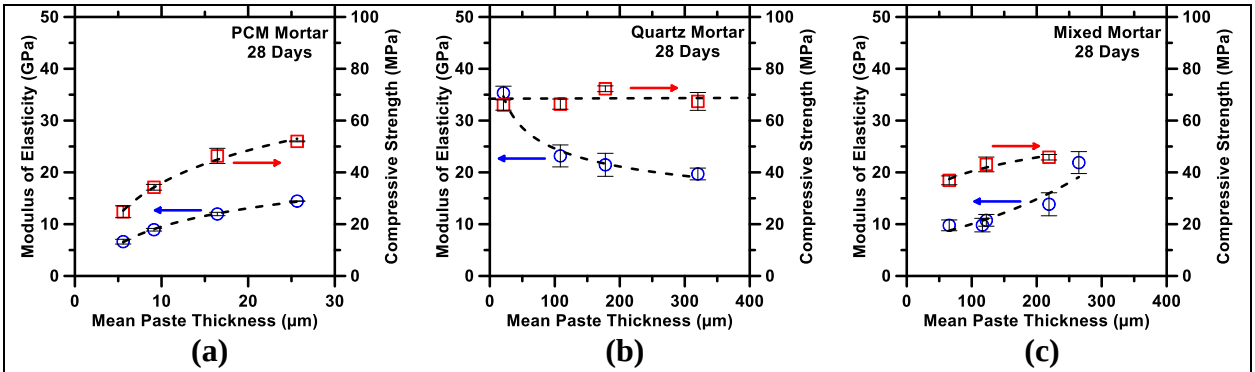

Figure 2.4: Correlations between measured mechanical properties and calculated mean paste thickness between inclusions for: **(a)** PCM mortar, **(b)** quartz mortar, and **(c)** mixed mortars.

One practical limitation associated with embedment of PCMs into cementitious materials that is elucidated by the microstructure constructions is the inability to pack significant volume fractions of these particles into a composite while maintaining a continuous paste (matrix) layer between inclusions. For example, Figure 2.5(a) shows the maximum volumetric loading of inclusions for different assumed paste "film" thicknesses. As a point of validation of the packing algorithm, for random close packing of polydisperse particulates, the maximum inclusion packing fraction was ≈ 0.67 as the minimum surface-to-surface distance approached zero. On account of their larger particle size, quartz particles may be included at higher volume fractions within the composite than PCM microcapsules while maintaining the same paste film thickness.

To aid in the design of cementitious mortars containing PCMs, the packing algorithm was used to calculate the largest volume fraction of PCM which can be embedded simultaneously with quartz (see Figure 2.5b). The compositions of the mixtures considered in this study are also included in this figure for the sake of comparison. The minimum inter-surface distance achieved in these mixtures was around 3 μm for the mixture containing inclusion volume fractions of 0.20 PCM microcapsules and 0.35 quartz particles. Assuming that this minimum spacing of around 3 μm was required to maintain a continuous matrix, the maximum permissible PCM microcapsule volume fraction (i.e., without quartz inclusions) that was achievable was $\phi_p \approx 0.43$, which agreed qualitatively with our experimental observations. For example: PCM mortars produced for $\phi_p > 0.40$ were non-cohesive highlighting that a minimum paste layer is needed to ensure cohesion.

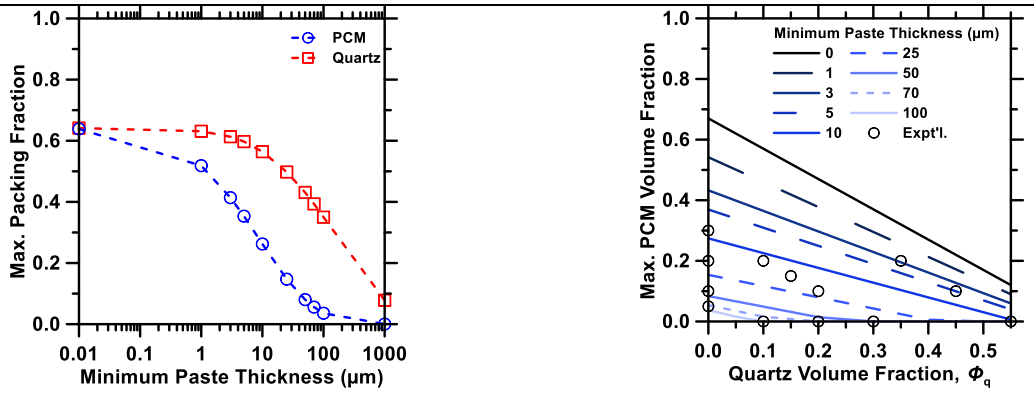

(a) **(b)**

Figure 2.5: (a) The maximum packing limit (by volume) of inclusions in single-inclusion mortars as a function of minimum paste thickness between inclusions and **(b)** The maximum PCM loading as a function of the quartz volume fraction in mixed mortar systems. These calculations utilized the particle size distributions of each inclusion type displayed in Figure 2.1.

2.4.3 Single-inclusion mortars

Figure 2.6 displays the modulus of elasticity predicted by the Hobbs EMA, the Reuss-Voigt (R-V) equations, and Hashin-Shtrikman (H-S) bounds for composites containing either PCM or quartz, respectively. As expected, the H-S and R-V bounds were unreasonably wide in the case of the PCM mortar, due to the substantial mismatch in matrix-inclusion moduli, i.e., since $170 \leq E_m/E_p \leq 300$, for paste ages ranging from 1 day to 28 days. The Hobbs EMA, implemented for the case of substantial mismatch in the Poisson's ratio between the matrix and inclusions (Equation 2.2b), was able to favorably describe the effective moduli of PCM mortars across the entire range of volume fractions considered.

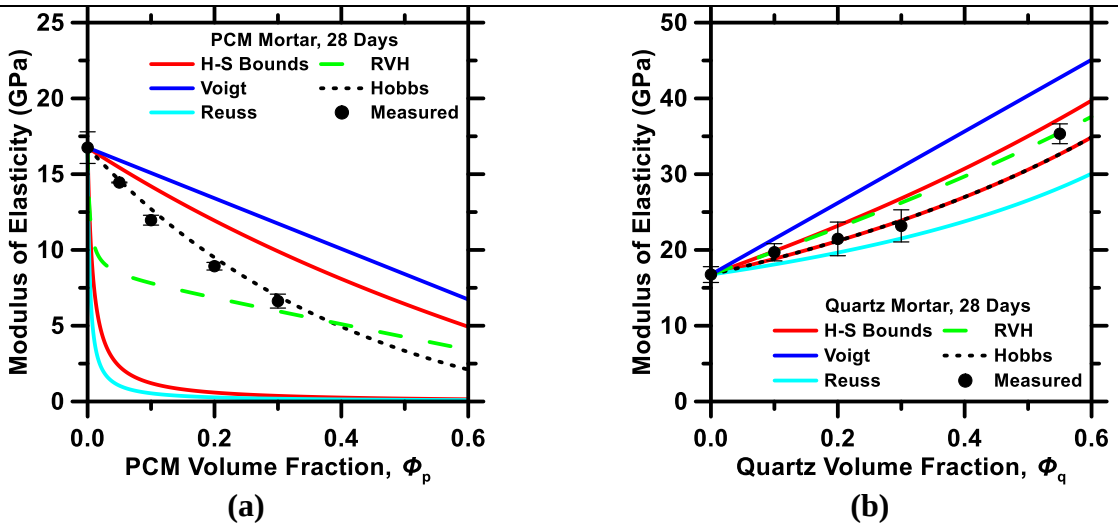

Figure 2.6: The predictions of two-component EMAs for: **(a)** PCM mortars and **(b)** quartz mortars compared with experimental data as a function of inclusion volume fractions ϕ_p and ϕ_q, respectively.

When applied to the quartz mortars (not shown), essentially all EMAs were able to describe the composite modulus favorably with all predictions lying within the narrow H-S bounds. This was attributed to the similarity in properties, i.e., modulus of elasticity and Poisson's ratio, between quartz and the cement paste. Here, the ratio E_m/E_q ranged between 0.13 and 0.23 for cement paste aging from 1 day to 28 days. Once again, the Hobbs EMA (Equation 2.2a) favorably predicted composite moduli, in this case coinciding with the lower H-S bound.

In the next step, the K-T, M-T, GSCM, and D-EMT EMAs of composite modulus of elasticity were evaluated to ascertain their predictive abilities. In the case of the PCM mortars, the majority of these EMAs produced predictions equivalent to, or in proximity to the H-S upper bound (Figure 2.7a), i.e., resulting in overestimations vis-à-vis the experimental data. One possible explanation may be that an essential microstructure component, such as the ITZ, was disregarded. To assess this possibility, an ITZ was introduced into the calculation scheme under the assumptions stated in Section 2.3.

Figure 2.7(b) indicates that EMA predictions reduced considerably upon consideration of the ITZ, to more accurately describe experimental data. For example, the H-S upper bound reduced, while the lower H-S bound remained broadly unchanged. The Kuster-Toksöz EMA remained similar to the H-S upper bound while the Mori-Tanaka formulation significantly reduced, and showed a near-linear reduction in modulus of elasticity with the PCM volume fraction. The D-EMT method utilized by Garboczi and Berryman (G-B)[76] showed excellent agreement with the experimental data. The success of the G-B EMA was perhaps unsurprising as it was previously demonstrated to accurately predict the elastic response of cementitious materials containing an ITZ.[76]

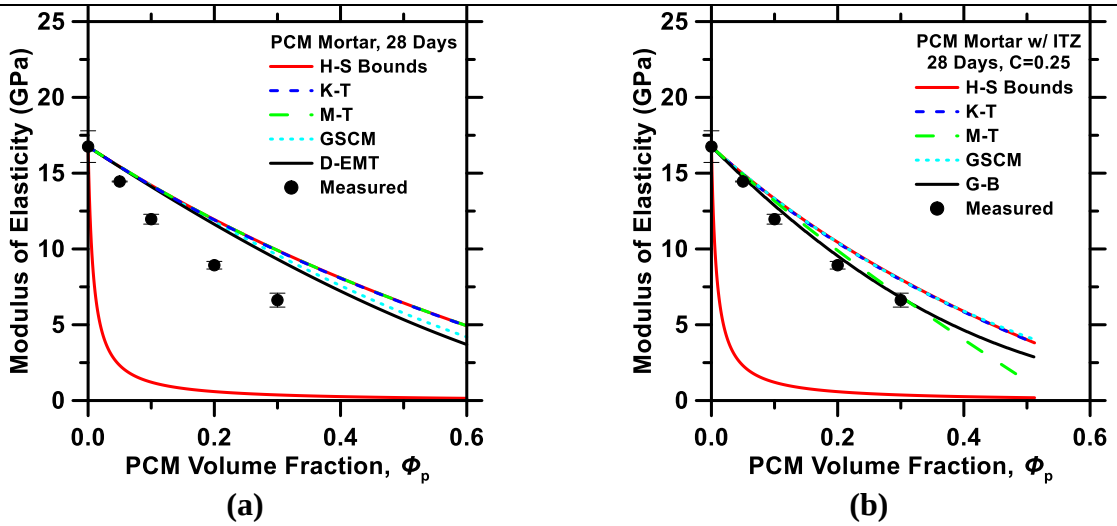

Figure 2.7: The predictions of: **(a)** two-component EMAs for PCM mortars and **(b)** three-component EMAs, which consider the presence of an ITZ in PCM mortars, as a function of the PCM volume fraction. The overestimation of the modulus of elasticity noted in Figure 2.7(a) is suitably corrected by the consideration of an ITZ component.

Following the example of PCM mortars, the same EMAs were also evaluated for quartz mortars with and without consideration of an ITZ component. In both two/three-component systems, the H-S lower bound provided an acceptable prediction of the effective composite modulus. Given the

small property contrast in the matrix-inclusion-ITZ properties, the consideration of an ITZ, or lack thereof had little bearing on the results. It should be noted that two-component EMAs, in spite of their physical incompleteness (i.e., lack of an ITZ component) were sufficient because the ITZ exerted little effect on the quartz mortars' properties. Similarly, three-component EMAs containing an ITZ were sufficient because the added detail (i.e., accounting for the ITZ phase), had little if any effect. This may suggest that in the case of inclusions similar to the paste matrix, at moderate volume fractions for moderately sized inclusions, the application of two-component EMAs is reasonable.

Since the selected ITZ characteristics impact the predictions of EMAs, the effect of the ITZ layer thickness (i.e., for a constant stiffness) was elucidated by parametric analysis carried out using the EMA of Garboczi and Berryman (G-B, Figure 2.8 and Figure 2.14). A range of ITZ thickness from 0.1-to-1.0 times the median PCM microcapsule radius and from 10-to-50 μm around the quartz particles was considered.[84,86,115,116] At any given PCM volume fraction (e.g., $\phi_p = 0.30$), the volume fraction of the ITZ $\phi_{ITZ,p}$ varied from 0.099-to-0.36 as C varied from 0.10 to 0.30. For the same volume fraction of quartz ϕ_q, increasing the ITZ thickness from 10 μm to 50 μm increased the ITZ volume fraction $\phi_{ITZ,q}$ from 0.15 to 0.32. When considering PCM mortars (Figure 2.8a), the ITZ volume fraction became very large at high inclusion loading. For example, when the volume fraction of microencapsulated PCM is 0.30, $C > 0.43$ yielded a total volume fraction of ITZ and PCM microcapsules in excess of one. This was due to the lack of consideration of overlap of the ITZ shells. The error induced by neglecting ITZ overlap was minimized by selecting thin ITZ layers and considering composites with smaller inclusion loadings. Although the PCM modulus

of elasticity was far lower than that of the ITZ, increasing the ITZ volume fraction significantly reduced the predicted modulus (see Figure 2.8a).

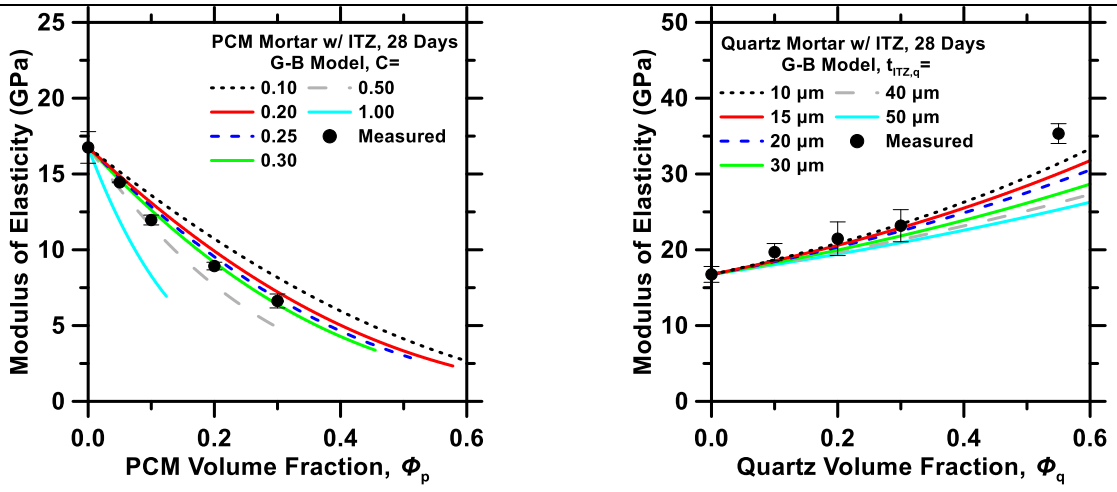

(a) **(b)**

Figure 2.8: The influence of the ITZ thickness on the effective modulus of elasticity at 28 days for: **(a)** PCM mortars, where $t_{ITZ,p} = C \cdot r_p$ and **(b)** quartz mortars. The effective composite modulus is predicted using the G-B EMA [76] for a three-component composite (i.e., one containing ITZ, quartz/PCM inclusions and the cement paste matrix).

The G-B model predictions for quartz mortars showed a similar reduction in composite properties with increasing ITZ thickness (Figure 2.8b), although the volumetric dependence on ITZ was weaker. This was expected as the stiffness of the ITZ was the least of all components in the quartz mortar system. For the input properties selected herein, an *effective* ITZ thickness of 10 μm appeared appropriate in support of the choices made in Section 2.2.3 above.

2.4.4 Mixed inclusion mortars

In the next step, the effective moduli of the cementitious composites containing both stiff and soft inclusions were modeled. Here, the EMA implementations considered discrete components,

including inclusions of quartz and microencapsulated PCM, the paste matrix, and in certain cases, the ITZ. When the ITZ component was not considered, only the EMAs of Hobbs and the RVH average provided acceptable estimates across the range of formulations considered (see Figure 2.9a-b). Note however, since some of the EMAs only consider two-component composites, e.g., in Hobbs EMA, a two-step homogenization process was followed. Thus, first, the quartz particles were embedded into the cement paste matrix (using Equation 2.2a), which yielded an *effective matrix* into which the PCM microcapsules were then embedded using Equation 2.2(b). Further discussion is noted in Section 2.6.3 in the supplementary information.

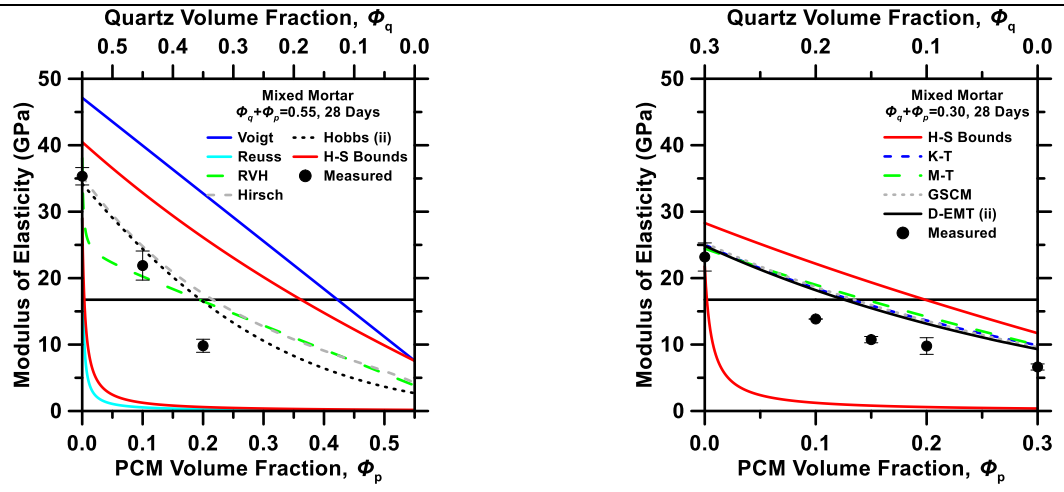

Figure 2.9: The measured and calculated modulus of elasticity for composites containing both soft and stiff inclusions for: **(a)** 0.55 inclusion volume fraction, and **(b)** 0.30 inclusion volume fraction. The solid horizontal line shows the modulus of elasticity of the plain cement paste matrix. EMAs denoted (ii) represent quartz-first homogenization (see Section 2.6.3).

The effective composite modulus for both mixed mortars was generally overestimated, although the D-EMT and K-T EMAs provided the most favorable results. In the case of multi-component composites (i.e., those having more than two components), the order of homogenization of the inclusions into the paste matrix influenced the predicted moduli. This order-dependence of

inclusion homogenization in the D-EMT has been previously discussed.[77] A clear comparison of these predictions is provided in the supplementary material (see Figure 2.13).

Since the ITZ was observed to impact EMA predictions (Figure 2.7), this component was added to composites containing both the soft (PCM microcapsules) and stiff (quartz particles) inclusions. Based upon the modulus of elasticity estimations shown in Figure 2.9, the EMAs of Hobbs and of Garboczi and Berryman (G-B) were selected for predicting the composite moduli (see also Figure 2.13 in the supplementary information). For both EMAs, a sequential implementation was carried out such that each inclusion was first homogenized with its surrounding ITZ, and then introduced into the matrix. In each EMA, it was observed that consideration of the ITZ reduced the predicted effective modulus of the composite, with a stronger effect as PCM volume fraction increased (Figure 2.10). The fit of the EMAs to experimental data was improved when the ITZ was considered (with $t_{ITZ,q}$ = 10 μm and C = 0.25).

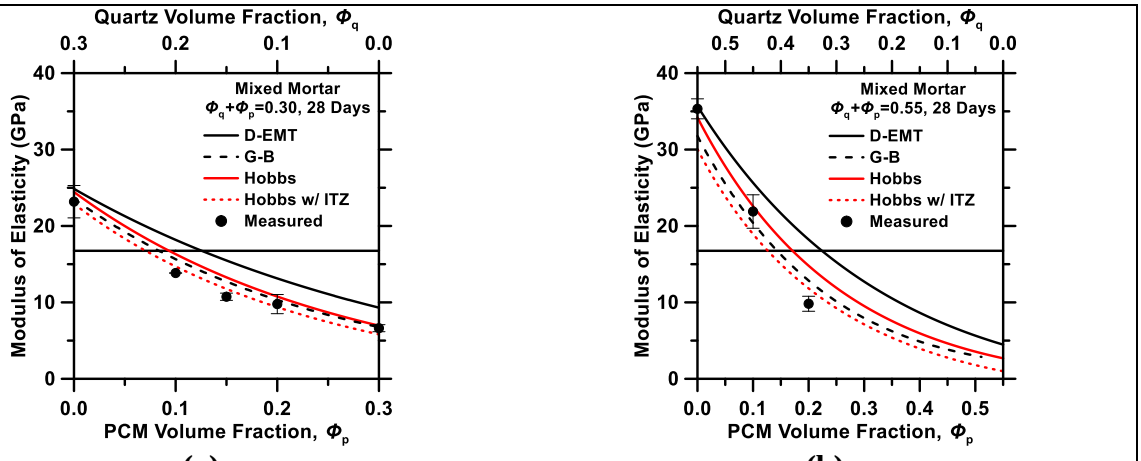

Figure 2.10: The alteration of predicted composite moduli due to consideration of the ITZ in the EMAs of Garboczi and Berryman (G-B) and Hobbs, resulting in 4-component (matrix, ITZ, PCM and quartz inclusion, i.e., mixed mortar) composites for: **(a)** 0.30 inclusion volume fraction and **(b)** 0.55 inclusion volume fraction. The solid horizontal line shows the modulus of elasticity of the cement paste matrix.

2.4.5 Design rules for ensuring performance equivalence of stiffness in cementing composites

Cementitious composites containing both PCM and quartz inclusions have demonstrated elastic moduli greater than or less than that of the paste matrix, depending on the volume fraction of each type of inclusion in the composite. This suggested that strategic additions of stiff and soft inclusions may be used to ensure "no compromise" (i.e., vis-a-vis, the cement paste matrix) in the modulus of elasticity of cementitious materials containing PCMs. For design purposes, such equivalence in properties can be achieved by identifying the critical ratio of inclusion volume fractions (ϕ_q/ϕ_p) such that the composite modulus of elasticity remains:

(a) similar to the paste matrix, i.e., $E_{eff}/E_m = 1$, or,

(b) superior to the paste matrix, i.e., $E_{eff}/E_m > 1$.

As an example, this critical ratio was calculated using the Hobbs EMA[60] on account of its simple implementation and its ability to accurately predict composite properties. Conditions (a) and (b) were sequentially input into the Hobbs (four-component; PCM, quartz, cement paste matrix, and ITZ) EMA, which was solved numerically for ϕ_p to yield a given (total) inclusion volume fraction $\phi_q + \phi_p$. These values of PCM volume fraction are displayed in Figure 2.11(a) for composite elastic moduli ranging from 1.0 to 2.0 times the cement paste at 28 days age. In general, to attain a higher modulus, or to accommodate a higher PCM volume, the quantity of quartz or any other inclusions stiffer than the matrix, needs to be increased to counteract the softening caused by a given PCM dosage. Note, however, that below a certain total inclusion volume, PCMs may not be introduced into the composite, since the quantity of quartz present is far too low to ensure equivalence in modulus of elasticity.

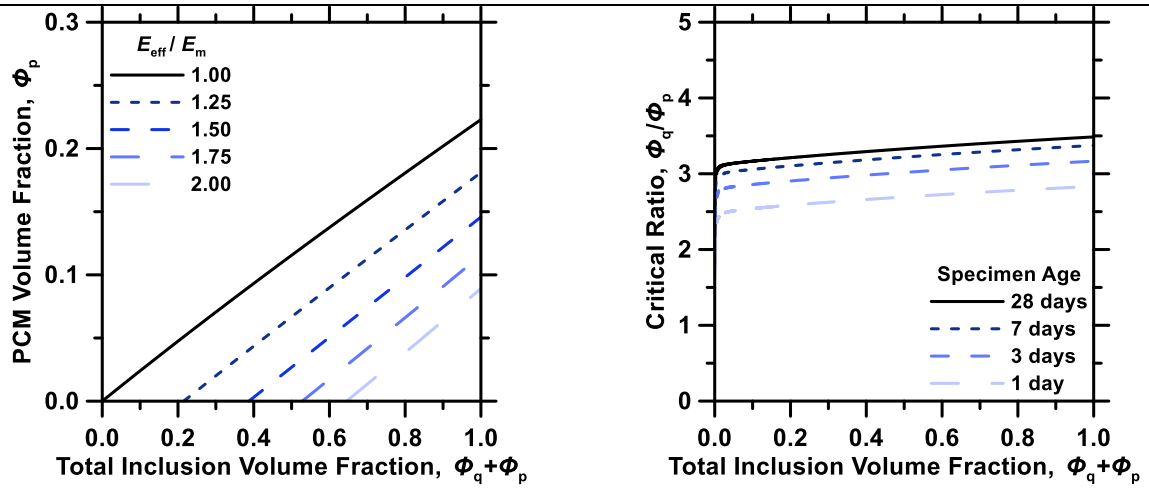

Figure 2.11: (a) The maximum PCM volume that can be accommodated in 28 days aged mixed mortars to yield a composite modulus greater than or equal to the cement paste matrix. **(b)** The critical ratio of stiff (quartz) to soft inclusions (PCM) which yields an effective modulus E_{eff} equal to the modulus of elasticity of the cement paste matrix. Each of these calculations are implemented using the Hobbs EMA (form "ii") including the ITZ component (see Section 2.6.3).

Dividing the quartz volume by the PCM volume yielded the ***critical ratio*** of the quartz-to-PCM inclusion volumes, as shown in Figure 2.11(b) as a function of the total inclusion volume in the composite. These results indicated that, in general, quartz inclusions should be present at a level ≈ 2.5-3.5 times (i.e., due to age dependence) greater than the PCM volume fraction to produce a composite with a modulus of elasticity equivalent to that of the cement paste. The increase in critical ratio with volume fraction suggests that the PCM-associated ITZ played a significant role in decreasing the composite stiffness. The results were also strongly dependent on the modulus of the matrix (aging of matrix), the modulus of ITZ, and the volume of ITZ assumed. Embedding inclusion particles of even higher stiffness than quartz, proportioning the cement paste with a lower w/c (water-to-cement ratio, mass basis, e.g., to increase the matrix stiffness), or adding supplementary cementitious materials (e.g., silica fume)[23,48,117] to reduce the porosity of the ITZ

may be additional means to reduce the critical ratio for maintaining mechanical performance. Note however, that the present study considered only the case of fine aggregate inclusions. As such, while it captured the effects of aggregate volume fraction and properties – other aspects which improve mechanical load capacity in the case of coarse aggregates, e.g., that of aggregate frictional interlock and stress transfer, were not considered. Therefore, while the outcomes of this work serve as a design tool for ensuring property equivalence for cementitious composites containing PCMs, the designs/predictions rendered are expected to be somewhat conservative when extended to concretes.[30]

2.5. Summary and conclusions

The use of soft PCM microcapsules in functional cementitious materials requires estimations of their deleterious effects on the effective mechanical properties of the composite. To enable such estimations, the modulus of elasticity was measured for cement mortar formulations containing PCM microcapsules, quartz sand, or mixtures of both inclusions. A range of effective medium approximations (EMAs) were evaluated for their ability to predict the modulus of elasticity of such composites. Several EMAs were able to describe the stiffness of composites containing hard inclusions, which in this case had a small matrix-to-inclusion property mismatch. However, only the EMAs of Hobbs and of Garboczi and Berryman (G-B) were able to accurately describe the effective moduli of elasticity of PCM mortars and mixed (i.e., PCM + quartz) mortars across a wide range of inclusion volume fractions (up to 0.55). In each case, the accuracy of the EMAs was improved by considering the interfacial transition zone (ITZ) formed around the inclusion due to improper "packing" at the matrix-inclusion interface. A critical ratio of stiff-soft inclusion volume fractions was proposed as a design tool to formulate stiffness-equivalent cementing composites containing PCMs. The identification of more accurate EMAs offers structural engineers/designers a means to estimate the influence of PCMs, and other soft inclusions, on the modulus of elasticity of multifunctional concretes for construction applications.

2.6 Supplementary information

2.6.1 Influence of effective Poisson's ratio calculation scheme on Hobbs EMA results

The influence of the scheme utilized to calculate the effective Poisson's ratio of PCM-containing composites is substantial due to the significant mismatch in Poisson's ratio between the PCM and the cement paste. The Poisson's ratio calculated from the RVH-averaged bulk and shear moduli shows a sharp increase in the effective Poisson's ratio at very small PCM fractions (Figure 2.12a), resulting in a sharp decrease in the predicted modulus of elasticity (Figure 2.12b) – which is not in accordance with experimental data. This results in substantial differences in the modulus of elasticity calculated via Hobbs' EMA; if the RVH scheme incorporating bulk and shear moduli is used for estimating Poisson's ratio. The use of Equation 2.2(c) shows a more reasonable evolution of the Poisson's ratio and therefore also produces a better match to experimental data.

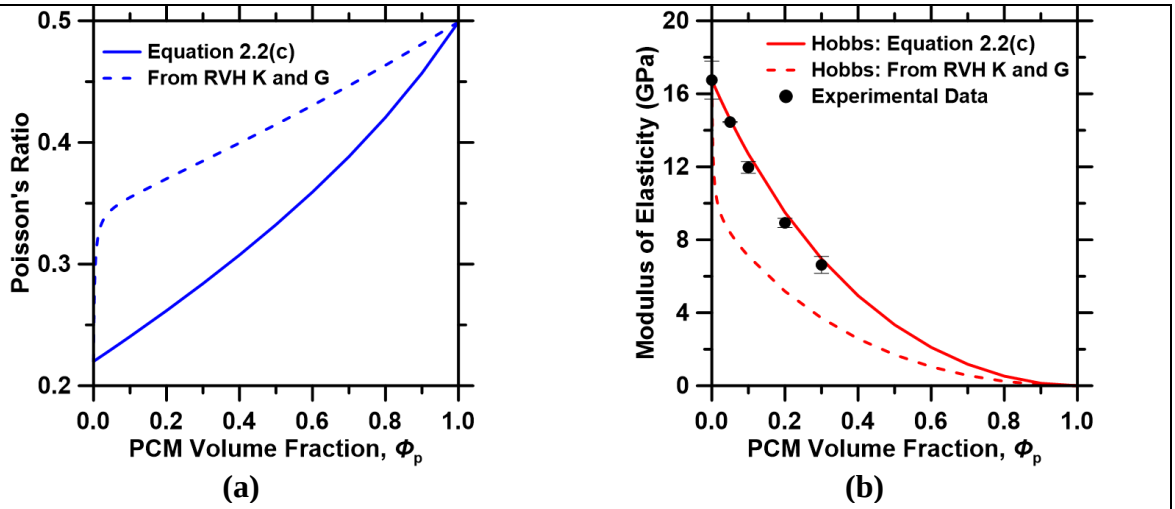

Figure 2.12: (a) The effective Poisson's ratio calculated using Equation 2.2(c), i.e., the RVH average of Poissons ratio's and that calculated from the RVH-averaged bulk and shear moduli. **(b)** The influence of the effective Poisson's ratio on the effective modulus of elasticity calculated using the Hobbs EMA (Equation 2.2b).

2.6.2 Comparison of EMA predictions to experimental data utilizing different stress levels

The chord modulus of elasticity was calculated from experimental stress-strain data as described in ASTM C469, up to an upper stress level (σ_2) of 40 % of the peak stress, which is comparable to typical loading conditions in a structure. To investigate the effects of the stress level on the identification of best-performing EMAs, experimental modulus data calculated for an upper stress level of 10 % and 40 % of the peak stress were compared to EMA predictions (Figure 2.13). First, the modulus of elasticity of the plain cement paste determined to be 16.75 GPa regardless of stress level (Figure 2.3). Therefore, the modulus of elasticity of the cement paste (E_m, used as an input) does not influence the EMA predictions. For PCM mortars (Figure 2.13a-b) the experimental modulus data estimated for an upper stress level of 10 % shows a good fit to the EMA of Garboczi and Berryman and the other EMAs; similar to that noted for an upper stress level of 40 % peak stress. The EMA of Garboczi and Berryman is highlighted as it shows a good-fit across all stress levels and does not result in over-predictions of the experimental modulus of elasticity at service-stress levels. When considering quartz mortars (Figure 2.13c-d), experimental modulus data estimated for an upper stress level of 10 % of peak stress follow the same general trend as that is noted for an upper stress level of 40 %. However, the EMA's slightly under predict the modulus of elasticity with increasing inclusion dosage. This indicates a smaller effect of softening due to microcracking in the ITZ for lower stress levels; an effect which becomes more is more impactful as inclusion volume fraction increases. Therefore, data using σ_2 = 10 % of the peak stress lie closer to the H-S upper bound, than the lower bound, as in the case of σ_2 = 40 % stress level. However, the 10 % data set still demonstrates a reasonable fit to the EMAs which perform well at σ_2 = 40 %,

as these fall within the narrow H-S bounds. Finally, the modulus of elasticity of mixed mortars (Figure 2.13e-f) demonstrates very weak dependence on the upper stress level, and the EMAs of Hobbs (i.e., with or without considering an ITZ component), and of Garboczi and Berryman are able to suitably describe the experimental data. Following these observations, it can concluded that the selection of an upper stress level in the range of 10 %-to-40 % of peak stress produces no meaningful difference in the interpretation of experimental results of in the identification of best-performing EMAs, as microcracking-induced softening slightly impacts the calculated modulus values – but more so in mixtures featuring high dosages of stiff inclusions.

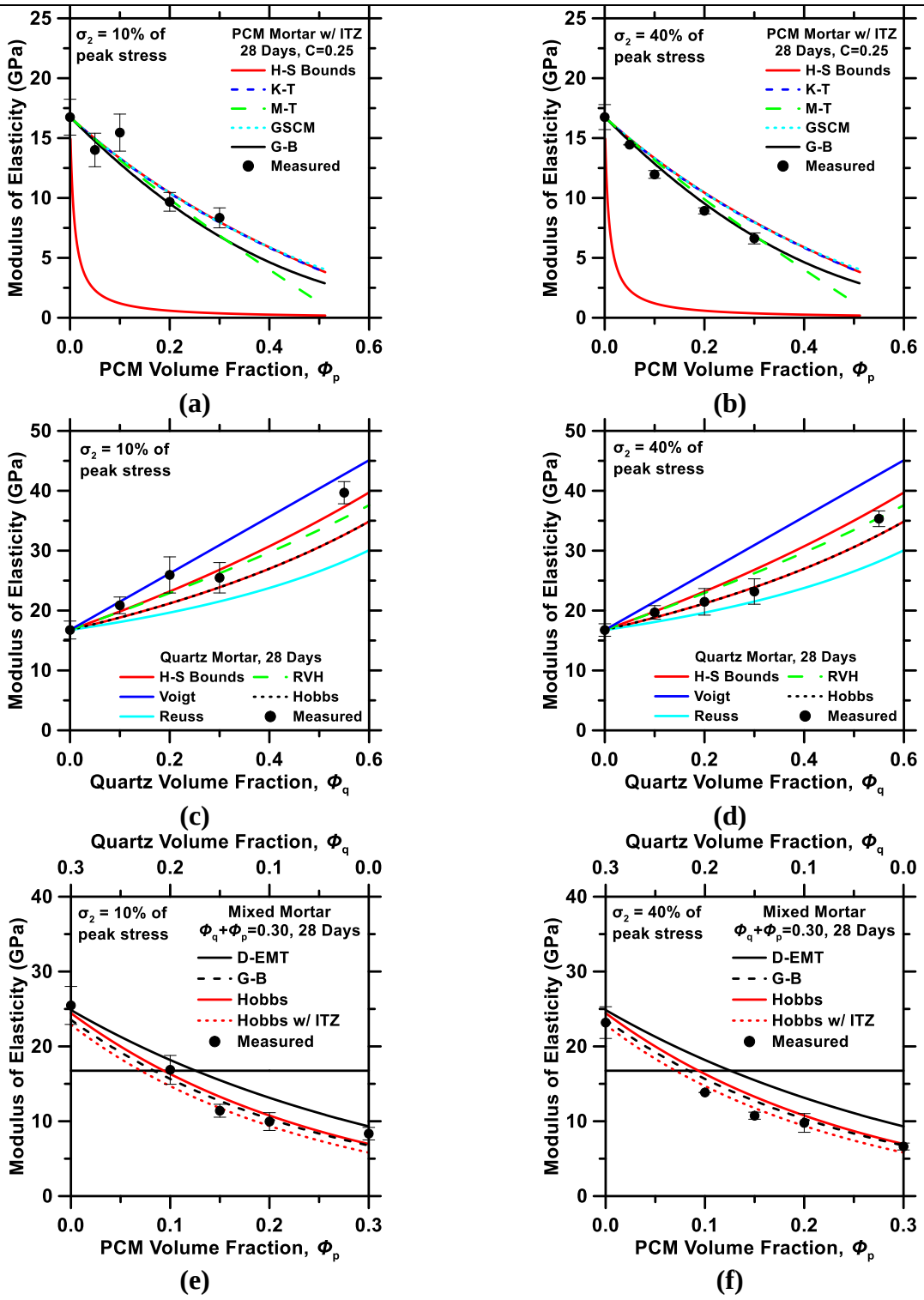

Figure 2.13: Influence of upper stress level (σ_2) on the comparison between experimental data and EMA predictions for the case of **(a-b)** PCM mortars, **(c-d)** quartz mortars, and **(e-f)** mixed inclusion mortars ($\phi_q + \phi_p = 0.30$).

2.6.3 Dependence of EMA predictions on the order of homogenization of the components

It has been noted that D-EMT exhibits a dependence on the order in which the different inclusion components are homogenized into the stiffness matrix.[77] In a similar fashion, the Hobbs EMA also exhibited homogenization order dependence. Figure 2.14 shows effective moduli predicted by the Hobbs and D-EMT EMAs for mixed mortar composites. In both cases, the "quartz-first" homogenization (i.e., EMAs that are denoted 'ii') produced slightly reduced composite moduli in comparison to the "PCM-first" case (i.e., EMAs that are denoted 'i'). In general, the "quartz-first" implementation ('ii') provided an improved fit to the experimental data. As the EMAs utilized herein homogenized one phase entirely before the other, they represent the bounding cases of predicted moduli. Even so, the difference between these EMAs is not great, so any error imposed by choice of homogenization path is expected to be limited.

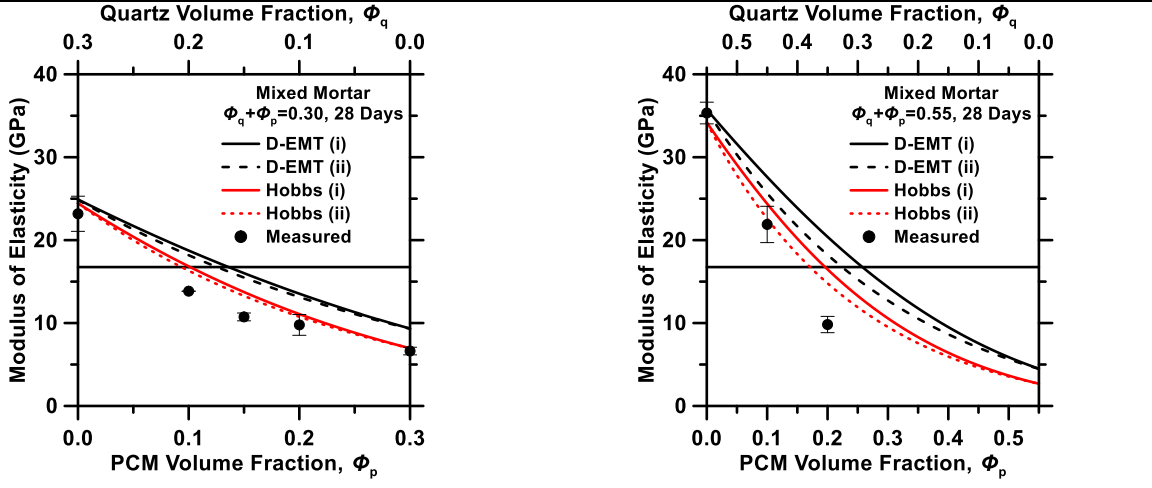

Figure 2.14: An illustration of the influence of homogenization order for D-EMT and Hobbs EMAs for mixed (PCM + quartz) mortars containing: **(a)** 0.30 total inclusion volume fraction and **(b)** 0.55 total inclusion volume fraction. The EMAs designated '(i)' refer to PCM-first homogenization, and '(ii)' refers to quartz-first homogenization. The solid horizontal line shows the modulus of elasticity of the cement paste matrix.

2.6.4 Parametric study of EMAs of mixed-mortar composites

To further investigate the sensitivity of the input component properties of the ITZ and quartz inclusions in the G-B EMA, these parameters were varied over a reasonable range when applied to "mixed mortars".[79,84,118] Altering the elastic modulus of the PCM by ≈ 10 × showed negligible effects on the predictions, and was therefore not discussed further. First, the modulus of the quartz aggregates was varied (Figure 2.15a) while keeping all the other inputs fixed. As expected, increasing the quartz modulus of elasticity increased the composite modulus, with substantial changes being noted with an increasing volume fraction of quartz in the composite. For example, as opposed to the original selection of E_q = 72 GPa,[105] E_q = 80 GPa[119] better estimated the composite modulus when the quartz volume fraction reached 0.55 (unitless), while only slightly influencing the results at lower quartz volume fractions. Next, the stiffness of the ITZ was varied to range from: $0.5 \cdot E_m \leq E_{ITZ} \leq 0.8 \cdot E_m$, while keeping the quartz stiffness fixed, i.e., E_q = 72 GPa[78] (Figure 2.15b). Note that rather than at the quartz-rich end, the ITZ stiffness more substantially influenced the predicted composite modulus at the PCM-rich end, due to the larger ITZ volume fraction produced around these smaller inclusions.

In the final step, the ITZ thickness around the quartz particles (Figure 2.15c) and PCM particles (Figure 2.15d) was varied to study its influence on modulus predictions. At a fixed inclusion volume, increasing the ITZ thickness increased the ITZ volume fraction and therefore reduced the volume of matrix present. Therefore, when the volume fraction of inclusions was sufficiently large, the composite reached an unphysical circumstance where there was no paste (i.e., matrix) present. This occurred as the ITZ thickness around quartz particles exceeded 40 μm, or when the ITZ

thickness around PCM was > 0.25 × the PCM particle radius. These predictions showed a similar dependence on ITZ thickness to those in Figure 2.8. The inability of the EMAs, as formulated herein, to handle large inclusion volume fractions was a result of neglecting overlap of ITZ components in the case of neighboring particles, as the ITZ volume becomes unreasonably large at modest inclusion volume fractions. To avoid this issue, ITZ thicknesses were chosen within a range which accommodated modelling of physically realizable, and realistic mixtures.

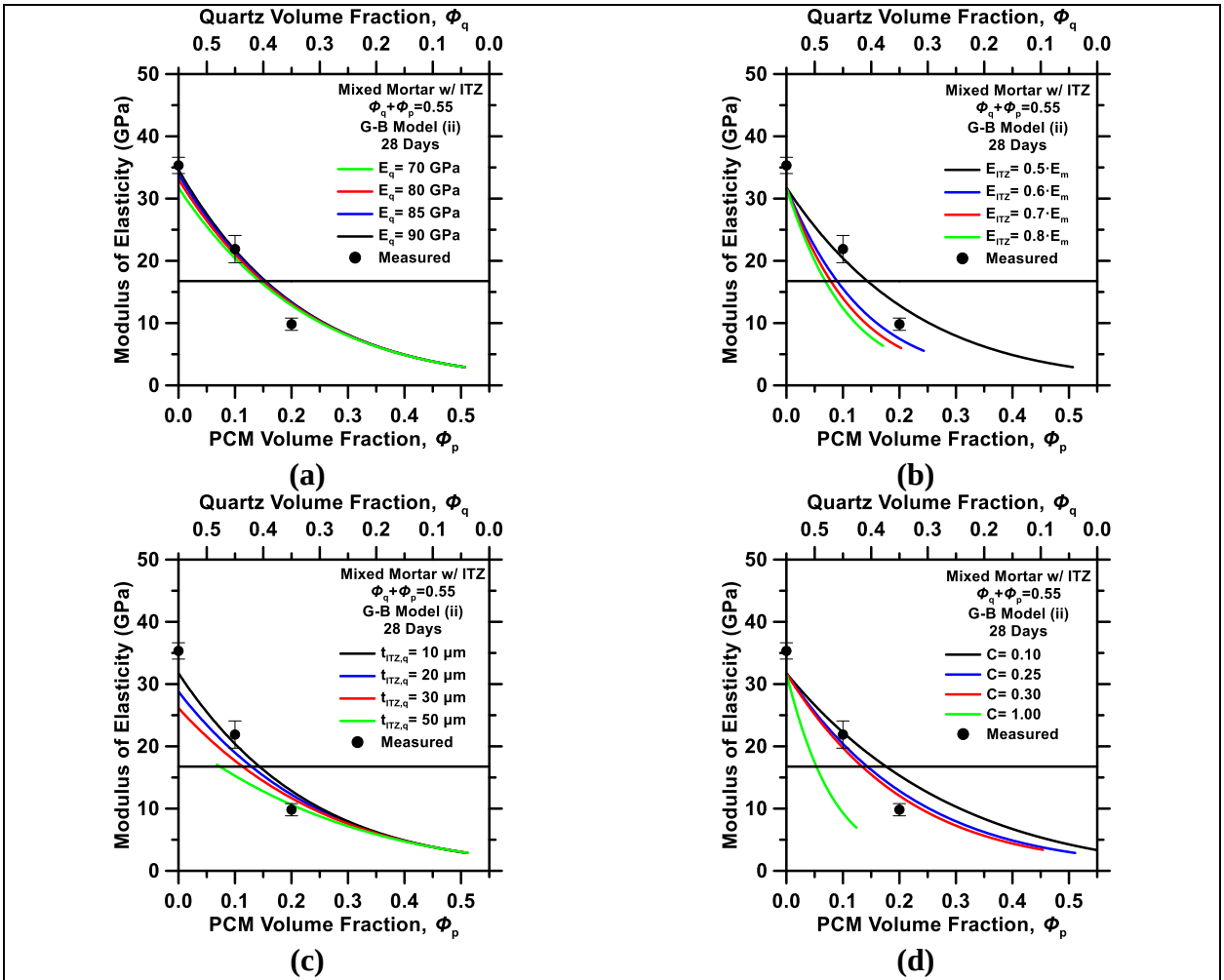

Figure 2.15: The influences of parametric variations of: **(a)** quartz modulus, **(b)** ITZ modulus, and **(c-d)** ITZ thickness on the properties of composites containing 0.55 inclusion volume fraction using the EMA of Garboczi and Berryman.[76] Unless stated, the ITZ thickness is fixed at 10 µm around quartz inclusions and $0.25 \cdot r_p$ around PCM particles, with $E_q = 72$ GPa and $E_{ITZ} = 0.5 \cdot E_m$. The solid horizontal line shows the modulus of elasticity of the paste matrix.

Chapter 3. X-AFm stabilization as a mechanism of bypassing conversion phenomena in calcium aluminate cements

3.1 Introduction and background: Conversion phenomena in CACs

Calcium aluminate cements (CACs) are an attractive class of binders which find use when rapid strength gain, high abrasion resistance and resistance to acid attack are desirable. These binders are additionally utilized independently, and also in combination with ordinary portland cement (OPC) and calcium sulfates when rapid setting and shrinkage control may be desired.[120] In spite of their attractive properties, on account of their cost (i.e., ≈ 5 × higher than OPC), and a susceptibility to phase conversions, they remain utilized only in specialty applications. The conversion phenomenon in CACs is linked to their temperature dependent progress of chemical reactions and evolutions of phase balances.[2,121] More specifically, at short times and at lower temperatures, often ≤ 30 °C, the initial hydrates formed, i.e., CAH_{10} and C_2AH_8 (and amorphous AH_{3-x}, where x denotes variable water content*), undergo phase conversion to form the stable hydrates C_3AH_6 and AH_{3-x}. This phase conversion mechanism is influenced by both kinetic and thermodynamic controls; such that the eventual formation of C_3AH_6 at the expense of CAH_{10} and C_2AH_8 is assured.†,[2,120,121] The chemical reactions that results in such phase conversions are noted in Equations (3.1-3.3). The impacts of the conversion phenomenon are substantial as they:

* It should be noted that the crystallinity of the AH_x phase changes over time, with an eventual microcrystalline organization being formed. This results in correspondent changes in density, solubility etc. [Error! Bookmark not defined.].

† Standard cement chemistry notation is used. As per this notation: C = CaO, A = Al_2O_3, F = Fe_2O_3, S = SiO_2, CS = $CaSO_4.2H_2O$ and H = H_2O

Result in a porosity increase: as the stable hydrates, on account of a higher density, occupy a smaller solid volume than their metastable precursors, and thus the void space (porosity) in the microstructure increases, resulting in strength reductions, and,

Result in the release of water from the metastable hydrates: which upon being supplied to residual anhydrous clinker, if present in excess (anhydrous form), can continue to hydrate to somewhat offset the porosity increase(s) noted above.

$$CA + 10H \rightarrow CAH_{10} \quad \textbf{(3.1a)}$$

$$2CAH_{10} \rightarrow C_2AH_8 + AH_3 + 9H \quad \textbf{(3.1b)}$$

$$2CA + 11H \rightarrow C_2AH_8 + AH_3 \quad \textbf{(3.2a)}$$

$$3C_2AH_8 \rightarrow 2C_3AH_6 + AH_3 + 9H \quad \textbf{(3.2b)}$$

$$3CA + 12H \rightarrow C_3AH_6 + 2AH_3 \quad \textbf{(3.3)}$$

Understandably, the effects of conversion may exert a dramatic impact on the compressive strength of CAC binders, which increases initially and then decreases to a stable value.[122] As such, if the long-term, i.e., converted strength of these materials is not considered properly, the consequences can be disastrous. While conversion-related strength loss in CACs has been known and discussed in building codes dating back to at least the 1960s, the potential for conversion was thought to be

minimized so long as: (a) the CAC specimen was not exposed to elevated temperatures during curing, or (b) to prolonged exposure to temperatures above 27 °C and, high relative humidity (RH) over its service-life. The collapse of three CAC containing buildings in the U.K. in the 1970s raised serious concerns about the use of CACs, with the consequence that CACs were banned from use in structural construction, until the findings of a Concrete Society report in 1997 caused a reevaluation of certain CAC uses in 1999.[2,120,121] Although the collapse incidents were related to factors including: improper structural design, poor mixture proportioning, and chemical attack, these incidents resulted in a loss of confidence in the use of CACs, and especially in the futility of attempting to mitigate phase conversion phenomena – thus promulgating the ban on CAC use.

While numerous efforts to avoid conversion have been attempted, success has been limited. Only the addition of siliceous substances (i.e., silica fume, with supporting alkali ions) resulting in the formation of strätlingite (i.e., C_2ASH_8, which also forms to a limited extent when phases such as gehlenite, C_2AS, or belite, C_2S, may be present in the anhydrous CAC) and phosphate additions have been shown to be capable of inhibiting the conversion process.[123–125] To mitigate the effects of conversion, nowadays, CACs are often proportioned at low w/c (water-to-cement ratio, mass basis), i.e., $w/c \leq 0.40$ – resulting in CAC use at levels higher than would otherwise be necessary, and in an inefficient manner – as some of the CAC remains unreacted, serving only as *hard inclusions* in the composite. Furthermore, design of CAC mixtures and structural elements based on converted strength (i.e., approximated by testing of samples cured at 38 °C for 5 days) does not make full use of the rapidly developed maximum strength of the material, an advantage of CACs, and results in inefficient cement use, due to the use of a lower than necessary w/c – at least from a strength perspective.

The discussion above is significant in that, while cost is certainly a crucial factor in limiting the use of CACs, the risks of conversion and the complications therein, are critical factors which have contributed to the suppressed usage of such materials. It is conjectured that solving the conversion problem could unlock numerous applications of CAC systems, where their other advantages may be beneficial. This may be especially so in a CO_2-penalized economy, where the reduced CO_2 impact of CAC production may offer cost efficiency, and environmental benefits.

3.2 Thermodynamic selectivity: A means of bypassing phase conversions in CACs

The phase conversion process in CACs is ensured by thermodynamic considerations. Thus, while kinetic factors describe the evolution(s) of phases and their balances at short time scales, and at lower temperatures, in the limit of long time scales and at temperatures in excess of 30 °C,[126] the stable (preferred) phases dominate. The phase conversion process is driven by the system's inclination to minimize its (Gibbs) free energy and achieve the most stable state. This desire to minimize free energy can be applied to discriminate preferred (and hence stable phases) from those susceptible to conversions. This suggests that manipulation of the CAC system's chemical composition to form preferred phases (i.e., as indicated by the Gibbs free energy)[127,128] whose formation is fast, i.e., not subject to kinetic restraint, would be an effective means of avoiding phase conversion phenomena in CAC systems. Figure 3.1 shows solubility products (K_{sp}) of the different hydrates that may form in CAC systems.‡ Solubility data of the form noted below can be applied to estimate the preference for the formation of one phase, as compared to another.

‡ It is difficult to equitably compare K_{sp} data of the different phases as an indicator of *phase stability*, due to the different numbers of participating species involved in their formation. While one option would be to normalize the K_{sp} of a given phase by the number of ions participating in its formative reactions (as an indicator of phase stability), this choice is imperfect. However, K_{sp} data can be related to the preference, or potential for phase formation, absent any kinetic restraint, via the Gibbs free energy of reaction (ΔG_R, kJ/mole), which for a given (*p*,T) can be written as: $\Delta G_R = \Delta G_{PR} - \Delta G_{RE} = -RT\ln(K_{sp})$ where the subscripts PR and RE designate the product and reactant components respectively, R is the gas constant (8.314 J/K.mole), T is the thermodynamic temperature (K) and K_{sp} is the thermodynamic solubility product (unitless). Therefore, pending the presence (i.e., both abundance and activity) of suitable ion species, preferred product phases (e.g., NO_3-AFm) will form in a manner designed to minimize the overall free energy of the system, and so as to maximize the difference in free energies between the reactants and products involved in a given chemical reaction.

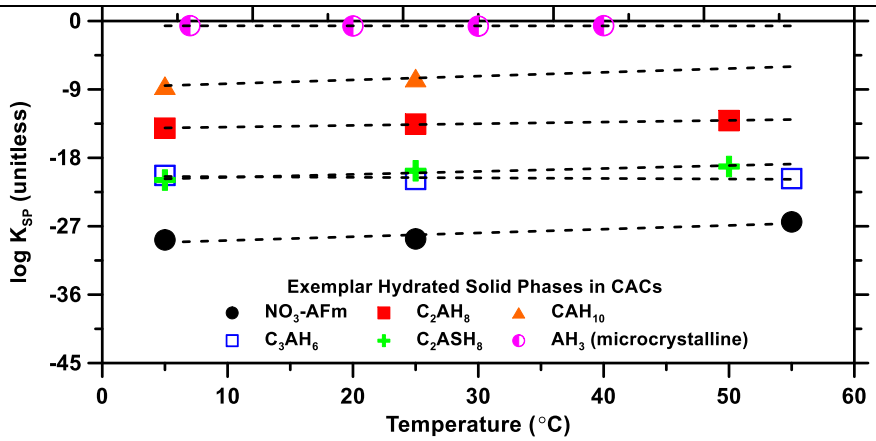

Figure 3.1: The solubility constants (K_{SP}) of a variety of phases relevant to hydrated CACs and for comparison, the NO_3-AFm phase, as a function of temperature.[129,130] Simple linear fittings of measured solubility data are shown as dashed lines.

Based on the reasoning above, the general mechanism of conversion avoidance proposed and demonstrated herein is as follows. When CN is added to a CAC system, it makes available mobile NO_3^- ions to participate in chemical reactions. The presence of NO_3^- ions ensures that, in relation to the added CN dosage, a NO_3-AFm phase (but with additional AH_{3-x} and C_2ASH_8, if gehlenite or belite are present in the CAC) forms as the major hydrate in CACs, at the expense of the CAH_{10}, C_2AH_8 and C_3AH_6 hydrates that form in typical hydrated CAC systems. The NO_3-AFm phase is preferred (and dominant) on account of its ability to depress the free energy of the system, i.e., to a more stable state than that induced by the formation of conversion sensitive hydrates; e.g., CAH_{10} and C_2AH_8 which are susceptible to time and temperature linked conversions. It is important to note that the formation of the NO_3-AFm phase at the expense of all the other CAC hydrates is significant, as the concept of *thermodynamic selectivity* permits the hydrated CAC's composition to be directed towards a more favorable solid phase equilibrium. Further, it should be noted that as per estimations drawn from currently available thermochemical data,[130–132] the NO_3-AFm dominant solid phase assemblage that develops in CN-dosed systems is expected to remain stable *at least* across the temperature range 5 °C to 55 °C (see Section 3.6 for further detail).

The idea of "thermodynamic selectivity" and its application to CACs was stimulated by the work of Balonis and Glasser who showed that NO_3^- ions can be sequestered in the AFm (i.e., alumino-ferrite, monosubstituent) phase commonly formed in cement systems.[131] Such NO_3^- ion incorporation can occur via the direct precipitation of a NO_3-AFm phase, and/or ion exchange reactions. However, and importantly, NO_3^- is not the only ion which can be hosted within the AFm interlayer, as other species including Cl^-, NO_2^-, CO_3^{2-}, SO_4^{2-} and OH^- can also occupy such positions in the AFm phase. The AFm-interlayer site occupation preference scales as: $Cl^->NO_3^->NO_2^->CO_3^{2-}>SO_4^{2-}>OH^-$.[131] This is an important aspect, which highlights that other AFm phases, hence X-AFm (i.e., where X is a single type or a multiplicity of ions including Cl^-, NO_3^-, NO_2^-, CO_3^{2-}, SO_4^{2-} and/or OH^-), could also serve as alternate pathways to avoid phase conversion phenomena in CACs. In unfavorable chemical and thermodynamic *(p,T)* environments, a given X-AFm phase would decompose to produce hydrogarnet (C_3AH_6) and the corresponding calcium salt, whose anion is that which occupies the interlayer positions in the parent X-AFm phase.[2] Based on current understanding, X-AFm phases would destabilize with reducing alkalinity (pH) or increasing temperature, in relation to the chemical environment. For example, the SO_4-AFm phase under typical conditions decomposes around a pH $\approx$ 11.6.[2] However, the limits of such stability are not so clear, especially so in cases as relevant to this paper, wherein very concentrated solutions, abundant in X-AFm constituent ions are present. As such, further study is needed is needed to elucidate limits of AFm stability, in relation to both solution conditions, and reaction temperatures. In accordance with the site occupation preference noted above, a given X-AFm phase would transform to an alternate AFm structure when a more preferred anionic species is present, e.g., Cl-AFm would form at expense of NO_3-AFm if Cl^- ions were to ingress into the

material. However, this is not so much an issue of decomposition, but rather ion-exchange induced (reversible) phase interconversion.

In this work, CN is highlighted as a new phase conversion avoiding additive for CACs given its: very high solubility in aqueous systems, low cost, abundant availability, existing use as a construction chemical and corrosion inhibition agent, and ability for reaction rate regulation in cementitious systems.[133,134] Corrosion inhibition in the context of CACs binders is particularly attractive, as the lower pH of these systems (e.g., pH ≈ 11-12) renders reinforcing steel therein more susceptible to corrosion than in OPC based systems (pH ≈ 13.1-13.6).[135] Furthermore, it should be noted that the strategy demonstrated herein using CN has also been recently validated using both $Ca(NO_2)_2$ and Na_2CO_3 as conversion-bypassing additives. This is an important validation of the X-AFm designation, and the generality of the outcomes presented.

3.3 Materials and Mixing Procedures

A commercially available grey calcium aluminate cement Secar®51 manufactured by Kerneos Aluminate Technologies was used. The oxide composition of the CAC as determined by X-ray florescence (XRF) is, by mass: 51.05 % Al_2O_3, 38.94 % CaO, 4.77 % SiO_2, 2.23 % Fe_2O_3, 0.59 % MgO, 2.02 % TiO_2, 0.11 % P_2O_5, 0.31 % K_2O and 0.07 % Na_2O. The mineralogical composition of the CAC as determined using X-ray diffraction and Rietveld refinement is, by mass: 73.3 % CA, 18.1 % C_2AS, 4.9 % CT with minor phases in the form of 0.8 % CaO, 0.6 % C_2F, 1.5 % C_3FT and 0.8 % Fe_3O_4.[§] Cementitious pastes were prepared using de-ionized (DI) water at fixed water (i.e., solution) to cement ratio (w/c = 0.45 and w/c = 0.70, mass basis) as described in ASTM C305. Calcium nitrate (CN) was added in dosages of 0, 5, 10, 20, and 30 % by mass of CAC. The upper bound on the CN dosage, i.e., 30 % (by mass of CAC) was chosen as around 28 % CN (by mass of CAC) is required in a water-sufficient system at complete hydration (as calculated using the GEMS-PSI distribution, see Section 3.6) to fully suppress the formation of the C_3AH_6 phase for the current CAC, at w/c = 0.70, at 25 °C. A commercially available liquid CN admixture (53.93 % CN, by mass, of CN in water) manufactured by Yara Industrial Nitrates was added to additional DI-water with the water and the liquid (CN) admixture proportions being adjusted to achieve the desired CN proportions while maintaining the w/c (or more correctly, solution-to-cement ratio, by mass) at desired levels.

[§] Standard cement chemistry notation is used throughout this paper. As such, unless specified: C= CaO, A = Al_2O_3, H = H_2O, S = SiO_2, T = TiO_2, F = Fe_2O_3. In general, NO_3-AFm = $Ca_4Al_2(NO_3)_2(OH)_{12}\cdot 4H_2O$,$C_2ASH_8$ = strätlingite = $Ca_2Al_2SiO_2(OH)_{10}\cdot 3H_2O$,$C_3AH_6$ = hydrogarnet (Si-free katoite) = $Ca_3Al_2(OH)_{12}$, C_2AH_8 = $Ca_2Al_2(OH)_{10}\cdot 3H_2O$,$CAH_{10}$ = $CaAl_2(OH)_8\cdot 6H_2O$

3.4 Experimental Methods

The particle size distribution (PSD, Figure 3.2) of the CAC was measured using a Beckman Coulter Light Scattering Analyzer (LS13-320) using isopropanol and sonication to disperse the powders to primary particles. The highest uncertainty in the light scattering analysis was determined to be around 6 % based on multiple measurements performed on six replicate samples assuming the density of the cement (CAC) to be 3040 kg/m^3.

Compressive strength measurements were carried out at 1, 3, 7, 14, 28, 56, and 90 days using cubic specimens (i.e., 50 mm x 50 mm x 50 mm) cured at 25 ± 0.1 °C and 45 ± 0.1 °C in a thermostated chamber. Curing was carried out by placing the cubes in their molds over a water source in an enclosed container for the first 24 hours, and thereafter in saturated conditions (i.e. by immersing the demolded samples under water) until the time of their evaluation. Strength evaluations were carried out for dosages of 0 % and 10 % CN, by mass of CAC for the w/c = 0.45 mixtures. In addition, strength measurements were also carried out for the 5 % CN paste mixtures, cured at 45 ± 0.1 °C. The strength reported is the average of three specimens cast from the same mixing batch. The highest coefficient of variation in the measured strength was determined to be ≈ 10 %.

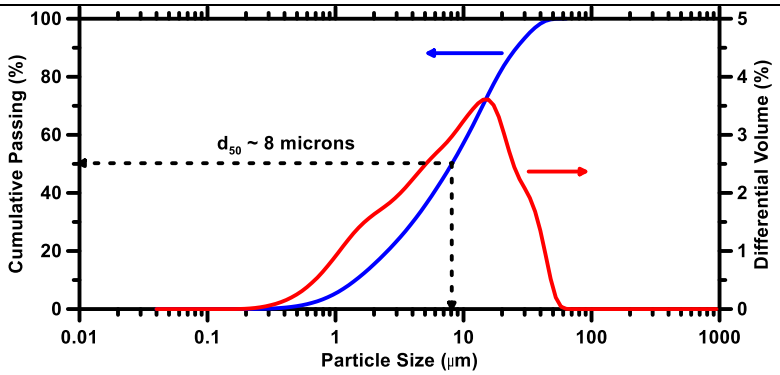

Figure 3.2: The particle size distribution (PSD) of the SECAR®51.

To prepare samples for analysis of solid phases, the fresh CAC pastes were poured into HDPE containers (cylindrical form, [d] 32 mm x [h] 16 mm), with an airtight lid. The pastes were cured under sealed conditions until a desired age. To arrest CAC hydration at any given age, solvent exchange was performed using isopropanol wherein at a desired age, the hydrated pastes were crushed (to a size less than 5 mm) and submerged in isopropanol for 14 days, with isopropanol being replaced at 7 days.[136] Following solvent exchange, the samples were then placed under vacuum in a desiccator for another 7 days to remove the solvent. After this, the samples were finely powdered to pass through a 75 μm sieve, after which, further analysis was carried out.

Thermal analysis of the solid phases was carried out for w/c = 0.45 and w/c = 0.70 CAC mixtures across all CN dosages. A Perkin Elmer STA 6000 simultaneous thermal analyzer (TGA/DTG/DTA) with a Pyris data acquisition interface was used to characterize solid phases. The temperature and the mass sensitivity of the analyzer used were 0.25 °C and 0.1 μg respectively. The powder samples were heated under UHP-N_2 purge at a flow rate of 20 ml/minute and at a heating rate of 10 °C/minute in pure aluminum oxide crucibles over a temperature range from 35 °C to 975 °C. The weight loss (TG) and differential weight loss (DTG) patterns acquired were used to identify solid phases including: C_3AH_6, AH_{3-x}, NO_3-AFm etc.

Qualitative X-ray diffraction analyses were carried out on powdered CAC mixtures after solvent exchange at each desired age using a Bruker-D8 Advance diffractometer in a θ-θ configuration using Cu-Kα radiation (λ=1.54 Å). The samples were scanned on a rotating stage between 5-and-

70° (2θ) in continuous mode with an integrated step scan of 0.021° (2θ) using a VANTEC-1 detector. The total time required for acquisition of a x-ray diffraction pattern was ≈ 8 minutes. A fixed divergence slit of 1.00° was used during x-ray data acquisition. The potential for preferred orientation was errors was minimized by: (a) using a fine powder, (b) texturing the powder surface to induce small imperfections, and (c) using a rotating sample holder. All X-ray structure information for relevant anhydrous/hydrated crystalline phases was sourced from the literature or standard databases.[137]

Thermodynamic calculations were carried out using the Gibbs Energy Minimization Software (GEMS-PSI), version 2.0.[138,139] GEMS is a broad-purpose geochemical modeling code which uses a Gibbs energy minimization criteria to compute equilibrium phase assemblages and ionic speciation in a complex chemical system from its total bulk elemental composition. The GEMS software applies a convex programming approach based on the Interior Points Method[140] in conjunction with information of the thermodynamic properties of phases (i.e., solids, liquid and air) to calculate phase balances. Chemical interactions involving solid phases, solid solutions and the aqueous electrolyte(s) are considered simultaneously. The thermodynamic properties of all the solid and the aqueous species were sourced from the GEMS-PSI database, and then amended with additional information relevant to CAC systems, including data for NO_3-AFm, and microcrystalline AH_3.[130–132,141–145]

Table 3.1: Standard molar thermodynamic properties of relevant hydrated phases at 25 °C and *p* = 1 bar as used in the thermodynamic calculations.[130–132,141–145]

Phase	Log K_{sp}	$\Delta_f G^0$ *[kJ/mol]*	$\Delta_f H^0$ *[kJ/mol]*	S^0 *[J/(mol·K]*	a_0 *[J/(mol·K)]*	a_1 *[J/(mol·K²)]*	a_2 *[J·K/mol]*	a_3 *[J/(mol·K^0.5)]*	V°* *[cm³/mol]*
C_3AH_6	-20.84	-5010.1	-5540	419	292	0.561	0	0	150
$C_4A(NO_3)_2H_{10}$	-28.67	-6778.0	-7719	821	580	1.02	-2.77e+06	872.2	297
CAH_{10}	-7.5	-4622.3	-5320	501	150.5	1.11	0	3200	193
C_2AH_8	-13.56	-4812.8	-5433	438	392	0.714	0	-800	183
C_2ASH_8	-19.70	-5705.1	-6360	546	438	0.749	-1.13e+06	-800	216
water (H_2O)		-237.2	-286	70	75	0	0	0	18
SiO_2 (amorph.)		-848.9	-903	41	47	0.034	-1.13e+06	0	29
$Fe(OH)_3$	-711.6	-843	88	27.8	0.052	0	0	34	
$Al(OH)_3$ (amorph.)	-1143.2	-1280	70	36	0.190	0	0	31	
$Al(OH)_3$ (gibbsite)	-1151.0	-1289	70	36	0.191	0	0	32	
$Al(OH)_3$ (microcryst.)	-1148.4	-1265	140	36	0.191	0	0	32	

Thermodynamic properties of selected hydrates relevant to CACs, and those containing CN is presented in Table 3.1. Thermodynamic modeling was performed for systems containing CAC (SECAR®51) and various dosages of CN admixture. Calculations were carried out at atmospheric pressure (p = 1 bar) across a wide range of temperatures. The calculations were carried out for CAC mixtures across two different w/c, i.e., w/c = 0.45 and w/c = 0.70. The vapor phase at equilibrium with the solid/liquid phases is set to be CO_2-free air. The calculations were carried out so as to account for the fractional reactivity (partial reaction) of the anhydrous CAC. Other calculations were carried out for the same systems, but across a span of temperatures between 5 °C to 55 °C. This set of simulations were undertaken to demonstrate stabilities of CAC hydrates across a range of temperatures relevant to field conditions.

3.5 Experimental Results and Discussion

3.5.1 Compressive Strength Evolutions

Figure 3.3 shows the development of paste compressive strength in plain and CN-containing CAC mixtures prepared at w/c = 0.45. In general, it is noted that CN additions produce an increase in strength and an increase the rate of strength development. Since the strength and porosity in cement-based systems are inversely correlated, higher strength corresponds to lower porosity. This will be further elucidated in Section 3.6. While a component of this strength improvement could be attributed to accelerated hydration (on account of the acceleratory effects of CN), a portion of such differences could also be attributed to changes in the solid hydrate assemblage, i.e., the formation of the NO_3-AFm at the expense of CAH_{10}, C_2AH_8 or C_3AH_6. In materials cured at 45 °C, especially when CN is present, after the initial rapid strength gain, little if any increase in strength is noted as compared to samples cured at 25 °C. No reduction in the compressive strength is noted in the case of plain CAC (0 % CN) samples cured at 25 °C. Also, no effects of phase conversions are noted at a 10 % CN dosage, across both curing temperatures. As noted in Figure 3.3(b), strength evolutions in the 5 % CN system are intermediate to the 0 % CN and 10 % CN cases. This is because the strength scales in relation to the quantity of NO_3-AFm formed in the system (see Figure 3.6 and Section 3.6). Limited analysis carried out for CAC mixtures containing 20 % CN denotes that this trend of improving strength with increasing CN dosage is consistent with that noted in Figure 3.3(a-b).

At this point, it is appropriate to note that, over the course of the study, two different sample geometries were used for analysis, i.e., 50 mm cubes for strength and 32 mm x 16 mm (d x l) cylindrical samples for XRD/TGA analysis. Therefore, three possibilities assume relevance with regard to explaining the lack of reduced strength (i.e., the effects of conversion), in the case of the CN-free, and CN-containing CAC mixtures cured at 25 °C (Figure 3.3a):

- The samples used for strength measurement were cured underwater after the first 24 hours. While unlikely due to the dense nature of the CAC microstructure,[146] perhaps, some external water intruded into the system, permitting the unhydrated CAC to react, due to its slightly water deficient nature (w/c = 0.45). This reaction of unhydrated CAC with external water may minimize the effects of conversion on compressive strength, by in-filling the porosity. An analogous issue would be for conversion to occur, but independent of the supply of external water. Since conversion releases water due to the decomposition of high-water hydrates, it permits the unhydrated CAC to react "internally". This aspect of internal water provision (i.e., due to high-to-low water hydrate conversion) is one likely cause of no strength reduction being noted in the strength samples cured at 25 °C.
- As noted in the XRD plots (Figure 3.4a), while conversion is occurring, until 56 days its effects are modest, and appear to enhance in the period between 56-to-90 days. As such, there may be some time lag until the microstructural implications of conversion are to manifest, which may occur past 90 days, a time period which was not sampled herein. This is a key issue with CACs, as it is difficult to estimate the timing of the conversion process, and its resultant effects on strength, especially for moderate curing temperatures (≤ 25 °C).
- Due to the different sample sizes (and presumably temperature histories) of the samples used in strength and TGA/XRD analysis, the strength samples, due to a potentially higher

early-age temperature may have experienced some (but presumably small level) of phase conversion. This conclusion of a *small level of conversion is reached* as ranging over the period of study, i.e., up to 90 days, the samples cured at 25 °C show a significantly higher strength (≈ 20 % to 35 % higher) than samples cured at 45 °C as noted in Figure 3.3(c). But since XRD analysis was carried out on different samples, i.e., not on the material sourced from the strength samples, this aspect is not fully clear and needs better clarification.

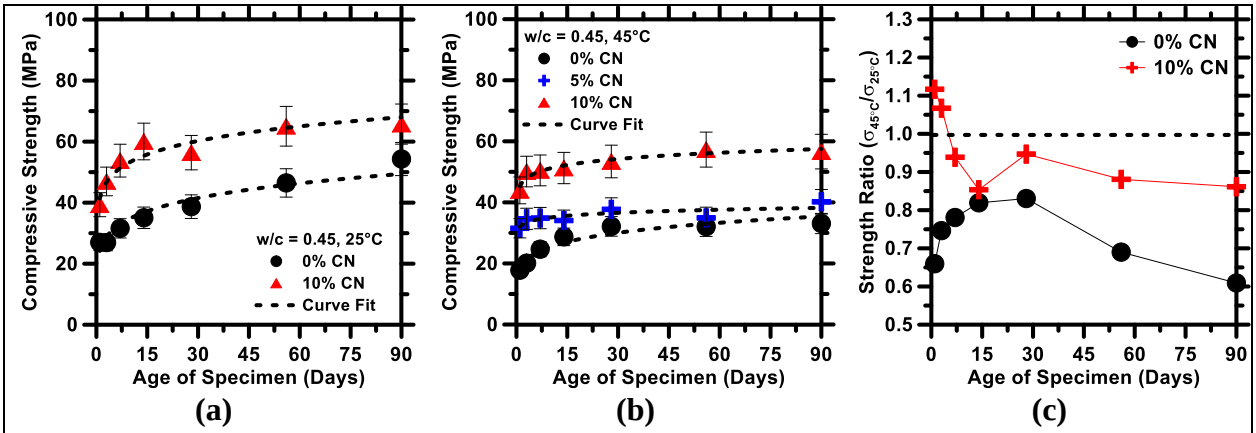

Figure 3.3: The evolution of the compressive strength as a function of age for CAC mixtures cured at: **(a)** 25 °C, **(b)** 45 °C and **(c)** the strength ratio of mixtures cured at 25 °C and 45 °C as a function of age. In general, the strength ratio should take a value of unity to discount phase conversion, microstructural and temperature dependencies on compressive strength.

To better illustrate effects of phase conversion(s), Figure 3.3(c) shows the strength ratio of the CAC mixtures cured at 25 °C and 45 °C. In general, it is noted that for a CN dosage ≤ 10 % (by mass of CAC), the strength measured at 25 °C is considerably higher than the strength measured at 45 °C indicative of solid phase conversion occurring at higher temperatures or with increasing time. However, at higher CN dosages (i.e., CN ≥ 10 %, by mass of CAC), the strength ratio tends closer to unity (i.e., within the uncertainty of the strength measurements) suggesting that the

influences of conversion are reduced with increasing CN additions. As such, and as will be highlighted later, it is the formation of NO_3-AFm in increasing quantities at the expense of the C_3AH_6 phase which is responsible for such beneficial behaviors. These trends noted in the strength ratio are significant as they highlight that, in agreement with the initial hypothesis, NO_3-AFm formation would indeed act to mitigate the detrimental effects of any solid phase conversion in CACs; with increasing success with increasing CN dosage.

3.5.2 X-Ray Diffraction (XRD)

To better understand trends in compressive strength development, x-ray diffraction analyses were carried out to identify the solid phases present in hydrated CACs, both with and without CN additions at different ages. Figures 3.4-3.8 show the evolution of hydrated phases in plain CAC pastes cured at two different temperatures, 25 °C and 45 °C. Significant differences are noted in the types of phases existing as a function of reaction time at the two curing temperatures.

For example: pastes cured at 25 °C show the presence of the CAH_{10} and C_2AH_8 phases from early times, and it is only by 90 days that the former phase is no longer present. On the other hand, the CAH_{10} phase is not observed in CAC systems cured at 45 °C wherein the other hydrates, such as C_3AH_6, are more stable.[2,142] At this temperature, the existence of C_2AH_8 is transitory, i.e., being observed only at 1 day, likely as an intermediate step leading to C_3AH_6 formation – on account of reaction kinetics favoring the initial formation of C_2AH_8 as compared to C_3AH_6.[142] Significantly, between 56 and 90 days, for CACs cured at 25 °C, both the CAH_{10} and C_2AH_8 phases are nearly eliminated by conversion (i.e., given lack of diffraction peaks), as supported by the large increase

in the intensity of C_3AH_6 peaks in the XRD pattern (Figure 3.4a). The conversion reactions also augment the quantity of the AH_3 phase which forms along the conversion pathway (Eqs. 3.1-3.3). Other phases present include unhydrated monocalcium aluminate (CA), gehlenite (C_2AS), and strätlingite (C_2ASH_8) which forms due to the release of silica from C_2AS which is present in the CAC.[143,147] As will be discussed later, CA is expected to persist in these systems, even at very late ages, given their water deficient nature (low w/c) which prevents complete hydration (see also Figure 3.11). In the case of plain CAC pastes hydrated at 45 °C (Figure 3.4b), C_3AH_6 is stable from very early times. The only presence of a metastable phase is that of C_2AH_8 at 1 day, since this phase is known to act as a transitory step in C_3AH_6 formation.[148–150] The hydration of CA is very rapid at this elevated temperature, as the principal x-ray reflection at 30° shows small intensities at even 1 day. This explains why at 45 °C, little, if any, strength gain occurs in the CAC mixtures after 1 day of reaction (Figure 3.3b). The precipitation of C_3AH_6 and AH_3 is immediate at this higher temperature, and the quantities (see peak intensities) of these hydrates remains relatively constant with age. C_2ASH_8 is noted to be present at the higher temperatures, as a consequence of enhanced silicon release from the anhydrous CAC phases (in this case, C_2AS).

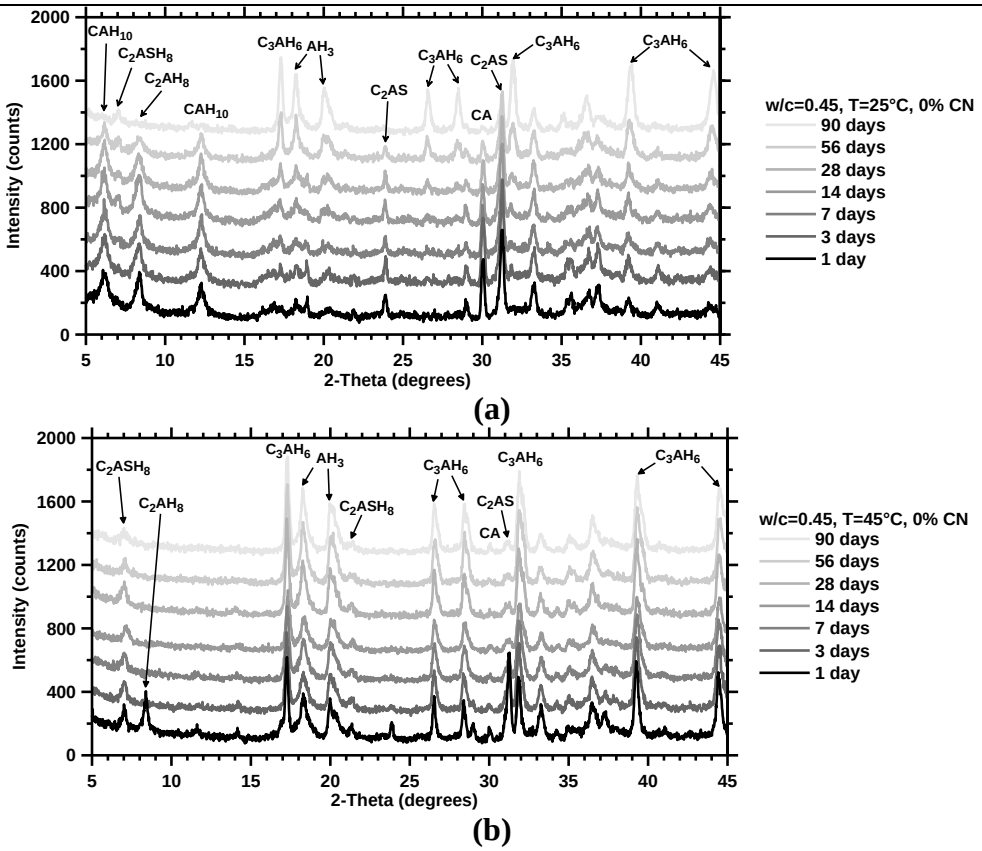

Figure 3.4: X-ray reflections of plain CAC pastes at different ages for mixtures cured at: **(a)** 25 °C and **(b)** 45 °C. Time and temperature dependent phase conversions are identified.

Figure 3.5 shows the evolution of phases over time for 20 % CN-containing CAC systems hydrated at different temperatures. Significantly, independent of the curing temperature, from early times both NO_3-AFm and AH_{3-x} are noted to be the major stable phases that exist – with the formation of all other hydrates (e.g., the CAH_{10}, C_2AH_8 and C_3AH_6) being suppressed. In time the quantity of NO_3-AFm and AH_{3-x} formed increases systematically. CA is depleted rapidly, but a small quantity persists even at 90 days due to the insufficient availability of water. It should be noted that while the principal x-ray reflection for NO_3-AFm should be located at 10° (2θ), a small peak shift is noted, likely on account of changes in the water state of this X-AFm phase.[130,131] Because the NO_3-AFm phase is thermodynamically more favorable, it is proposed that the reaction of the C_2AS is suppressed due to limited water availability, and its relatively low reactivity – as evidenced

by the constant intensity of the C_2AS peak (31.4°), and the lack of strätlingite** at any age in these systems. The influence of pH on C_2AS reactivity is expected to be slight, as the pH of CN-doped mixtures is noted to decrease only for CN additions exceeding 25% (by mass of CAC), prior to which it maintains a fixed level (i.e., pH ≈ 12.06 for 0% ≤ CN dosage ≤ 25%). More specifically, as per calculations, the pH decreases from 12.06 to 10.28 as the CN addition level is raised from 25 % to 30 %. While minor peaks are noted around 39.3° and 44.4° (2θ) in the CAC systems hydrated at 25 °C with 20 % CN, they likely do not correspond to C_3AH_6 given the lack of an accompanying principal intensity x-ray reflection for this phase (17.3°, 2θ), across all ages.

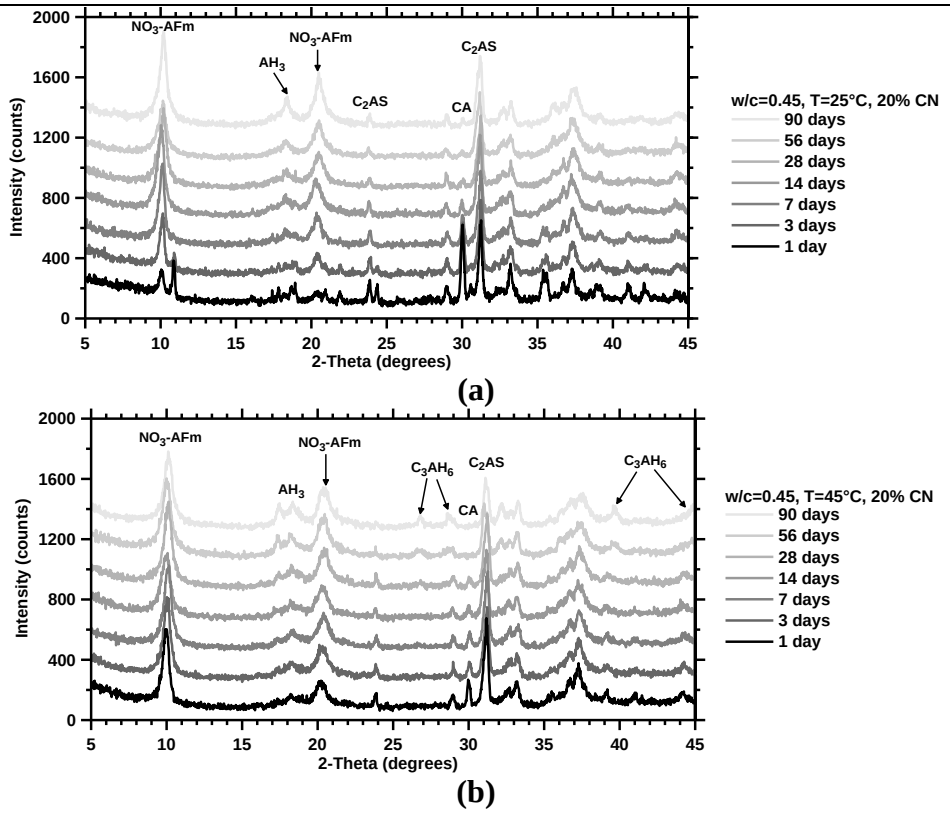

Figure 3.5: X-ray reflections of 20 % CN-containing CAC pastes at different ages for mixtures cured at: **(a)** 25 °C and **(b)** 45 °C. CN additions eliminate metastable phases.

** Thermodynamic simulations predict the formation of the C_2ASH_8 phase in CAC systems. Thus, one explanation for the lack of peaks corresponding to this phase in the XRD patterns is its poor structural order (low crystallinity).

In the case of the 20 % CN-containing CAC system hydrated at 45 °C, one difference as compared to the parallel 25 °C system is noted in that a very small quantity of C_3AH_6 has formed by 56 days, and remains essentially constant thereafter. It should be noted that the formation of the C_3AH_6 phase is not due to the decomposition of the NO_3-AFm phase. This conclusion is fully supported by the outcomes of thermodynamic calculation (Section 3.6, see Figure 3.13a) which indicate that, towards terminal evolutions of hydration (i.e., tending towards ≈ 78%), C_3AH_6 forms, while the NO_3-AFm content remains fixed. This indicates that in CN-rich systems, the formation of C_3AH_6 occurs at the expense of NO_3-AFm when water availability is limited;[††] due to the higher molecular water content of the latter as compared to the former (see Figure 3.13a). In any event, it is expected that at a CN dosage of 20 %, some quantity of C_3AH_6 would form, not only due to water activity/availability effects, but because this CN dosage is insufficient to fully suppress formation of the C_3AH_6 phase. For the CAC considered, a CN dosage of ≈ 28% (by mass of CAC) is needed to completely suppress C_3AH_6 formation; see also Figure 3.13(b). These aspects are more rigorously discussed as CN-dosage and water availability would both influence phase balances in water deficient CN-doped CAC systems. In any event, it is notable that the NO_3-AFm phase remains stable across the entire duration of these evaluations with no phase conversions (i.e., decomposition of NO_3-AFm) being noted in the system.

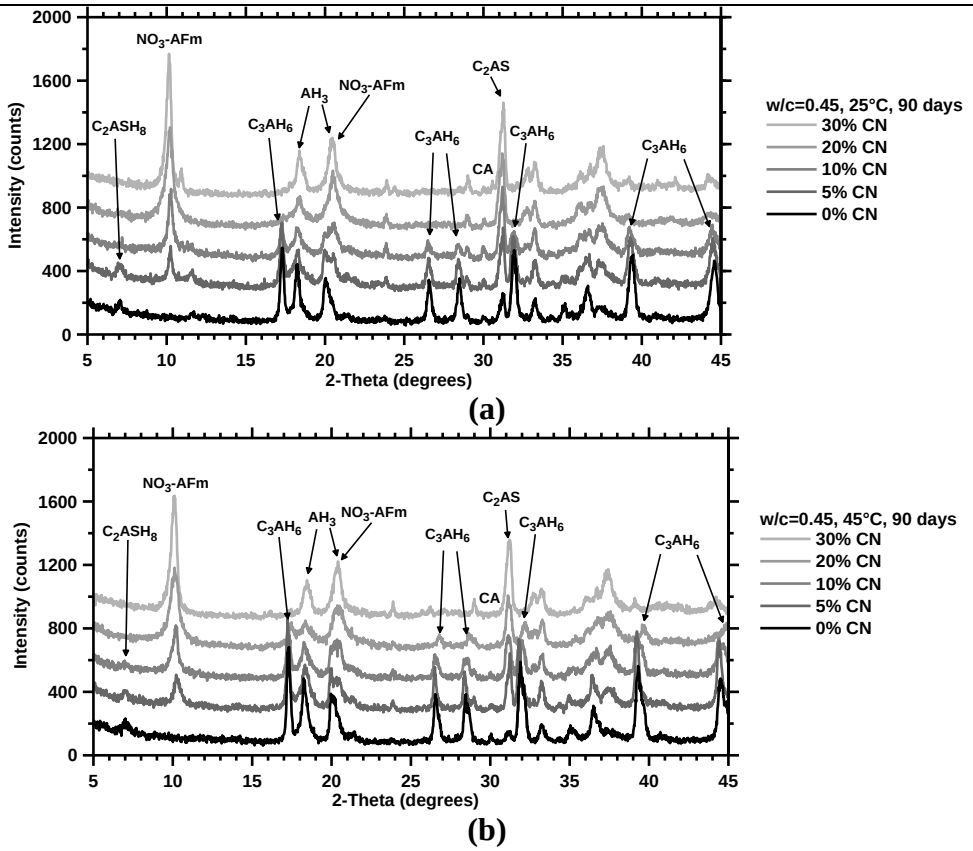

Figure 3.6: The effects of incremental CN additions on phase assemblages of CAC pastes hydrated for 90 days at: **(a)** 25 °C and **(b)** 45 °C. Due to the long duration of hydration, conversion of metastable phases to C_3AH_6 is evident. At both temperatures, increasing the CN dosage yields more NO_3-AFm and reduces the prevalence of C_3AH_6.

Figure 3.6 shows the effects of increasing CN dosage on the phase assemblage of CAC pastes cured at 25 °C and 45 °C. Expectedly, intermediate dosages of CN (e.g., 5 % CN and 10 % CN) yield phase balances intermediate to the 0 % CN and 20 % CN systems discussed in Figures 3.4 and 3.5. As the CN dose increases, a larger proportion of NO_3-AFm forms, while the relative amounts of CAH_{10}, C_2AH_8 and C_3AH_6 formed are either sequentially reduced or eliminated. For example, at a CN dosage of 5 % at 25 °C, while CAH_{10} does not form, a small amount of C_2AH_8 is present at early ages which in time converts into C_3AH_6. This mixture also contains a small amount of C_2ASH_8 in addition to the NO_3-AFm and AH_3 phases. However, at a CN dosage of 10 % (and higher), the CAH_{10}, C_2AH_8 and C_2ASH_8 phases are eliminated, but some C_3AH_6 persists

in the system. At yet higher CN dosages i.e., at 20 % and 30 % CN, and at 25 °C, C_3AH_6 is no longer observed – which corresponds to the elimination of the convertible/metastable phases in CAC systems. While these behaviors are generally applicable to CACs hydrated in the presence of CN admixtures at higher temperatures, one important difference persists. In this case (i.e., at 45 °C), even at CN dosages ≥ 20 % CN (by mass of CAC), the C_3AH_6 phase yet persists. This is on account of two reasons including: (a) insufficient CN addition, and (b) the limited availability and the reduced activity of water, which may favor the formation of a lower water phase (e.g., C_3AH_6) as compared to a higher water content phase (NO_3-AFm). [††,151]

To better resolve the implications of liquid water availability on phase conversion behavior, a series of studies were carried out on CAC pastes both with and without CN-additives for systems containing excess water, i.e., w/c = 0.70 at similar curing temperatures (25 °C and 45 °C) as was described above. Similar trends are noted as in the case of lower w/c systems with a few critical differences. As shown in Figure 3.7(a), for systems cured at 25 °C the conversion of C_2AH_8 to C_3AH_6 is observed by 28 days of hydration. However, CAH_{10} persists in the system, likely due to the availability of excess water.[152] In time however, the CAH_{10} is expected to convert to C_3AH_6 via the C_2AH_8 pathway (Eq. 3.1). Anhydrous CA is largely consumed by 3 days, and completely consumed by around 28 days given its access to sufficient water. C_2AS also hydrates (see progressive decrease in peak intensity) resulting in the formation of C_2ASH_8 (strätlingite) which forms in larger quantities due to access to sufficient water as compared to the w/c = 0.45 systems

[††] In this case, high water content and low water content is simply an indication of whether a phase may contain molecular water (NO_3-AFm), or hydroxylated water (C_3AH_6). In general, phases containing hydroxylated water are more compact, i.e., of higher density, than phases that contain molecular water. At a first indication, phases containing molecular water will experience loss of such water at temperatures ≤ 150°C.

which are water deficient. For the plain w/c = 0.70 systems hydrated at 45 °C, C_3AH_6 (and AH_3) and C_2ASH_8 are observed starting from 1 day. The principal peaks intensities for these phases remains roughly constant over time, as the hydration of the CAC is essentially complete. A weak X-ray reflection for the CAH_{10} phase is observed at all ages, but the transitory C_2AH_8 phase is not observed indicating its conversion to C_3AH_6.

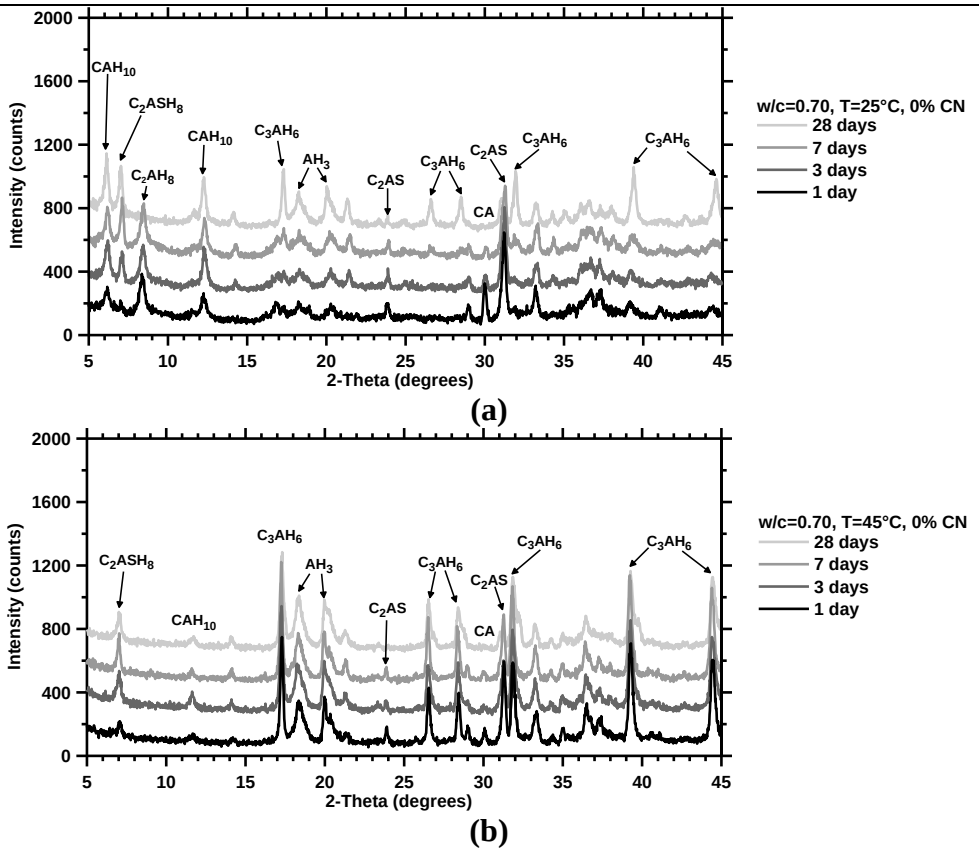

Figure 3.7: X-ray diffraction patterns of a plain CAC system, w/c = 0.70, hydrated at: **(a)** 25 °C and **(b)** 45 °C. Anhydrous CA is largely consumed by around 3 days in these systems due to the abundance of water at this higher w/c.

Figure 3.8 shows the evolutions of solid phases in w/c = 0.70 CAC mixtures containing 20 % CN. It is noted that at both curing temperatures, i.e., 25 °C and 45 °C, the formation of CAH_{10}, C_2AH_8 and/or C_3AH_6 is suppressed. Expectedly then, the hydrated phase composition is dominated by the

NO_3-AFm phase with AH_3 being present. Expectedly enough, when sufficient water is present the CAC achieves *near complete* hydration rapidly, i.e., by 3 days and 1 day respectively for mixtures cured at the lower and higher curing temperatures. It is important to note here, in spite of access to sufficient water, the C_2AS phase remains unreacted; the reasons for which are not completely clear at this time. This suggests that C_2AS reaction is suppressed dominantly by the progressively reduced water activity (due to water consumption and increasing levels of CN addition) rather than by water availability.[151,153] However, this requires further clarification. It is also likely that the addition of CN accelerates CAC hydration, though this aspect has not been studied in detail.[154] Furthermore, in the presence of sufficient water, in contrast to the behaviors of the w/c = 0.45 mixtures, C_3AH_6 is not observed at any age at a higher curing temperature. This may indicate that the conversion avoidance provoked by X-AFm formation is far more effective in water sufficient systems, as compared to water deficient systems (e.g., see Figures 3.5-3.6).[‡‡] While the reasons for this are not fully clear, the formation of the lower water content C_3AH_6 phase may be facilitated under conditions of reduced water activity and water availability; at the expense of NO_3-AFm in spite of *near sufficient* CN being present (see Figure 3.6). However, the XRD observations do clarify that so long as water and NO_3^- are present, the formation of conversion sensitive phases can be partially or fully suppressed by CN additions in CAC systems. In water-sufficient systems, for CN ≤ 28% (by mass), the formation of some C_3AH_6 at long time scales is expected as this is

[‡‡] It is indeed correct to state that phase conversion is prevented by dispermitting/bypassing the formation of the metastable phases including: CAH_{10} and C_2AH_8. While it could be argued that such "dispermitting/bypassing" is not a means of conversion prevention, but rather the formation of a different set of hydrated phases, this is not so, as other than the metastable phases, other CAC typical phases, e.g., AH_3, C_2ASH_8 (and C_3AH_6) are permitted to form. While arguably, this is an issue of semantics, for consistency with the spirit of the approach, the authors use the terminology of "conversion prevention" to the dispermitting/bypassing of metastable phase formation.

the critical CN dosage needed to completely avoid the formation of the C_3AH_6 phase (see also Figure 3.13b).

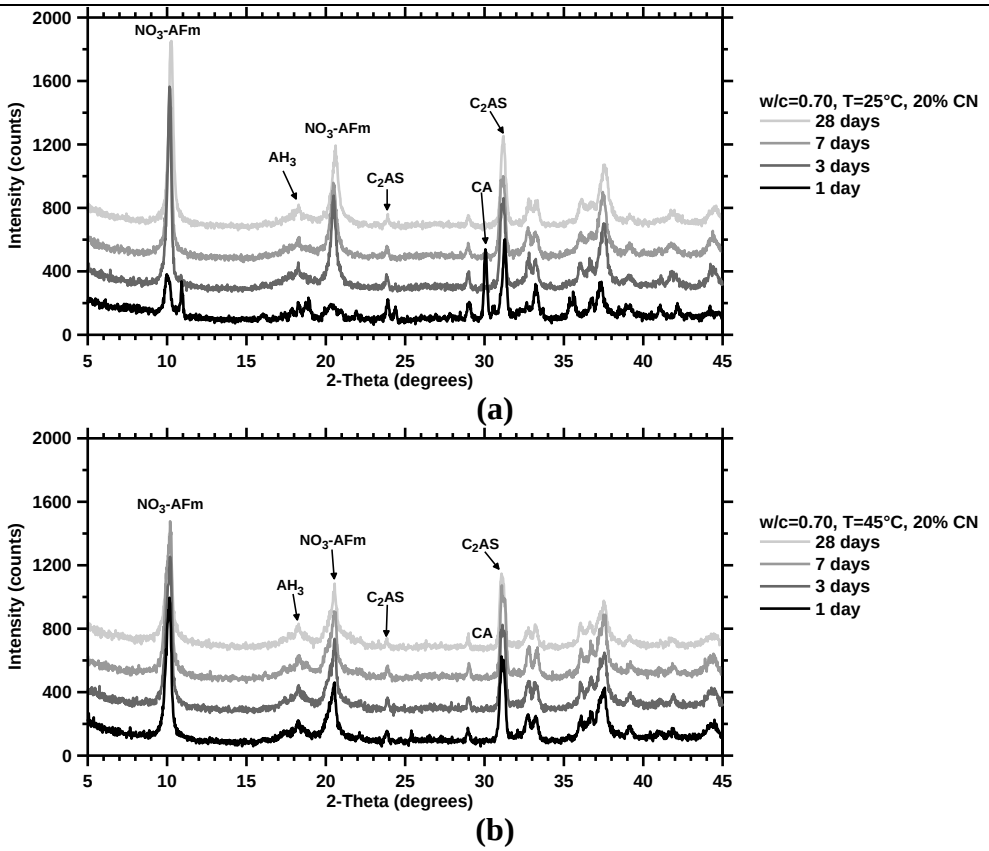

Figure 3.8: X-ray diffraction patterns of a 20 % CN-containing CAC, w/c = 0.70, cured at: **(a)** 25 °C and **(b)** 45 °C. C_3AH_6 formation is suppressed at the expense of NO_3-AFm formation. The hydration of the CA phase is largely complete by 3 days and 1 day, respectively, at the lower and higher curing temperatures.

3.5.3 Thermogravimetric Analysis (TGA)

Figure 3.9 shows representative TGA curves for plain CAC and 10 % CN-dosed systems hydrated at 45 °C for 28 days for w/c = 0.45. In each case evaporable water is lost in the temperature range below 150 °C. In agreement with the XRD datasets (Figure 3.4a), AH_3 and C_3AH_6 are identified as the dominant phases present in the CN-free system with decomposition peaks for these phases

being identified at 280 °C and 300 °C, respectively. Though present, C_2ASH_8 is not identified via TG/DTG analysis due to its small content, or overlap in decomposition peaks with the AH_3 and C_3AH_6 phases.[155] The decomposition of the primary hydrates (i.e., AH_3 and C_3AH_6) forms a large doublet in the DTG curve due to the superposition of their similar decomposition peaks. In the case of the 10 % CN-dosed system, NO_3-AFm is identified to be present, though quantitative analysis of the TG/DTG curves is complicated due to over-lapping peak positions.

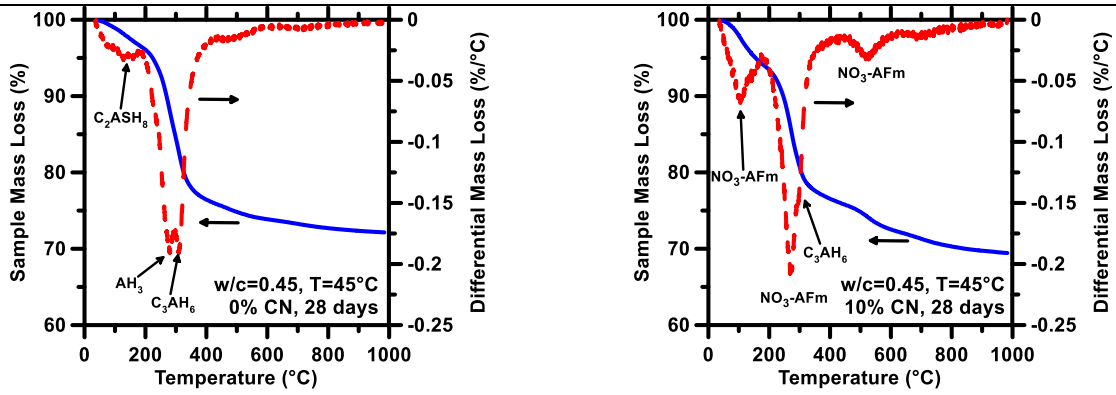

Figure 3.9: Representative TGA and DTG curves obtained for: **(a)** plain CAC system and **(b)** 10 % CN-dosed CAC, both cured at 45 °C for 28 days for w/c = 0.45. The DTG peak corresponding to the decomposition of C_3AH_6 is reduced in the 10 % CN sample, as NO_3-AFm forms at the partial expense of C_3AH_6 (see Section 3.6).

Renaudin et al.[156] and Balonis et al.[130] via studies of phase pure NO_3-AFm highlighted that the decomposition of this phase follows three major steps: (1) a dehydration occurring at 110 °C, (2) a decomposition of nitrate in the AFm phase to nitrite at 250 °C, and (3) decomposition of nitrite at 520 °C. In the 10 % CN sample, the peak for nitrate decomposition closely matches that of AH_3 (and C_3AH_6), so the doublet observed in the plain system is reduced to a single peak in the 10 % CN system as NO_3-AFm, AH_3 and C_3AH_6 are the dominant hydrates. In this case, it should be

noted that the 10 % CN dosage is insufficient to fully avoid the formation of the C_3AH_6 phase in the system in agreement with the XRD determinations.

In a second series, TG/DTG patterns were acquired for plain and CN-dosed CAC pastes of w/c = 0.70, cured at 25 °C and 45 °C after 1 day and 28 days of curing (see Figure 3.10). After 1 day of curing at 25 °C, the metastable hydrates CAH_{10} and C_2AH_8 are noted to decompose at 100 °C and 180 °C, respectively, with NO_3-AFm being identified when CN is added. C_2ASH_8 is also present, but only in the case of systems cured at 45 °C (decomposition temperature around 160 °C), due to the less reactive nature of C_2AS as compared to CA;[157] in the 0 % CN and 10 % CN-dosed samples. However, C_2ASH_8 is not detected at higher CN dosages – observations which agree with the XRD results. In general, increasing the CN dosage increases the amount of NO_3-AFm formed, across all ages and curing temperatures. This trend is easily identified by noting the increase in nitrite decomposition at 520 °C, as no other relevant phases decompose around this temperature.

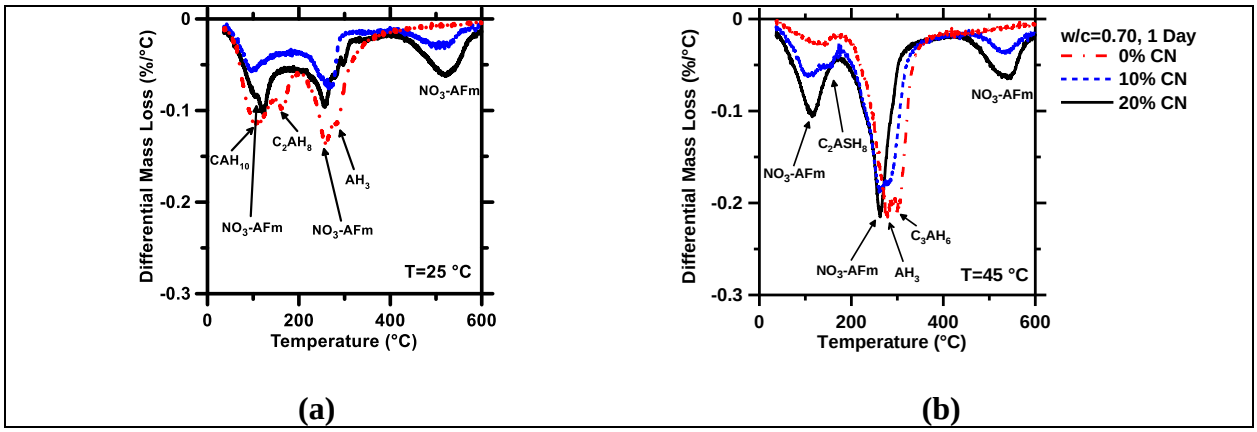

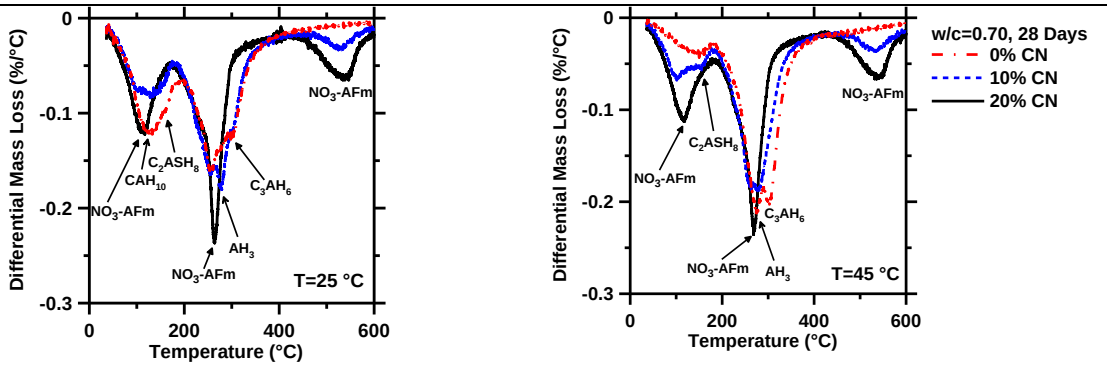

Figure 3.10: Representative DTG curves of plain and CN-dosed CAC pastes prepared at w/c = 0.70 cured at: **(a and c)** 25 °C and **(b and d)** 45 °C. Conversion is noted in the plain system, which is increasingly suppressed by the formation of NO_3-AFm upon CN addition(s).

The lack of C_3AH_6 formation at higher CN dosages reduces the area under the DTG curve noted at 300 °C.[156] Significantly, as the CN dose increases and the quantity of C_3AH_6 formed diminishes, the lumped peak present around 250 °C to 300 °C loses its bimodality, and shifts towards the lower bound, i.e., 250 °C, which then represents nitrate decomposition. The observations noted above, are broadly applicable at both early (1 day) and later (28 days), though with one difference. For example: C_2ASH_8 is noted in w/c = 0.45 only by 28 days, and not earlier, likely as a consequence of the water-poor nature of this system and the low(er) reactivity of C_2AS as compared to CA. This summary of observations is in good agreement with XRD results and the results of thermodynamic modeling, which highlights self-consistency in the nature of the investigations and the conclusions reached therein.

3.6 Thermodynamic modeling of phase assemblages in calcium aluminate cement

Thermodynamic calculations carried out using consistent thermochemical data are a powerful means to estimate and describe phase constitutions in cementitious systems. Such calculations are applied to describe the influence of CN additions on suppressing conversion behaviors in CACs. It should be noted that while the phase assemblages discussed below are quantitative (i.e., accurate descriptions of mass and volume balance), for systems containing large dosages of CN (e.g., ≥ 20 % CN), the results present a level of uncertainty. This is because the solution phase models applied herein are most reliable for ionic strengths ≤ 2.0-3.0 mol/L,[138] beyond which, accuracy is reduced.

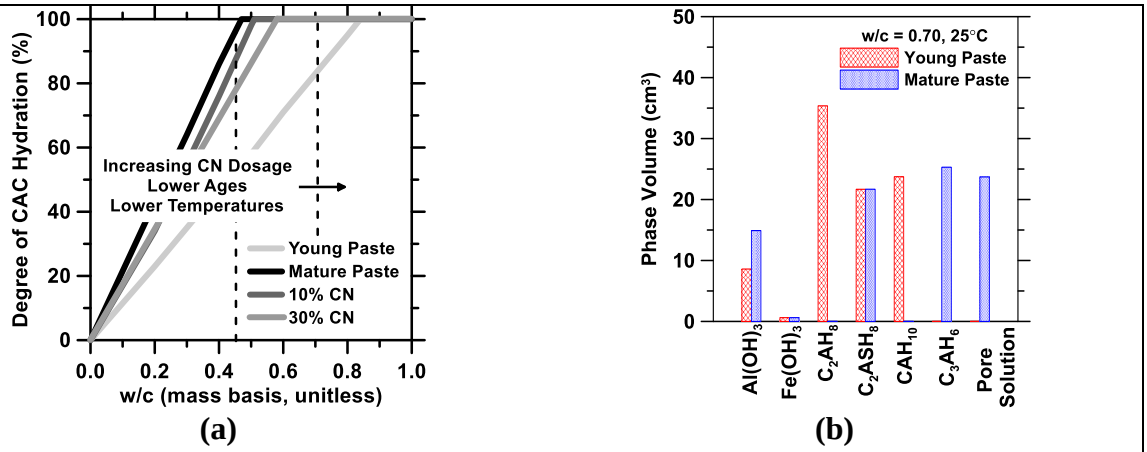

Figure 3.11: (a) The critical degree of hydration for CACs hydrating with and without CN and **(b)** the phase volumes for different phases in a "young" and "mature" CAC paste (w/c = 0.70, T = 25 °C). The young and mature pastes are simulated by suppressing the formation of the C_3AH_6 and the CAH_{10} and C_2AH_8 phases, respectively.

As a starting point, calculations are carried out to determine the critical w/c at which hydration would cease as a function of the CAC constitution and CN dosage (i.e., due to water uptake in the NO_3-AFm which contains more water than the C_3AH_6 phase), which may influence the nature of phases that exist. For example: at short time scales and at 25 °C, C_3AH_6 would not form, and the

critical w/c is only a function of water uptake into the CAH_{10} and C_2AH_8 phases. However, in time as the metastable phases decompose and release water, hydration would proceed, but with the critical w/c having two "steps", i.e., before and after conversion. On the other hand, at higher temperatures, ≥ 30 °C, the critical w/c is only a function of water uptake in the C_2ASH_8 and C_3AH_6 phases, which requiring less water, permits a greater extent of CAC to hydrate (see Figure 3.11a).

Figure 3.11(a) shows the evolution of the critical w/c for CAC pastes hydrating at ambient and higher temperatures. It is clear that the assemblage of phases formed substantially influences the extent of CAC reaction that can occur, prior to and after the conversion process. This explains as an example why the extent of hydration of the CAC (represented to the first order by the presence of unreacted CA and C_2AS; see Figures 3.4-3.8) varies with the: (i) w/c, (ii) curing temperature and (iii) the presence of CN additives. Additionally, Figure 3.11(b) shows the change in the hydrated phase balances as relevant to a young paste (i.e., pre-conversion in which CAH_{10} and C_2AH_8 are dominant) and mature paste (i.e., post-conversion in which C_3AH_6 forms at the expense of CAH_{10} and C_2AH_8). The solid volume decreases ≈ 22.5 cm^3 post-conversion, which translates to increase in porosity (i.e., described here as the fraction of void-space occupied by solution) of ≈ 19 %. Given that strength and porosity in cementitious systems are exponentially correlated,[158] in a phase conversion sensitive system (i.e., having a high w/c), this increase in the porosity would cause a large decrease in strength. While this representation is indeed more extreme than typical, e.g., see Figure 3.3 and discussion that follows, the implications are clear; in time, conversion would degrade the compressive strength, and the mechanical properties, in general, of high w/c CAC systems.

To better display the effects of CN additions on phase balances, calculations are carried out for a variety of systems while considering the effects of the: (i) w/c, (ii) CN dosage and (iii) the curing temperature. It should be noted that while the calculations display the effect of the fractional reactivity of the CAC, the effects of kinetics are not considered. Thus these results can only be qualitatively linked to the *later-age* experimental (XRD) data described above. As a key point, the calculations are applied to show how the addition of CN is able to avoid formation of C_3AH_6 in CAC systems, across a range of conditions. It should be noted, all calculations are only qualitatively linked to XRD data shown above, since reaction time is not considered herein.

Figure 3.12(a) shows simulated phase assemblages for a plain "mature" CAC system. As observed via XRD, it is noted that as hydration proceeds, at longer times (or at elevated temperatures), the major phases include C_3AH_6, C_2ASH_8 and AH_3. It should be noted that simulations do not consider the state of the system at shorter times and lower temperatures when CAH_{10} and C_2AH_8 would exist. Since CAC hydration is incomplete for w/c = 0.45, residual quantities of the anhydrous phases including CA and C_2AS are observed in such systems (see Figures 3.4 and 3.12a). Predictions of thermodynamic calculations for CACs hydrated at higher w/c (Figure 3.12b) are consistent with predictions for lower w/c, except that the availability of water is no longer a limiting variable in avoiding the completion of hydration (see also Figure 3.7 for XRD). This is in good agreement with experimental observations and highlights that water availability (and activity) is a very significant factor which influences the extent of reaction in CAC systems, as also their rate, as reductions in water availability/activity would hinder the hydration of the anhydrous phases and the formation of their hydration products, in relation to their moisture sensitivity (reactants) and contents (products).[151,153]

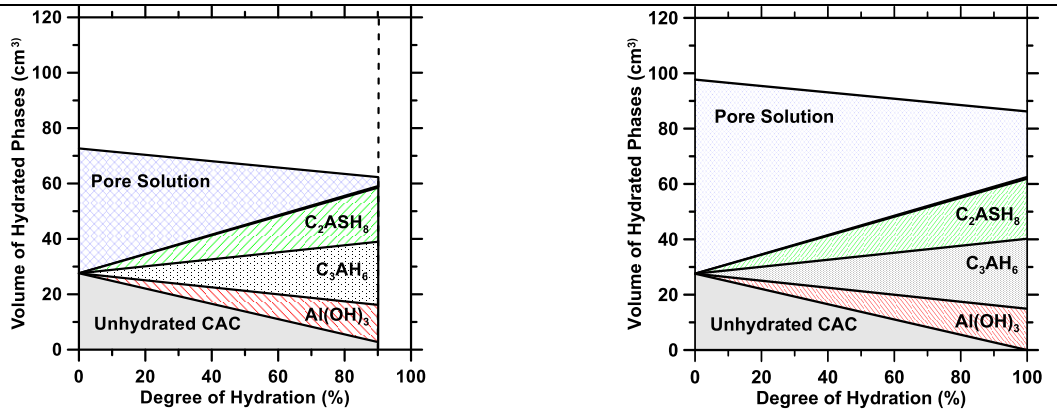

Figure 3.12: Calculated phase balances of "mature" CAC pastes hydrated at 25 °C as a function of the degree of hydration for: **(a)** w/c = 0.45 and **(b)** w/c = 0.70. The availability of excess water permits complete hydration in the latter, but not the former case. These simulations consider 100 g of CAC and 45 g or 70 g of water reacting with each other.

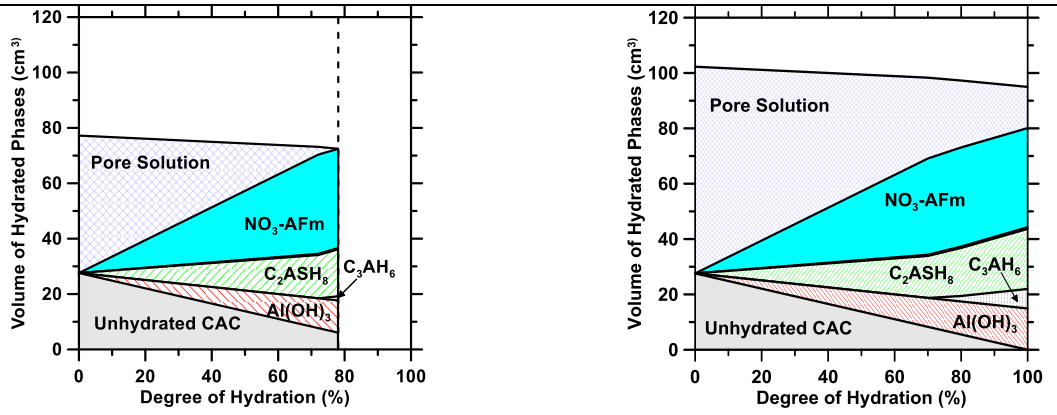

Figure 3.13: Calculated phase balances of "mature" CAC pastes hydrated at 25 °C as a function of the degree of hydration containing 20 % CN for: **(a)** w/c = 0.45 and **(b)** w/c = 0.70. The availability of excess water permits complete hydration in the latter, but not the former case. These simulations consider 100 g of CAC, 45 g or 70 g of water and 20 g of CN (dissolved in the water) reacting with each other.

As shown in Figure 3.13, when CN is added to CAC systems, NO_3-AFm forms at the expense of C_3AH_6. This outcome is consistently observed across a wide-range of CN dosages. Obviously, the extent of formation of NO_3-AFm is proportional to the initial CN dosage, i.e., less C_3AH_6 and

more NO_3-AFm forms with an increase in the CN dosage. This is significant in that, in relation to the CAC chemistry, the CN admixture dosage can be altered to partially or completely suppress the formation of convertible phases. At lower w/c, it is noted that as the CN dose is increased, in addition to C_3AH_6, the formation of C_2ASH_8 is also suppressed; an observation supported by experimental data (Figure 3.6) – which may suggest that the hydration of C_2AS is suppressed in the presence of high concentrations of CN additives. This may also be on the account of C_2AS hydration being more influenced by the availability/activity of water, as compared to CA, which can hydrate in environments of reduced water availability and the fact that NO_3-AFm is more favorable to precipitate. However, as the w/c is increased (e.g., at w/c = 0.70), the calculations predict that both C_2ASH_8 and NO_3-AFm can co-exist. This is in contrast with XRD data which indicates that C_2AS hydration is suppressed, even when excess water is present. This may suggest that in addition to the points noted above, the solubility mismatch between the NO_3-AFm and C_2ASH_8 phases may indeed be responsible for the suppressed formation of the latter phase as compared to the former. As a comment of substance it should be noted that while all through the calculations AH_3 is considered as a poorly-crystalline phase, the crystallinity of this phase does evolve in relation to age/time, temperature and the chemical environment in which it is present.[2,142] While this would impact aspects such as its density, solubility (K_{SP}) etc., these aspects are not considered in this study. Regarding Ti and Fe present in the CAC: no account is made for the precipitation of titanium bearing phases (due to lack of suitable solubility data), in hydrated CACs. Fe is expected to exist dominantly as $Fe(OH)_3$ in minor quantities (not shown in plots), though some “Fe” may partially substitute “Al” in the X-AFm or C_3AH_6 structures.[2,144,145]

It is well-known that the hydration rate, and the nature of product(s) formed in CACs is sensitive to the curing temperatures.[2,150,159,160] For example: while the CAH_{10} and C_2AH_8 phases are stabilized at lower temperatures, generally ≤ 25 °C,[142,150] C_3AH_6 will form at higher temperatures. However, for CN to be used as a conversion avoiding additive, it is necessary to determine the temperature stability of NO_3-AFm in CAC systems. As such, a series of calculations were carried out over a range of temperatures (i.e., 5 °C to 55 °C) to assess the stability of the hydrated phases for CACs reacted with and without CN. As noted in Figure 3.14, in general the hydrate assemblage remains stable and essentially unchanged across the entire range of temperatures that is considered. While this is obviously sensitive to the database of solubility inputs (see [142] for influences of solubility data), in general, for typical temperatures experienced under field conditions, CN-dosed CACs will remain stable in terms of phase relations. It should be noted that, based on our current understanding, any changes in hydrate assemblages produced at lower temperatures are likely relevant to the CAH_{10} and C_2AH_8 phases, rather than the NO_3-AFm (e.g., see [142] for discussion). While it may be argued that at early ages, CACs can experience elevated temperatures, this is not expected to impact the formation of NO_3-AFm phase or its stability.[§§] Of course, if the temperature were to dramatically exceed 55 °C and then remain so continually, the NO_3-AFm phase formed may begin to decompose (in proportion to the level of increase in temperature) to form C_3AH_6 and CN of which the latter would likely remain solubilized in the pore fluid (i.e., due to its high solubility). However, this outcome is not clear as: (i) if there existed sufficient quantities of mobile

[§§] Unpublished data suggests that in the presence of elevated abundances of NO_3^- species, the temperature stability of the NO_3-AFm is wider than currently expected (e.g., around 55°C) [**Error! Bookmark not defined.**]. In support of this reasoning, phase equilibria calculated within the GEMS-PSI distribution indicate that in addition to temperature, the stability of the NO_3-AFm depends on the how much mobile NO_3^- is available in the pore solution, i.e., the aqueous $[NO_3^-]/[Al(OH)_4^-]$ ratio, where the "[]" parenthesis indicate molar units [**Error! Bookmark not defined.**]. Based on these points, at high levels of CN, e.g., ≥ 20% (by mass of CAC), it is indeed likely at temperatures higher than 55°C the NO_3-AFm phase will indeed remain stable, but more evidence is needed to confirm this point.

NO_3^- ions in the pore fluid, the stability of the NO_3-AFm may remain unchanged over a much wider range of temperatures than is currently estimated[131] and (ii) in time, C_3AH_6 would decompose, to form NO_3-AFm due to their differences in thermodynamic solubility (i.e., since these are negative logarithmic terms, in terms of their K_{SP}, NO_3-AFm < C_3AH_6[‡]). However, it is reasonable to expect that the hydrates formed in CN-dosed CAC systems would remain stable over temperatures relevant to field applications. Finally, it is also noted, that the volume of NO_3-AFm formed at lower temperatures (see Figure 3.14b) is slightly lower than that at higher temperatures. This is likely on account of: (a) the increased solubility CN at higher temperatures that provisions a higher abundance of solubilized [Ca^{2+}] and [NO_3^-] species,[161] and (b) changes in solubility of NO_3-AFM with temperature; which explains the evolutions of NO_3-AFm volume.

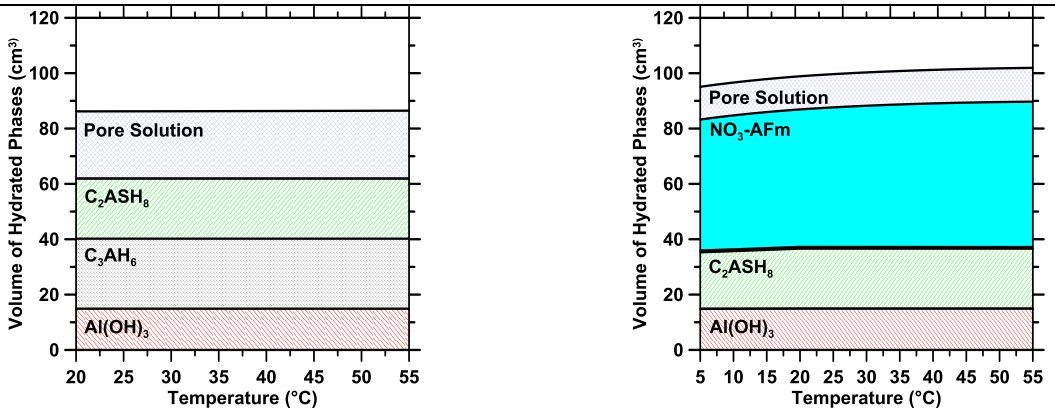

Figure 3.14: Calculated phase balances of "mature" CAC pastes hydrated for a w/c = 0.70 CAC paste across a range of temperatures for: **(a)** 0 % CN and **(b)** 30 % CN. The availability of excess water permits complete hydration of the CAC. For the plain CAC system, a limited temperature range from 20 °C to 55 °C is shown due to lack of consensus regarding the specific nature of the phase assemblage that would exist at temperatures ≤ 20 °C. This is not an issue for the CN-containing systems, as NO_3-AFm is expected to be stable across the entire range of temperatures considered.

A significant outcome of the calculations noted in Figure 3.14 is that in the case of mature CAC systems, at a constant w/c, the solid hydrate volume is much higher in systems containing CN as compared to CN-free systems. This is a consequence of the space-filling effect provided by the water-rich NO_3-AFm phase (i.e., as compared to C_3AH_6), and ensures that CN-containing systems, in general, display lower porosity than their CN-free counterparts. As a significant closing point, this explains why the CN-doped systems shown in Figure 3.3 show higher strengths across all curing temperatures than their CN-free counterparts. Interestingly in Figure 3.3, it is also noted that even at early ages and at ambient temperatures, the CN-dosed hydrated CACs show higher strengths than their CN-free counterparts, in spite of the presence of high-water content (and hence space-filling CAH_{10} and C_2AH_8) phases in the latter. This increased early-age strength in the CN-dosed systems compared to CN-free systems may suggest that: (i) the effective porosity is lower in CN-dosed systems as compared to CN-free systems, and/or (ii) the presumably higher-stiffness of the NO_3-AFm phase (i.e. stiffer than CAH_{10}, C_2AH_8 and C_3AH_6) similar to the CO_3-AFm phase provides benefits in strength and mechanical properties.[162] From an engineering perspective, this would consistently allow for lesser CAC use (i.e., for higher w/c formulations, and CAC replacement by mineral fillers) when CN is added to CACs to achieve strengths that would otherwise be achieved only by reducing the w/c in a CN-free CAC system. This provides an additional benefit for CN usage, i.e., as a strength enhancing additive for CAC-dominant and CAC containing binder (e.g., floor screeds, and repair) formulations.

3.7 Cl^- capture coatings for infrastructure elements

An important outcome of the title research is the development of *"Cl^- capture and corrosion hindering technologies"*, deployed in the form of thin coatings and toppings, for both horizontal and vertical infrastructure elements including pavements, bridges, etc. and metallic elements such as pipes and girders. For example, consider placement of a thin-coating of a CN-doped CAC formulation on a reinforced concrete bridge-deck. Upon contact with, and surficial intrusion of Cl^- species, Cl^- ions would displace NO_3^- ions from the AFm structure via an anion exchange reaction, that is dictated by the interlayer site occupation preference noted above. This action would act to trap Cl^- and release NO_3^- species into the pore solution, which shows potential for steel rebar corrosion inhibition.[163] Similar actions would be induced in the case of $Ca(NO_2)_2$-containing thin CAC toppings given the well-known corrosion inhibition capacities of NO_2^- species.[164] Significantly, by trapping Cl^- species in the near surficial regions of the covercrete, and delaying their intrusion towards the steel rebar; steel corrosion initiation could be substantially delayed, e.g., by retarding the rate of change in the $[NO_2^-, NO_3^-]/[Cl^-]$ ratio[163–165] in the pore solution. This would be an innovative strategy for steel corrosion protection via anion capture and exchange (ACE). Arguably, Cl^- capture, and hence corrosion protection limits would be governed by the anion exchange capacity and the quantities of AFm phases present, but periodic coating/topping renewal could address issues of saturation of the anion exchange capacity (AEC) of the material. Importantly, given the clear structural similarity of the X-AFm phases, the exchange of NO_3^- (or NO_2^-) by Cl^- will not induce changes in volume, as the molar volumes of these AFm phases are near equivalent.[130,131,141,166] Therefore, deleterious volume changes are not expected to accompany the ACE process. It is expected, that in accompaniment to admixing of any corrosion inhibitors into the mixing water, especially in high Cl^- exposure applications, e.g., when deicing salts, or sea

water exposure is relevant, such Cl^- capture coatings would be highly beneficial. While more work is needed to better understand the durability characteristics of X-AFm modified CAC binders, e.g., in the context of their volume instability upon drying, their transport behavior etc. it is clear that the outcomes presented herein offer innovative value in relation to admixture design, corrosion protection and improved infrastructure (material) performance.

3.8 Summary and Conclusions

Calcium aluminate cements are prone to phase conversion phenomena which has caused a stigma associated with their use in structural construction applications. Such conversions are controlled by "thermo-kinetic" factors, and result in unpredictable strength evolutions in time. Knowing that conversion behaviors are regulated by thermodynamic preferences of phases and reactions, an innovative means is proposed to stabilize NO_3-AFm, and more generally any of the X-AFm phases, at the expense of the other less preferred, and metastable calcium aluminate hydrate phases (CAH_{10}, C_2AH_8, C_3AH_6) that typically form in CAC systems. In this paper, this stabilization mechanism is demonstrated for the case of CN additions. This specific mechanism stabilizes a NO_3-AFm phase, though other phases of the wider X-AFm family, i.e., where, X is a single type or a multiplicity of ions including Cl^-, NO_3^-, NO_2^-, CO_3^{2-}, SO_4^{2-} and/or OH^- can also serve as conversion avoidance alternatives. It should be noted that the success of the stated approach is contingent on provision of an inorganic additive that is rapidly soluble, and able to support large abundances of X-AFm relevant anionic species in solution. If not, success would be limited. As an example, this explains why phase conversion avoidance attempted using calcitic (and dolomitic) additives is ineffective as compared to the "*soluble salt approach"* (i.e., in terms of their dissolution rate, and/or absolute solubility in water) whose success is demonstrated in this study. As a crucial field-relevant aspect, the outcomes of this research explain how CAC binders would be influenced by the use aggregates of differing gradation, as also composition, and why aggregates which are carbonaceous, siliceous or which may contain sulfate impurities may influence in different ways, the tendency of a CAC mixture to undergo phase conversion. The general approach of the study demonstrates means of manipulating stable phase equilibria in

cementitious materials such that by **"solubility based-design"**, desired solid phases of specific compositions and properties can be stabilized to produce cementitious (i.e., CAC, OPC, as also blended) binders which display much improved engineering properties, while eliminating their individual detrimental characteristics.

A wide range of analytics including strength determinations, x-ray and thermal analyses, and thermodynamic calculations are employed to study the evolutions of properties, and solid phases in time. Across a range of w/c and curing temperatures, and for durations up to 90 days, the NO_3-AFm phase is noted to be stable, and able to avoid the formation of the metastable calcium aluminate hydrate phases. Obviously, the efficiency of conversion avoidance is related to the CN dosage, with higher CN dosages being increasingly successful in avoiding phase conversion. Significantly, it is highlighted that at equivalent w/c, CN-dosed CAC systems will consistently demonstrate higher strengths than their CN-free counterparts. This is on account of the space-filling/stiffness effects of the NO_3-AFm phase which reduces the porosity of CN-doped systems, as compared to their CN-free counterparts. While arguably, it is yet necessary to study the kinetic evolutions of reactions (e.g., since some salts function as accelerators and others as retarders), evolutions of phase balances and engineering/durability properties of CN-doped CAC systems over longer durations to better evaluate the robustness of *conversion bypass*, and the durability (e.g., porosity, transport, etc.) characteristics of CN-doped CAC systems – it is clear that the title study provokes innovative opportunities to develop chemical admixtures based on inorganic salts for avoiding phase conversion phenomena, and to serve as strength enhancers in CAC (and ordinary portland cement) systems. Based on the outcomes presented, a novel means for metallic corrosion protection, via inorganic Cl^- capture coatings and toppings is proposed.

Chapter 4. – Anion capture and exchange by functional coatings: New routes to mitigate steel corrosion in concrete infrastructure

4.1 Introduction and background

Chloride (Cl^-) induced corrosion of reinforcing steel is a significant cause of premature damage and degradation of concrete infrastructure.[167–169] Concrete may be subject to chloride ingress as a result of contact with de-icing salts, seawater exposure, etc.[170] In the U.S. alone, over $8 billion is spent annually on corrosion-related repair, maintenance, and rehabilitation of bridges.[171] In addition, 11 % of the 600,000 highway bridges in the U.S. are deemed to be structurally deficient;[171,172] the majority due to corrosion-related degradation.

Due to the alkalinity of cementitious pore solutions (pH > 12), steel embedded in concrete is generally covered with a passivating oxide layer (γ-Fe_2O_3).[173,174] The ingress of Cl^- ions into the concrete is thought to initiate steel corrosion by displacing OH^- from this passivating layer.[168,175] Cl^--induced depassivation results in localized pitting and corrosion product formation, which reduces the cross-sectional area of the reinforcing steel, and, therefore, its load-bearing capacity.[169,173,175] The Cl^-/OH^- ratio (in molar units), which accounts for the passivating effects of OH^- ions, is often used to describe the risk of steel corrosion.[175,176] Although the precise value of Cl^-/OH^- required to initiate corrosion is a subject of debate,[175,176] a survey of the literature suggests that corrosion initiates when $Cl^-/OH^- \geq 0.6$.[175–177]

The presence of NO_3^- and NO_2^- anions in the pore solution can counteract the corrosive actions of Cl^- ions.[164,178–182] These species mitigate corrosion processes by oxidizing Fe^{2+} species to Fe^{3+} ions, which precipitate and re-form passivating films.[173,183] A critical Cl^-/NO_2^- ratio for corrosion initiation has been suggested to range from 0.25-to-2.0 (unitless, molar ratio).[165,184] While data regarding NO_3^- is lacking, indirect evidence suggests that NO_3^- provides similar corrosion inhibition as NO_2^- (i.e., for $Cl^-/NO_3^- \leq 0.25$).[133] While the use of NO_2^- or NO_3^- is valuable, the corrosion inhibition offered by these species offer is often limited by their initial dosage into the concrete.[185] Moreover, both $Ca(NO_3)_2$ and $Ca(NO_2)_2$ are highly soluble and, therefore, are subject to leaching, which may reduce their potential for corrosion mitigation.

The binding of Cl^- by cementitious phases can significantly suppress Cl^-/OH^- in the pore solution and thereby increase the service life of infrastructure.[186–188] For example, Cl^- binding can occur by ion exchange into alumino-ferrite monosubstituent (AFm) compounds, or by sorption onto C-S-H or other compounds.[129] AFm's are represented by $[Ca_2(Al,Fe)(OH)_6]\cdot X\cdot nH2O$, where X is the exchangeable interlayer anion, and *n* is the number of water molecules. The site (i.e., anion) occupation preference within the AFm-interlayer has the ranking $Cl^- > NO_3^- > NO_2^- > CO_3^{2-} > SO_4^{2-} > OH^-$,[131] assuring that AFm's present in cementitious formulations (i.e., those containing CO_3^{2-}, SO_4^{2-}, or OH^- in their interlayers) will capture Cl^- ions from solution to form Cl-AFm (i.e., Friedel's salt) or Kuzel's salt.[131,189] Ion exchange results in the release of the anion initially present in the AFm interlayer by a process of anion capture and exchange (ACE); a process that is guided by thermodynamic selectivity.[131,189]

ACE by AFm's is significant as (i) it operates in a Cl^- concentration range relevant to typical ingress conditions (≥ 14 mmol/L[190]), (ii) it has a much larger binding capacity per unit mass than Cl^- sorption by C-S-H,[188] and (iii) Cl^- species taken up by AFm's are more strongly bound into their structure (i.e., reflecting structural incorporation), than binding by the C-S-H which represents weaker physisorption. Therefore, the Cl^- binding capacity of cementitious formulations is linked to the mass fraction of AFm phases present.[191] Even though the specific binding capacity of AFm phases is high, the total binding capacity of OPC-based formulations is limited, since AFm's comprise only 5 % to 15 % by mass of the solids in a hydrated OPC binder, offering only limited retardation of steel corrosion.[184,186–188] The Cl^- binding capacity of OPC-based binders can be increased by the addition of supplementary cementing materials (SCMs: e.g., ground-granulated blast-furnace slag,[192,193] fly ash[194]) which increases the Al_2O_3/SO_3 ratio of the mixture, leading to the enhanced formation of AFm's at the expense of Aft.[184,195,196] However, these effects are confounded with changes in the transport properties (e.g., permeability, and diffusivity) and the limited reaction of the SCMs that become relevant when OPC is replaced by SCMs at high levels.[188,195,197] As a result, while SCMs do indeed contribute reactive alumina that is required for AFm formation, they do so at a level that only slightly increases the mass of AFm's formed.

Several numerical models have been developed to describe mass transport of ions that influence the service life of reinforced concrete infrastructure.[186,187,198–203] These transport models vary in complexity from single-species models governed by Fick's laws of diffusion,[186,198] to multi-species Poisson-Nernst-Planck (PNP) models which account for electric coupling between ions due to their differing mobilities.[201,202] Other models may also consider the effect of advective transport due to moisture gradients (e.g., replicating the effects of wet-dry cycles)[204,205] and/or

reactions between ions and cementitious solids, which may be accounted for by mass-transport and chemical equilibrium calculations,[201,202,206] or by considering sorption isotherms.[186,187,198,207] A wide-range of models especially describe the role of Cl^- binding by cementitious phases on service life predictions.[186,187] Although quantitative prediction of the service lifetime of real structures is notoriously difficult, carefully formulated transport models can illustrate the role of enhanced Cl^- binding by cementitious compounds on delaying the onset of corrosion.

Calcium aluminate cement (CAC) mixtures, when suitably formulated, can exhibit a significantly higher Cl^- binding capacity as compared to those of OPC systems.[208] However, this approach has not been studied as a pathway to mitigate corrosion due to a lack of clarity as to how AFm formation can be increased in a controlled manner to scavenge/sequester Cl^- species. Recently, Falzone et al. suggested that NO_3-AFm dominant hydrated CAC mixtures (e.g., those containing up to 60 mass % AFm) could produce ACE benefits, by sequestering Cl^- ions while simultaneously releasing NO_3^- (or NO_2^-) species, i.e., an anodic corrosion inhibitor.[189] This *smart release* of NO_3^- and NO_2^- ions was first described by Balonis and Glasser.[184] Significantly, since volume changes accompanying NO_3^- to Cl^- exchange in the AFm's are minimal, no internal damage develops, e.g., due to deleterious shrinkage or expansion.[130] With this concept in mind, this study investigates the efficacy of CAC + $Ca(NO_3)_2$ based *top-layers* (i.e., formed by replacing a fractional thickness of the OPC concrete cover) that engender ACE as a means to delay corrosion. Besides corrosion delay, CAC-based binders are anecdotally expected to feature equivalent (or superior) durability to OPC systems as relevant to bridge deck applications (e.g., resistance to freeze-thaw damage,[121] and mechanical abrasion[122]), but are restricted to a top-layer due to their high cost ($\approx 5 \times$ that of OPC). The beneficial effects of Cl^- binding (i.e., reduced Cl^- abundance around the steel

reinforcement) and NO_3^- ion release are explained by considering thermodynamic and transport properties that are influential in the initiation and progression of corrosion. As such, this study explains how ACE is a robust pathway to delay corrosion degradation of infrastructure and thereby prolong service life.

4.2 Materials and methods

4.2.1 Materials

A commercially available calcium aluminate cement (Secar®51 produced by Kerneos Aluminate Technologies)[***] was used. The oxide composition of the CAC as determined by X-ray fluorescence (XRF) was (51.05 ± 0.20) % Al_2O_3, (38.94 ± 0.40) % CaO, (4.77 ± 0.40) % SiO_2, (2.23 ± 0.10) % Fe_2O_3, (2.02 ± 0.01) % TiO_2, (0.59 ± 0.10) % MgO, (0.11 ± 0.01) % P_2O_5, (0.31 ± 0.04) % K_2O and (0.07 ± 0.03) % Na_2O by mass.[209] Unless otherwise noted, the uncertainty represents one standard deviation. The mineralogy of the CAC as determined by X-ray diffraction and Rietveld refinement, was 73.3 ± 3.3 % CA, 18.1 ± 3.3 % C_2AS, 4.9 ± 2.0 % CT with minor phases in the form of 0.8 % CaO, 0.6 % C_2F, 1.5 % C_3FT and 0.8 % Fe_3O_4 by mass.[210]

CAC pastes were prepared at a fixed water-to-cement ratio (*w/c* = 0.45, mass basis) using de-ionized (DI) water, as described in ASTM C305.[99] Calcium nitrate ($Ca(NO_3)_2$, CN) was added to the CAC mixtures in dosages of 0 %, 10 %, and 30 % by mass of anhydrous CAC. The CN admixture was provided in the form of an aqueous solution (52 mass % CN in water). This admixture was first combined with additional water prior to mixing with the anhydrous CAC. CAC mortars were also prepared at the same CN dosages using ASTM C778[95] compliant graded quartz sand at volume fractions ϕ_q = 0.00, 0.25, and 0.50. To suppress the formation of metastable

[***] Certain commercial products are identified in this report to specify the materials used and procedures employed. In no case does such identification imply endorsement or recommendation by the University of California, Los Angeles or the National Institute of Standards and Technology, nor does it indicate that the products are necessarily the best available for the purpose.

hydrates,[121,126] the mixtures were cured under sealed conditions at 45 °C ± 0.2 °C for a period of 28 d. Reagent grade calcium chloride dihydrate ($CaCl_2 \cdot 2H_2O$, > 99 % purity) was added to Milli-Q water (i.e., 18 MΩ·cm deionized water) to prepare solutions at Cl^- concentrations of: 0.01, 0.05, 0.1, 0.3, 1, and 3 mol/L.

4.2.2 Methods

4.2.2.1 Thermodynamic calculations

To ascertain the phase assemblages of the CAC mixtures prepared in Section 4.2.1, thermodynamic calculations were carried out using the Gibbs Energy Minimization Software*** (GEMS-PSI), version 2.1.[138,139,211,212] Thermodynamic modeling was performed for systems containing CAC (Secar®51) for *w/c* = 0.45, and for the three CN dosages listed above.[189] The calculations were carried out at p = 101 kPa and T = 45 °C, with the solid and liquid phases being set to equilibrium with CO_2-free air. The predicted CAC phase assemblages represent mature CAC pastes in which the formation of metastable hydrates CAH_{10} and C_2AH_8 is suppressed.[126] The calculations account for the partial reaction of the anhydrous CAC, to obtain phase assemblages as a function of degree of CAC hydration. The thermodynamic properties of solid and aqueous species were sourced from the GEMS-PSI database, and amended with additional information sourced from the literature for CACs.[129–131,141–145] Falzone et al.[189] contains further details and a compilation of the thermodynamic properties of compounds relevant to the simulations. Qualitative agreement between GEMS-predicted and experimental phase assemblages for both

plain and CN-dosed CAC mixtures has already been established (i.e., via X-ray diffraction and thermogravimetric analysis) elsewhere.[189]

4.2.2.2 Cl^- binding isotherms

After 28 d of curing, to minimize transport hindrances on chloride binding, the hydrated CAC pastes were crushed to a fine powder, sieved ($d \leq 63$ μm, d is the particle diameter) and used in Cl^- binding experiments at 25 °C ± 3 °C. Cl^- binding isotherms of CAC pastes dosed with CN admixture (0 %, 10 %, and 30 % by mass) were quantified using the equilibrium method.[207] Triplicate powdered CAC pastes (m_{paste} = 30 g) were immersed in $CaCl_2$ solutions (V_{sol} = 0.1 L) prepared across a range of concentrations.[188] $CaCl_2$ was selected to minimize the potential for cation-dependent alterations to the hydrated phase assemblages, and to provide sufficient Ca^{2+} ions required for the formation of Friedel's salt from hydrogarnet (C_3AH_6).[190,213] Following immersion of CAC pastes in $CaCl_2$ solutions, the free Cl^- concentration ($C_{Cl,f}$) in solution was measured at 7 d time-intervals over a 21 d period. A multi-parameter benchtop meter (Orion VersaStar, ThermoScientific***) that was provided with a Cl^- selective electrode (ISE; 9617BNWP, ThermoScientific***) was used to measure $C_{Cl,f}$.

The ISE was calibrated using calibration solutions prepared using Milli-Q water + $CaCl_2{\cdot}2H_2O$ over the concentration range 0.001 mol/L $\leq C^0_{Cl,f} \leq$ 3 mol/L, at 25 °C ± 3 °C. To perform the binding measurements, ≈ 5 mL of solution was extracted, and filtered using a syringe fitted with a 0.2 μm filter to remove solids. The extracted solution was diluted in 100 mL Milli-Q water, and acidified using 0.3 mol/L HNO_3 to adjust the pH to a range of $3 \leq pH \leq 4$, as required to meet operational

specifications of the ISE. The pH was measured using a ThermoScientific Ross Ultra electrode*** calibrated using buffer solutions over the range $3 \leq pH \leq 13$ at 25 °C ± 3 °C. To minimize any ionic interferences on the concentration measurement, the solution was then dosed with a suitable amount of ionic strength adjuster (ISA; 2 mL ISA per 100 mL solution), following which $C_{Cl,f}$ was measured using a Cl^- specific ISE.

4.2.2.3 Static light scattering

Since solid surface area influences binding isotherms, the particle size distributions (PSDs) of the crushed CAC pastes were determined by static light scattering (SLS). An SLS particle analyzer (LS13-320, Beckman Coulter***) was used to assess the surface area, using isopropyl alcohol (IPA) as the carrier fluid. Prior to characterization, each powder was added to IPA and ultrasonicated to ensure its dispersion to primary particles. The complex refractive indices of the IPA and hydrated CAC pastes were taken as $n_{IPA} = 1.37 + 0.00i$,[214] and $n_{CAC} = 1.70 + 0.10i$,[96] respectively. The maximum uncertainty in the median diameter (d_{50}) was around 6 % based on 6 replicate measurements. The d_{50} of the powdered CAC pastes were nominally similar and on the order of 1.3 μm, 1.1 μm, and 2.5 μm for the 0 % CN, 10 % CN, and 30 % CN mixtures, respectively. The densities of these mixtures were estimated as 1700 kg/m^3, 1900 kg/m^3, and 2000 kg/m^3, respectively, based on the thermodynamic calculations. The specific surface areas of the powders was estimated as 150 m^2/kg, 250 m^2/kg, and 50 m^2/kg, respectively, assuming spherical particles.

4.2.2.4 Electrical impedance spectroscopy

Electrical impedance spectroscopy was used to assess ion-diffusion in hydrated CAC pastes and mortars based on measurements of their bulk resistance (R_b, ohms).[215] Custom conductivity cells were fabricated by modifying cylindrical polystyrene containers (diameter = 53.9 mm, height = 47.6 mm). Precision-ground 316 stainless steel rods (diameter = 3.18 mm ± 0.01 mm) served as parallel electrodes spanning the entire height of the container, at a center-to-center separation of 25.4 mm ± 0.5 mm. The geometry factor (k, m^{-1}) of each cell was determined by calibrating the measured conductivity to reference NaOH solutions in DI-water (0.1 % and 5 % by mass).

Hydrated CAC compositions dosed with 0 %, 10 %, 30 % by mass CN and containing different volume fractions of graded quartz sand (ϕ_q = 0.00, 0.25, 0.50) were cast into these cells, sealed, and cured for 28 d at 45 °C ± 0.2 °C; and their bulk electrical conductivity measured in duplicate. EIS spectra were obtained using a Solartron Analytical 1287 Electrochemical Interface*** with a 1252A Frequency Response Analyzer using an AC input signal of 100 mV. A frequency range of 10^{-1}-to-10^{5} Hz was sampled with 10 points recorded per decade.

The effective diffusion coefficient of an ionic species in a cementitious microstructure is related to its bulk conductivity (σ_{eff}; i.e., equivalent to inverse resistivity), and to the conductivity of the solution saturating its pores (σ_0) as described by the Nernst-Einstein relation[216]

$$D_i = D_i^{\inf} \frac{\sigma_{eff}}{\sigma_0} \quad \textbf{(4.1)}$$

where, D_i^{inf} is the diffusion coefficient of the i^{th} species at infinite dilution in water. This approach was used to account for transport hindrances on chloride (and on nitrate transport), as would be applicable to real concrete systems. As a significant quantity of pore solution from the hydrated CAC pastes[217] could not be obtained, the pore solution conductivity (σ_0) of CAC mixtures (without CN) was calculated based on the initial pore solution concentrations ($I_M \leq 30$ mmol/kg, see Table 1) obtained from GEMS using the Kohlrausch limiting law, with electrochemical activity corrections carried out using the extended Debye-Hückel relation.[218] The conductivity of the pore solutions of the 10 mass % CN and 30 mass % CN mixtures was estimated by performing EIS on solutions with CN dosage equivalent to their mixing water, as the conductivity is expected to be dominated by the abundant CN species.

4.3 Results

4.3.1 Thermodynamic calculations

Following on from Falzone et al.[189] (i.e., Chapter 3), Figure 4.1 shows calculated phase assemblages for CAC pastes (*w/c* = 0.45) containing different dosages of CN admixture (0-to-30 mass % CN). In the plain CAC paste (0 % CN, Figure 4.1a) C_3AH_6, C_2ASH_8, and $Al(OH)_3$ are noted as the predominant hydrated phases. These calculations consider a "mature" CAC paste, meaning that metastable hydrates that could be present at early ages (e.g., CAH_{10}, C_2AH_8) are not expected to exist as they convert, in time (i.e., at equilibrium), to C_3AH_6 and $Al(OH)_3$. When CAC is admixed with a sufficient dosage (30 mass % of CN), C_3AH_6 and C_2ASH_8 formation is entirely suppressed in favor of NO_3-AFm (see Figure 4.1c). At intermediate CN dosages (e.g., 10 % CN; Figure 4.1b), the phase assemblage demonstrates an intermediate composition, containing a mixture of NO_3-AFm, C_2ASH_8, and C_3AH_6. These systems are all expected to demonstrate substantial capacity for Cl^- binding, in proportion to their CN dosage. It should be noted that the systems evaluated are water-deficient, meaning that reaction would cease before all the anhydrous CAC is consumed. This is significant as any unhydrated CAC present, in relation to its content, during binding studies (see Section 4.3.2) will sequester Cl^- by the formation of Friedel's salt. Furthermore, the porosity of the CAC pastes is expected to decrease as the CN dosage increases, due to the larger molar volume of the AFm compounds in comparison to that of C_3AH_6.[189]

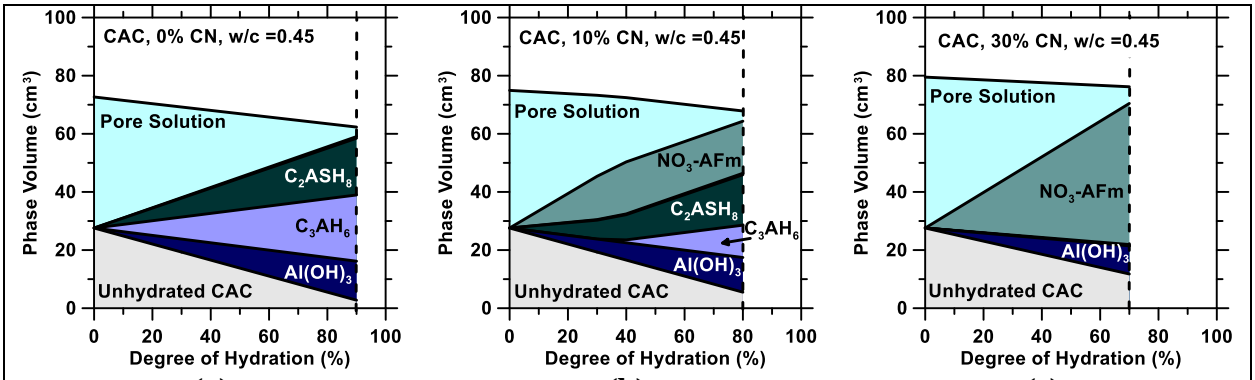

Figure 4.1: The hydrated phase assemblages calculated using GEMS for CAC systems for *w/c* = 0.45 containing: **(a)** 0 mass % CN, **(b)** 10 mass % CN, and **(c)** 30 mass % CN.[189] These calculations consider 100 g of anhydrous CAC reacting with 45 g of water/CN solution. The dashed vertical line shows the maximum simulated degree of hydration for each system. At a degree of hydration greater than this value, chemical reactions will cease due to limitations on water availability.

4.3.2 Cl^- binding isotherms

Figure 4.2 shows the free Cl^- concentration, $C_{Cl,f}$ as a function of time from 0 to 21 d. The solution concentrations are seen to stabilize by 21 d wherein the relative difference in Cl^- concentrations at 21 d and the previous measurement was ≤ 5 % (i.e., within the measurement resolution). Thus, the measured free Cl^- concentrations at 21 d were used to calculate the bound Cl^- content (i.e., expressed in terms of moles of Cl^- bound per kg of hydrated CAC paste) as

$$C_{Cl,b}^{eq} = \frac{(C_{Cl,f}^{0} - C_{Cl,f}^{21}) \cdot V_{sol}}{m_{paste}} \quad \textbf{(4.2)}$$

where, $C_{Cl,f}^{0}$ and $C_{Cl,f}^{21}$ represent the concentrations of free Cl^- in solution (in terms of mol Cl^- per L of solution) measured initially, and after 21 d of immersion (t near-equilibrium), respectively.

Figure 3 shows the equilibrium Cl^- binding isotherms for each hydrated CAC paste. The bound Cl^- content is substantially larger for CN-dosed CAC pastes for CN dosage levels ≥ 10 mass %. As expected, the isotherms are non-linear, and demonstrate a plateau in binding at higher Cl^- concentrations. The binding isotherms can be described by a Langmuir expression as[219]

$$C_{Cl,b}^{eq}(C_{Cl,f}) = \frac{\alpha \cdot C_{Cl,f}}{1 + \beta \cdot C_{Cl,f}} \qquad \textbf{(4.3)}$$

where, $C_{Cl,b}^{eq}$ is the equilibrium bound Cl^- concentration (mol Cl^-/ kg CAC paste), $C_{Cl,f}$ is the free Cl^- concentration in solution at equilibrium (mol Cl^-/L solution), and α (L solution/kg CAC paste) and β (L solution/mol Cl^-) are fitting parameters (see Table 4.2).[207,220] As a point of comparison, it should be noted that the Cl^- binding capacity of a typical "neat-OPC" system is approximately 25 % that of the "neat CAC" system shown in Figure 3; at a similar *w/c* and temperature.[193]

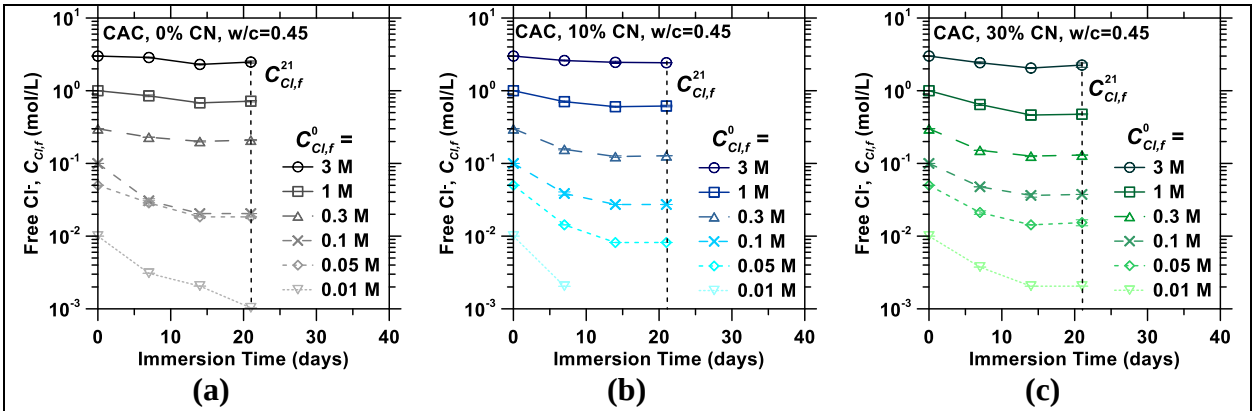

Figure 4.2: The free Cl^- concentration ($C_{Cl,f}$) in solution as a function of time for $CaCl_2 \cdot 2H_2O$ solutions in contact with hydrated CAC pastes containing: **(a)** 0 mass % CN, **(b)** 10 mass % CN, and **(c)** 30 mass % CN over the concentration range: 0.01 mol/L ≤ $C_{Cl,f}^0$ ≤ 3 mol/L. The coefficient of variation of the $C_{Cl,f}$ measurements was ≈ 5 %.

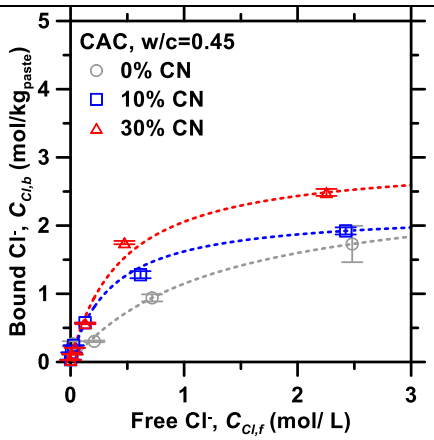

Figure 4.3: The measured Cl^- binding isotherms for the hydrated CAC pastes following 21 d of immersion in $CaCl_2 \cdot 2H_2O$ solutions. The error bars indicate ± one standard deviation in the experimental measurements, which were performed in triplicate.

To better explain the measured Cl^- binding isotherms, the phase assemblages calculated using GEMS were used to estimate the binding capacity of the CAC pastes. Assuming the destabilization of 1 unit of C_3AH_6 (i.e., which occurs at ≈ 0.01 mol Cl^-/L[190]) allows the incorporation of 2 units of Cl^- to form Friedel's salt ($C_3A \cdot CaCl_2 \cdot H_{10}$), C_3AH_6 features a Cl^- binding capacity of 5.36 mol Cl^-/kg C_3AH_6. This binding capacity is greater than that resulting from the uptake of Cl^- into NO_3-AFm (3.10 mol Cl^-/kg NO_3-AFm). This explains why the 0 mass % CN and 10 mass % CN mixtures show similar binding isotherms. But, increasing the CN dosage enhances Cl^- binding in spite of reducing the quantity of C_3AH_6 present by suppressing the formation of C_2ASH_8 (which is not expected to bind Cl^- ions) while enhancing the quantity of NO_3-AFm that is formed; wherein the latter shows significant Cl^- binding by ion exchange.

To discriminate the effects of Cl^- binding via ACE, which releases NO_3^- ions, and binding via C_3AH_6 destabilization (i.e., which does not result in NO_3^- release), the Cl^- binding capacity of each CAC formulation was calculated as the mass-average based on its thermodynamically modeled

phase assemblage, and while assuming complete conversion of C_3AH_6 to Friedel's salt. Figure 4.4 shows the calculated Cl^- binding contributions for each CAC paste overlaid onto its respective Cl^- binding isotherm. The majority of the Cl^- binding isotherm of each CAC paste is explained by its binding capacity calculated based on its predicted phase assemblage. The difference in the measured and calculated isotherms is thought to arise from discrepancies between the thermodynamically modeled phase assemblages and those of the "real" experimental system. However, seeing that this difference increases with CN dosage (i.e., or rather, the quantity of unreacted CAC present; see Figure 4.3), it is postulated that the difference dominantly results from the reaction between unreacted CAC with Cl^- in solution, and physisorption of Cl^- species onto the residual hydrated phases (e.g., C_2ASH_8). Assuming that C_3AH_6 converts to Cl-AFm before Cl-for-NO_3 exchange by the AFm initiates, the influence of ACE binding can be modeled by a multi-step function. This function equals zero below a critical concentration of free Cl^-, following which it traces the Cl^- binding isotherm. As confirmed by Puerta-Falla et al., Cl-for-NO_3 exchange is set to be equivalent (i.e., to ensure 1:1 monovalent ion exchange) to satisfy conditions of electroneutrality in solution.[221]

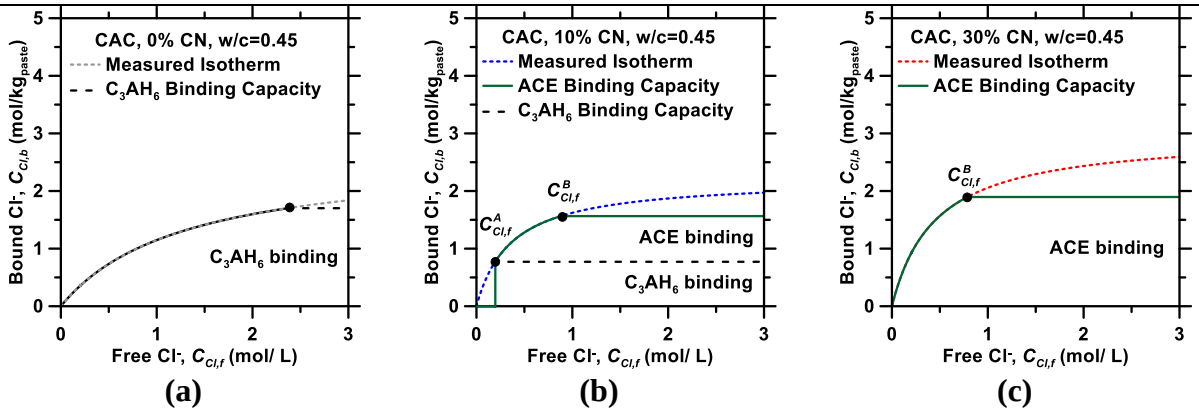

Figure 4.4: A representation of the different contributions to Cl^- binding which describe the uptake capacity of hydrated CAC pastes containing: **(a)** 0 mass % CN, **(b)** 10 mass % CN, and **(c)** 30 mass % CN.

4.3.3 Electrical impedance spectroscopy

The EIS response (i.e., a Nyquist plot) of a representative CAC mortar (ϕ_q = 0.50) for different CN dosages is shown in Figure 4.5(a). The bulk resistance was quantified as the real component of impedance (Z') at which the imaginary impedance (Z'') displayed a minimum. The bulk electrical conductivity (σ_{eff}, S/m) of the hydrated specimens was calculated as (see Section 4.2.2.4)

$$\sigma_{eff} = k/R_b \quad \textbf{(4.4)}$$

Figure 4.5(b) shows the effective conductivity of CAC mortars as a function of quartz sand volume fraction. At a given quartz volume fraction, the effective conductivity decreases as the CN dosage increases from 0 mass % to 10 mass % CN, and then increases dramatically at the 30 mass % CN dosage. This conductivity minimum is thought to be produced on account of alterations in pore structure/connectivity due to the changes in phase assemblages, although this aspect requires further study. In each case, the bulk conductivity decreases as the volume fraction of quartz sand increases. This is due to dilution of the porous CAC paste matrix, and the reduction in its connectivity (i.e., an increase in tortuosity) due to the presence of non-porous (sand) inclusions.[222,223] This trend is opposite to that observed in OPC mortars, in which ionic diffusivity increases when aggregates are present due to the percolation of the porous interfacial transition zones (ITZ) between the aggregates.[222,223] The values of D_i^{inf} for ions pertinent to seawater are listed in Table 4.1. The calculated values of σ_0 and the factor σ_{eff}/σ_0 for each cementitious composition are given in Table 4.2. As a point of reference it should be noted that the CAC mortars feature ionic diffusion coefficients that are equivalent to, or approximately one order of magnitude less than that of a typical OPC concrete.[224]

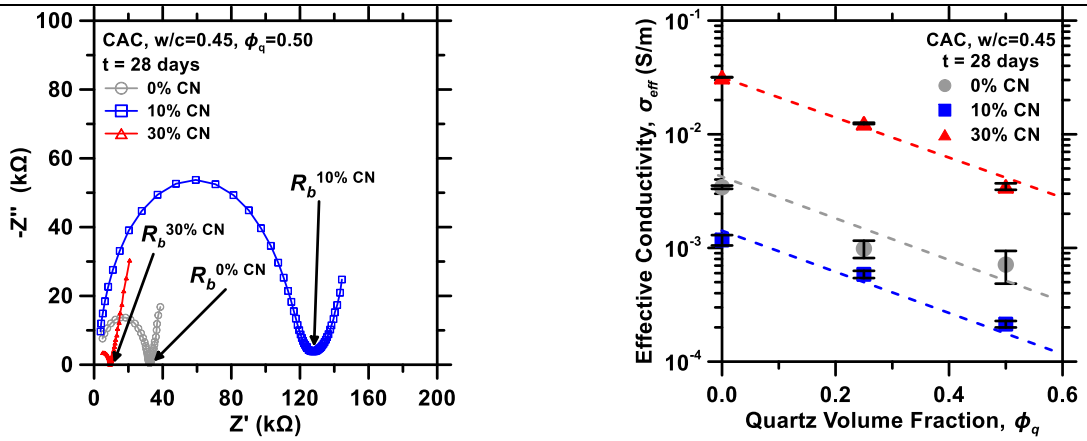

Figure 4.5: (a) A Nyquist plot obtained from EIS measurements depicting the bulk resistance (R_b, kΩ) of the hydrated CAC + CN mixtures (ϕ_q =0.50). **(b)** The effective conductivity of hydrated CAC + CN mixtures as a function of the quartz dosage. The data points represent the average of two replicates, with error bars indicating the upper and lower values.

4.4 Formulation of multispecies reaction-transport model

4.4.1 Schematic and assumptions

To elucidate the benefits of ACE, a simplified concrete bridge-deck geometry (also representative of a pier with one-face exposed to seawater) was developed. This 1D-domain of a pristine (i.e., uncracked) concrete section is shown in Figure 4.6. The concrete section has a thickness of L = 0.2 m, a fraction of which comprises a CAC-based top-layer of thickness x_c = 0.025 m. The depth of the reinforcing steel from the upper surface (i.e., the cover depth) is assumed to be x_r = 0.050 m. To describe ion transport, the following assumptions were made:

- The porosity of the concrete and the CAC-based top-layers is saturated with pore solution,
- Advective transport of ions is negligible as a zero pressure gradient is assumed in the pores, hence the pore solution velocity (and Péclet number) is zero, assuming no moisture transport is induced by cyclic wetting-and-drying,[204,225]
- The effects of ion-activity (i.e., non-ideality of the solution) on transport are not accounted for since this factor exerts second order contributions to the transport response.[226,227] But, ideally, the model should consider activities, rather than concentrations of ionic species,
- The effects of electrical coupling between ions is significant enough to warrant multispecies modeling,[203,228] and,
- The electrical double layer present on the hydrated solids does not affect transport,[229] since ion transport takes place dominantly through larger capillary pores which remain percolated, rather than through the nanoscale gel pores, e.g., as present in the C-S-H.[216]

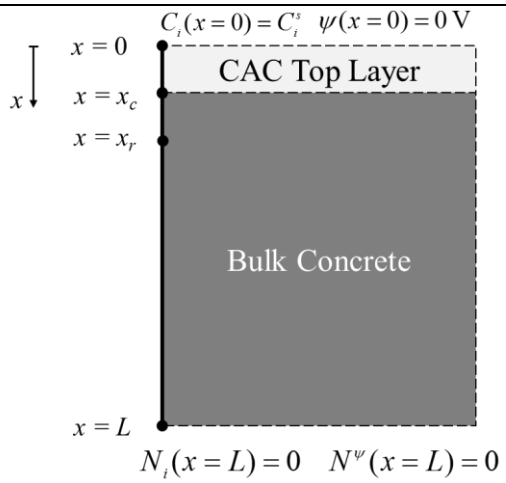

Figure 4.6: A schematic of the simulated concrete bridge-deck section subject to Cl^- ingress at (x = 0) that features a CAC-based top-layer of thickness x_c.

4.4.2 Governing equations

For the assumptions noted above, the concentrations of multiple ionic species in solution as a function of space (x) and time (t) can be described by the Nernst-Planck (NP) equation

$$\frac{\partial C_{i,f}}{\partial t}+\frac{\partial}{\partial x}\cdot\left(-D_i\frac{\partial C_{i,f}}{\partial x}-z_i\frac{D_i}{RT}FC_{i,f}\cdot\frac{\partial \psi}{\partial x}\right)=\upsilon_i \qquad \textbf{(4.5)}$$

where, $C_{i,f}$ is the free concentration of the i^{th} species within the pore solution (mol/L), D_i is the diffusion coefficient of the i^{th} ionic species within the relevant cementitious matrix (m^2/s), z_i is the valence of the i^{th} species, R is the universal gas constant (8.314 J/mol·K), T is the temperature (K), F is Faraday's constant (96484.56 C/mol), ψ is the electric potential (V), and v_i is the reaction rate of the i^{th} species (mol/(L· s)). It should be noted that compared to a Fickian approach (e.g., considering the diffusion of Cl^- and NO_3^- species excluding electrical coupling), the NP equation

predicts a slower rate of Cl^- ingress. This is because the presence of cations (with lower diffusion coefficients) in the pore solution hinders Cl^- transport due to the need to ensure electroneutrality in solution. The NP equation is governed by the ionic concentrations of *n-1* species, where *n* is the total number of ionic species considered. The concentration of the final (n^{th}) species is governed by the electroneutrality assumption (i.e., zero charge density) which is a simplification of the Poisson equation[230]

$$\sum_i z_i C_{i,f} = 0 \qquad \textbf{(4.6)}$$

The reaction rate (v_i) in Equation (4.5) for all species except Cl^- and NO_3^- was assumed to be zero (i.e., no reaction between species). The reaction rates corresponding to the Cl^- and NO_3^- species are expressed by the following first order reactions

$$\upsilon_{Cl} = k_{Cl}\left(C_{Cl,b} - C_{Cl,b}^{eq}(C_{Cl,f})\right) \qquad \textbf{(4.7)}$$

$$\upsilon_{NO_3} = -k_{Cl}\left(C_{NO_3}^{\max} - C_{NO_3}^{eq}(C_{Cl,f})\right) \qquad \textbf{(4.8)}$$

where, k_{Cl} is the reaction rate constant of Cl-for-NO_3 ion exchange (s^{-1}), and $C_{NO_3}^{\max}$ is the maximum NO_3^- concentration predicted in the pore solution upon exhaustion of the system's ACE capacity. Since Cl^- for NO_3^- exchange in AFm is stoichiometric (i.e., 1 mol Cl^- replaces 1 mol NO_3^-), the molar fluxes of these species are equal and opposite when ACE is the means of Cl^- binding.[221] The

Cl^- binding isotherm $C_{Cl,b}^{eq}(C_{Cl,f})$ for any cementitious formulation is given by the Langmuir isotherm parameters noted in Figure 4.3, scaled to the appropriate units by the paste content and porosity given in Table 4.2. The binding response, i.e., including the effects of C_3AH_6 conversion, Cl^--for-NO_3^- exchange and the hydration of residual CAC, if any, is given by a piecewise function written as

$$C_{NO_3}^{eq}(C_{Cl,f}) = \begin{cases} 0, & 0 \text{ mol/L} \le C_{Cl,f} \le C_{Cl,f}^{A} \\ \dfrac{\alpha \cdot C_{Cl,f}}{1+\beta \cdot C_{Cl,f}}, & C_{Cl,f}^{A} \le C_{Cl,f} \le C_{Cl,f}^{B} \\ C_{NO_3}^{\max}, & C_{Cl,f}^{B} \le C_{Cl,f} \end{cases} \quad \textbf{(4.9)}$$

where, $C_{Cl,f}^{A}$ and $C_{Cl,f}^{B}$ are the free Cl^- concentrations at which binding by ACE begins, and ends, respectively. Cl^- binding was modeled as a first-order reaction, in which the driving force is given simply by the difference between the currently bound Cl^- content, and the equilibrium bound Cl^- content predicted by the relevant (mixture dependent) binding isotherm shown in Figure 4.3. Thus, the following equation was solved for $C_{Cl,b}$

$$\frac{dC_{Cl,b}}{dt} = k_{Cl}\left(C_{Cl,b} - C_{Cl,b}^{eq}(C_{Cl,f})\right) \quad \textbf{(4.10)}$$

4.4.3 Initial and boundary conditions

The concentrations of ions at the exposed surface (i.e., $x = 0$) was set to conform with those of seawater;[231] as noted in Table 4.1. Table 4.1 also details the concentrations of ions in the pore

solution of the OPC and CAC formulations. The compositions of pore solutions were estimated by thermodynamic calculations (for the CAC formulations) or sourced from the literature (for the OPC system). As expected, the CN-dosed CAC systems show large concentrations of NO_3^- species in their pore solutions, and a pH (OH^- abundance) that is lower than an OPC-concrete system.[2]

Assuming ions cannot escape the bottom of the bridge-deck (e.g., due to the presence of stay-in-place metal forms), a zero-flux boundary condition is imposed at $x = L$

$$N_i(x = L) = -\left(D_i \frac{\partial C_i}{\partial x} - z_i \frac{D_i}{RT} F C_i \cdot \frac{\partial \psi}{\partial x} \right) = 0 \qquad \textbf{(4.11a)}$$

where, N is the flux of the i^{th} ionic species (mol/m^2·s). Additionally, this lack of "ion escape" also implies electrical insulation (i.e., zero current) at the same boundary

$$N^{\psi}(x = L) = F \sum_i z_i \left(- D_i \frac{\partial C_i}{\partial x} - z_i \frac{D_i}{RT} F C_i \cdot \frac{\partial \psi}{\partial x} \right) = 0 \qquad \textbf{(4.11b)}$$

where, N^{ψ} *i*s the electrical current density (A/m^2). The potential at the exposed surface of the concrete bridge deck was assumed to be zero, i.e., grounded

$$\psi(x = 0) = 0 \text{ V} \qquad \textbf{(4.12)}$$

A perfect bond was assumed between the CAC top-layer and the bulk OPC concrete, and no buildup of electric charge was assumed at the interface. Therefore, ionic flux and electric current density were assumed to be continuous across the interface ($x = L_c$).

Table 4.1: The ion-dependent diffusion coefficients at infinite dilution (D_i^{inf}) at $T = 25$ °C,[232] the boundary conditions (i.e., concentrations of each ionic species at the exposed surface; $x = 0$ m, with C_i^s corresponding to seawater[231]), and the initial conditions of the simulations (i.e., the concentrations of ions within the pore solution of each cementitious matrix).

Ionic Species	D_i^{inf} (10^{-9} m^2/s)	C_i^s (mmol/L)	$C_i^{0\%\ CN}$ (mmol/L)	$C_i^{10\%\ CN}$ (mmol/L)	$C_i^{30\%\ CN}$ (mmol/L)	$C_i^{OPC\ *}$ (mmol/L)
Na^+	1.33	480	0	0	0	140
K^+	1.96	10	0	0	0	210
Ca^{2+}	0.793	10	23.1	23.2	57.1	0
Mg^{2+}	0.705	53	0	0	0	0
$Al(OH)_4^-$	1.04	0	20.0	20.0	20.0	0
OH^-	5.27	0.0013	26.1	24.5	7.8	330
Cl^-	2.03	560	0	0	0	0
NO_3^-	1.90	0	0	1.9	86.3	0
SO_4^{2-}	1.07	29	0	0	0	10

(*) Aguayo et al. **233**

Table 4.2: The material-specific input parameters representing: Cl^- binding, formation factor (i.e., which dictates ion diffusion rates within a constrained microstructure), and the mixture compositions (i.e., the porosity and paste content of the CAC mortars and OPC concrete).

Material	α (L/ kg_{paste})	β (L / mol Cl^-)	Binding rate constant, k_{Cl} (s^{-1})	σ_{eff} / σ_0	Porosity (ϕ_p)	Paste content (kg / m^3 concrete)
CAC + 0% CN	0.00204	0.00077	1×10^{-7}	1.14×10^{-3}	0.14	870
CAC + 10% CN	0.00608	0.00275	1×10^{-7}	3.50×10^{-4}	0.09	970
CAC + 30% CN	0.00661	0.00222	1×10^{-7}	3.68×10^{-3}	0.06	1020
OPC Concrete	0.00352*	0.00416*	1×10^{-7}	4.0×10^{-3} †	0.11‡	920

(*) Dhir et al.,**193** (†) Bentz et al.,**224** (‡) Birdsall et al.**234**

Table 4.2 displays additional material-specific parameters used in the simulations. These include the Langmuir isotherm parameters and reaction rate constants, the factor σ_{eff}/σ_0, porosity and paste content. The maximum uncertainties in α and β were ± 0.0005, and ± 0.0001, respectively. The porosity of each CAC composition was calculated – from its volumetric phase assemblage at a

degree of reaction of 70 % – as the fractional volume of the liquid phase present in the system.[235] Although the binding rate constant of Cl^- for NO_3^- exchange in AFm's has been measured to be on the order of $[1.0 \pm 0.2] \times 10^{-5}$ s^{-1}, to improve numerical convergence, the rate constant was estimated as 1×10^{-7} s^{-1} across all mixture compositions.[221] This reduction however, does not significantly influence the results, as the process remains diffusion-limited (i.e., with Damköhler number $\gg 1$) and binding can be approximated as instantaneous. Indeed, over simulated time scales of 1-to-100 years, the simulated Cl^- and NO_3^- concentrations vary by < 1 % at any *x* as the binding rate constant is increased (not shown).

4.4.4 Method of solution

The governing equations (Equations 4.5 to 4.10) were solved using the specific initial and boundary conditions (Equations 4.11 and 4.12 and Table 4.1) within COMSOL Multiphysics 4.3,[***] a commercial finite element solver, using the "Chemical Reaction Engineering Module". Numerical convergence was considered to be reached when the highest relative difference in Cl^- concentration profiles was ± 1 %, when reducing the element size or time step by a factor of 2. In practice, converged solutions were obtained by imposing a maximum time step of 1×10^5 s, while using the adaptive time-stepping algorithm built-in to COMSOL and a fixed element size of 5×10^{-4} m.

4.5 Results of finite element simulations

4.5.1 Cl^- transport from seawater

The first set of simulations considered surface exposure of an OPC bridge-deck to seawater, the concentration and volume of which remain fixed. Figure 4.7(a) shows simulated Cl^- concentration profiles within a neat-OPC concrete as a function of distance, x, from the exposed surface. As expected, Cl^- concentrations rise dramatically through the depth of the concrete over time. The corresponding Cl^-/OH^- ratio at various depths in the cover-zone typical for bridge-decks is shown in Figure 4.7(b). It is seen that Cl^-/OH^- ratios exceed 0.6 within 30 years; i.e., which would assure corrosion initiation and its progression. Conservatively, the service life of the bridge-deck is defined by the time interval prior to corrosion initiation (t_{init}); i.e., the period in which $Cl^-/OH^- \leq 0.6$. For an OPC cover depth $x_r = 0.050$ m, that is typical for bridge decks, corrosion is expected to initiate for $t_{init} = 6.4$ years. Obviously, increasing the cover depth above steel reinforcement (x_r) to 0.075 m or 0.100 m delays t_{init} to 14.6 years or 25.5 years, respectively. Figure 4.7(c) displays t_{init} as a function of x_r within an OPC concrete bridge-deck. The influence of Cl^- binding within the OPC concrete is significant, as a result of which t_{init} approximately doubles for $x_r \geq 0.025$ m. While increasing the cover depth does delay the onset of corrosion, this is often considered as an inefficient and cost-prohibitive mitigation approach.

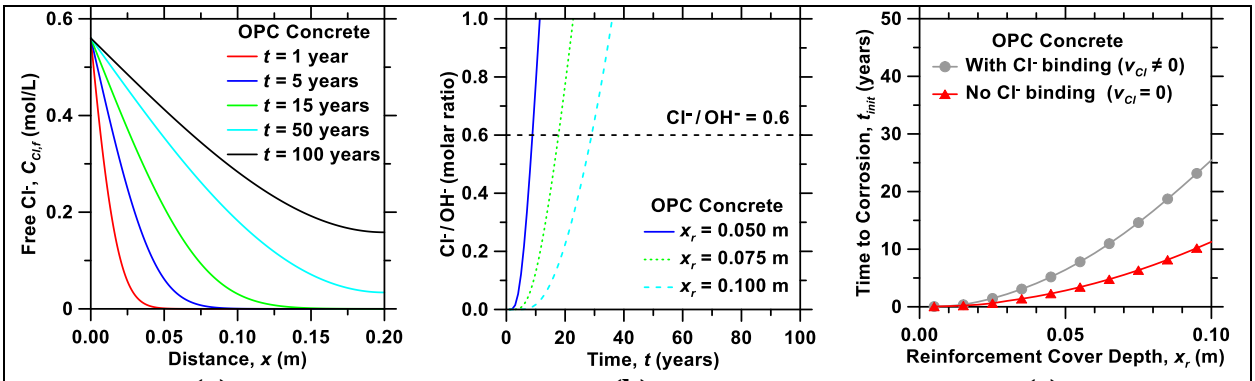

Figure 4.7: (a) The simulated Cl^- concentration profiles within the OPC concrete, and, **(b)** The Cl^-/OH^- ratio within an OPC concrete as a function of time for different cover depths. The dashed line indicates the critical Cl^-/OH^- ratio at which steel corrosion initiates. **(c)** The calculated time to corrosion initiation (t_{init}) as a function of the reinforcement cover depth x_r.

Second, a scenario was simulated wherein the top 0.025 m of OPC concrete was replaced with a plain CAC mortar top-layer. Figure 4.8(a) displays Cl^- concentration profiles for such a bridge-deck, wherein the mortar (CAC + 0 % CN) contains a quartz inclusion volume fraction, $\phi_q = 0.50$. In this case, the combined effects of lower ionic diffusivity (≈ ¼ that of OPC concrete) and enhanced Cl^- binding of the CAC top-layer retard Cl^- ingress relative to the OPC concrete (i.e., by increasing t_{init} from 6.4 years to 28.5 years). To highlight these effects on t_{init}, detailed simulations were carried out while assuming: (i) the Cl^- binding capacity of the CAC paste to be similar to the OPC system ($Bind_{top} = Bind_{bulk}$), and, (ii) the ion-diffusivity of the CAC mortar is equivalent to that of the OPC concrete ($D_{top} = D_{bulk}$). The resulting Cl^-/OH^- ratios are displayed in Figure 4.8(b) for a fixed cover depth, $x_r = 0.050$ m. The reduced ionic diffusivity of the CAC mortar is identified as the primary cause of an increased time to corrosion initiation, as $t_{init} = 18.4$ years solely on the account of retarded ion diffusion (case i, $Bind_{top} = Bind_{bulk}$), while $t_{init} = 9.1$ years when only an increase in Cl^- binding capacity is considered (case ii, $D_{top} = D_{bulk}$). Nevertheless, the effects of enhanced Cl^- binding are significant. When the effects of enhanced binding are negated (i.e., by

setting $Bind_{top} = Bind_{bulk}$), Cl^- concentrations in solution are greater as compared to when enhanced binding and reduced diffusivity function in tandem. This clearly indicates the potential benefits of enhanced Cl^- binding in increasing service life.

To further compare the efficacy of CAC top-layers in corrosion mitigation, a corrosion delay factor (d_f) was defined as $d_f = t_{init}$(CAC)/t_{init}(OPC concrete). Figure 4.8(c) displays the corrosion delay factor as a function of the reinforcement cover depth in the 0 % CN CAC case. In each case, the corrosion delay factor shows a maximum for $0.01 \text{ m} \leq x_r \leq 0.03$ m, illustrating an optimal efficacy of the CAC top-layer thickness relative to the depth of reinforcing steel. Maximum delay factors range from 2.9 to 13.9, depending on the parameters imposed. It should be noted that the t_{init} values presented herein represent a "worst-case scenario", as the present modeling approach induced a more rapid reduction in pore solution pH than would be expected in a (real) system, which offers a pH buffer ensured by the presence of the solid hydrates. The effect of solid pH buffering on service life predictions was examined by constructing a "best-case" scenario, wherein the OH^- concentration remains fixed due to progressive solid hydrate dissolution as seawater intrusion occurs. It was found that maintaining a fixed OH^- concentration does indeed significantly (and artificially) extend the predicted service lifetime from $t_{init} \approx 6.5$ years (worst-case) to $t_{init} \approx 13.5$ years (best-case). However, the corrosion delay factor is very weakly influenced by considering pH buffering (e.g., for CAC + 0% CN, $d_f = 4.5$ (worst-case) versus 4.7 (best-case)). Additionally, it should be noted that these outcomes are broadly independent of the (assumed) critical Cl^-/OH^- ratio at which corrosion initiates, as the critical Cl^-/OH^- ratio influences the magnitude of t_{init}, but only weakly affects d_f. Therefore, despite the limitations of the simulation approach (i.e., lack of consideration of a solid-buffer, and assuming a single value for the critical Cl^-/OH^- ratio), since

the simulation predictions are conservative and self-consistent, they offer a suitable means to highlight the beneficial effects of Cl^- binding and NO_3^- release on delaying corrosion processes.

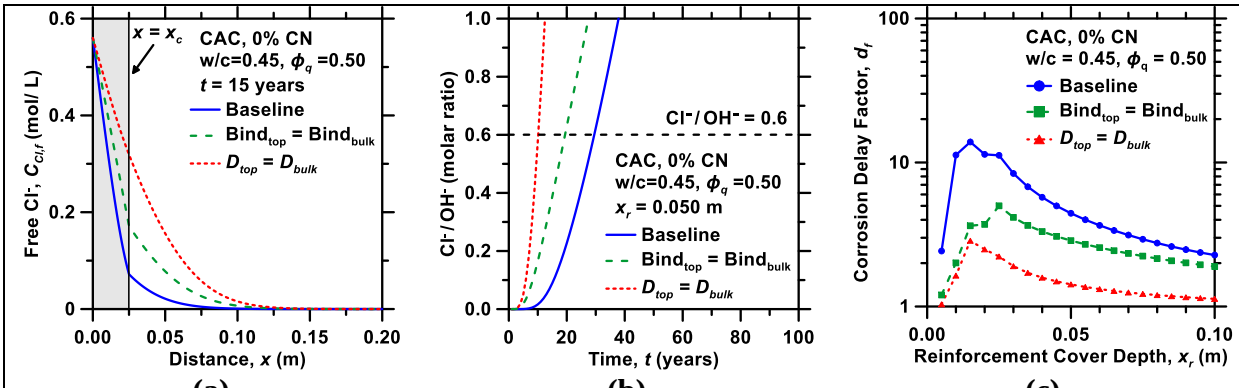

Figure 4.8: (a) The simulated Cl^- concentration profiles within an OPC concrete topped with a 0 mass % CN CAC top-layer (ϕ_q = 0.50, x_c=0.025 m) after 15 years of exposure to seawater. The dashed lines show scenarios wherein a Cl^- binding isotherm equal to that of the OPC paste was assumed in the CAC top-layer ($Bind_{top}$ = $Bind_{bulk}$), or, wherein the CAC top-layer and the OPC concrete are assumed to have similar ionic diffusivities (D_{top} = D_{bulk}). **(b)** The Cl^-/OH^- ratio as a function of time at a cover depth x_r = 0.050 m. The horizontal dashed line in **(b)** indicates the critical Cl^-/OH^- ratio when steel corrosion initiates. **(c)** The corrosion delay factor (d_f) produced by replacement of the OPC concrete with a 0 mass % CN CAC top-layer, as a function of reinforcement cover depth x_r.

The effects of CN additions to CACs were also investigated. Figure 4.9(a) shows calculated Cl^- /OH- ratios at x_r = 0.050 m when an OPC-concrete is topped with a CAC top-layer dosed with 30 mass % CN. The coupled effects of (very slightly) reduced ion-diffusion and substantially enhanced Cl^- binding dramatically hinders Cl^- transport in comparison to OPC concrete. In fact, the 30 % CN composition shows a greater delay efficacy than the 0 % CN composition, despite the fact that its ionic diffusivity is 3x higher. This indicates that the benefits of amplified Cl^- binding capacity of the 30 % CN system far outweighs its increased diffusivity. Unlike the 0 mass % CN case, in which the ion-diffusivity reduction plays a prominent role, enhanced Cl^- capture and the associated NO_3^- exchange are observed to be the dominant mechanisms of corrosion delay.

Due to the similarity of the diffusivity within the CAC mortar and OPC concrete, when Cl^- binding within the CAC top-layer is equated to that of OPC (Figure 4.9a, $Bind_{top} = Bind_{bulk}$); Cl^- ingress is only slightly reduced, resulting in a predicted time to corrosion of t_{init} = 8.9 years at a cover depth x_r = 0.050 m (i.e., when $Cl^-/OH^- \leq 0.60$). However, due to the high initial NO_3^- concentration in the pore solution, and NO_3^- exchange enabled by the NO_3-AFm, the time to corrosion is expected to be extended.

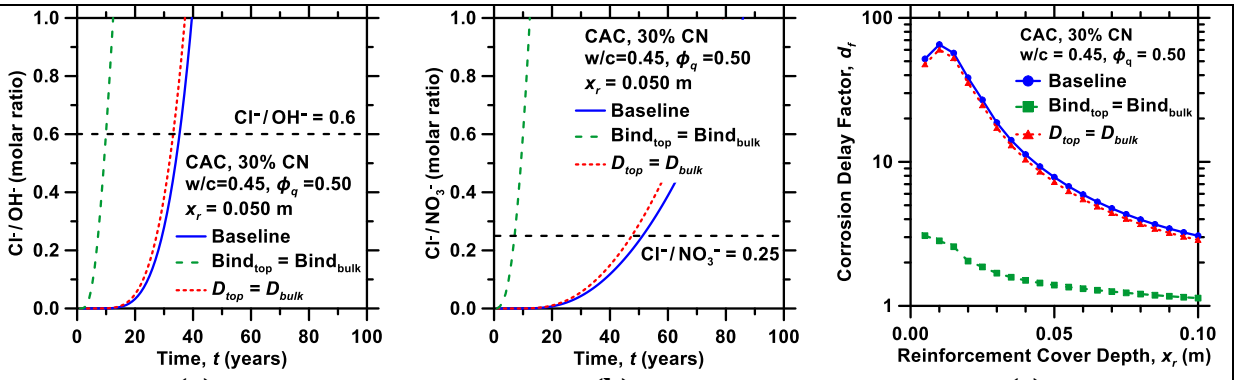

Figure 4.9: (a) The Cl^-/OH^- ratio, and, **(b)** The Cl^-/NO_3^- ratio within OPC concrete topped with a 30 mass % CN CAC top-layer (ϕ_q = 0.50, x_c=0.025 m) as a function of time for a cover depth x_r = 0.050 m. The horizontal dashed lines in **(a)** and **(b)** indicate the critical Cl^-/OH^- and Cl^-/NO_3^- ratios for the initiation of steel corrosion or inability for the re-passivation of steel by NO_3^-. **(c)** The corrosion delay factor (d_f) produced by replacing OPC concrete with a 30 mass % CN CAC top-layer, as a function of reinforcement cover depth x_r.

For clarity, Figure 4.9(b) displays the relevant Cl^-/NO_3^- ratios as a function of time. When both ionic diffusivity and binding effects are considered, the presence of NO_3^- in the pore solution extends t_{init} to 50.2 years (i.e., when $Cl^-/NO_3^- \geq 0.25$). But, when Cl^- binding is equivalent to the OPC system (i.e., $Bind_{top} = Bind_{bulk}$), Cl^-/NO_3^- quickly exceeds the critical passivation ratio resulting in corrosion initiation. In this case, the presence of NO_3^- does not improve service life, as the time period when $Cl^-/NO_3^- \leq 0.25$ is less than that at which $Cl^-/OH^- \leq 0.6$. These findings

are supported by the significant increase in the corrosion delay factor (d_f, e.g., see Figure 4.9c) which exceeds 65 due to the combined effects of reduced diffusivity and enhanced ACE, as compared to only 3 when the effects of enhanced ACE are neglected.

4.5.2 Parametric study

To deconvolute the effects of enhanced Cl^- binding, reduced ionic diffusivity, and of NO_3^- release (i.e., simultaneous anion capture and exchange) on the time to corrosion initiation, a parametric study was carried out. The simulations considered CAC top-layers with 0 %, 10 %, and 30 % by mass CN, with binding isotherms corresponding to Figure 3; but with an ionic diffusivity equal to that of the OPC concrete. Figure 4.10(a) displays the corrosion delay factor (d_f) that is predicted for these conditions as a function of the fraction of cover depth composed of CAC (x_c/x_r); for a cover depth x_r = 0.050 m. To set the performance of the baseline scenario, the time to steel corrosion initiation for the OPC concrete system is determined to be 6.4 years.

For all CAC compositions, increasing the CAC layer thickness increases the time to steel corrosion initiation, resulting in corrosion delay factors > 1. For example, when 0.050 m of OPC cover is replaced by a 0 mass % CN CAC mortar top-layer, the time to corrosion initiation doubles. As the CN dosage increases, the provision of CAC top-layers increasingly extends the time to steel corrosion initiation. This is largely due to the release of the NO_3^- ions via ACE ensuring that the $Cl^-/NO_3^- \leq 0.25$. To carefully illustrate the benefits of NO_3^- release in the CAC + 10 mass % CN top-layer, the NO_3^- reaction rate (i.e., v_{NO3}, Equation 4.8) was set to zero. In this case, due to the insufficient concentration of free NO_3^- in the pore solution, the service life predicted by the Cl^-

/OH^- ratio exceeds that predicted by the critical Cl^-/NO_3^- ratio. However, due to enhanced Cl^- binding, the time to achieve the critical Cl^-/OH^- ratio (Figure 4.10) is significantly extended relative to the OPC concrete. Despite the similarity between their Cl^- binding isotherms, the CAC + 10 mass % CN top-layer demonstrates larger delay factors than the 0 mass % CN CAC mortar top-layer. This can be attributed to the lower porosity and the higher solid content in the CAC + 10 mass % CN system, which increases the amount of CAC paste available for Cl^- capture from the pore solution (Figure 4.1). While the effects of enhanced Cl^- capture in this system are substantial, the corrosion delay factor is only one-half of that when ACE (NO_3^- release) is considered.

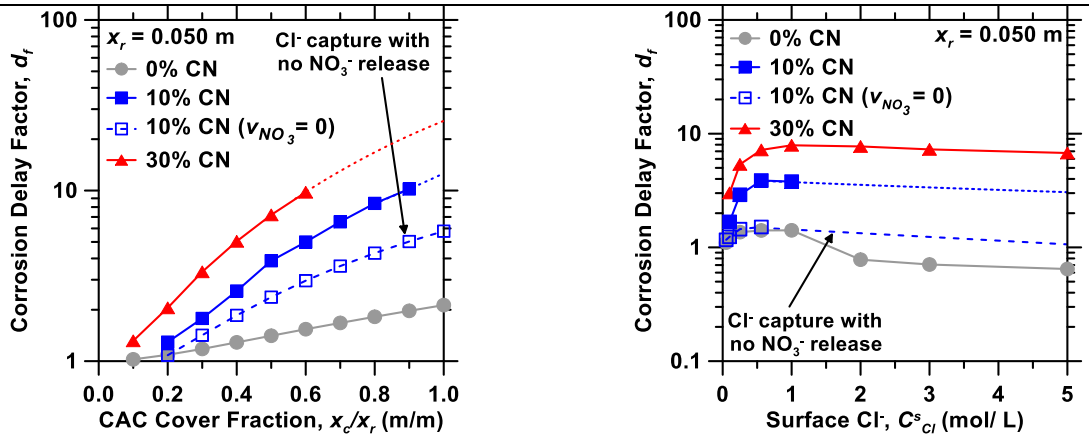

Figure 4.10: The corrosion delay factor relative to OPC concrete as a function of: **(a)** The fractional thickness of the CAC top-layer (x_c/x_r), and **(b)** The surface Cl^- concentration (C^S_{Cl}), for a reinforcement cover depth x_r = 0.050 m.

To examine the benefits of ACE over a wider range of surface Cl^- concentrations, i.e., beyond just seawater exposure, a broader set of simulations were carried out. Here, electroneutrality in the solution at the surface was maintained by modifying the Na^+ concentration concurrently with that of Cl^- (i.e., assuming NaCl as the Cl^- source) – and the thickness of the CAC top-layer was fixed

at 0.025 m, while the total cover depth was 0.050 m. Once again, the effects of Cl^- binding and NO_3^- release were separated from that of ion-transport (i.e., diffusion) by setting the diffusion coefficient of the CAC layers equivalent to that of the bulk OPC concrete. The resulting corrosion delay factor is shown as a function of the surface Cl^- concentration (C^S_{Cl}); from 0.1 mol/L to 5 mol/L (Figure 4.10b). These concentrations span conditions from seawater, to exposure to deicing salts, or standing seawater that is concentrated by evaporation. When surface Cl^- concentrations rise beyond a limiting concentration, steel corrosion initiates very rapidly independent of the cover layer composition. In the 0 mass % CN CAC mortar, the corrosion delay factor diminishes to <1 at large surface Cl^- concentrations indicating performance inferior to the OPC concrete. This is due to the reduced OH^- concentration within the CAC pore solution and the high exterior Cl^- concentration overwhelming the binding capacity of the system.

Similarly, CN-dosed systems demonstrate a maximum corrosion delay factor for Cl^- concentration on the order of 0.5-to-1 mol/L, with a slight decrease as C^S_{Cl} is increased. However, even at 5 mol Cl^-/L, representative of exposure to concentrated seawater,[236,237] the 30 % CN CAC layer delays corrosion by 6.7 times relative to OPC concrete. In this case, NO_3^- release due to ACE is revealed to be the critical parameter in delaying corrosion. When NO_3^- release is not considered in the 10 mass % CN CAC top-layer, the corrosion delay factor is halved, thus approaching that of the OPC concrete at high Cl^- concentrations. This suggests that the provision of coatings capable of ACE is an efficient approach to – under suitable exposure conditions – more than double the service life of concrete infrastructure. It should be noted, however, that the conclusions of this study are applicable to uncracked concrete, or concrete in which a surface penetrating crack does not intersect or approach the steel reinforcement. However, due to the rapid kinetics of Cl^- uptake in

CAC systems,[221] ACE binding is expected to exert beneficial effects even when the cover is cracked. Depending on the Cl^- exposure conditions, the ACE capacity of the CAC mortar top-layers is estimated to reach saturation within 10 years to 20 years. However, “mill-and-fill” operations could be used to periodically replace these layers, re-enhancing the ACE capacity of such top-layers. These outcomes suggest new routes to mitigate steel corrosion in concrete infrastructure.

4.6 Summary and conclusions

Cl^--induced corrosion of steel embedded in reinforced concrete is a major cause of premature degradation of concrete infrastructure. AFm phases present in cementitious systems are able to sequester and release anions in relation to their thermodynamic preference for interlayer site occupation.[131,189] This bestows AFm compounds with an ability for anion capture and exchange (ACE); a novel route to mitigate Cl^- penetration and resulting corrosion. Indeed, CAC formulations dosed with CN are shown to be capable of sequestering Cl^- species, while releasing corrosion inhibiting NO_3^- species.[184] Precise input data of Cl^- binding and NO_3^- exchange, and ion-diffusion rates are input into a multi-species Nernst-Planck model to quantitatively describe the evolutions of Cl^-/OH^- and Cl^-/NO_3^- ratios in the pore solution. It is noted that across all potential combinations of diffusion coefficients, the effects of Cl^- binding and NO_3^- exchange are crucial in delaying the onset of steel corrosion – thereby enhancing service life. As an example, in the case of seawater exposure, the provision of CAC + CN-based top-layers is estimated to increase the service life (or conversely delay the onset of steel corrosion) by a factor ranging between $5 \leq d_f \leq 10$, where d_f is the delay factor (unitless). These outcomes are independent of the threshold values selected for corrosion risk indicators – i.e., commonly taken as $Cl^-/OH^- \geq 0.6$ and $Cl^-/NO_3^- \leq 0.25$ – as, in general, ACE is beneficial in delaying, or preventing the onset of steel reinforcement corrosion. The outcomes make a case for the use of functional ACE coatings that act as more than just a physical barrier (e.g., a sealer, or a high-performance concrete topping that only reduces ion-diffusion rates)[238,239] as an innovative means to mitigate steel corrosion related degradation of concrete infrastructure.

Chapter 5. Understanding CO_2 mineralization kinetics and conversion limits of alkaline solid particulates and composites

5.1 Introduction and background

Inorganic alkaline materials that undergo CO_2 mineralization (*carbonation*) reactions have been envisioned as a greener alternative for portland cement in concrete,[240–246] which accounts for nearly 9 % of yearly global CO_2 emissions.[247,248] In contact with water, Ca/Mg-bearing reactants dissolve, releasing Ca/Mg species that react with CO_2 to precipitate carbonate minerals (e.g., $CaCO_3$).[249] The cementation that results from carbonate mineral precipitation enables fabrication of concrete components such as blocks, beams and slabs – i.e., monolithic bodies with length scales on the order of 0.01 - 1.0 m – that fulfill construction performance requirements.[250] Importantly, CO_2 mineralization is not poisoned by the presence of acid gas impurities (e.g., SO_x and NO_x), and may therefore exploit various post-combustion (flue) gas streams (with CO_2 concentration [CO_2] $\approx$ 4 - 30 mol %) for direct CO_2 conversion/utilization.[251]

Carbonation of minerals in contact with flue gases is thermodynamically favored at near-ambient temperatures. However, achieving sufficiently rapid reaction kinetics within cementing components without prohibitively expensive gas conditioning (i.e., CO_2 capture/enrichment and pressurization) has remained a foundational challenge. This difficulty results in part from insufficient understanding of how temperature *T*, relative humidity *RH*, and CO_2 concentration [CO_2] influence the carbonation reactions of Ca-bearing reactants at both the particulate and component scales. For example, although *RH* is known to impact the achievable carbonation extent

(i.e., the final conversion X_f) of portlandite particulates,[252,253] influential parameters limiting reactant carbonation within cementing composite monoliths (i.e., shape-stabilized mixtures of reactants, water, and inert mineral fillers) have not been thoroughly described. The conversion limits and carbonation kinetics of cementing composites may be impacted by CO_2 transport (diffusion) limitations through interparticle pore networks, to a degree dependent on component's length scale and vapor diffusivity.[245] Such transport limitations may also alter the sensitivity of carbonation kinetics to CO_2 concentration and temperature, which are critical control parameters for CO_2 mineralization processes.

Through detailed experimentation, this study aims to improve understanding of the influences of processing conditions on CO_2 mineralization reactions within cementing composites. The conversion limits and carbonation kinetics of alkaline solid reactants – in both the particulate and component scale – are described in relation to *RH*, *T*, and [CO_2]. Incorporation of reactants into monolithic components is found to impose additional conversion limits resulting from the occlusion of reactant surfaces and transport limitations through pore networks. The apparent carbonation rate constants of reactant particulates and components are quantified in relation to their surface area-to-volume ratio (*SA/V*, mm^{-1}). The carbonation kinetics of monoliths are strongly linked to the degree of pore saturation with water, which delays the initiation of carbonation to an extent dependent upon the rate of moisture diffusion. Taken together, these findings inform the design of processing routes to promote rapid CO_2 mineralization within monolithic cementing components. Information of this nature is critical to enable the manufacture of low-carbon concrete products strengthened by cementation agents that mineralize CO_2 from flue gases, while retaining fabrication cycles typical of pre-fabricated concrete products (e.g., ≈ 24 h curing).

5.2 Materials and methods

5.2.1 Materials and specimen preparation

Three particulate reactants were used for carbonation experiments: (i) a commercially available portlandite ($Ca(OH)_2$) powder (Mississippi Lime Co.), with a purity of 94.8 ± 0.5 mass % determined by thermogravimetric analysis (TGA), and a balance of $CaCO_3$, (ii) a calcium-rich coal fly ash (FA; Class C, m_{CaO} = 28.01 mass % via X-ray fluorescence (XRF)), and (iii) a calcium-poor fly ash (Class F, m_{CaO} = 4.02 mass % via XRF).[254] The theoretical carbonation potentials of portlandite, calcium-rich FA, and calcium-poor FA were 0.56 g_{CO2}/g_r, 0.29 g_{CO2}/g_r, and 0.054 g_{CO2}/g_r, respectively, based on their purity/oxide compositions.[255] Their densities (ρ) were 2340 kg/m^3, 2720 kg/m^3, and 2380 kg/m^3 (Accupyc II 1340, Micromeritics), respectively. An ASTM C778[95] compliant graded quartz sand (ρ = 2650 kg/m^3) was used as an inert inclusion (i.e., fine aggregate).

Carbonate binder composites featuring equivalent volume fractions of inclusion and binder (reactants) ($V_i/V_b = 1$) were formulated on a mass basis using the component densities. Composites with initial saturation $S_{w,i}$ ranging from 0 (dry) to 1 (fully saturated) were formed by adjusting the water-to-binder volume ratio V_w/V_b. The composite mixtures were homogenized by hand mixing and loaded into a cylindrical steel pellet mold with a 51 mm diameter. The composite pellets were dry-cast (i.e., compacted to exhibit shape stability) via hydraulic press, which applied 2 MPa compaction pressure. The resulting pellets had a relative density (ρ_b/ρ_s, the ratio of bulk density to

skeletal density) of ≈ 0.60. The pellet thickness was varied from 4.5 mm to 18 mm by altering the quantity of material loaded into the mold.

5.2.2 Carbonation reactor and operating procedure

A custom-built reactor system was used to expose powder reactants and composite pellets to CO_2 streams with varying temperature *T*, relative humidity *RH*, and CO_2 concentration [CO_2]. Parallelized cylindrical reactors with an internal diameter of 100 mm and a length of 150 mm were housed in a digitally-controlled oven (Quincy Lab, Inc.) for temperature control. Relative humidity (*RH*) and temperature (*T*) were monitored within each reactor (HX71V-A, Omega; Type T thermocouples, respectively) with a data acquisition system (cDAQ-9178, National Instruments; LabVIEW 2014). Dry gas mixtures with varying [CO_2] were prepared by mixing air and CO_2 at prescribed flow rates using mass flow controllers (Alicat), providing an inlet flow rate of 2 slpm per reactor. The dry gas mixtures were humidified by bubbling through gas washing bottles containing deionized water, which were housed in a separate oven to achieve the desired *RH*. Twelve samples of each particulate reactant (0.5 g each) were loaded into cylindrical sample cells (10 mm diameter) within the reactors. After loading, the particulate specimens were equilibrated for 30 min to *T* and *RH* setpoints using air, during which negligible carbonation was observed, before initiating CO_2 flow. The dry-cast composite pellets were loaded into the reactors supported by flat plates, with the bottom surface obscured to ensure dominantly one-dimensional CO_2 transport from the top surface. Following 1, 3, 7, and 24 hours of CO_2 exposure, samples were extracted for characterization. Triplicate powder samples distributed across the reactor length were

taken at each time-point. Powder samples were extracted through the thickness of the composite pellets using a drill press with a 4.76 mm diameter masonry bit.

5.2.3 Material characterization

Thermogravimetric analysis (TGA; STA 6000, Perkin Elmer) was used to assess the extent of carbonation reactions (i.e., conversion level, X) in the powder reactants and composites. Around 50 mg of powder was heated from 35 °C to 975 °C at 15 °C/min in an aluminum oxide crucible, under a 20 mL/min ultra-high purity N_2 purge. The CO_2 content of the solid was quantified by assessing the mass loss associated with $CaCO_3$ decomposition over the temperature range of 550 °C to 900 °C, normalized by the mass of dry solids, i.e., excluding the evaporable water which was lost during heating to 120 °C. The conversion X was calculated as the fraction of the theoretical carbonation potential achieved, accounting for reactant purity and the initial carbonate content.

A Bruker-D8 Advance diffractometer using Cu-Kα radiation (λ = 1.54 Å) was used to collect X-ray diffraction (XRD) patterns of the reactant powders. Scans were performed in a θ-θ configuration from 5° to 70° 2θ, in continuous mode, with an integrated step scan of 0.021°. A VANTEC-1 detector was used with a fixed divergence slit of 1.00°. The surfaces of the powder samples were slightly textured and a rotating sample stage was used.

The surface morphology of the pristine and carbonated particulates was examined using a field emission-scanning electron microscope (FEI NanoSEM 230). Secondary electron imaging was performed in high-vacuum mode, with a spot size 4.0 and an accelerating voltage of 10 kV. The

powder samples were attached to sample stubs using double-sided conductive carbon tape, and gold-coated to facilitate charge dissipation.

5.3 Results and discussion

5.3.1 Carbonation conversion limits of particulates and monoliths

The time-dependent conversion profiles $X(t)$ of three alkaline solid particulates: portlandite, calcium-rich fly ash, and calcium-poor fly ash (FA), were evaluated in contact with gas streams of varying [CO_2], T, and RH (Figure 5.1a). A kinetics model of the form $X(t) = (X_f \cdot t)/(X_f/k + t)$ [Eq. 5.1],[256] where X_f is the final conversion level (fraction) and k is the apparent rate constant of carbonation (s^{-1}), was fitted to the conversion data by plotting the $1/X$ against $1/t$ (Figure 5.1a inset).[256] This relation adequately described the shape of the observed $X(t)$ profiles, including the incomplete final conversion (i.e., $X_f < 1$).[257,258] The final conversion of each reactant increased with RH (Figure 5.1b) in a sigmoidal manner, e.g., following $X_f(RH) = a_1/[a_2 + \exp(-a_3 \cdot RH)]$ [Eq. 5.2], where a_1, a_2, and a_3 are fitting constants. Both FA remained effectively unreacted below a threshold $RH \approx 60$ %, above which X_f increased, but remained substantially below the carbonation potential. Temperature and CO_2 concentration had negligible influence on X_f at all RH. The poor conversion is attributed to limited FA dissolution in the absence of liquid water, as $X_f > 0.3$ may be realized when reaction conditions favor dissolution, e.g., direct aqueous carbonation or carbonation of pastes (i.e., FA-water mixtures with water-to-solids mass ratios ≥ 0.2).[259] Therefore, the low FA conversion limits herein likely indicate kinetic limitations resulting from the limited experimental timescale, rather than those associated with reaction thermodynamics or physical barriers formed by reaction products. Nevertheless, adsorbed water alone is insufficient to promote significant carbonation of FA particulates within the evaluated conditions.

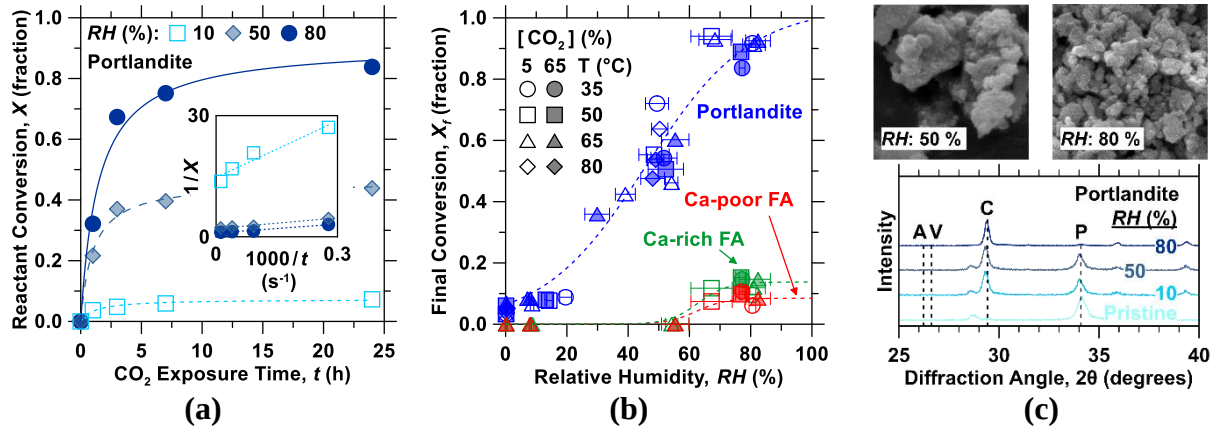

Figure 5.1: (a) Representative time-dependent traces of portlandite particulate conversion X (i.e., the fraction of the maximum stoichiometric CO_2 uptake)[255] during CO_2 exposure at T = 65 °C, [CO_2] = 5 % and varying relative humidity (RH). Best-fit curves of the form given by Eq. 5.1 are shown.[256] Error bars representing the standard deviation of triplicate samples are within the data points. The figure inset shows fitting of $1/X$ vs. $1000/t$ for each curve. **(b)** The final conversion X_f of each reactant follows a sigmoidal relationship that increases with RH and is independent of T and [CO_2]. **(c)** SEM images (field width = 5 μm) and XRD patterns (using Cu-Kα) of portlandite particulates after 24 h CO_2 exposure at T = 65 °C and [CO_2] = 5 % at different RH. The principle diffraction peaks of aragonite (A), vaterite (V), calcite (C) and portlandite (P) are indicated.[137] "Pristine" corresponds to the non-carbonated reactant.

Contrastingly, the conversion limits of portlandite particulates increased strongly with the RH of the contacting gas stream, from a plateau of $X_f \approx 0.1$ for $RH < 20$ %, to nearly complete conversion for water-saturated gas (RH = 100 %). The limiting X_f in dry CO_2 mixtures was indicative of surface passivation induced by direct gas-solid carbonation.[253] As RH was increased, the adsorbed water on particulate surfaces promoted a non-passivating dissolution-precipitation reaction pathway. Similar trends have been previously observed, albeit with lower magnitudes of X_f at a given RH.[252,253] These differences may be attributed to the finer size gradation of portlandite particles utilized herein (i.e., median diameter d_{50} = 3.8 μm vs. 30 - 89 μm),[252,253] as the higher surface area-to-volume ratio of fine particulates lessens the degree of surface passivation induced by a given quantity of reaction products. As with FA particulates, changes to [CO_2] and T had no

discernable effect on X_f at a given *RH* within the studied ranges (5 % < [CO_2] < 65 % and 35 °C < *T* < 80 °C), suggesting that thermodynamic conversion limitations are insignificant to portlandite carbonation within conditions relevant to direct flue gas exposure, i.e., sub-boiling temperature and super-atmospheric CO_2 concentration. Although related to surface passivation by reaction products, the changing conversion limit of portlandite carbonation was not induced by alterations to the reaction products. XRD and SEM characterization revealed that calcite was the sole (crystalline) product regardless of *RH* (Figure 5.1c), *T*, and [CO_2], as the conditions utilized herein favored high calcite supersaturation.[249] These findings establish that *RH* robustly indicates the conversion limits of common alkaline solid particulates – which scale with the availability of calcium therein – regardless of *T* and [CO_2] within flue gas relevant conditions.

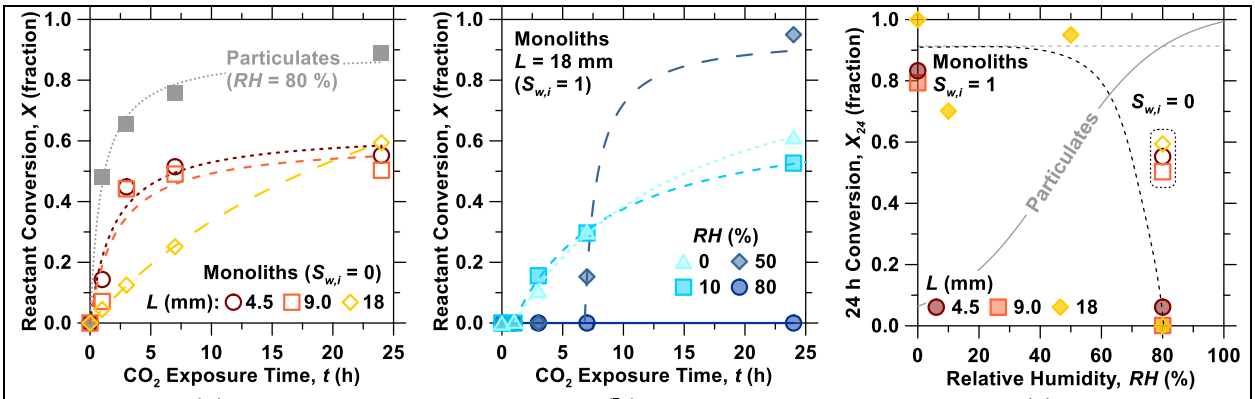

Figure 5.2: (a) Conversion-time curves of dry-cast portlandite composite monoliths with zero initial saturation ($S_{w,i}$ = 0) and varying thicknesses (*L*), in contacts with a gas stream of *RH* = 80 %, [CO_2] = 12 % at *T* = 65 °C. The conversion profile for portlandite particulates under similar conditions are shown as a reference. **(b)** Conversion-time curves of initially saturated ($S_{w,i}$ = 1) dry-cast portlandite monoliths (*L* = 18 mm) during exposure to gas streams of varying *RH*, at [CO_2] = 12 % at *T* = 65 °C. Curve fits are of the form of Eq. 5.3. **(c)** The 24 h conversion X_{24} of portlandite monolith specimens with varying *L* and $S_{w,i}$ as a function of *RH*. CO_2 exposure used gas streams with [CO_2] = 12 % at *T* = 65 °C. The observed trend X_f (*RH*) for portlandite particulates (solid gray curve) and the average portlandite conversion at *RH* = 80 % (dashed gray line) are also shown. The dashed line for monoliths with $S_{w,i}$ = 1 is a guide for the eye.

The carbonation of monolithic portlandite composites was assessed to elucidate scaling effects on carbonation conversion limits – i.e., as reactant length increased from the particulate (~ μm) to component (~ cm) scale. Monolithic components feature reactant particulates, inert quartz sand (filler), and pore networks that may be partially saturated with water, which influences carbonation behavior. For example, dry portlandite monoliths, i.e., with initial pore water saturation $S_{w,i} = 0$, reacted readily (Figure 5.2a), but featured lower conversion levels than portlandite particulates (Figure 5.2c). This reduction signals that incorporation of portlandite into monolithic components induces additional conversion limitations beyond that which is intrinsic to particulate carbonation, which may include (i) occlusion of reactant surfaces within the compacted monoliths, (ii) blocking of pores by water that was adsorbed from the humid gas stream or released by the carbonation reaction, or (iii) space-filling/pore blocking by reaction products. The monoliths with the greatest thickness *L* unexpectedly demonstrated an increased final conversion level compared to those with smaller thicknesses, despite their slower carbonation rate. This phenomenon may indicate a dependence of monolith conversion limits upon the rate of carbonation therein. In contrast, initially saturated monoliths ($S_{w,i} = 1$) demonstrated a time delay t_d before the onset of carbonation (Figure 5.2b). The relation $X(t) = (X_f \cdot (t - t_d)) \,/(X_f/k + (t - t_d))$ [Eq. 5.3] was therefore used to estimate the final conversion of monoliths with $S_{w,i} > 0$. The final conversion of saturated monoliths exceeded 0.7 for $RH \leq 50$ % and dropped to nearly zero at $RH = 80$ % (Figure 5.2c), revealing a conversion limitation imposed by the vanishingly slow diffusion of CO_2 through water-saturated pores (i.e., 10^4 × slower than in in air). At $RH < 50$ %, drying extracted sufficient pore water to enhance vapor phase diffusion while provisioning internally higher *RH* during early CO_2 exposure, which increased X_f beyond that of particulates at equivalent *RH*. These findings highlight

the influences of relative humidity and pore saturation on the conversion limits of portlandite monoliths.

5.3.2 Carbonation kinetics of particulates and monoliths

The influences of processing conditions on carbonation kinetics were subsequently investigated, with a primary focus on contacting gas streams featuring $RH \approx 80$ %, as (i) comparison of rate constants curves with varying X_f is not straightforward, and (ii) differences between conversion-time curves are more distinguishable when X_f is near 1. The carbonation kinetics of portlandite particulates featured a negligible dependence on CO_2 concentration within the studied range ($[CO_2]$ = 5 % to 65 %), as the inverse conversion-time profiles at varying $[CO_2]$ were effectively described by linear fits with a single slope ($m = 1/k$) (Figure 5.3a). Therefore, within conditions of sufficient gas flow and mixing, the carbonation kinetics of portlandite particulates may not be significantly accelerated by increasing the CO_2 concentration of the contacting flue gas stream, e.g., by membrane enrichment. For gases with $[CO_2]$ = 5 %, the reaction rate constant was smaller at early reaction times, i.e., described by bi-linear curves with $k_2 > k_1$, regardless of reaction temperature (Figure 5.3b). This increase in reaction rate constant was therefore attributed to the delayed attainment of the concentration set-point within the reactor system – an artifact of the imperfect gas mixing in the reactor volume. Despite this observation, both regimes demonstrated near-equivalent temperature dependence, i.e., with activation energy $E_a \approx 12 \pm 2$ kJ/mol revealed by Arrhenius analysis (Figure 5.3b inset). For gas streams with greater CO_2 concentration (e.g., 65 %), the inverse conversion-time trends were again bi-linear, but with $k_1 > k_2$ (Figure 5.3c). This decrease in reaction rate constant may be expected due to the increased surface coverage of

reactants with carbonation products. Arrhenius analysis for [CO_2] = 65 % revealed that initial carbonation (k_1) was effectively temperature insensitive ($E_a \approx 3$ kJ/mol), while the second regime (k_2) was more strongly temperature dependent ($E_a \approx 22$ kJ/mol). These results imply that the use of heating to accelerate reaction kinetics is more effective within the secondary reaction regime, and for gas streams with elevated CO_2 concentration.

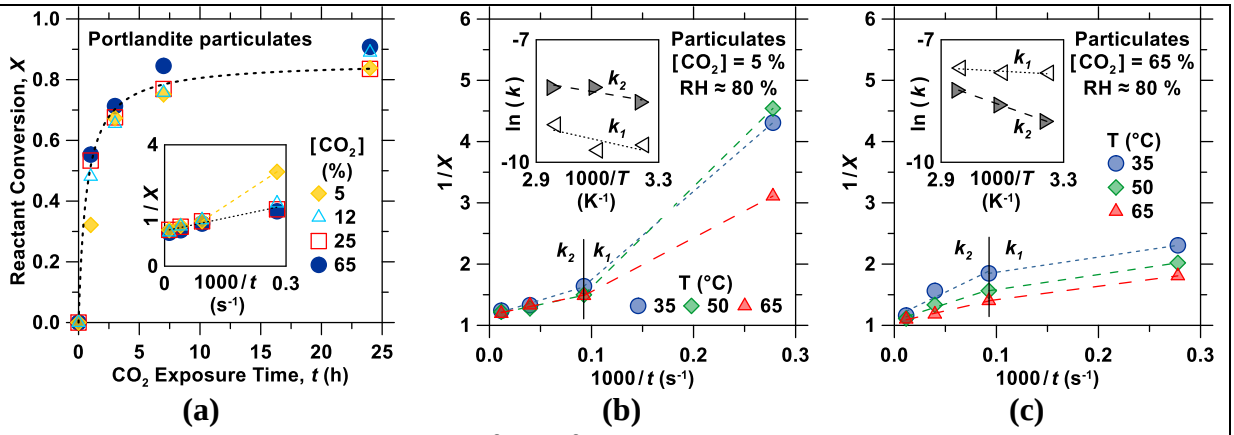

Figure 5.3: (a) Conversion-time profiles of portlandite particulates during CO_2 exposure to gas streams of varying CO_2 concentration [CO_2] at T = 65 °C and RH = 80 %. The figure inset shows linearized (inverse) conversion curves used to fit Eq. 5.1 to the experimental conversion data. **(b and c)** Inverse conversion-time curves representing portlandite particulate carbonation and varying T for RH = 80 % and [CO_2] = 5 % and 65 %, respectively. The figure insets show Arrhenius plots of the apparent carbonation rate constants k (s^{-1}) against the inverse temperature, which reveal the activation energy of portlandite particulate carbonation.

Dry portlandite monoliths ($S_{w,i}$ = 0) carbonated at RH = 80 % similarly demonstrated bi-linear inverse conversion-time profiles with $k_2 > k_1$ (Figure 5.4a). In the smaller monoliths, the conversion increased with rate constant k_1, until reaching $X \approx 0.5$, at which point, conversion followed a rate constant k_2 similar to that of particulate carbonation (red horizontal lines in Figure 5.4a inset). Smaller monoliths (L = 4.5 and 9.0 mm) showed this transition within ≈ 3 h CO_2 exposure, while in the larger monolith, k_2 was not observed within the CO_2 exposure duration. The mechanism determining this break point is likely related to the requirement of moisture diffusion

throughout the bulk of the monolith specimen, i.e., to achieve internal equilibration to *RH* = 80 % that is required to promote conversion to ≈ 0.8. Once this internal *RH* is met, carbonation proceeds at a rate similar to that of portlandite particulates.

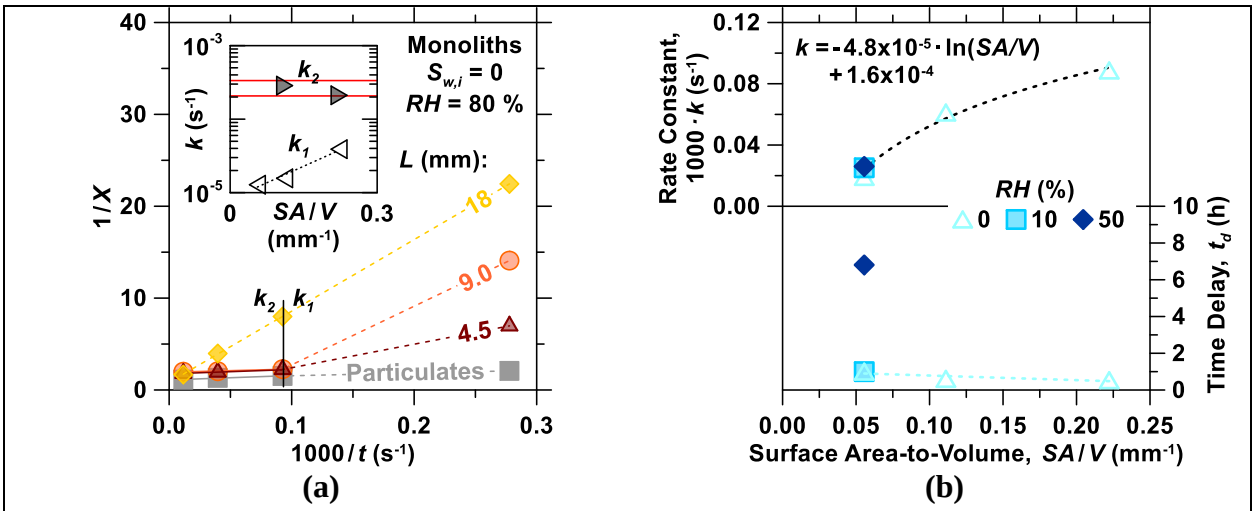

Figure 5.4: (a) The inverse conversion-time curves representing carbonation of dry portlandite monoliths ($S_{w,i}$ = 0) of varying thickness *L* at *RH* = 80 %, [CO_2] = 12 %, and *T* = 65 °C. The figure inset plots the apparent carbonation rate constant *k* (s^{-1}) from each regime against the monoliths' surface area-to-volume ratios (mm^{-1}). **(b)** The time delay to carbonation initiation t_d and the apparent carbonation rate constant *k* of initially saturated monoliths ($S_{w,i}$ = 1) with varying thicknesses at *RH* = 80 %, [CO_2] = 12 %, and *T* = 65 °C.

In the case of initially saturated monoliths, however, it is expected that carbonation is limited by the rate at which internal pore moisture dries out of the specimen by capillary transport and diffusion. The time delay before carbonation t_d was reduced as the *RH* was dropped, and for monoliths with greater *SA/V* (Figure 5.4b). These findings were congruent with an expected dependence on the rate of drying, which was increased when: (i) the driving force for drying (i.e., *RH* gradient) was greater, and (ii) the monoliths featured larger *SA/V*. Once carbonation was initiated, the rate constant *k* was nearly independent of the external *RH* but increased with *SA/V* (Figure 5.4b). Increasing temperature may alter these relations, as it would accelerate both drying

(moisture diffusion) and portlandite carbonation, but with different activation energies. Further, while [CO_2] minimally influenced the conversion limits and kinetics of portlandite particulates, it may be more strongly influential in the carbonation of portlandite monoliths, in which CO_2 diffusion rates are related to the concentration gradient across the specimen thickness.

5.4 Summary and conclusions

This paper has elucidated the influences of processing conditions on the CO_2 mineralization (carbonation) reactions of alkaline solids, with special focus on the scaling of reaction conversion limits and kinetics from the particulate to component length scales. The understanding engendered herein informs the design of direct CO_2 mineralization processes for the production of cementation agents that may replace CO_2-intensive portland cement. The final carbonation conversion of alkaline solid particulates was found to be controlled solely by the relative humidity *RH* of the contacting gas stream (i.e., independent of temperature *T* and CO_2 concentration [CO_2]), and the reactant's calcium availability. At a fixed *RH*, the carbonation kinetics of portlandite were largely insensitive to [CO_2] (zeroth order) and weakly dependent on temperature (i.e., showing an activation energy $E_a \approx 3$ - 22 kJ/mol). When formed into monolithic components (with length *L* on the order of cm), conversion behavior with respect to *RH* was altered by the imposition of additional conversion limitations related to the transport kinetics through pore networks and the occlusion of reactant surface area within the monolith microstructures. The outcomes of this work may aid in the development and validation of models describing the carbonation of portlandite-enriched composite monoliths towards the use of flue gas streams to produce low-CO_2 concrete components within practical fabrication cycles.

Chapter 6. How microstructure and pore moisture affect strength gain in portlandite-enriched composites that mineralize CO_2

6.1 Introduction and background

Conventional concrete consists of a mixture of calcium silicate-dominant ordinary portland cement (OPC; *traditional cement*), aggregates, water, and chemical/mineral additives. The reaction of OPC with water (*hydration*) precipitates calcium silicate hydrate (C-S-H) compounds, which bind proximate particles together and solidify the mixture.[5] Such cementation resulting from OPC hydration strengthens concrete over time.[260] Due to the significant impact of OPC production on global CO_2 emissions [N.B.: Nearly 9 % of global CO_2 emissions are attributed to OPC production], there is a pressing need to innovate new cementation solutions with a greatly reduced embodied CO_2 intensity.[261,262]

Cementation ensured by *in situ* carbonation is a promising alternative approach that relies upon the reaction of CO_2 with alkaline inorganic precursors to precipitate carbonate solids.[240–242] In this method based on the utilization of CO_2 waste streams, a shape-stabilized *green body* (e.g., block, slab, beam) is exposed to CO_2, e.g., in the gas, liquid, or supercritical states. Here, green bodies may be produced by either *wet-casting* (wherein a slurry is poured into a mold until it is self-supporting) or *dry-casting* (in which components having very low water contents are mechanically compacted until they are self-supporting). *In situ* CO_2 mineralization then proceeds via a dissolution-precipitation pathway,[240] entailing the following steps for calcium-bearing reactants:

- The dissolution of the reactants releases Ca^{2+} species within the pore liquid,

- The dissolution and transport of CO_2 (i.e., as a gas/vapor or dissolved carbonate ions) occurs from the outside environment through the green body's pore network, and,
- The reaction of dissolved species precipitates carbonate minerals (e.g., $CaCO_3$).

The embodied CO_2 intensity of the resulting carbonated binder is substantially reduced vis-à-vis OPC depending on the nature of reactants used.[241] This is attributed to: (i) the direct sequestration of CO_2 from an emissions stream thereby fulfilling the premise of *CO_2 utilization*, and (ii) to the *CO_2 avoidance* associated with the use of alternate binder components including industrial wastes (e.g., coal fly ash) or alkaline solids that may be produced by a low-temperature pathway, e.g., portlandite ($Ca(OH)_2$).[240,241]

In green bodies composed using readily-dissolving reactants such as portlandite, CO_2 transport through the body is often the rate limiting step in carbonation.[243,263] In the absence of pressure gradients, CO_2 transport occurs by diffusion, the rate of which is inversely proportional to the microstructural resistance factor $f(S_w, \phi)$.[264] The microstructural resistance to diffusion increases as the total porosity, ϕ, is reduced and as the volume fraction of pores that are saturated with liquid water, S_w, is increased.[265] The total porosity of portlandite-enriched composites is a function of their composition (e.g., water-to-binder mass ratio, aggregate content), method of forming (e.g., wet-cast vs. dry-cast, and degree of consolidation), and the extent of hydration and carbonation reactions that may have occurred. On the other hand, S_w can be controlled by drying before (or during) CO_2 exposure. CO_2 diffusion is hindered by elevated pore saturation, as diffusion through water is $\approx 10^4$ times slower than in air.[266] Thus, reducing S_w will accelerate carbonation kinetics. However, dramatic reductions in S_w depress the relative humidity, *RH*, inside the pores, which can hinder portlandite carbonation.[252] For example, Shih et al.[253] reported that a critical *RH* of 8 % was

required to initiate $Ca(OH)_2$ carbonation. Although the significance of *RH* has been observed in the carbonation of particulates, its effect on the carbonation of portlandite-enriched monoliths remains unclear.

The fabrication of carbonated wet-cast or dry-cast structural concrete components that fulfill specific performance criteria requires a detailed understanding of the mechanisms of cementation (strengthening) therein. Although it is known that carbonation, OPC hydration, and pozzolanic reactions can adhere proximate surfaces and induce reductions in porosity,[267] the contributions of these reactions to strength gain, especially in carbonated composites, remain unclear. For example, during CO_2 exposure, these reactions occur concurrently, making it difficult to isolate the contributions of each reaction to strength. Furthermore, C-S-H precipitation on reactant surfaces and within pore spaces, prior to carbonation, may limit strengthening by hindering CO_2 diffusion and reducing the availability of exposed reactant (portlandite) surfaces.[268] Finally, it is unknown whether conventional relationships between the extent of hydration and strength hold true during CO_2 exposure, as processing conditions that may favor carbonation (e.g., decreasing S_w by drying) may suppress OPC hydration[151,269] and pozzolanic reactions due to the consumption of portlandite. To address these open questions, this study elucidates the influences of microstructure on the carbonation kinetics of portlandite-enriched cementing composites ("mortars"). The premise of using portlandite is straightforward for a multiplicity of reasons including:

Making use of existing facilities: Portlandite can be produced using limestone as a precursor using existing OPC kilns and features a cost that is essentially similar to OPC,[270]

Lower processing temperature: Portlandite's production, by the decarbonation of limestone around 800 °C (at ambient pressure, in air), followed by the hydration of lime requires a processing temperature that is nearly 700 °C lower than OPC production,[270]

Straightforward carbonation: Unlike OPC and the other potential alkaline precursors, the carbonation of portlandite is slightly, if at all, affected by reaction pressure, temperature and CO_2 concentration and proceeds readily under exposure to dilute flue gases (< 15 % CO_2, v/v);[240] i.e., so long as a threshold relative humidity (RH) around 8 % is exceeded,[253] and,

Highest CO_2 uptake: Due to its substantial calcium content per unit mass,[240] portlandite features the among the highest potential CO_2 uptake per unit mass (59 mass %) of mineral reactants,[242] and may be achieved. For example, although $Mg(OH)_2$ has a higher potential CO_2 uptake (75 mass %), it requires greatly elevated temperature and pressure to achieve similar carbonation kinetics (rates) as portlandite.[271]

Taken together, the findings highlight that portlandite-enriched binders can serve as a viable *functional replacement* for OPC-based cementation agents and offer new insights to design concrete construction components that are cemented via *in situ* CO_2 mineralization.

6.2 Materials and methods

6.2.1 Materials and sample preparation

Portlandite-enriched binders were composed of: 42 mass % portlandite, 33 mass % ASTM C150-compliant[272] ordinary portland cement (Type II/V OPC) and 25 mass % ASTM C618-compliant[273] Class F fly ash (FA). OPC was incorporated to provide green strength and facilitate handling prior to drying and carbonation, whereas FA served as a source of aluminosilicates to promote pozzolanic reactions. A portlandite-free reference binder (i.e., 75 mass % OPC and 25 mass % FA) was also formulated to isolate portlandite's influences on reactions and strength evolution. The portlandite (Mississippi Lime) used featured a purity of 94 % ± 2 % (by mass) with the remainder being composed of $CaCO_3$ as determined by thermogravimetric analysis (TGA). The median particle diameters (d_{50}) of portlandite, FA, and OPC were 3.8 μm, 8.9 μm, and 17.2 μm, respectively, as determined using static light scattering (SLS; LS13-320, Beckman Coulter). Further details on the chemical composition and particle size distributions of binder solids are reported in the Supporting Information (SI).

The binders were combined with ASTM C33[274] compliant silica sand (fine aggregate) to form composites ("mortars") as described in ASTM C305.[275] Wet-cast composites were formulated at w/b = 0.45 (w/b = water-to-binder mass ratio) and a/b = 3.5 (a/b = aggregate-to-binder mass ratio). Dry-cast composites had w/b = 0.25 and a/b = 7.95. The fine aggregate had a density of 2650 kg/m^3 and a water absorption[276] of ≤1.0 mass %. A commercially-available polycarboxylate ether (PCE) dispersant was added to enhance the fluidity of the wet-cast composites at a dosage of 0.8 % of the binder mass. The wet-cast composites were molded into cylinders (50 mm × 100 mm; *d*

× h) and vibrated to remove entrapped air. Dry-cast composites were prepared by compaction using a hydraulic press to form cylindrical specimens (75 mm × 40 mm; d × h) that featured a surface area-to-volume ratio (SA/V, mm^{-1}) equivalent to the wet-cast specimens. The compaction pressure was varied between 0.5 MPa and 22.0 MPa to achieve relative densities (ρ/ρ_s, the ratio of bulk density to skeletal density) ranging between 0.58-to-0.88. Dry-cast portlandite composites with w/b = 0.25 and a/b = 7.95 as well as *neat* portlandite pellets (10 mm × 8 mm; d × h) with different water-to-solid (i.e., portlandite) mass ratios between 0 and 0.75 were also formed by compaction for comparative analyses.

6.2.2 Drying and carbonation processing

The wet-cast composites were cured under sealed conditions for 6 h at T = 22 ± 2 °C to achieve shape stability and a compressive strength $\sigma_c \approx 0.5$ MPa. The specimens were then either dried to different initial S_w prior to carbonation or carbonated immediately after forming. In contrast to the wet-cast composites in which initial S_w was controlled by drying, S_w of the dry-cast composites was altered by applying different compaction pressures. During drying and carbonation, the cylindrical specimens were placed in custom-built reactors with an internal diameter of 100 mm and a length of 150 mm (see schematic in Figure 6.7). The reactors were placed in an oven for temperature regulation and the flow rate of the inlet gas was controlled by mass-flow controllers. Different drying conditions were implemented by varying the: (i) air temperature (22 ± 0.5 °C, 45 ± 0.5 °C, and 65 ± 0.5 °C), (ii) air flow rate (0.5 slpm to 40 slpm; standard liters per minute), and, (iii) drying duration (0 to 12 h). Thereafter, the dried specimens were contacted with simulated flue gas at a flow rate of 0.5 slpm for up to 60 h at different isothermal temperatures (22 ± 0.5 °C, 45 ± 0.5 °C,

and 65 ± 0.5 °C). The simulated flue gas was prepared by mixing air and CO_2 to mimic the exhaust of a coal power plant.[277] The gas is composed of 12 ± 0.2% CO_2 [v/v] as confirmed using gas chromatography (GC; F0818, Inficon).

6.2.3 Experimental methods

Time-dependent CO_2 uptake was quantified using thermogravimetric analysis (TGA: STA 6000, Perkin Elmer). The values reported are the average CO_2 uptake of three powdered samples taken along the height of the cylindrical specimens. Around 30 mg of each powder was placed in pure aluminum oxide crucibles and heated at a rate of 15 °C/min over a temperature range of 35 °C to 975 °C under UHP-N_2 gas purge at a flow rate of 20 mL/min. The CO_2 uptake was quantified by assessing the mass loss associated with $CaCO_3$ decomposition over the temperature range of 550 °C to 900 °C,[240] normalized by the total mass of solids in the binder (i.e., portlandite, fly ash, and OPC). The non-evaporable water content (w_n, mass %) was calculated as the mass loss over the temperature range of 105 °C to 975 °C excluding the mass loss from the decomposition of $CaCO_3$ and $Ca(OH)_2$.[278,279]

The compressive strength of the composites was measured as per ASTM C39.[280] Appropriate strength correction factors were applied in consideration of the specimens' length-to-diameter ratios[280] to allow direct comparisons between the dry-cast and wet-cast specimens, which feature somewhat different geometries.

The total porosity and pore (moisture) saturation level of the composites before and after carbonation were quantified using a vacuum saturation method.[281] Cross-sectional disks, 25 mm-thick were sectioned from the middle of the cylindrical specimens using a low-speed saw. Isopropanol (IPA) was used as the solvent to arrest hydration. The CO_2 diffusivity was estimated from the total moisture diffusion coefficient, D_{tot} (m^2/s), (i.e., the sum of liquid water and water vapor diffusion coefficients)[264] of the composites prior to CO_2 exposure using Fick's 2nd law of diffusion,[266] as elaborated in Section 6.5.3.

6.3 Results and discussion

6.3.1 Influences of saturation on CO_2 uptake in portlandite-enriched binders

The carbonation kinetics of wet-cast composites pre-dried to different initial S_w (Figure 6.8) were evaluated. Figure 6.1(a) displays the time-dependent CO_2 uptake of each specimen $C(t)$ normalized by the mass of reactants, i.e., portlandite, fly ash, and OPC. The measured data points were fitted to an equation of the form $C(t) = C(t_u)[1 - \exp((-kt)/C(t_u))]$ by least squares regression to estimate the apparent carbonation rate constant (k, h^{-1}), and $C(t_u)$, the ultimate CO_2 uptake, where t_u is taken as 60 h. Reducing S_w from 1.00 (complete saturation) to 0.13 for the wet-cast composites increased both the carbonation rate constant and the ultimate CO_2 uptake by nearly 10× (Figure 6.1a). The same observation is true for dry-cast composites, demonstrating thenavignificance of S_w as a controlling variable on carbonation kinetics across different forming methods and microstructures. But, enhanced levels of CO_2 uptake were obtained for the dry-cast relative to wet-cast composites at comparable S_w (Figure 6.1b), as further discussed below.

The carbonation of both the dry-cast and wet-cast composites was nearly fully suppressed when S_w was reduced below a critical value, $S_{w,c} \approx 0.10$ (Figure 6.1c). Assuming that the water vapor sorption isotherms of portlandite-enriched binders are *functionally* similar to those of typical cementitious binders, $S_{w,c} \approx 0.10$ corresponds to an internal $RH \approx 10$ %.[282] These findings broadly agree with the minimum $RH_c = 8$ % previously suggested to ensure the carbonation of portlandite particulates at near ambient temperature.[253] Below RH_c, carbonation is hindered by the reduced mobility and availability of water to support the dissolution of portlandite; thus, carbonation is

expected to occur as a gas-solid reaction.[252,253] This observation suggests that carbonation suppression at low S_w results from a shift in the reaction mechanism, which is applicable across processing and preparation conditions. Therefore, maintaining $S_w > S_{w,c}$ is an important requirement for the carbonation of portlandite-enriched binders to enhance CO_2 uptake and the carbonation strengthening.

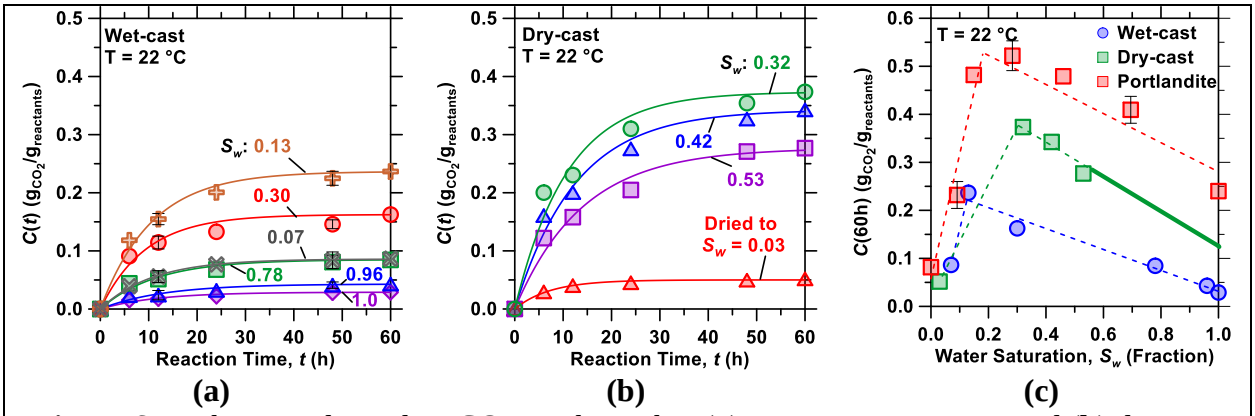

Figure 6.1: The time-dependent CO_2 uptake within **(a)** wet-cast composites and **(b)** dry-cast composites at varying initial saturation S_w. The data was fit by an equation of the form $C(t) = C(t_u)[1 - \exp((-kt)/C(t_u))]$ to estimate the apparent carbonation rate constant k (h^{-1}). **(c)** The CO_2 uptake after 60 h CO_2 exposure C(60 h) as a function of initial saturation S_w for wet-cast composites, dry-cast composites, and portlandite compacts. In all cases, reducing S_w enhanced CO_2 uptake for $S_w > 0.10$. Carbonation occurred in 12 % CO_2 [v/v] at 22 °C.

The differences in carbonation kinetics between wet-cast and dry-cast composites are on account of the composites' microstructural resistances to CO_2 diffusion. Here, the CO_2 diffusivity was indirectly estimated by the total moisture diffusivity, which was measured by one-dimensional drying experiments.[266,283] Although the mechanisms by which CO_2 and moisture (i.e., in the form of liquid and vapor phases) diffuse through pore networks may somewhat differ, they are proportional and controlled by the total porosity and saturation level of the pore structure.[284] The total moisture diffusivities of the composites were estimated at the time immediately prior to the initiation of carbonation. At equivalent S_w, the dry-cast composites showed a higher moisture

diffusivity than wet-cast composites, due to their lower degree of OPC hydration (Figure 6.2a). This reinforces the premise that microstructural resistance controls CO_2 diffusion and carbonation reaction kinetics. The carbonation rate constant of wet-cast and dry-cast composites at varying S_w shows a similar logarithmic scaling as a function of the total moisture diffusivity for $S_w \geq 0.13$ (Figure 6.2b). It should be noted, however, that the dry-cast composites showed rate constants that are systematically higher than those of wet-cast composites for equivalent diffusivities. This difference is postulated to result from the different extents of OPC hydration of the two composites, as reflected in their non-evaporable water contents (Figure 6.2c). Indeed, the CO_2 uptake of both wet-cast and dry-cast composites decreased at a similar rate with increasing non-evaporable water content. The enhanced carbonation kinetics of the dry-cast composites is therefore consistent with the elevated accessibility of portlandite surfaces therein, due to such surfaces being less occluded by C-S-H precipitates which may impose transport barriers to CO_2 contact and intrusion. This indicates that if OPC hydration in wet-cast composites was limited to a degree similar to that of the dry-cast composites (while ensuring shape stability) they may feature enhanced CO_2 uptake.

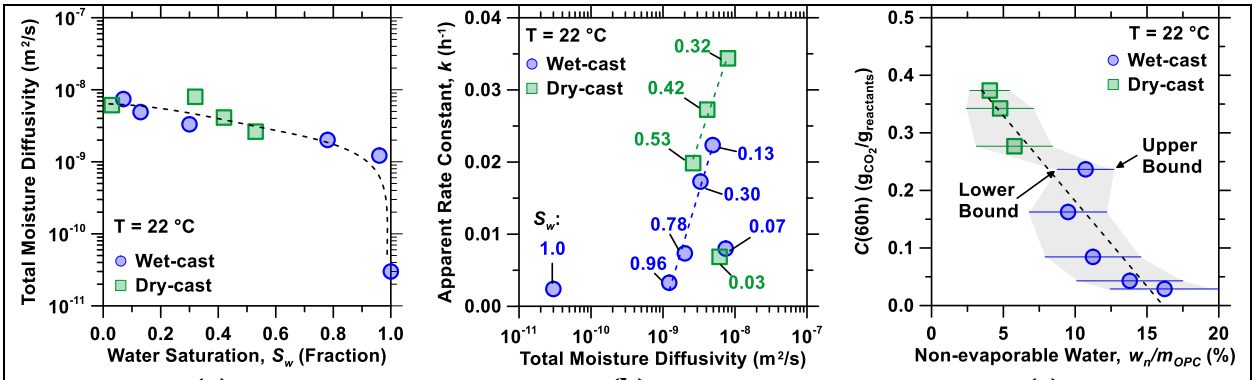

Figure 6.2: (a) The total moisture diffusivity of dry-cast and wet-cast composites as a function of their initial saturation S_w. The dashed line is a guide for the eye. **(b)** The apparent carbonation rate constant as a function of the total moisture diffusivity across dry-cast and wet-cast composites. **(c)** The 60-h CO_2 uptake as a function of the non-evaporable water content w_n/m_{OPC} of dry-cast and wet-cast composites following carbonation. The lower and upper bounds of w_n/m_{OPC} in **(c)** for each data point correspond to values at t = 0 h and t = 60 h of carbonation, respectively. The specimens with initial $S_w < S_{w,c}$ are excluded in **(c)**.

6.3.2 Carbonation strengthening of portlandite-enriched binders

The compressive strengths of the portlandite-enriched composites increased over the course of CO_2 exposure due to carbonation and OPC hydration (Figure 6.3a). Notably, despite their lower extents of OPC hydration (i.e., w_n/m_{OPC}), the carbonated composites featured strengths equivalent to or greater than that of a sealed composite, in which OPC was permitted to hydrate without CO_2 exposure. Strength slightly increased as the initial S_w was reduced, owing to the increased CO_2 uptake (Figure 6.9). However this was so only as long as $S_w > S_{w,c}$, because, in general, both carbonation and hydration are suppressed at low *RH*. The critical pore saturation required to sustain OPC hydration is substantially higher than that of carbonation reactions. For instance, the hydration of alite (Ca_3SiO_5, the major phase in OPC) is suppressed when the *RH* drops below 80 %.[151,269] The dry-cast composites showed a contrasting trend, whereby strength increased with S_w (Figure 6.3b). However, this in part an artifact resulting from the reduction in total porosity that

resulted from the increased levels of compaction that were used to elevate S_w. For example, analytical analysis of particle packing[285] within the dry-cast composites reveals a 4× reduction in the interparticle spacing as the relative density increased from 0.67 to 0.88. Not only does this improve particle-to-particle contacts, but it also permits an effective cohesion in the material by a smaller quantity of cementing agent (carbonate precipitates).

Unlike carbonated pastes composed only of fly ash,[241] the strength-CO_2 uptake curves of portlandite-enriched composites with different initial S_w *cannot* all be fitted by a single linear relation, i.e., with a shared slope $m = \Delta\sigma_c/\Delta C$; MPa/($g_{CO2}/g_{reactant}$) that remains constant over the course of carbonation (see Figure 6.3). Rather, both wet-cast and dry-cast composites demonstrated unique bi-linear trends wherein the secondary slope m_2 (i.e., between t = 6 h and t = 60 h) was steeper than the initial slope m_1 (i.e., between t = 0 h and t = 6 h)*;* i.e., indicating an increase in the strength gain per unit CO_2 uptake at later ages after the cementing agent first cohered the solid skeleton together. Interestingly, the later-age slope m_2 increased exponentially with the changes in the normalized non-evaporable water content $\Delta(w_n/m_{OPC})$ during carbonation and eventually sketched a single curve for both wet-cast and dry cast mixtures (Figure 6.10a). As such, extrapolation to $\Delta(w_n/m_{OPC}) = 0$ (i.e., when the OPC would remain unreacted during CO_2 exposure) yields a y-intercept of 14.7 MPa per unit mass CO_2 uptake ($g_{CO2}/g_{reactants}$). This value reflects the strength gain per unit mass of CO_2 uptake in the portlandite-enriched binder in the absence of concurrent strengthening by OPC hydration. This level of strengthening is substantially higher than the 3.2 MPa per unit mass of CO_2 uptake noted for fly ash reactant ($g_{CO2}/g_{fly\ ash}$) – an unsurprising outcome given the much higher mobility and availability of Ca-species and greater carbonation reaction rate provisioned by portlandite.[241] Similar analysis of the strength-w_n/m_{OPC} relation over the course of CO_2 exposure (Figure 6.10b) indicates that OPC hydration results in

strength gain of ≈ 0.38 MPa per fraction of OPC reacted (w_n/m_{OPC}). As such, assuming that the binding effects of carbonation and OPC hydration are additive, for processing carried out at 22 °C, the strength developed can be estimated by an equation of the form $\sigma_c(t) = A \cdot C(t) + B \cdot w_n(t)/m_{OPC}$ where A = 14.7 MPa / ($g_{CO2}/g_{reactants}$) and B = 0.38 MPa / (w_n/m_{OPC}) as determined from the slopes of the strength-CO_2 uptake and strength-w_n/m_{OPC} curves.

Note, the strength gain per degree of OPC hydration estimated above is similar to that observed during sealed curing in the absence of CO_2 exposure (see Figure 6.9) and to that within portlandite-free composites, indicating that carbonation, and the presence of portlandite as a reactant does not appear to induce a change in the composition or binding performance of the reaction products that are formed. It should be noted however, that the strength prediction equation noted above offers better estimates for the dry-cast, as opposed to the wet-cast composites. This is on account of the effects of drying (Figure 6.3c). For example, unlike drying at a low flow rate of 0.5 slpm (i.e., similar to that used for carbonation), increasing the flow rate to enhance drying depressed the rate of strength gain per degree of OPC hydration. This may be attributed to the effects of microcracking, and/or heterogeneity in microstructure with respect to the nature of hydration products that may form resulting from the accelerated extraction of water, especially at higher temperatures.[286,287] Due to the inherently lower water content of the dry-cast composites, and the reduced extent of OPC hydration that results – dry-cast composites are therefore less affected by processing conditions prior to carbonation. Nevertheless, analysis of the carbonation strengthening factor (F_{cs}, unitless), i.e., the ratio of the strength of carbonated to non-carbonated composites revealed that dry-cast composites composed of neat-portlandite achieved F_{cs} = 3.75 (Figure 6.3d). This was substantially higher than the strengthening factors achieved for wet-cast composites ($F_{cs} \leq 2.5$) and dry-cast composites ($F_{cs} \leq 3.25$) – and confirms that the strengthening offered by the *in*

situ formation of carbonates is foundational in ensuring cohesion and strength development (Figure 6.11). Interestingly, F_{cs} of dry-cast mixtures was inversely correlated to their relative density (ρ/ρ_s) indicating that the strengthening effect arising from compaction / particle interlock reduces the relative influence of carbonation and the bridging action of cementing precipitates.[288,289]

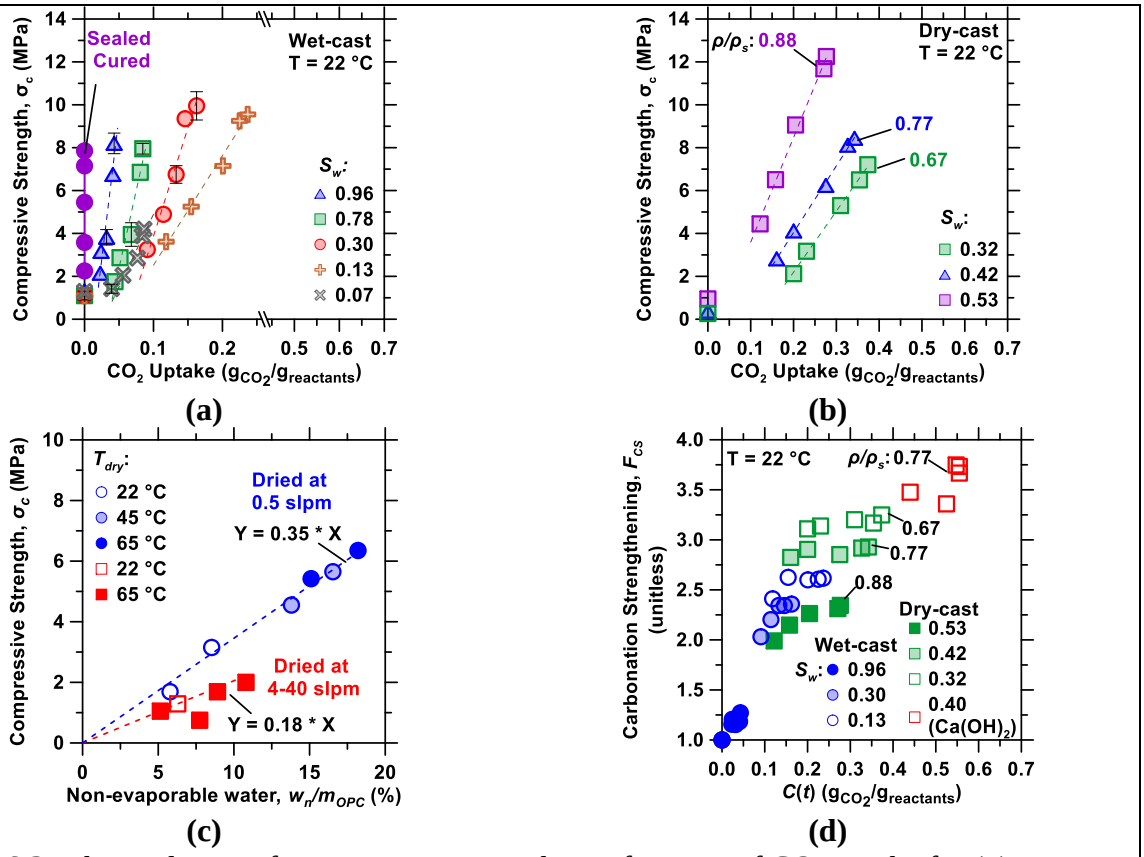

Figure 6.3: The evolution of compressive strength as a function of CO_2 uptake for **(a)** wet-cast composites at varying initial saturation levels induced by drying and **(b)** dry-cast composites at varying initial saturation levels induced by compaction pressure. **(c)** The dependence of the compressive strength on w_n/m_{OPC} during drying before CO_2 exposure across diverse drying conditions. **(d)** The carbonation strengthening factor as a function of the ultimate CO_2 uptake for wet-cast and dry-cast composites. In all cases, carbonation was carried out using 12 % CO_2 [v/v] at 22 °C.

$S_{w,}$ can be additionally controlled, especially in dry-cast composites, by changing the temperature, i.e., by imposing drying using a heated gas stream, prior to and during carbonation. As noted in Figure 6.4, elevating the reaction temperature substantially enhanced both CO_2 uptake and strength, resulting in the development of $\sigma_c \approx 25$ MPa in 24 h. This is attributed to both the facilitated CO_2 transport due to the removal of water by evaporation (increased carbonation reaction rate), and the stimulation of OPC hydration and pozzolanic reactions (as indicated by w_n/m_{OPC} in Figure 6.4). However, in agreement with the results for drying-induced changes in S_w, a temperature increase is beneficial to a limit – further increasing the temperature to 85 °C diminished both CO_2 uptake and strength gain on account of the insufficiency of pore water to support both CO_2 mineralization and OPC hydration reactions. This is attributed to: (a) the exothermic nature of carbonation reactions wherein temperature rise (unless the heat is rapidly dissipated) shifts the reaction equilibrium towards the reactants thereby resulting in a retardation in reaction progress; following Le Chatelier's principle, and (b) the rapid extraction of water, as a result of which carbonation and hydration are both suppressed. These observations suggest that using a partially humidified CO_2 (flue gas) stream could favor carbonation in composites having low water contents (e.g., dry-cast composites) that are processed at higher temperatures. As an example, the flue gas emitted from a coal-fired power plant features a temperature (T) and a water vapor content of (w_v, v/v) on the order of 50 °C ≤ T ≤ 140 °C and 12 % ≤ w_v ≤ 16 %.[290,291] The water present in flue gas could thus compensate for water loss due to evaporation at such temperatures.

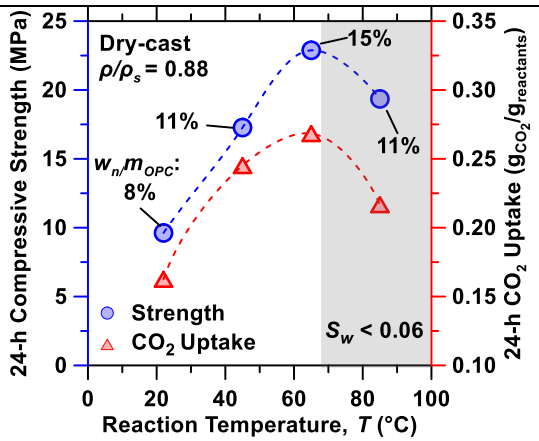

Figure 6.4: The evolution of 24-h compressive strength and CO_2 uptake as a function of the reaction temperature for dry-cast composites. Herein, carbonation was carried out using 12 % CO_2 [v/v].

6.3.3 Long-term strength development of carbonated composites

The strength evolution of carbonated composites after following CO_2 processing is relevant because the compressive strength of cementitious materials at 28 days currently serves as an important specification / compliance attribute in structural design.[292] Therefore, wet-cast portlandite-enriched composites with S_w = 0.65 were either: (a) cured in saturated limewater ($Ca(OH)_2$ solution) at 22 °C for up to 28 d or (b) carbonated for 12 h at 45 °C before curing in saturated limewater was continued until 28 d. To better assess the effects of portlandite enrichment, the strength evolutions of portlandite-free composites (i.e., where the binder was simply composed of OPC and FA) were also examined. In portlandite-free composites, carbonation induced a small increase in compressive strength and negligible CO_2 uptake at early ages (≈ 3 % by mass of binder), which is typical for early-age concrete carbonation.[267,293] However, this early-age strength gain diminished over time (Figure 6.5a) due to the coverage of reacting particle surfaces by carbonate precipitates, which hinders hydration and pozzolanic reactions relative to non-carbonated composites in the longer term, i.e., see reduced non-evaporable water contents as shown in Figure 6.5(b). This draws into question the approach of carbonating *fresh* OPC-based composites with respect to late-age strengthening and durability.[263,268,293] Similar reductions in the reactivity of OPC-based materials following carbonation have often been attributed to the formation of surficial barriers on anhydrous and/or hydrated OPC phases (C-S-H and $Ca(OH)_2$), and to the consumption of $Ca(OH)_2$ during carbonation (see Figure 6.5c).[263,294,295]

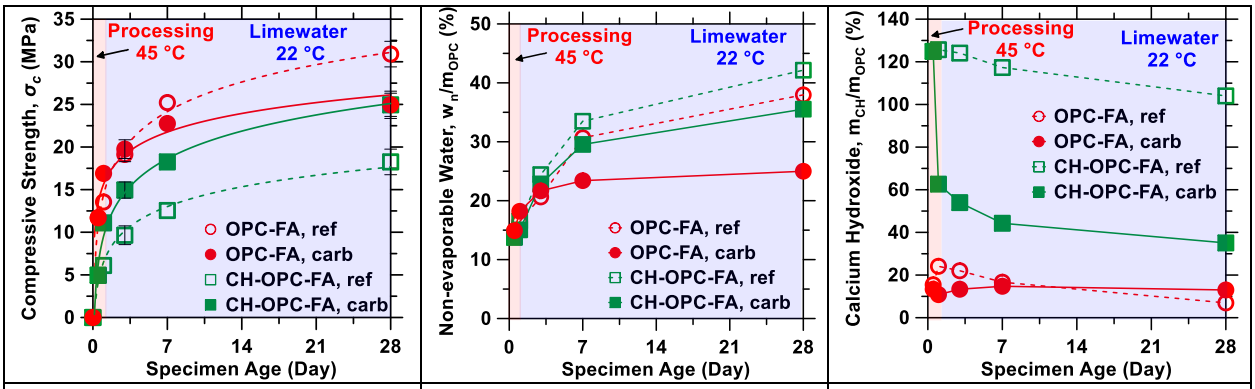

Figure 6.5: The evolution of **(a)** compressive strength, **(b)** normalized non-evaporable water content, and **(c)** normalized calcium hydroxide content in wet-cast portlandite-enriched (CH-OPC-FA) and portlandite-free (OPC-FA) composites during drying, carbonation, and limewater curing. The resuts of non-carbonated specimens with and without portlandite are also shown for comparison. The carbonated specimens were dried at 45 °C for 12 h then exposed to CO_2 for 12 h at 45 °C, whereas the non-carbonated specimens were dried at 45 °C for 24 h before limewater curing. Carbonation was carried out using 12 % CO_2 [v/v]. As indicated in **(a)**, the portlandite-enriched (CH-OPC-FA) composites featured 4.3× higher CO_2 uptake than portlandite-free (OPC-FA) composites. The "pink-shaded" and "blue-shaded" regions indicate vapor-phase processing (drying and carbonation) and limewater curing durations.

In contrast, the portlandite-enriched composites exposed to CO_2 featured strengths that are higher than that of the non-carbonated reference composite not only during CO_2 exposure but also when cured in limewater, manifesting a strength that is 7 MPa (≈ 40 %) higher after 28 days of aging (Figure 6.5a). OPC hydration in the carbonated portlandite-enriched composites, interestingly, was suppressed to only a minor degree relative to its non-carbonated reference (Figure 6.5b) and was nearly equivalent to that of the hydrated portlandite-free binder. This nature of enhanced later-age strength development of the portlandite-enriched composites suggests that surface localization of carbonation products in the vicinity of the *easier to carbonate portlandite grains* results in reduced surface obstructions on OPC (and other reactant) particulates in these composites.[240,268] Moreover, despite the significant consumption of portlandite during carbonation, the progress of pozzolanic

reactions of carbonated portlandite-enriched binders proceeded unabated during curing, as represented by the progressive increase in non-evaporable water content (Figure 6.5b) and the corresponding reduction in portlandite contents (Figure 6.5c). It is furthermore observed that despite substantial portlandite consumption in the carbonated portlandite-enriched composite, residual portlandite remains that is not converted into $CaCO_3$. While this does suggest the potential to extend the carbonation processing window (i.e., to consume more portlandite), it shows an ability to explicitly control how much residual portlandite remains, e.g., to maintain a sufficient pH buffer to allow for the formation of passivation films on reinforcing steel surfaces as appropriate to hinder corrosion.[243,296] Notably, the portlandite-enriched composite had an equivalent 28-d strength to the carbonated portlandite-free composite, while containing less than half of the OPC content and taking up 4.3× more CO_2. Admittedly, this strength was around 83 % that of the reference (non-carbonated) OPC-FA composite. However, the embodied CO_2 intensity of the carbonated portlandite-enriched composite is – conservatively, i.e., in spite of incomplete portlandite consumption – nearly 50 % lower when aspects of both CO_2 avoidance and uptake are taken into account. Furthermore, by applying a slightly higher temperature as typical for flue gas exhaust, it is noted that portlandite-enriched dry-cast composites were able to deliver the same strength as their wet-cast counterparts (Figure 6.4) – although in 24 h rather than 28 d, and once again, with a greatly reduced embodied CO_2 footprint.

6.4 Summary and conclusions

This paper has elucidated the potential of *in situ* CO_2 mineralization and the formation of carbonate precipitates as a pathway for: (a) ensuring the cementation of construction relevant composites, and (b) as a means for enabling the utilization of dilute CO_2 waste streams at ambient pressure, and near-ambient temperatures. The understanding gained offers new means to design *low-CO_2* cementation agents that can serve as a functional replacement to OPC, the CO_2-intensive cementation agent used by the construction sector for over a century. Special focus was paid to elucidate the roles of microstructure and pore (moisture) saturation on affecting CO_2 transport into 3D-monoliths, and the consequent impacts on the rate and progress of carbonation reactions and strength development. In general, while reducing pore saturation enhances carbonation, this is only true so long as $S_{w,c} > 0.10$, below which the hindered dissolution of portlandite suppresses carbonation. Unsurprisingly, dry-cast composites due to their lower water content, and the reduced surface coverage produced on their reactant surfaces (e.g., due to OPC hydration) are more effectively carbonated. Importantly, it is shown that the formation of carbonate precipitates is able to effectively bind proximate surfaces mineral particle surfaces thereby resulting in the carbonated dry-cast composites that achieve a compressive strength of ≈ 25 MPa in 24 h. It is furthermore shown that the formation of carbonate precipitates yields strengthening at the level of ≈ 15 MPa per unit CO_2 uptake of reactants. This is substantially higher, e.g., than that noted by Wei et al.[241] in their studies of fly ash carbonation. The outcomes of this work offer guidelines regarding process routes to develop portlandite-enriched cementation agents. This is significant as such novel binders, on account of their CO_2 uptake and avoidance, feature a CO_2 intensity (global warming potential, GWP) that is substantially lower than that of typical OPC-based binders, which are

commonly *diluted* using fly ash. Evidently, the nature of processing conditions discussed herein are well-suited for the precast manner of fabrication. This creates opportunities to utilize portlandite-enriched binders to manufacture concrete masonry and precast concrete components that can be used for both structural ("load bearing") and non-structural construction.

6.5 Supporting information

6.5.1 Materials

The bulk oxide compositions of the ordinary portland cement (OPC) and fly ash as determined using X-ray fluorescence (XRF) are presented in Table 6.1. The densities of the portlandite, fly ash, and OPC were measured using helium pycnometry (Accupyc II 1340, Micromeritics) are: 2235 kg/m^3, 2460 kg/m^3, and 3140 kg/m^3, respectively. The particle size distributions (PSDs) of the solids were measured using static light scattering (SLS; LS13-320, Beckman Coulter; see Figure 6.6).

Table 6.1: The oxide composition (by mass) of the fly ash and OPC as determined by XRF.

Oxide	Mass (%)	
	Fly ash	Type I/II OPC
SiO_2	60.84	21.21
Al_2O_3	22.30	4.16
Fe_2O_3	4.75	3.85
SO_3	0.62	2.81
CaO	6.38	65.50
Na_2O	2.07	0.18
MgO	1.80	1.98
K_2O	1.23	0.32

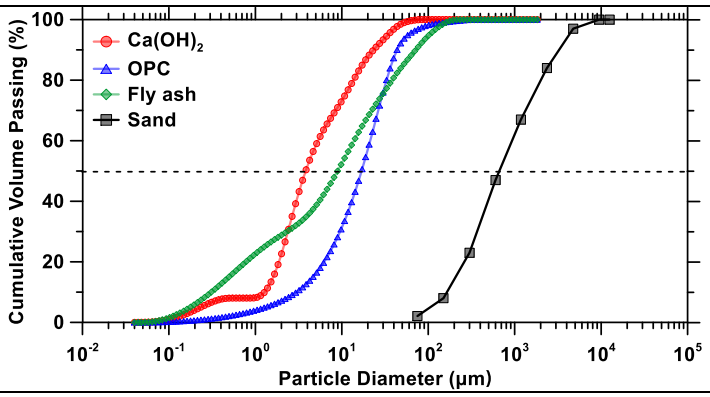

Figure 6.6: The particle size distributions of the solids as measured by static light scattering (for binder materials) and sieve analysis (for sand). The median particle diameters (d_{50}) were 3.8 µm, 8.9 µm, and 17.2 µm for the portlandite, fly ash, and OPC, respectively.

6.5.2 Drying and carbonation processing

A schematic of the drying/carbonation reactors and instrumentation is illustrated in Figure 6.7.

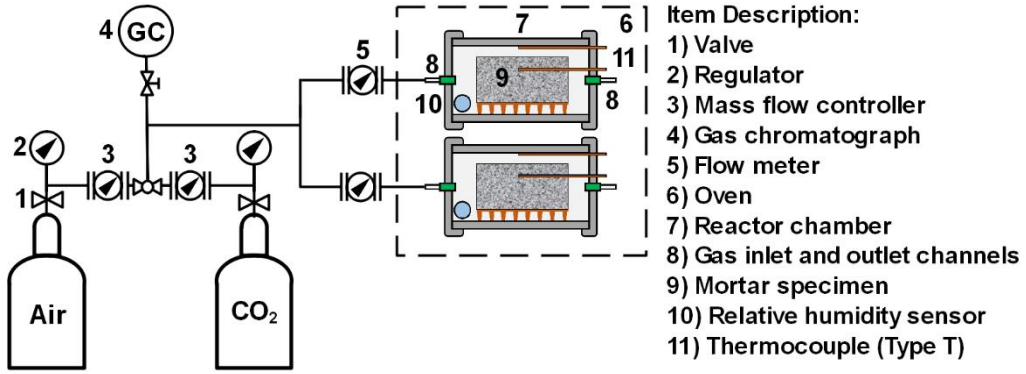

Figure 6.7: A schematic of the drying and carbonation apparatus showing the flow-through reactors and related online instrumentation. The experiments were carried out at ambient pressure (p ≈ 1 bar).

6.5.3 Experimental methods

Moisture diffusion coefficient: The sides of the cylinders (50 mm × 25 mm for wet-cast and 75 mm × 25 mm for dry-cast; $d \times h$) were sealed using a silicone sealant and aluminum tape to ensure 1-D diffusion. For this boundary condition, Fick's 2nd law can be expressed analytically using a Taylor expansion of the Error function as follows:[266]

$$\frac{m_t}{m_\infty} = 1 - \sum_{n=0}^{n=\infty} \frac{8}{(2n+1)^2\pi^2} \exp\left(\frac{-D_{tot}(2n+1)^2\pi^2 t}{4L^2}\right) \quad \textbf{(6.1)}$$

where m_t (g) is the mass loss at a given time, m_∞ (g) is the ultimate mass loss (i.e., at the infinite time; at equilibrium), t (s) is time, and L (m) = 0.0125 m is half of the sample thickness.

6.5.4 Kinetics of drying prior to carbonation

The effects of temperature and air flow rate on the drying kinetics of wet-cast composites ("mortars") and the reduction in the degree of liquid saturation, S_w, are shown in Figures 6.8(a-b). Expectedly, higher temperatures or air flow rates accelerated drying and resulted in a prominent decrease in S_w. S_w plateaued over time under all drying conditions, and more rapidly so at higher temperatures. This plateau indicates a progressive transition in the size of pores from which water is removed. Specifically, as the internal *RH* diminishes, water is first drawn out from larger and percolated pores, and thereafter, in time from smaller sub-micron and disconnected pores.[264] Figure 6.8(c) shows the effect of compaction pressure on increasing S_w for dry-cast composites that is induced by decreasing their total porosity.

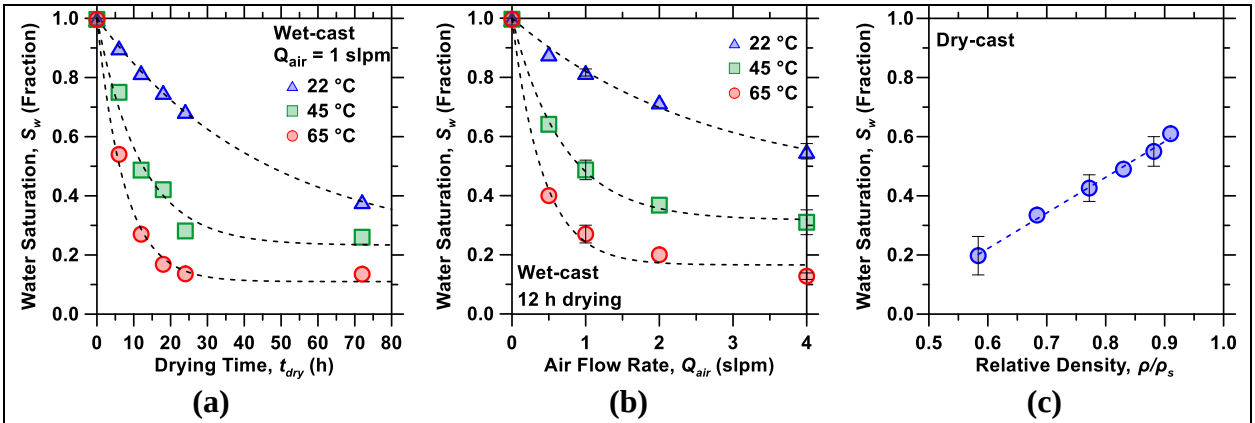

(a) **(b)** **(c)**

Figure 6.8: The time-dependent evolution of water saturation level, S_w, for wet-cast composites at different: **(a)** drying temperatures and **(b)** air flow rates**. (c)** The compaction-dependent S_w for the dry-cast composites for varying compaction levels.

6.5.5 Carbonation strengthening

Figure 6.9 displays the evolution of compressive strength as a function of the non-evaporable water content, w_n/m_{OPC}, for wet-cast composites across increasing carbonation durations. Significantly, the compressive strengths developed in carbonated composites are equivalent or superior to the sealed cured composites wherein, in the latter, strength development is simply ensured by the hydration of OPC.

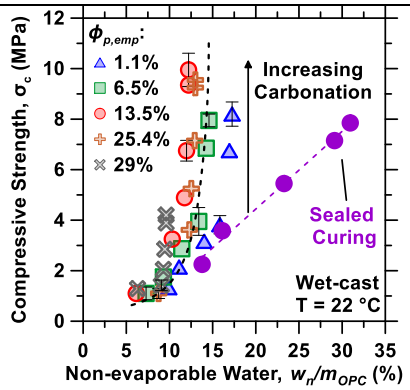

Figure 6.9: The correlation between compressive strength development and non-evaporable water content for wet-cast composites across increasing carbonation durations.

Figure 6.10(a) displays the dependence of slope of strength-CO_2 uptake relation on changes in non-evaporable water contents ($\Delta(w_n/m_{OPC})$) during carbonation for dry-cast and wet-cast composites. Similarly, the variations in strength-w_n/m_{OPC} relation with CO_2 uptake during carbonation are indicated in Figure 6.10(b).

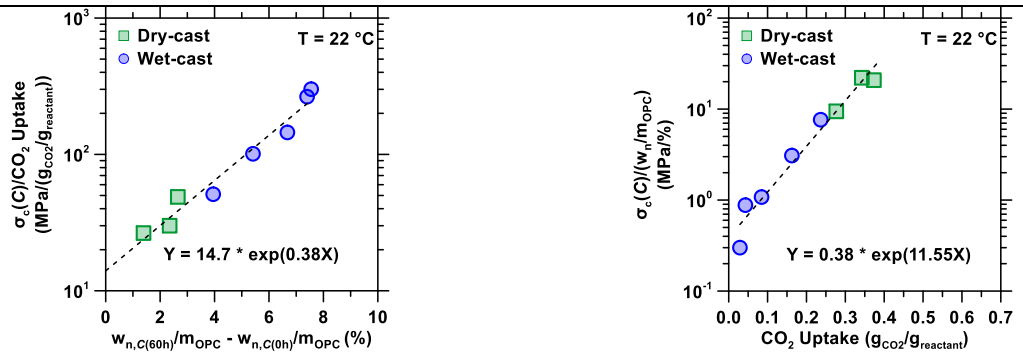

Figure 6.10: The dependence of slope of **(a)** strength-CO_2 uptake relation on changes in non-evaporable water contents ($\Delta(w_n/m_{OPC})$) and **(b)** strength-w_n/m_{OPC} relation on CO_2 uptake for dry-cast and wet-cast composites. In all cases, carbonation was carried out using 12% CO_2 [v/v] at 22 °C.

Figure 6.11 compares the microstructure and surface morphology of carbonated wet-cast and dry-cast composites at varying degrees of hydration. The images were acquired using a field emission-scanning electron microscope with an energy dispersive X-ray spectroscopy for elemental analysis (SEM-EDS; FEI NanoSEM 230). Cross-sectional disks were taken from the cylinders and immersed in IPA for 7 days to suppress OPC hydration.[297] The disks were then vacuum-dried in a desiccator for 7 days, before small coupons were taken from the disks and impregnated with epoxy, polished, and gold-coated. All SEM micrographs were acquired in secondary electron mode with a spot size of 4.0 nm, at an accelerating voltage of 10 kV, and a working distance of ≈ 5.5 mm.

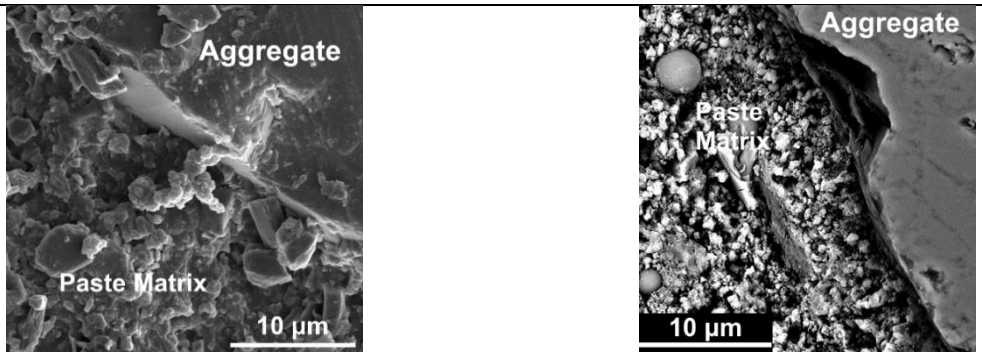

Figure 6.11: Representative SEM micrographs showing the surface morphology of carbonate products for **(a)** wet-cast (w_n/m_{OPC} = 11.5 %) and **(b)** dry-cast composites (w_n/m_{OPC} = 4.8 %).

Chapter 7. Concluding remarks

7.1 Summary of research contributions

This section highlights the specific contributions to the state of the art that were developed in the course of this research:

- The research described in Chapter 2 provided new experimental data describing the modulus of elasticity of cementitious composites containing microencapsulated phase change materials (PCMs), which was critical to understanding the influences of such soft inclusions. An exhaustive evaluation of effective medium approximations (EMAs) revealed that the EMAs of Hobbs and of Garboczi and Berryman (G-B) best-described the effective moduli of elasticity of cementitious composites containing PCM across a wide range of inclusion dosages. A design tool for the combined dosage of stiff and soft inclusions to limit the deleterious impact of PCM inclusions on modulus of elasticity was developed. The identification of more accurate EMAs offers structural engineers/designers a means to estimate the influence of PCMs and other soft inclusions, on the modulus of elasticity of multifunctional concretes.

- Chapter 3 describes the basis for the formulation of binders based on calcium aluminate cement chemistries and soluble salts (e.g., $Ca(NO_3)_2$), which bypass conventionally problematic phase conversions and demonstrate improved potential for chloride scavenging capacity. Based on the concept of thermodynamic selectivity, these formulations were designed to stabilize NO_3-AFm at the expense of metastable calcium

aluminate hydrate phases, the conversion of which degrades performance. The robustness of this process was rigorously via both thermodynamic modeling, and experimental characterization, and demonstrated to yield improved mechanical performance. These findings provoke a novel production route that may enhance the engineering properties of calcium aluminate cement mortars/concretes, while offering side benefits related to chloride capture.

- Chapter 4 demonstrated the potential for cementitious cover layers rich in NO_3-AFm to mitigate the corrosion of reinforcing steel embedded in concrete infrastructure. Novel experimental data are generated describing the physical properties, and anion capture and exchange (ACE) behavior of such formulations in response to chloride-containing solutions. The chloride binding capacity and associated nitrate release of such formulations are predicted to be sufficient to impact chloride ingress. A multi-species Nernst-Planck model was developed utilizing these experimental inputs, predicting service life increases in excess of a factor of 5 for cases of seawater exposure. These outcomes provoke the use of functional ACE coatings as a means to mitigate steel corrosion in concrete infrastructure.

- Chapter 5 elucidated the influences of processing conditions on the CO_2 mineralization (carbonation) reactions of alkaline solids, with special focus on the scaling of reaction conversion limits and kinetics from the particulate to component length scales. The final carbonation conversion of alkaline solid particulates was found to be controlled solely by the relative humidity *RH* of the contacting gas stream (i.e., independent of temperature *T* and CO_2 concentration [CO_2]), whereas conversion in monolithic components was limited

by the occlusion of reactant surfaces saturation of pores with liquid water. The carbonation kinetics of monoliths were described evaluated in relation to pore saturation, relative humidity, and surface area-to-volume ratio. The outcomes of this work inform the design of CO_2 mineralization processes that produce low-carbon concrete from flue gases.

- Chapter 6 described the strengthening of cementitious composites containing portlandite resulting from CO_2 mineralization reactions. A critical initial pore saturation $S_{w,c} > 0.10$, was identified as a requirement for significant CO_2 mineralization in dry gas streams. The carbonation performance and strengthening of both dry-cast and wet-cast composites were described in relation to microstructural diffusivity, porosity, and water saturation. The strengthening contributions of carbonate precipitates and cement hydration products were estimated. This study presents opportunities to utilize portlandite-enriched binders to manufacture load-bearing concrete masonry and precast concrete components.

7.2 Directions for future research

Based on the research advancements described herein, several directions for future research are provoked towards each research thrust:

1. Improving building energy efficiency: The study herein presented a design rule for the dosage of PCM microcapsules in cementitious composites without sacrificing composite modulus of elasticity. Further experimental study verifying the performance of the design rule and best-performing EMAs within concrete mixture formulations are of interest to further reduce risk in mixture design. The influences of soft PCM particles on the mechanical performance of concretes may be lessened relative to mortars, due to the increased impacts of aggregate interlock within concrete mixtures. Fundamentally, assumptions regarding the properties and thickness of the interfacial transition zone (ITZ) formed around inclusions of varying size and stiffness merit more detailed investigation and validation. Study of this nature may improve understanding of the mechanical performance of cementitious composites featuring functional inclusions that may be beneficial in a wide variety of applications. Alternatively, PCM microcapsules featuring shells with increased strength/stiffness may be developed as to mitigate their detrimental influences on composite performance. Such designs must be balanced with considerations of thermal performance (e.g., thermal conductivity and specific heat capacity) and feasibility of encapsulation, to ensure their viability as functional inclusions within concrete.

2. Increasing infrastructural service lifetimes: Although finite element modeling predicted service lifetime improvements associated with the use of chloride-scavenging cover layers,

experimental study validating these modeling predictions would aid in the refinement of these predictions, and identification of additional influential factors that may influence the performance of these systems in practical chloride exposure. For example, while strong bonding between the cover layer and bulk concrete is expected due to the favorable engineering properties of calcium aluminate cements, aspects related of bonding and differential expansion induced by coefficient of thermal expansion mismatch across the layers require further investigation. Detailed assessments of engineering performance and cracking of these formulations under cyclical loading are also required to enable their uses as bridge-deck covers. Furthermore, the cost effectiveness of such cover layers must be evaluated in more detail in comparison to conventional corrosion-mitigation strategies. These calculations may be informed by (validated) outputs of finite element models and should consider costs associated with the cover-layer (i.e., related to the binder content, calcium nitrate dosage, and thickness) against the incremental improvements in service life-time thus engendered. Modeling should also consider the influences of periodic "mill-and-fill" operations, which may be used to replace the cover layer and replenish its chloride binding capacity. Such actions will further establish the attractiveness of chloride-scavenging cover layers as corrosion mitigation measures.

3. Developing low-carbon cementing binders that mineralize CO_2: The research herein established the dependence of carbonation reactions and the resulting strengthening within cementing composites on processing conditions and material compositions. Although carbonation reaction kinetics and conversion limitations were noted to scale in relation to specimen surface area-to-volume ratio, the carbonation performance of actual concrete geometries (e.g., concrete masonry units) in properly scaled reactors must be directly evaluated. In such conditions, imperfect

gas flow and mixing across the component's surfaces, and within the bulk of the free reactor volume may significantly decrease reaction rates. Better elucidating the influences of gas flow patterns on carbonation is a critical step towards upscaling the CO_2 mineralization process into reactor systems that may be integrated with actual emissions sources to produce low-carbon concrete products. Such understanding will define the control schemes necessary to successfully achieve the design properties of the mineralized concretes (e.g., CO_2 uptake per unit mass, compressive strength, density, water absorption, and drying shrinkage) within the allotted CO_2 exposure cycles. These actions towards mineralization process design will concurrently inform more highly refined lifecycle and technoeconomic analysis of the carbonated concrete products / fabrication process, which are required to improve mixture design and processing in relation to a given CO_2 source. Efforts towards these ends are currently underway in support of a field demonstration of the CO_2 mineralization process.

References

(1) Mehta, P. K. Concrete. Structure, Properties and Materials. **1986**.

(2) Taylor, H. F. W. *Cement Chemistry*; Thomas Telford, 1997.

(3) Sant, G.; Ferraris, C. F.; Weiss, J. Rheological Properties of Cement Pastes: A Discussion of Structure Formation and Mechanical Property Development. *Cem. Concr. Res.* **2008**, *38* (11), 1286–1296. https://doi.org/10.1016/j.cemconres.2008.06.008.

(4) Kosmatka, S. H.; Wilson, M. L. *Design and Control of Concrete Mixtures*, 15th ed.; Portland Cement Association: Skokie, IL, USA, 2011.

(5) Mehta, P. K.; Monteiro, P. J. *Concrete: Microstructure, Properties, and Materials*, 3rd ed.; McGraw-Hill Education, 2014.

(6) Miller, S. A.; Horvath, A.; Monteiro, P. J. M. Readily Implementable Techniques Can Cut Annual CO2 Emissions from the Production of Concrete by over 20%. *Environ. Res. Lett.* **2016**, *11* (7), 074029. https://doi.org/10.1088/1748-9326/11/7/074029.

(7) Barcelo, L.; Kline, J.; Walenta, G.; Gartner, E. Cement and Carbon Emissions. *Mater. Struct.* **2013**, *47* (6), 1055–1065. https://doi.org/10.1617/s11527-013-0114-5.

(8) California Environmental Protection Agency Air Resources Board. Assembly Bill 32 Overview http://www.arb.ca.gov/cc/ab32/ab32.htm.

(9) The China Carbon Market Just Launched, And It's The World's Largest. Here's How It Can Succeed. *Forbes*. December 19, 2017.

(10) *2016 California Green Building Standards Code, Part 11*; International Code Council.

(11) ZERO Code.

(12) USGBC. LEED https://new.usgbc.org/leed.

(13) The Living Future Institute. Living Building Challenge https://living-future.org/lbc/.

(14) Newsham, G. R.; Mancini, S.; Birt, B. J. Do LEED-Certified Buildings Save Energy? Yes, But…. *Energy Build.* **2009**, *41* (8), 897–905. https://doi.org/10.1016/j.enbuild.2009.03.014.

(15) Scofield, J. H. Do LEED-Certified Buildings Save Energy? Not Really…. *Energy Build.* **2009**, *41* (12), 1386–1390. https://doi.org/10.1016/j.enbuild.2009.08.006.

(16) The 2030 Challenge for Products | Architecture 2030.

(17) Zero Net Energy http://www.cpuc.ca.gov/ZNE/ (accessed Jun 11, 2018).

(18) Zero Energy. *International Living Future Institute*.

(19) Bonta, R.; Eggman, S.; Steinorth, M. *Assembly Bill 262 - Buy Clean California Act*; 2017.

(20) Le Quéré, C.; Andrew, R. M.; Friedlingstein, P.; Sitch, S.; Pongratz, J.; Manning, A. C.; Korsbakken, J. I.; Peters, G. P.; Canadell, J. G.; Jackson, R. B. Global Carbon Budget 2017. *Earth Syst. Sci. Data* **2018**, *10* (1), 405.

(21) CBRE; Maastricht University. *2017 National Green Building Adoption Index*; 2017.

(22) ASCE. 2017 Infrastructure Report Card http://www.infrastructurereportcard.org (accessed Apr 25, 2017).

(23) Mindess, S.; Young, J. F.; Darwin, D. *Concrete*, 2nd ed.; Prentice Hall: Upper Saddle River, NJ, 2003.

(24) Cabeza, L. F.; Castellón, C.; Nogués, M.; Medrano, M.; Leppers, R.; Zubillaga, O. Use of Microencapsulated PCM in Concrete Walls for Energy Savings. *Energy Build.* **2007**, *39* (2), 113–119. https://doi.org/10.1016/j.enbuild.2006.03.030.

(25) Arce, P.; Castellón, C.; Castell, A.; Cabeza, L. F. Use of Microencapsulated PCM in Buildings and the Effect of Adding Awnings. *Energy Build.* **2012**, *44*, 88–93. https://doi.org/10.1016/j.enbuild.2011.10.028.

(26) Tyagi, V. V.; Buddhi, D. PCM Thermal Storage in Buildings: A State of Art. *Renew. Sustain. Energy Rev.* **2007**, *11* (6), 1146–1166. https://doi.org/10.1016/j.rser.2005.10.002.

(27) Khudhair, A. M.; Farid, M. M. A Review on Energy Conservation in Building Applications with Thermal Storage by Latent Heat Using Phase Change Materials. *Energy Convers. Manag.* **2004**, *45* (2), 263–275. https://doi.org/10.1016/S0196-8904(03)00131-6.

(28) Kuznik, F.; David, D.; Johannes, K.; Roux, J.-J. A Review on Phase Change Materials Integrated in Building Walls. *Renew. Sustain. Energy Rev.* **2011**, *15* (1), 379–391. https://doi.org/10.1016/j.rser.2010.08.019.

(29) Tyagi, V. V.; Kaushik, S. C.; Tyagi, S. K.; Akiyama, T. Development of Phase Change Materials Based Microencapsulated Technology for Buildings: A Review. *Renew. Sustain. Energy Rev.* **2011**, *15* (2), 1373–1391. https://doi.org/10.1016/j.rser.2010.10.006.

(30) Fernandes, F.; Manari, S.; Aguayo, M.; Santos, K.; Oey, T.; Wei, Z.; Falzone, G.; Neithalath, N.; Sant, G. On the Feasibility of Using Phase Change Materials (PCMs) to Mitigate Thermal Cracking in Cementitious Materials. *Cem. Concr. Compos.* **2014**, *51*, 14–26. https://doi.org/10.1016/j.cemconcomp.2014.03.003.

(31) Hunger, M.; Entrop, A. G.; Mandilaras, I.; Brouwers, H. J. H.; Founti, M. The Behavior of Self-Compacting Concrete Containing Micro-Encapsulated Phase Change Materials. *Cem. Concr. Compos.* **2009**, *31* (10), 731–743. https://doi.org/10.1016/j.cemconcomp.2009.08.002.

(32) Fenollera, M.; Míguez, J.; Goicoechea, I.; Lorenzo, J.; Ángel Álvarez, M. The Influence of Phase Change Materials on the Properties of Self-Compacting Concrete. *Materials* **2013**, *6* (8), 3530–3546. https://doi.org/10.3390/ma6083530.

(33) Meshgin, P.; Xi, Y.; Li, Y. Utilization of Phase Change Materials and Rubber Particles to Improve Thermal and Mechanical Properties of Mortar. *Constr. Build. Mater.* **2012**, *28* (1), 713–721. https://doi.org/10.1016/j.conbuildmat.2011.10.039.

(34) Eldin, N.; Senouci, A. Rubber-Tire Particles as Concrete Aggregate. *J. Mater. Civ. Eng.* **1993**, *5* (4), 478–496.

(35) Siddique, R.; Naik, T. R. Properties of Concrete Containing Scrap-Tire Rubber–an Overview. *Waste Manag.* **2004**, *24* (6), 563–9. https://doi.org/10.1016/j.wasman.2004.01.006.

(36) Siddique, R.; Khatib, J.; Kaur, I. Use of Recycled Plastic in Concrete: A Review. *Waste Manag.* **2008**, *28* (10), 1835–52.

(37) Babu, K. G.; Babu, D. S. Behaviour of Lightweight Expanded Polystyrene Concrete Containing Silica Fume. *Cem. Concr. Res.* **2003**, *33* (5), 755–762. https://doi.org/10.1016/S0008-8846(02)01055-4.

(38) Bouvard, D.; Chaix, J. M.; Dendievel, R.; Fazekas, A.; Létang, J. M.; Peix, G.; Quenard, D. Characterization and Simulation of Microstructure and Properties of EPS Lightweight Concrete. *Cem. Concr. Res.* **2007**, *37* (12), 1666–1673. https://doi.org/10.1016/j.cemconres.2007.08.028.

(39) Mazaheripour, H.; Ghanbarpour, S.; Mirmoradi, S. H.; Hosseinpour, I. The Effect of Polypropylene Fibers on the Properties of Fresh and Hardened Lightweight Self-Compacting Concrete. *Constr. Build. Mater.* **2011**, *25* (1), 351–358. https://doi.org/10.1016/j.conbuildmat.2010.06.018.

(40) Miled, K.; Sab, K.; Le Roy, R. Particle Size Effect on EPS Lightweight Concrete Compressive Strength: Experimental Investigation and Modelling. *Mech. Mater.* **2007**, *39* (3), 222–240. https://doi.org/10.1016/j.mechmat.2006.05.008.

(41) Shin, K. J.; Bucher, B.; Weiss, J. Role of Lightweight Synthetic Particles on the Restrained Shrinkage Cracking Behavior of Mortar. *J. Mater. Civ. Eng.* **2011**, *23* (5), 597–605. https://doi.org/10.1061/(ASCE)MT.1943-5533.0000213.

(42) Popovics, S. A Hypothesis Concerning the Effects of Macro-Porosity on Mechanical Properties of Concrete. In *Fracture of Concrete and Rock*; Springer, 1989; pp 170–174.

(43) Le Roy, R.; Parant, E.; Boulay, C. Taking into Account the Inclusions' Size in Lightweight Concrete Compressive Strength Prediction. *Cem. Concr. Res.* **2005**, *35* (4), 770–775. https://doi.org/10.1016/j.cemconres.2004.06.002.

(44) Cui, H.; Liao, W.; Memon, S. A.; Dong, B.; Tang, W. Thermophysical and Mechanical Properties of Hardened Cement Paste with Microencapsulated Phase Change Materials for Energy Storage. *Materials* **2014**, *7* (12), 8070–8087. https://doi.org/10.3390/ma7128070.

(45) Ghaly, A. M.; Gill, M. S. Compression and Deformation Performance of Concrete Containing Postconsumer Plastics. *J. Mater. Civ. Eng.* **2004**, *16* (4), 289–296. https://doi.org/10.1061/(ASCE)0899-1561(2004)16:4(289).

(46) Ganjian, E.; Khorami, M.; Maghsoudi, A. A. Scrap-Tyre-Rubber Replacement for Aggregate and Filler in Concrete. *Constr. Build. Mater.* **2009**, *23* (5), 1828–1836. https://doi.org/10.1016/j.conbuildmat.2008.09.020.

(47) Xu, J.; Chu, H.; Xu, Y.; Li, Y.; Jiang, L. Prediction of Compressive Strength and Elastic Modulus of Expanded Polystyrene Lightweight Concrete. *Mag. Concr. Res.* **2015**, *67* (17), 954–962. https://doi.org/10.1680/macr.14.00375.

(48) Scrivener, K. L.; Crumbie, A. K.; Laugesen, P. The Interfacial Transition Zone (ITZ) Between Cement Paste and Aggregate in Concrete. *Interface Sci.* **2004**, *12* (4), 411–421. https://doi.org/10.1023/B:INTS.0000042339.92990.4c.

(49) Monteiro, P.; Maso, J. C.; Ollivier, J. P. The Aggregate-Mortar Interface. *Cem. Concr. Res.* **1985**, *15* (6), 953–958.

(50) Ping, X.; Beaudoin, J. J.; Brousseau, R. Effect of Aggregate Size on Transition Zone Properties at the Portland Cement Paste Interface. *Cem. Concr. Res.* **1991**, *21* (6), 999–1005. https://doi.org/10.1016/0008-8846(91)90059-Q.

(51) Maekawa, K.; Ishida, T.; Kishi, T. *Multi-Scale Modeling of Structural Concrete*; CRC Press, 2008.

(52) Voigt, W. Ueber Die Beziehung Zwischen Den Beiden Elasticitätsconstanten Isotroper Körper. *Ann. Phys.* **1889**, 573–587.

(53) Reuss, A. Berechnung Der Fließ Grenze von Mischkristallen Auf Grund Der Plastizitätsbedingung Für Einkristalle. *ZAMM - Z. Für Angew. Math. Mech.* **1929**, *9* (1), 49–58. https://doi.org/10.1002/zamm.19290090104.

(54) Hansen, T. Influence of Aggregate and Voids on Modulus of Elasticity of Concrete, Cement Mortar, and Cement Paste. *ACI J. Proc.* **1965**, No. 62, 193–216.

(55) Hill, R. The Elastic Behaviour of a Crystalline Aggregate. *Proc. Phys. Soc. Sect. A* **1952**, *65* (5), 349–354.

(56) Hashin, Z.; Shtrikman, S. A Variational Approach to the Theory of the Elastic Behaviour of Multiphase Materials. *J. Mech. Phys. Solids* **1963**, *11* (2), 127–140.

(57) Walpole, L. On Bounds for the Overall Elastic Moduli of Inhomogeneous Systems—I. *J. Mech. Phys. Solids* **1966**, *14* (1964).

(58) Nilsen, A. U.; Monteiro, P. Concrete: A Three Phase Material. *Cem. Concr. Res.* **1993**, *23* (1), 147–151.

(59) Hashin, Z. Analysis of Composite Materials—a Survey. *J. Appl. Mech.* **1983**, *50* (September 1983), 481–505.

(60) Hobbs, D. W. The Dependence of the Bulk Modulus, Young's Modulus, Creep, Shrinkage and Thermal Expansion of Concrete upon Aggregate Volume Concentration. *Matér. Constr.* **1971**, *4* (2), 107–114. https://doi.org/10.1007/BF02473965.

(61) Zimmerman, R.; King, M.; Monteiro, P. The Elastic Moduli of Mortar as a Porous-Granular Material. *Cem. Concr. Res.* **1986**, *16* (2), 239–245.

(62) Christensen, R.; Lo, K. Solutions for Effective Shear Properties in Three Phase Sphere and Cylinder Models. *J. Mech. Phys. Solids* **1979**, *27*, 315–330.

(63) Smith, J. C. Simplification of van Der Poel's Formula for the Shear Modulus of a Particulate Composite. *J. Res. Natl. Bur. Stand. Sect. Phys. Chem.* **1975**, *79A* (2), 419. https://doi.org/10.6028/jres.079A.007.

(64) Christensen, R. A Critical Evaluation for a Class of Micro-Mechanics Models. *J Mech Phys Solids* **1990**, *38* (3), 379–404.

(65) Hashin, Z. The Elastic Moduli of Heterogeneous Materials. *J. Appl. Mech.* **1962**, 143–150.

(66) Huang, Y.; Hu, K.; Wei, X.; Chandra, A. A Generalized Self-Consistent Mechanics Method for Composite Materials with Multiphase Inclusions. *J. Mech. Phys. Solids* **1994**, *42* (3).

(67) Mori, T.; Tanaka, K. Average Stress in Matrix and Average Elastic Energy of Materials with Misfitting Inclusions. *Acta Metall.* **1973**, 1–4.

(68) Yaman, I. O.; Aktan, H. M.; Hearn, N. Active and Non-Active Porosity in Concrete Part II: Evaluation of Existing Models. *Mater. Struct.* **2002**, *35* (2), 110–116.

(69) Weng, G. Some Elastic Properties of Reinforced Solids, with Special Reference to Isotropic Ones Containing Spherical Inclusions. *Int. J. Eng. Sci.* **1984**, *22* (7), 845–856.

(70) Norris, A. An Examination of the Mori-Tanaka Effective Medium Approximation for Multiphase Composites. *J. Appl. Mech.* **1989**, *56* (March 1989), 83–88.

(71) Kuster, G.; Toksöz, M. Velocity and Attenuation of Seismic Waves in Two-Phase Media: Part I. Theoretical Formulations. *Geophysics* **1974**, *39* (5), 587–606.

(72) Berryman, J. G.; Berge, P. A. Critique of Two Explicit Schemes for Estimating Elastic Properties of Multiphase Composites. *Mech. Mater.* **1996**, *22* (2), 149–164. https://doi.org/10.1016/0167-6636(95)00035-6.

(73) McLaughlin, R. A Study of the Differential Scheme for Composite Materials. *Int. J. Eng. Sci.* **1977**, *15*, 237–244.

(74) Hildebrand, F. B. *Introduction to Numerical Analysis*; Courier Corporation, 1987.

(75) Miled, K.; Sab, K.; Le Roy, R. Effective Elastic Properties of Porous Materials: Homogenization Schemes vs Experimental Data. *Mech. Res. Commun.* **2011**, *38* (2), 131–135. https://doi.org/10.1016/j.mechrescom.2011.01.009.

(76) Garboczi, E. J.; Berryman, J. G. Elastic Moduli of a Material Containing Composite Inclusions: Effective Medium Theory and Finite Element Computations. *Mech. Mater.* **2001**, *33* (8), 455–470. https://doi.org/10.1016/S0167-6636(01)00067-9.

(77) Norris, A. N. A Differential Scheme for the Effective Moduli of Composites. *Mech. Mater.* **1985**, *4*, 1–16.

(78) Lutz, M.; Monteiro, P.; Zimmerman, R. Inhomogeneous Interfacial Transition Zone Model for the Bulk Modulus of Mortar. *Cem. Concr. Res.* **1997**, *27* (7), 1113–1122.

(79) Hashin, Z.; Monteiro, P. J. M. An Inverse Method to Determine the Elastic Properties of the Interphase between the Aggregate and the Cement Paste. *Cem. Concr. Res.* **2002**, *32* (8), 1291–1300. https://doi.org/10.1016/S0008-8846(02)00792-5.

(80) Wang, J. A.; Lubliner, J.; Monteiro, P. J. M. Effect of Ice Formation on the Elastic Moduli of Cement Paste and Mortar. *Cem. Concr. Res.* **1988**, *18* (6), 874–885.

(81) Königsberger, M.; Pichler, B.; Hellmich, C. Micromechanics of ITZ-Aggregate Interaction in Concrete Part I: Stress Concentration. *J. Am. Ceram. Soc.* **2014**, *97* (2), 535–542. https://doi.org/10.1111/jace.12591.

(82) Sun, Z.; Garboczi, E. J.; Shah, S. P. Modeling the Elastic Properties of Concrete Composites: Experiment, Differential Effective Medium Theory, and Numerical Simulation. *Cem. Concr. Compos.* **2007**, *29* (1), 22–38. https://doi.org/10.1016/j.cemconcomp.2006.07.020.

(83) Yang, C. Effect of the Interfacial Transition Zone on the Transport and the Elastic Properties of Mortar. *Mag. Concr. Res.* **2003**, *55* (4), 305–312. https://doi.org/10.1680/macr.2003.55.4.305.

(84) Li, C. Q.; Zhou, X. Z.; Zheng, J. J. Thickness of Interfacial Transition Zone and Cement Content Profiles around Aggregates. *Mag. Concr. Res.* **2005**, *57* (7), 397–406. https://doi.org/10.1680/macr.2005.57.7.397.

(85) Königsberger, M.; Pichler, B.; Hellmich, C. Micromechanics of ITZ-Aggregate Interaction in Concrete Part II: Strength Upscaling. *J. Am. Ceram. Soc.* **2014**, *97* (2), 543–551. https://doi.org/10.1111/jace.12606.

(86) Zheng, J. J.; Li, C. Q.; Zhou, X. Z. Characterization of Microstructure of Interfacial Transition Zone in Concrete. *ACI Mater. J.* **2005**, *102* (4), 265–271.

(87) Garboczi, E. J.; Douglas, J. F. Intrinsic Conductivity of Objects Having Arbitrary Shape and Conductivity. *Phys. Rev. E* **1996**, *53* (6), 6169–6180. https://doi.org/10.1103/PhysRevE.53.6169.

(88) Garboczi, E. J.; Douglas, J. F.; Bohn, R. B. A Hybrid Finite Element-Analytical Method for Determining the Intrinsic Elastic Moduli of Particles Having Moderately Extended Shapes and a Wide Range of Elastic Properties. *Mech. Mater.* **2006**, *38* (8–10), 786–800. https://doi.org/10.1016/j.mechmat.2005.06.012.

(89) Garboczi, E. J.; Douglas, J. F. Elastic Moduli of Composites Containing a Low Concentration of Complex-Shaped Particles Having a General Property Contrast with the Matrix. *Mech. Mater.* **2012**, *51*, 53–65. https://doi.org/10.1016/j.mechmat.2012.03.009.

(90) Neithalath, N.; Ramamurthy, K. Microstructural Investigations on Aerated Concrete. *Cem. Concr. Res.* **2000**, *30* (3), 457–464. https://doi.org/10.1016/S0008-8846(00)00199-X.

(91) Ma, H.; Li, Z. Multi-Aggregate Approach for Modeling Interfacial Transition Zone in Concrete. *ACI Mater. J.* **2014**, *111* (2).

(92) Bui, D. D.; Hu, J.; Stroeven, P. Particle Size Effect on the Strength of Rice Husk Ash Blended Gap-Graded Portland Cement Concrete. *Cem. Concr. Compos.* **2005**, *27* (3), 357–366. https://doi.org/10.1016/j.cemconcomp.2004.05.002.

(93) Stroeven, P.; Stroeven, M. Reconstructions by SPACE of the Interfacial Transition Zone. *Cem. Concr. Compos.* **2001**, *23* (2–3), 189–200. https://doi.org/10.1016/S0958-9465(00)00076-7.

(94) *ASTM Standard C150/C150M-16e1. Standard Specification for Portland Cement*; ASTM International: West Conshohocken, PA, 2016.

(95) *ASTM Standard C778-17. Standard Specification for Standard Sand*; ASTM International: West Conshohocken, PA, 2013.

(96) Ferraris, C. F.; Hackley, V. A.; Avilés, A. I. Measurement of Particle Size Distribution in Portland Cement Powder: Analysis of ASTM Round Robin Studies. *Cem. Concr. Aggreg.* **2004**, *26* (2), 1–11.

(97) Gao, G.; Moya, S.; Lichtenfeld, H.; Casoli, A.; Fiedler, H.; Donath, E.; Mohwald, H. The Decomposition Process of Melamine Formaldehyde Cores: The Key Step in the Fabrication

of Ultrathin Polyelectrolyte Multilayer Capsules. *Macromol. Mater. Eng.* **2001**, *286* (6), 355–361.

(98) Ghosh, G. Dispersion-Equation Coefficients for the Refractive Index and Birefringence of Calcite and Quartz Crystals. *Opt. Commun.* **1999**, *163* (1–3), 95–102. https://doi.org/10.1016/S0030-4018(99)00091-7.

(99) *ASTM Standard C305-14. Standard Practice for Mechanical Mixing of Hydraulic Cement Pastes and Mortars of Plastic Consistency*; ASTM International: West Conshohocken, PA, 2014.

(100) *ASTM C469/C469M-14. Standard Test Method for Static Modulus of Elasticity and Poisson's Ratio of Concrete in Compression*; ASTM International: West Conshohocken, PA, 2014.

(101) Smadi, M. M.; Slate, F. O. Microcracking of High and Normal Strength Concretes Under Short and Long-Term Loadings. *ACI Mater. J.* **1989**, *86* (2), 117–127. https://doi.org/10.14359/2264.

(102) Han, S.-H.; Kim, J.-K. Effect of Temperature and Age on the Relationship between Dynamic and Static Elastic Modulus of Concrete. *Cem. Concr. Res.* **2004**, *34* (7), 1219–1227. https://doi.org/10.1016/j.cemconres.2003.12.011.

(103) *ASTM Standard C109/C109M. Compressive Strength of Hydraulic Cement Mortar (Using 2-in. or [50-Mm] Cube Specimens)*; ASTM International: West Conshohocken, PA, 2014.

(104) Hossain, M.; Ketata, C.; Islam, M. Experimental Study of Physical and Mechanical Properties of Natural and Synthetic Waxes Using Uniaxial Compressive Strength Test. In *Proceedings of third international conference on modeling, simulations, and applied optimization*; 2009; pp 1–5.

(105) Chen, X.; Zhang, S.; Wagner, G. J.; Ding, W.; Ruoff, R. S. Mechanical Resonance of Quartz Microfibers and Boundary Condition Effects. *J. Appl. Phys.* **2004**, *95* (9), 4823–4828. https://doi.org/10.1063/1.1697635.

(106) ACI 318. *Building Code Requirements for Reinforced Concrete*; Am Conc Inst: Detroit, MI, 2014.

(107) Hirsch, T. Modulus of Elasticity of Concrete Affected by Elastic Moduli of Cement Paste Matrix and Aggregate. *ACI J. Proc.* **1962**, *59* (12), 427–452.

(108) Rice, R. W. *Porosity of Ceramics: Properties and Applications*; CRC Press, 1998.

(109) Rice, R. W. Evaluating Porosity Parameters for Porosity–Property Relations. *J. Am. Ceram. Soc.* **1993**, *76* (7), 1801–1808. https://doi.org/10.1111/j.1151-2916.1993.tb06650.x.

(110) Rice, R. W. Evaluation and Extension of Physical Property-Porosity Models Based on Minimum Solid Area. *J. Mater. Sci.* **1996**, *31* (1), 102–118. https://doi.org/10.1007/BF00355133.

(111) Torquato, S. *Random Heterogeneous Materials: Microstructure and Macroscopic Properties*; Springer Science & Business Media, 2002.

(112) Bentz, D. P. Three-Dimensional Computer Simulation of Portland Cement Hydration and Microstructure Development. *J. Am. Ceram. Soc.* **1997**, *80* (1), 3–21. https://doi.org/10.1111/j.1151-2916.1997.tb02785.x.

(113) Kumar, A.; Oey, T.; Kim, S.; Thomas, D.; Badran, S.; Li, J.; Fernandes, F.; Neithalath, N.; Sant, G. Simple Methods to Estimate the Influence of Limestone Fillers on Reaction and Property Evolution in Cementitious Materials. *Cem. Concr. Compos.* **2013**, *42*, 20–29. https://doi.org/10.1016/j.cemconcomp.2013.05.002.

(114) de Larrard, F.; Sedran, T. Optimization of Ultra-High-Performance Concrete by the Use of a Packing Model. *Cem. Concr. Res.* **1994**, *24* (6), 997–1009. https://doi.org/10.1016/0008-8846(94)90022-1.

(115) Scrivener, K. L.; Nemati, K. M. The Percolation of Pore Space in the Cement Paste/Aggregate Interfacial Zone of Concrete. *Cem. Concr. Res.* **1996**, *26* (1), 35–40.

(116) Elsharief, A.; Cohen, M. D.; Olek, J. Influence of Aggregate Size, Water Cement Ratio and Age on the Microstructure of the Interfacial Transition Zone. *Cem. Concr. Res.* **2003**, *33* (11), 1837–1849. https://doi.org/10.1016/S0008-8846(03)00205-9.

(117) Khatri, R. P.; Sirivivatnanon, V.; Gross, W. Effect of Different Supplementary Cementitious Materials on Mechanical Properties of High Performance Concrete. *Cem. Concr. Res.* **1995**, *25* (1), 209–220. https://doi.org/10.1016/0008-8846(94)00128-L.

(118) Liao, K.-Y.; Chang, P.-K.; Peng, Y.-N.; Yang, C.-C. A Study on Characteristics of Interfacial Transition Zone in Concrete. *Cem. Concr. Res.* **2004**, *34* (6), 977–989. https://doi.org/10.1016/j.cemconres.2003.11.019.

(119) Lee, K. M.; Park, J. H. A Numerical Model for Elastic Modulus of Concrete Considering Interfacial Transition Zone. *Cem. Concr. Res.* **2008**, *38* (3), 396–402. https://doi.org/10.1016/j.cemconres.2007.09.019.

(120) Barnes, P.; Bensted, J. *Structure and Performance of Cements, Second Edition*; CRC Press, 2002.

(121) Scrivener, K. L.; Capmas, A. Calcium Aluminate Cements. In *Lea's Chemistry of Cement and Concrete*; Hewlett, P., Ed.; Elsevier Science & Technology Books, 2004; pp 713–782.

(122) Scrivener, K. L.; Cabiron, J.-L.; Letourneux, R. High-Performance Concretes from Calcium Aluminate Cements. *Cem. Concr. Res.* **1999**, *29* (8), 1215–1223. https://doi.org/10.1016/S0008-8846(99)00103-9.

(123) Fu, Y.; Ding, J.; Beaudoin, J. J. Conversion-Preventing Additive for High Alumina Cement Products. US5624489 A, April 29, 1997.

(124) Ding, J.; Fu, Y.; Beaudoin, J. J. Strätlingite Formation in High Alumina Cement - Silica Fume Systems: Significance of Sodium Ions. *Cem. Concr. Res.* **1995**, *25* (6), 1311–1319. https://doi.org/10.1016/0008-8846(95)00124-U.

(125) Chavda, M. A.; Kinoshita, H.; Provis, J. L. Phosphate Modification of Calcium Aluminate Cement to Enhance Stability for Immobilisation of Metallic Wastes. *Adv. Appl. Ceram.* **2014**, *113* (8), 453–459. https://doi.org/10.1179/1743676114Y.0000000147.

(126) Pérez, M.; Vázquez, T.; Triviño, F. Study of Stabilized Phases in High Alumina Cement Mortars Part I Hydration at Elevated Temperatures Followed by Carbonation. *Cem. Concr. Res.* **1983**, *13* (6), 759–770. https://doi.org/10.1016/0008-8846(83)90077-7.

(127) Damidot, D.; Lothenbach, B.; Herfort, D.; Glasser, F. P. Thermodynamics and Cement Science. *Cem. Concr. Res.* **2011**, *41* (7), 679–695. https://doi.org/10.1016/j.cemconres.2011.03.018.

(128) Anderson, G. M.; Crerar, D. A. *Thermodynamics in Geochemistry: The Equilibrium Model*; Oxford University Press, 1993.

(129) Matschei, T.; Lothenbach, B.; Glasser, F. P. The AFm Phase in Portland Cement. *Cem. Concr. Res.* **2007**, *37* (2), 118–130. https://doi.org/10.1016/j.cemconres.2006.10.010.

(130) Balonis, M.; Glasser, F. P.; Mędala, M. Influence of Calcium Nitrate and Nitrite on the Constitution of AFm and AFt Cement Hydrates. *Adv. Cem. Res.* **2011**, *23* (3), 129–143. https://doi.org/10.1680/adcr.10.00002.

(131) Balonis, M. The Influence of Inorganic Chemical Accelerators and Corrosion Inhibitors on the Mineralogy of Hydrated Portland Cement Systems. Ph.D. Dissertation, University of Aberdeen: Aberdeen, UK, 2010.

(132) Matschei, T.; Lothenbach, B.; Glasser, F. P. Thermodynamic Properties of Portland Cement Hydrates in the System CaO–Al2O3–SiO2–CaSO4–CaCO3–H2O. *Cem. Concr. Res.* **2007**, *37* (10), 1379–1410. https://doi.org/10.1016/j.cemconres.2007.06.002.

(133) Justnes, H.; Nygaard, E. C. Calcium Nitrate as a Multi-Functional Concrete Admixture. *Concrete* **2010**, *44* (1), 34.

(134) Justnes, H.; Nygaard, E. C. Technical Calcium Nitrate as Set Accelerator for Cement at Low Temperatures. *Cem. Concr. Res.* **1995**, *25* (8), 1766–1774. https://doi.org/10.1016/0008-8846(95)00172-7.

(135) Bentur, A.; Berke, N.; Diamond, S. *Steel Corrosion in Concrete: Fundamentals and Civil Engineering Practice*; CRC Press, 1997.

(136) Zhang, J.; Scherer, G. W. Comparison of Methods for Arresting Hydration of Cement. *Cem. Concr. Res.* **2011**, *41* (10), 1024–1036. https://doi.org/10.1016/j.cemconres.2011.06.003.

(137) RRUFF. American Mineralogist Crystal Structure Database http://rruff.geo.arizona.edu/AMS/amcsd.php.

(138) Kulik, D.; Berner, U.; Curti, E. Modelling Chemical Equilibrium Partitioning with the GEMS-PSI Code. **2004**.

(139) Kulik, D. A.; Wagner, T.; Dmytrieva, S. V.; Kosakowski, G.; Hingerl, F. F.; Chudnenko, K. V.; Berner, U. R. GEM-Selektor Geochemical Modeling Package: Revised Algorithm and GEMS3K Numerical Kernel for Coupled Simulation Codes. *Comput. Geosci.* **2012**, *17* (1), 1–24. https://doi.org/10.1007/s10596-012-9310-6.

(140) Mehrotra, S. On the Implementation of a Primal-Dual Interior Point Method. *SIAM J. Optim.* **1992**, *2* (4), 575–601. https://doi.org/10.1137/0802028.

(141) Balonis, M.; Glasser, F. P. The Density of Cement Phases. *Cem. Concr. Res.* **2009**, *39* (9), 733–739.

(142) Lothenbach, B.; Pelletier-Chaignat, L.; Winnefeld, F. Stability in the System CaO–Al2O3–H2O. *Cem. Concr. Res.* **2012**, *42* (12), 1621–1634. https://doi.org/10.1016/j.cemconres.2012.09.002.

(143) Jappy, T. G.; Glasser, F. P. Synthesis and Stability of Silica-Substituted Hydro Garnet Ca 3 Al 2 Si 3-x O 12-4x (OH) 4x. *Adv. Cem. Res.* **1991**, *4* (13), 1–8.

(144) Dilnesa, B. Z.; Lothenbach, B.; Le Saout, G.; Renaudin, G.; Mesbah, A.; Filinchuk, Y.; Wichser, A.; Wieland, E. Iron in Carbonate Containing AFm Phases. *Cem. Concr. Res.* **2011**, *41* (3), 311–323.

(145) Dilnesa, B. Z.; Lothenbach, B.; Renaudin, G.; Wichser, A.; Wieland, E. Stability of Monosulfate in the Presence of Iron. *J. Am. Ceram. Soc.* **2012**, *95* (10), 3305–3316.

(146) Sant, G.; Lura, P.; Weiss, J. Measurement of Volume Change in Cementitious Materials at Early Ages: Review of Testing Protocols and Interpretation of Results. *Transp. Res. Rec. J. Transp. Res. Board* **2006**, *1979*, 21–29. https://doi.org/10.3141/1979-05.

(147) Midgley, H. G.; Bhaskara Rao, P. Formation of Stratlingite, 2CaO.SiO2.Al2O3.8H2O, in Relation to the Hydration of High Alumina Cement. *Cem. Concr. Res.* **1978**, *8* (2), 169–172. https://doi.org/10.1016/0008-8846(78)90005-4.

(148) Rashid, S.; Barnes, P.; Bensted, J.; Turrillas, X. Conversion of Calcium Aluminate Cement Hydrates Re-Examined with Synchrotron Energy-Dispersive Diffraction. *J. Mater. Sci. Lett.* **1994**, *13* (17), 1232–1234. https://doi.org/10.1007/BF00270944.

(149) Rashid, S.; Barnes, P.; Turrillas, X. The Rapid Conversion of Calcium Aluminate Cement Hydrates, as Revealed by Synchrotron Energy-Dispersive Diffraction. *Adv. Cem. Res.* **1992**, *4* (14), 61–67.

(150) Nonnet, E.; Lequeux, N.; Boch, P.; Colston, S. L.; Barnes, P. In Situ X-Ray Diffraction and Young's Modulus Measurement during Heat Treatment of High-Alumina Cement Castables. *J. Am. Ceram. Soc.* **2001**, *84* (3), 583–587.

(151) Flatt, R. J.; Scherer, G. W.; Bullard, J. W. Why Alite Stops Hydrating below 80% Relative Humidity. *Cem. Concr. Res.* **2011**, *41* (9), 987–992.

(152) Midgley, H. G.; Midgley, A. The Conversion of High Alumina Cement*. *Mag. Concr. Res.* **1975**, *27* (91), 59–77.

(153) Jensen, O. M.; Hansen, P. F.; Lachowski, E. E.; Glasser, F. P. Clinker Mineral Hydration at Reduced Relative Humidities. *Cem. Concr. Res.* **1999**, *29* (9), 1505–1512.

(154) Oey Tandre; Stoian Julyan; Li Jialin; Vong Cecilia; Balonis Magdalena; Kumar Aditya; Franke Wolfram; Sant Gaurav. Comparison of Ca(NO3)2 and CaCl2 Admixtures on Reaction, Setting, and Strength Evolutions in Plain and Blended Cementing Formulations. *J. Mater. Civ. Eng.* **2015**, *27* (10), 04014267. https://doi.org/10.1061/(ASCE)MT.1943-5533.0001240.

(155) Gosselin, C. Microstructural Development of Calcium Aluminate Cement Based Systems with and without Supplementary Cementitious Materials. Ph.D. Thesis, EPFL: Switzerland, 2009.

(156) Renaudin, G.; Rapin, J.-P.; Humbert, B.; François, M. Thermal Behaviour of the Nitrated AFm Phase Ca4Al2(OH)12(NO3)2 • 4H2O and Structure Determination of the Intermediate Hydrate Ca4Al2(OH)12(NO3)2 • 2H2O. *Cem. Concr. Res.* **2000**, *30* (2), 307–314. https://doi.org/10.1016/S0008-8846(99)00251-3.

(157) Chaipanich, A.; Nochaiya, T. Thermal Analysis and Microstructure of Portland Cement-Fly Ash-Silica Fume Pastes. *J. Therm. Anal. Calorim.* **2009**, *99* (2), 487–493.

(158) Matusinović, T.; Šipušić, J.; Vrbos, N. Porosity–Strength Relation in Calcium Aluminate Cement Pastes. *Cem. Concr. Res.* **2003**, *33* (11), 1801–1806.

(159) Antonovič, V.; Kerienė, J.; Boris, R.; Aleknevičius, M. The Effect of Temperature on the Formation of the Hydrated Calcium Aluminate Cement Structure. *Procedia Eng.* **2013**, *57*, 99–106.

(160) Gosselin, C.; Gallucci, E.; Scrivener, K. Influence of Self Heating and Li 2 SO 4 Addition on the Microstructural Development of Calcium Aluminate Cement. *Cem. Concr. Res.* **2010**, *40* (10), 1555–1570.

(161) Speight, J. G. *Lange's Chemistry Handbook*; McGraw-Hill Professional, 2004.

(162) Moon, J.; Oh, J. E.; Balonis, M.; Glasser, F. P.; Clark, S. M.; Monteiro, P. J. M. High Pressure Study of Low Compressibility Tetracalcium Aluminum Carbonate Hydrates 3CaO·Al2O3·CaCO3·11H2O. *Cem. Concr. Res.* **2012**, *42* (1), 105–110. https://doi.org/10.1016/j.cemconres.2011.08.004.

(163) Justnes, H. Calcium Nitrate as Corrosion Inhibitor for Reinforced Concrete. *Innov. Dev. Concr. Mater. Constr. Thomas Telford Publ.* **2002**, 391–401.

(164) Berke, N. S.; Hicks, M. C. Predicting Long-Term Durability of Steel Reinforced Concrete with Calcium Nitrite Corrosion Inhibitor. *Cem. Concr. Compos.* **2004**, *26* (3), 191–198. https://doi.org/10.1016/S0958-9465(03)00038-6.

(165) Valcarce, M. B.; Vázquez, M. Carbon Steel Passivity Examined in Alkaline Solutions: The Effect of Chloride and Nitrite Ions. *Electrochimica Acta* **2008**, *53* (15), 5007–5015. https://doi.org/10.1016/j.electacta.2008.01.091.

(166) Balonis, M.; Lothenbach, B.; Le Saout, G.; Glasser, F. P. Impact of Chloride on the Mineralogy of Hydrated Portland Cement Systems. *Cem. Concr. Res.* **2010**, *40* (7), 1009–1022. https://doi.org/10.1016/j.cemconres.2010.03.002.

(167) Hansson, C. M. The Impact of Corrosion on Society. *Metall. Mater. Trans. A* **2011**, *42* (10), 2952–2962. https://doi.org/10.1007/s11661-011-0703-2.

(168) Poursaee, A. *Corrosion of Steel in Concrete Structures*, 1st ed.; Woodhead Publishing, 2016.

(169) Angst, U.; Elsener, B.; Jamali, A.; Adey, B. Concrete Cover Cracking Owing to Reinforcement Corrosion–Theoretical Considerations and Practical Experience. *Mater. Corros.* **2012**, *63* (12), 1069–1077.

(170) Amey, S. L.; Johnson, D. A.; Miltenberger, M. A.; Farzam, H. Predicting the Service Life of Concrete Marine Structures: An Environmental Methodology. *ACI Struct. J.* **1998**, *95* (2).

(171) Koch, G. H.; Brongers, M. P. H.; Thompson, N. G.; Virmani, Y. P.; Payer, J. H. *Corrosion Cost and Preventative Strategies in the United States*; FHWA-RD-01-156; NACE International, 2002.

(172) Federal Highway Administration. Deficient Bridges by Highway System 2015 http://www.fhwa.dot.gov/bridge/nbi/no10/defbr15.cfm (accessed Jul 10, 2016).

(173) Bertolini, L.; Elsener, B.; Pedeferri, P.; Redaelli, E.; Polder, R. B. *Corrosion of Steel in Concrete: Prevention, Diagnosis, Repair*; John Wiley & Sons, 2013.

(174) Bazant, Z. P. Physical Model for Steel Corrosion in Concrete Sea Structures—Theory. *J. Struct. Div.* **1979**, *105* (6), 1137–1153.

(175) Broomfield, J. P. *Corrosion of Steel in Concrete: Understanding, Investigation, and Repair*; E & FN Spon: London; New York, 1997.

(176) Angst, U.; Elsener, B.; Larsen, C. K.; Vennesland, Ø. Critical Chloride Content in Reinforced Concrete — A Review. *Cem. Concr. Res.* **2009**, *39* (12), 1122–1138. https://doi.org/10.1016/j.cemconres.2009.08.006.

(177) Hausmann, D. A. Steel Corrosion in Concrete- How Does It Occur? *Mater. Prot.* **1967**, *6* (11), 19–23.

(178) Ann, K. Y.; Buenfeld, N. R. The Effect of Calcium Nitrite on the Chloride-Induced Corrosion of Steel in Concrete. *Mag. Concr. Res.* **2007**, *59* (9), 689–697. https://doi.org/10.1680/macr.2007.59.9.689.

(179) Mammoliti, L.; Hansson, C. M.; Hope, B. B. Corrosion Inhibitors in Concrete Part II: Effect on Chloride Threshold Values for Corrosion of Steel in Synthetic Pore Solutions. *Cem. Concr. Res.* **1999**, *29* (10), 1583–1589.

(180) Ormellese, M.; Berra, M.; Bolzoni, F.; Pastore, T. Corrosion Inhibitors for Chlorides Induced Corrosion in Reinforced Concrete Structures. *Cem. Concr. Res.* **2006**, *36* (3), 536–547. https://doi.org/10.1016/j.cemconres.2005.11.007.

(181) Reou, J. S.; Ann, K. Y. The Electrochemical Assessment of Corrosion Inhibition Effect of Calcium Nitrite in Blended Concretes. *Mater. Chem. Phys.* **2008**, *109* (2), 526–533.

(182) Rosenberg, A. M.; Gaidis, J. M.; Kossivas, T. G.; Previte, R. W. A Corrosion Inhibitor Formulated with Calcium Nitrite for Use in Reinforced Concrete. In *Chloride corrosion of steel in concrete*; ASTM International, 1977.

(183) Gaidis, J. M. Chemistry of Corrosion Inhibitors. *Cem. Concr. Compos.* **2004**, *26* (3), 181–189.

(184) Balonis, M.; Glasser, F. P. Calcium Nitrite Corrosion Inhibitor in Portland Cement: Influence of Nitrite on Chloride Binding and Mineralogy. *J. Am. Ceram. Soc.* **2011**, *94* (7), 2230–2241. https://doi.org/10.1111/j.1551-2916.2010.04362.x.

(185) Ngala, V. T.; Page, C. L.; Page, M. M. Corrosion Inhibitor Systems for Remedial Treatment of Reinforced Concrete. Part 1: Calcium Nitrite. *Corros. Sci.* **2002**, *44* (9), 2073–2087.

(186) Martín-Pérez, B.; Zibara, H.; Hooton, R. D.; Thomas, M. D. A. A Study of the Effect of Chloride Binding on Service Life Predictions. *Cem. Concr. Res.* **2000**, *30* (8), 1215–1223. https://doi.org/10.1016/S0008-8846(00)00339-2.

(187) Oh, B. H.; Jang, S. Y. Effects of Material and Environmental Parameters on Chloride Penetration Profiles in Concrete Structures. *Cem. Concr. Res.* **2007**, *37* (1), 47–53. https://doi.org/10.1016/j.cemconres.2006.09.005.

(188) Galan, I.; Glasser, F. P. Chloride in Cement. *Adv. Cem. Res.* **2014**, *27* (2), 63–97. https://doi.org/10.1680/adcr.13.00067.

(189) Falzone, G.; Balonis, M.; Sant, G. X-AFm Stabilization as a Mechanism of Bypassing Conversion Phenomena in Calcium Aluminate Cements. *Cem. Concr. Res.* **2015**, *72*, 54–68. https://doi.org/10.1016/j.cemconres.2015.02.022.

(190) Birnin-Yauri, U. A.; Glasser, F. P. Friedel's Salt, Ca2Al(OH)6(Cl,OH)·2H2O: Its Solid Solutions and Their Role in Chloride Binding. *Cem. Concr. Res.* **1998**, *28* (12), 1713–1723. https://doi.org/10.1016/S0008-8846(98)00162-8.

(191) Hirao, H.; Yamada, K.; Takahashi, H.; Zibara, H. Chloride Binding of Cement Estimated by Binding Isotherms of Hydrates. *J. Adv. Concr. Technol.* **2005**, *3* (1), 77–84. https://doi.org/10.3151/jact.3.77.

(192) Luo, R.; Cai, Y.; Wang, C.; Huang, X. Study of Chloride Binding and Diffusion in GGBS Concrete. *Cem. Concr. Res.* **2003**, *33* (1), 1–7. https://doi.org/10.1016/S0008-8846(02)00712-3.

(193) Dhir, R. K.; El-Mohr, M. A. K.; Dyer, T. D. Chloride Binding in GGBS Concrete. *Cem. Concr. Res.* **1996**, *26* (12), 1767–1773. https://doi.org/10.1016/S0008-8846(96)00180-9.

(194) Cheewaket, T.; Jaturapitakkul, C.; Chalee, W. Long Term Performance of Chloride Binding Capacity in Fly Ash Concrete in a Marine Environment. *Constr. Build. Mater.* **2010**, *24* (8), 1352–1357. https://doi.org/10.1016/j.conbuildmat.2009.12.039.

(195) Loser, R.; Lothenbach, B.; Leemann, A.; Tuchschmid, M. Chloride Resistance of Concrete and Its Binding Capacity – Comparison between Experimental Results and Thermodynamic Modeling. *Cem. Concr. Compos.* **2010**, *32* (1), 34–42. https://doi.org/10.1016/j.cemconcomp.2009.08.001.

(196) Jones, M. R.; Macphee, D. E.; Chudek, J. A.; Hunter, G.; Lannegrand, R.; Talero, R.; Scrimgeour, S. N. Studies Using 27 Al MAS NMR of AFm and AFt Phases and the Formation of Friedel's Salt. *Cem. Concr. Res.* **2003**, *33* (2), 177–182.

(197) Ampadu, K. O.; Torii, K. Chloride Ingress and Steel Corrosion in Cement Mortars Incorporating Low-Quality Fly Ashes. *Cem. Concr. Res.* **2002**, *32* (6), 893–901. https://doi.org/10.1016/S0008-8846(02)00721-4.

(198) Bentz, D. P.; Garboczi, E. J.; Lu, Y.; Martys, N.; Sakulich, A. R.; Weiss, W. J. Modeling of the Influence of Transverse Cracking on Chloride Penetration into Concrete. *Cem. Concr. Compos.* **2013**, *38*, 65–74. https://doi.org/10.1016/j.cemconcomp.2013.03.003.

(199) Bentz, D. P.; Guthrie, W. S.; Jones, S. Z.; Martys, N. S. Predicting Service Life of Steel-Reinforced Concrete Exposed to Chlorides. *Concr. Int.* **2014**, *36* (9), 55–64.

(200) Jones, S.; Martys, N.; Lu, Y.; Bentz, D. Simulation Studies of Methods to Delay Corrosion and Increase Service Life for Cracked Concrete Exposed to Chlorides. *Cem. Concr. Compos.* **2015**, *58*, 59–69. https://doi.org/10.1016/j.cemconcomp.2014.12.014.

(201) Jensen, M. M.; De Weerdt, K.; Johannesson, B.; Geiker, M. R. Use of a Multi-Species Reactive Transport Model to Simulate Chloride Ingress in Mortar Exposed to NaCl Solution or Sea-Water. *Comput. Mater. Sci.* **2015**, *105*, 75–82. https://doi.org/10.1016/j.commatsci.2015.04.023.

(202) Samson, E.; Marchand, J.; Beaudoin, J. J. Modeling the Influence of Chemical Reactions on the Mechanisms of Ionic Transport in Porous Materials: An Overview. *Cem. Concr. Res.* **2000**, *30* (12), 1895–1902. https://doi.org/10.1016/S0008-8846(00)00458-0.

(203) Truc, O.; Ollivier, J.-P.; Nilsson, L. O. Numerical Simulation of Multi-Species Diffusion. *Mater. Struct.* **2000**, *33* (9), 566–573. https://doi.org/10.1007/BF02480537.

(204) Samson, E.; Marchand, J. Modeling the Transport of Ions in Unsaturated Cement-Based Materials. *Comput. Struct.* **2007**, *85* (23–24), 1740–1756. https://doi.org/10.1016/j.compstruc.2007.04.008.

(205) Sleiman, H.; Amiri, O.; Ait-Mokhtar, A.; Loche, J.-M. Chloride Transport through Unsaturated Concrete: Chloride Profile Simulations and Experimental Validation. *Mag. Concr. Res.* **2012**, *64* (4), 351–359. https://doi.org/10.1680/macr.9.00153.

(206) Jensen, M. M.; Johannesson, B.; Geiker, M. R. Framework for Reactive Mass Transport: Phase Change Modeling of Concrete by a Coupled Mass Transport and Chemical Equilibrium Model. *Comput. Mater. Sci.* **2014**, *92*, 213–223. https://doi.org/10.1016/j.commatsci.2014.05.021.

(207) Luping, T.; Nilsson, L.-O. Chloride Binding Capacity and Binding Isotherms of OPC Pastes and Mortars. *Cem. Concr. Res.* **1993**, *23* (2), 247–253.

(208) Mohammed, T. U.; Hamada, H. Relationship between Free Chloride and Total Chloride Contents in Concrete. *Cem. Concr. Res.* **2003**, *33* (9), 1487–1490. https://doi.org/10.1016/S0008-8846(03)00065-6.

(209) Le Saoût, G.; Kocaba, V.; Scrivener, K. Application of the Rietveld Method to the Analysis of Anhydrous Cement. *Cem. Concr. Res.* **2011**, *41* (2), 133–148. https://doi.org/10.1016/j.cemconres.2010.10.003.

(210) Guirado, F.; Galí, S.; Chinchón, S. Quantitative Rietveld Analysis of Aluminous Cement Clinker Phases. *Cem. Concr. Res.* **2000**, *30* (7), 1023–1029. https://doi.org/10.1016/S0008-8846(00)00289-1.

(211) PSI. GEMS Selektor http://gems.web.psi.ch.

(212) Wagner, T.; Kulik, D. A.; Hingerl, F. F.; Dmytrieva, S. V. GEM-Selektor Geochemical Modeling Package: TSolMod Library and Data Interface for Multicomponent Phase Models. *Can. Mineral.* **2012**, *50* (5), 1173–1195. https://doi.org/10.3749/canmin.50.5.1173.

(213) Filippov, L.; Thomas, F.; Filippova, I.; Yvon, J.; Morillon-Jeanmaire, A. Stabilization of NaCl-Containing Cuttings Wastes in Cement Concrete by in Situ Formed Mineral Phases. *J. Hazard. Mater.* **2009**, *171* (1–3), 731–738. https://doi.org/10.1016/j.jhazmat.2009.06.065.

(214) Chu, K.-Y.; Thompson, A. R. Densities and Refractive Indices of Alcohol-Water Solutions of n-Propyl, Isopropyl, and Methyl Alcohols. *J. Chem. Eng. Data* **1962**, *7* (3), 358–360. https://doi.org/10.1021/je60014a011.

(215) Christensen, B. J.; Coverdale, T.; Olson, R. A.; Ford, S. J.; Garboczi, E. J.; Jennings, H. M.; Mason, T. O. Impedance Spectroscopy of Hydrating Cement-Based Materials: Measurement, Interpretation, and Application. *J. Am. Ceram. Soc.* **1994**, *77* (11), 2789–2804. https://doi.org/10.1111/j.1151-2916.1994.tb04507.x.

(216) Garboczi, E. J.; Bentz, D. P. Computer Simulation of the Diffusivity of Cement-Based Materials. *J. Mater. Sci.* **1992**, *27* (8), 2083–2092. https://doi.org/10.1007/BF01117921.

(217) Barneyback Jr., R. S.; Diamond, S. Expression and Analysis of Pore Fluids from Hardened Cement Pastes and Mortars. *Cem. Concr. Res.* **1981**, *11* (2), 279–285. https://doi.org/10.1016/0008-8846(81)90069-7.

(218) Miller, R. L.; Bradford, W. L.; Peters, N. E. *Specific Conductance: Theoretical Considerations and Application to Analytical Quality Control*; U.S. Geological Survey Water-Supply Paper 2311; U.S. Geological Survey, 1988.

(219) Adamson, A. W.; Gast, A. P. *Physical Chemistry of Surfaces*, 5th ed.; Wiley, 1997.

(220) Sergi, G.; Yu, S. W.; Page, C. L. Diffusion of Chloride and Hydroxyl Ions in Cementitious Materials Exposed to a Saline Environment. *Mag. Concr. Res.* **1992**, *44* (158), 63–69. https://doi.org/10.1680/macr.1992.44.158.63.

(221) Puerta-Falla, G.; Balonis, M.; Falzone, G.; Bauchy, M.; Neithalath, N.; Sant, G. Monovalent Ion Exchange Kinetics of Hydrated Calcium-Alumino Layered Double Hydroxides. *Ind. Eng. Chem. Res.* **2017**, *56* (1), 63–74. https://doi.org/10.1021/acs.iecr.6b03474.

(222) Caré, S. Influence of Aggregates on Chloride Diffusion Coefficient into Mortar. *Cem. Concr. Res.* **2003**, *33* (7), 1021–1028. https://doi.org/10.1016/S0008-8846(03)00009-7.

(223) Shane, J. D.; Mason, T. O.; Jennings, H. M.; Garboczi, E. J.; Bentz, D. P. Effect of the Interfacial Transition Zone on the Conductivity of Portland Cement Mortars. *J. Am. Ceram. Soc.* **2000**, *83* (5), 1137–1144. https://doi.org/10.1111/j.1151-2916.2000.tb01344.x.

(224) Bentz, D. P.; Jensen, O. M.; Coats, A. M.; Glasser, F. P. Influence of Silica Fume on Diffusivity in Cement-Based Materials: I. Experimental and Computer Modeling Studies on Cement Pastes. *Cem. Concr. Res.* **2000**, *30* (6), 953–962. https://doi.org/10.1016/S0008-8846(00)00264-7.

(225) Martys, N. S. *Survey of Concrete Transport Properties and Their Measurement*; National Institute of Standards and Technology, 1996.

(226) Nguyen, T. Q.; Baroghel-Bouny, V.; Dangla, P. Prediction of Chloride Ingress into Saturated Concrete on the Basis of a Multi-Species Model by Numerical Calculations. *Comput. Concr.* **2006**, *3* (6), 401u422.

(227) Samson, E.; Marchand, J. Numerical Solution of the Extended Nernst–Planck Model. *J. Colloid Interface Sci.* **1999**, *215* (1), 1–8. https://doi.org/10.1006/jcis.1999.6145.

(228) Barbarulo, R.; Marchand, J.; Snyder, K. A.; Prené, S. Dimensional Analysis of Ionic Transport Problems in Hydrated Cement Systems: Part 1. Theoretical Considerations. *Cem. Concr. Res.* **2000**, *30* (12), 1955–1960. https://doi.org/10.1016/S0008-8846(00)00383-5.

(229) Friedmann, H.; Amiri, O.; Aït-Mokhtar, A. Physical Modeling of the Electrical Double Layer Effects on Multispecies Ions Transport in Cement-Based Materials. *Cem. Concr. Res.* **2008**, *38* (12), 1394–1400. https://doi.org/10.1016/j.cemconres.2008.06.003.

(230) MacGillivray, A. D. Nernst-Planck Equations and the Electroneutrality and Donnan Equilibrium Assumptions. *J. Chem. Phys.* **1968**, *48* (7), 2903–2907. https://doi.org/10.1063/1.1669549.

(231) Dickson, A. G.; Goyet, C. *Handbook of Methods for the Analysis of the Various Parameters of the Carbon Dioxide System in Sea Water*; publisher not identified, 1994.

(232) Haynes, W. M. *CRC Handbook of Chemistry and Physics*, 96th ed.; CRC Press, 2015.

(233) Aguayo, M.; Yang, P.; Vance, K.; Sant, G.; Neithalath, N. Electrically Driven Chloride Ion Transport in Blended Binder Concretes: Insights from Experiments and Numerical Simulations. *Cem. Concr. Res.* **2014**, *66*, 1–10. https://doi.org/10.1016/j.cemconres.2014.07.022.

(234) Birdsall, A.; Guthrie, W.; Bentz, D. Effects of Initial Surface Treatment Timing on Chloride Concentrations in Concrete Bridge Decks. *Transp. Res. Rec. J. Transp. Res. Board* **2007**, *2028*, 103–110. https://doi.org/10.3141/2028-12.

(235) Lothenbach, B.; Matschei, T.; Möschner, G.; Glasser, F. P. Thermodynamic Modelling of the Effect of Temperature on the Hydration and Porosity of Portland Cement. *Cem. Concr. Res.* **2008**, *38* (1), 1–18. https://doi.org/10.1016/j.cemconres.2007.08.017.

(236) Berke, N. S.; Hicks, M. C. Predicting Chloride Profiles in Concrete. *Corrosion* **1994**, *50* (3), 234–239. https://doi.org/10.5006/1.3293515.

(237) Kassir, M. K.; Ghosn, M. Chloride-Induced Corrosion of Reinforced Concrete Bridge Decks. *Cem. Concr. Res.* **2002**, *32* (1), 139–143. https://doi.org/10.1016/S0008-8846(01)00644-5.

(238) Żemajtis, J.; Weyers, R. Concrete Bridge Service Life Extension Using Sealers in Chloride-Laden Environments. *Transp. Res. Rec. J. Transp. Res. Board* **1996**, *1561*, 1–5. https://doi.org/10.3141/1561-01.

(239) Harris, D.; Sarkar, J.; Ahlborn, T. Characterization of Interface Bond of Ultra-High-Performance Concrete Bridge Deck Overlays. *Transp. Res. Rec. J. Transp. Res. Board* **2011**, *2240*, 40–49. https://doi.org/10.3141/2240-07.

(240) Vance, K.; Falzone, G.; Pignatelli, I.; Bauchy, M.; Balonis, M.; Sant, G. Direct Carbonation of Ca (OH) 2 Using Liquid and Supercritical CO2: Implications for Carbon-Neutral Cementation. *Ind. Eng. Chem. Res.* **2015**, *54* (36), 8908–8918.

(241) Wei, Z.; Wang, B.; Falzone, G.; La Plante, E. C.; Okoronkwo, M. U.; She, Z.; Oey, T.; Balonis, M.; Neithalath, N.; Pilon, L. Clinkering-Free Cementation by Fly Ash Carbonation. *J. CO2 Util.* **2018**, *23*, 117–127.

(242) National Academies of Sciences, Engineering, and Medicine. *Gaseous Carbon Waste Streams Utilization: Status and Research Needs*; The National Academies Press. https://doi.org/10.17226/25232: Washington, DC, 2018; p 254.

(243) Zhang, D.; Ghouleh, Z.; Shao, Y. Review on Carbonation Curing of Cement-Based Materials. *J. CO2 Util.* **2017**, *21*, 119–131.

(244) Nielsen, P.; Baciocchi, R.; Costa, G.; Quaghebeur, M.; Snellings, R. Carbonate-Bonded Construction Materials from Alkaline Residues. *RILEM Tech. Lett.* **2017**, *2*, 53–58. https://doi.org/10.21809/rilemtechlett.2017.50.

(245) Mehdipour, I.; Falzone, G.; Callagon La Plante, E.; Pilon, L.; Simonetti, D.; Neithalath, N.; Sant, G. How Microstructure and Pore Moisture Affect Strength Gain in Portlandite-Enriched Composites That Mineralize CO2. *ACS Sustain. Chem. Eng.* **2019**, *Submitted*.

(246) Biernacki, J. J.; Bullard, J. W.; Sant, G.; Brown, K.; Glasser, F. P.; Jones, S.; Ley, T.; Livingston, R.; Nicoleau, L.; Olek, J.; et al. Cements in the 21st Century: Challenges, Perspectives, and Opportunities. *J. Am. Ceram. Soc.* **2017**, *100* (7), 2746–2773. https://doi.org/10.1111/jace.14948.

(247) Miller, S. A.; John, V. M.; Pacca, S. A.; Horvath, A. Carbon Dioxide Reduction Potential in the Global Cement Industry by 2050. *Cem. Concr. Res.* **2018**, *114*, 115–124. https://doi.org/10.1016/j.cemconres.2017.08.026.

(248) Lehne, J.; Preston, F. *Making Concrete Change: Innovation in Low-Carbon Cement and Concrete*; Chatham House Report; The Royal Institute of International Affairs: London, UK, 2018; p 122.

(249) Cizer, Ö.; Rodriguez-Navarro, C.; Ruiz-Agudo, E.; Elsen, J.; Van Gemert, D.; Van Balen, K. Phase and Morphology Evolution of Calcium Carbonate Precipitated by Carbonation of Hydrated Lime. *J. Mater. Sci.* **2012**, *47* (16), 6151–6165. https://doi.org/10.1007/s10853-012-6535-7.

(250) Leclaire, J.; Heldebrant, D. J. A Call to (Green) Arms: A Rallying Cry for Green Chemistry and Engineering for CO 2 Capture, Utilisation and Storage. *Green Chem.* **2018**.

(251) Hoenig, V.; Hoppe, H.; Emberger, B. *Carbon Capture Technology - Options and Potentials for the Cement Industry*; PCA R&D Serial No. 3022; Portland Cement Association: Skokie, IL, USA, 2007; p 98.

(252) Beruto, D. T.; Botter, R. Liquid-like H2O Adsorption Layers to Catalyze the Ca (OH) 2/CO2 Solid–Gas Reaction and to Form a Non-Protective Solid Product Layer at 20° C. *J. Eur. Ceram. Soc.* **2000**, *20* (4), 497–503.

(253) Shih, S.-M.; Ho, C.-S.; Song, Y.-S.; Lin, J.-P. Kinetics of the Reaction of Ca (OH) 2 with CO2 at Low Temperature. *Ind. Eng. Chem. Res.* **1999**, *38* (4), 1316–1322.

(254) *ASTM C618 - 19: Standard Specification for Coal Fly Ash and Raw or Calcined Natural Pozzolan for Use in Concrete*; ASTM International: West Conshohocken, PA, 2019.

(255) Steinour, H. H. Some Effects of Carbon Dioxide on Mortars and Concrete-Discussion. *J Am Concr Inst* **1959**, *30* (2), 905–907.

(256) Lee, D. K. An Apparent Kinetic Model for the Carbonation of Calcium Oxide by Carbon Dioxide. *Chem. Eng. J.* **2004**, *100* (1), 71–77. https://doi.org/10.1016/j.cej.2003.12.003.

(257) Dickinson, C. F.; Heal, G. R. Solid–Liquid Diffusion Controlled Rate Equations. *Thermochim. Acta* **1999**, *340–341*, 89–103. https://doi.org/10.1016/S0040-6031(99)00256-7.

(258) Castellote, M.; Fernandez, L.; Andrade, C.; Alonso, C. Chemical Changes and Phase Analysis of OPC Pastes Carbonated at Different CO2 Concentrations. *Mater. Struct.* **2008**, *42* (4), 515–525. https://doi.org/10.1617/s11527-008-9399-1.

(259) Wei, Z.; Wang, B.; Falzone, G.; La Plante, E. C.; Okoronkwo, M. U.; She, Z.; Oey, T.; Balonis, M.; Neithalath, N.; Pilon, L.; et al. Clinkering-Free Cementation by Fly Ash Carbonation. *J. CO2 Util.* **2018**, *23*, 117–127. https://doi.org/10.1016/j.jcou.2017.11.005.

(260) Beaudoin, J. J.; Feldman, R. F.; Tumidajski, P. J. Pore Structure of Hardened Portland Cement Pastes and Its Influence on Properties. *Adv. Cem. Based Mater.* **1994**, *1* (5), 224–236.

(261) Gartner, E. M.; Macphee, D. E. A Physico-Chemical Basis for Novel Cementitious Binders. *Cem. Concr. Res.* **2011**, *41* (7), 736–749. https://doi.org/10.1016/j.cemconres.2011.03.006.

(262) Provis, J. L. Grand Challenges in Structural Materials. *Front. Mater.* **2015**, *2*, 31.

(263) Bertos, M. F.; Simons, S. J. R.; Hills, C. D.; Carey, P. J. A Review of Accelerated Carbonation Technology in the Treatment of Cement-Based Materials and Sequestration of CO2. *J. Hazard. Mater.* **2004**, *112* (3), 193–205.

(264) Baroghel-Bouny, V. Water Vapour Sorption Experiments on Hardened Cementitious Materials: Part I: Essential Tool for Analysis of Hygral Behaviour and Its Relation to Pore Structure. *Cem. Concr. Res.* **2007**, *37* (3), 414–437.

(265) Millington, R. J.; Quirk, J. P. Permeability of Porous Solids. *Trans. Faraday Soc.* **1961**, *57*, 1200–1207.

(266) Crank, J. *The Mathematics of Diffusion*; Oxford university press, 1979.

(267) Rostami, V.; Shao, Y.; Boyd, A. J.; He, Z. Microstructure of Cement Paste Subject to Early Carbonation Curing. *Cem. Concr. Res.* **2012**, *42* (1), 186–193.

(268) Zhang, D.; Li, V. C.; Ellis, B. R. Optimal Pre-Hydration Age for CO2 Sequestration through Portland Cement Carbonation. *ACS Sustain. Chem. Eng.* **2018**, *6* (12), 15976–15981.

(269) Oey, T.; Kumar, A.; Falzone, G.; Huang, J.; Kennison, S.; Bauchy, M.; Neithalath, N.; Bullard, J. W.; Sant, G. The Influence of Water Activity on the Hydration Rate of Tricalcium Silicate. *J. Am. Ceram. Soc.* **2016**, *99* (7), 2481–2492.

(270) Gartner, E.; Sui, T. Alternative Cement Clinkers. *Cem. Concr. Res.* **2018**, *114*, 27–39.

(271) Butt, D. P.; Lackner, K. S.; Wendt, C. H.; Conzone, S. D.; Kung, H.; Lu, Y.-C.; Bremser, J. K. Kinetics of Thermal Dehydroxylation and Carbonation of Magnesium Hydroxide. *J. Am. Ceram. Soc.* **1996**, *79* (7), 1892–1898.

(272) *ASTM C150/C150M − 18: Standard Specification for Portland Cement*; ASTM International: West Conshohocken, PA, 2018.

(273) *ASTM C618 − 15: Standard Specification for Coal Fly Ash and Raw or Calcined Natural Pozzolan for Use in Concrete*; ASTM International: West Conshohocken, PA, 2015.

(274) *ASTM C33/C33M − 18: Standard Specification for Concrete Aggregates*; ASTM International: West Conshohocken, PA, 2018.

(275) *ASTM C305 − 14: Standard Practice for Mechanical Mixing of Hydraulic Cement Pastes and Mortars of Plastic Consistency*; ASTM International: West Conshohocken, PA, 2014.

(276) *ASTM C128 − 15: Standard Test Method for Relative Density (Specific Gravity) and Absorption of Fine Aggregate*; ASTM International: West Conshohocken, PA, 2015.

(277) Rochelle, G. T. Amine Scrubbing for CO2 Capture. *Science* **2009**, *325* (5948), 1652–1654.

(278) Pane, I.; Hansen, W. Investigation of Blended Cement Hydration by Isothermal Calorimetry and Thermal Analysis. *Cem. Concr. Res.* **2005**, *35* (6), 1155–1164.

(279) Arora, A.; Sant, G.; Neithalath, N. Ternary Blends Containing Slag and Interground/Blended Limestone: Hydration, Strength, and Pore Structure. *Constr. Build. Mater.* **2016**, *102*, 113–124.

(280) *ASTM C39/C39M − 18: Standard Test Method for Compressive Strength of Cylindrical Concrete Specimens*; ASTM International: West Conshohocken, PA, 2018.

(281) Montes, F.; Valavala, S.; Haselbach, L. M. A New Test Method for Porosity Measurements of Portland Cement Pervious Concrete. *J. ASTM Int.* **2005**, *2* (1), 1–13.

(282) Kumar, A.; Ketel, S.; Vance, K.; Oey, T.; Neithalath, N.; Sant, G. Water Vapor Sorption in Cementitious Materials—Measurement, Modeling and Interpretation. *Transp. Porous Media* **2014**, *103* (1), 69–98.

(283) Egan, G.; Kumar, A.; Neithalath, N.; Sant, G. Re-Examining the Influence of the Inclusion Characteristics on the Drying Shrinkage of Cementitious Composites. *Constr. Build. Mater.* **2017**, *146*, 713–722.

(284) Houst, Y. F.; Wittmann, F. H. Influence of Porosity and Water Content on the Diffusivity of CO2 and O2 through Hydrated Cement Paste. *Cem. Concr. Res.* **1994**, *24* (6), 1165–1176.

(285) Vance, K.; Kumar, A.; Sant, G.; Neithalath, N. The Rheological Properties of Ternary Binders Containing Portland Cement, Limestone, and Metakaolin or Fly Ash. *Cem. Concr. Res.* **2013**, *52*, 196–207.

(286) Baănt, Z. P.; Raftshol, W. J. Effect of Cracking in Drying and Shrinkage Specimens. *Cem. Concr. Res.* **1982**, *12* (2), 209–226.

(287) Deschner, F.; Lothenbach, B.; Winnefeld, F.; Neubauer, J. Effect of Temperature on the Hydration of Portland Cement Blended with Siliceous Fly Ash. *Cem. Concr. Res.* **2013**, *52*, 169–181.

(288) Hüsken, G.; Brouwers, H. J. H. On the Early-Age Behavior of Zero-Slump Concrete. *Cem. Concr. Res.* **2012**, *42* (3), 501–510.

(289) Wolfs, R. J. M.; Bos, F. P.; Salet, T. A. M. Early Age Mechanical Behaviour of 3D Printed Concrete: Numerical Modelling and Experimental Testing. *Cem. Concr. Res.* **2018**, *106*, 103–116.

(290) Wang, D.; Bao, A.; Kunc, W.; Liss, W. Coal Power Plant Flue Gas Waste Heat and Water Recovery. *Appl. Energy* **2012**, *91* (1), 341–348.

(291) Shuangchen, M.; Jin, C.; Kunling, J.; Lan, M.; Sijie, Z.; Kai, W. Environmental Influence and Countermeasures for High Humidity Flue Gas Discharging from Power Plants. *Renew. Sustain. Energy Rev.* **2017**, *73*, 225–235.

(292) Committee, A. C. I.; Institute, A. C.; Standardization, I. O. for. Building Code Requirements for Structural Concrete (ACI 318-14) and Commentary; American Concrete Institute, 2014.

(293) Monkman, S.; MacDonald, M. Carbon Dioxide Upcycling into Industrially Produced Concrete Blocks. *Constr. Build. Mater.* **2016**, *124*, 127–132.

(294) Alvarez, D.; Abanades, J. C. Determination of the Critical Product Layer Thickness in the Reaction of CaO with CO2. *Ind. Eng. Chem. Res.* **2005**, *44* (15), 5608–5615.

(295) Galan, I.; Glasser, F. P.; Baza, D.; Andrade, C. Assessment of the Protective Effect of Carbonation on Portlandite Crystals. *Cem. Concr. Res.* **2015**, *74*, 68–77.

(296) Rostami, V.; Shao, Y.; Boyd, A. J. Carbonation Curing versus Steam Curing for Precast Concrete Production. *J. Mater. Civ. Eng.* **2011**, *24* (9), 1221–1229.

(297) Collier, N. C.; Sharp, J. H.; Milestone, N. B.; Hill, J.; Godfrey, I. H. The Influence of Water Removal Techniques on the Composition and Microstructure of Hardened Cement Pastes. *Cem. Concr. Res.* **2008**, *38* (6), 737–744.